

MINISTÉRIO DA EDUCAÇÃO  
UNIVERSIDADE FEDERAL DO RIO GRANDE DO SUL  
PROGRAMA DE PÓS-GRADUAÇÃO EM ENGENHARIA MECÂNICA

NUMERICAL ANALYSIS OF THE SOLIDITY EFFECTS OVER THE AERODYNAMIC  
PERFORMANCE OF A SMALL WIND TURBINE

por

Gustavo Dias Fleck

Tese para obtenção  
do Título de Doutor em Engenharia

Porto Alegre, Outubro de 2017

NUMERICAL ANALYSIS OF THE SOLIDITY EFFECTS OVER THE AERODYNAMIC  
PERFORMANCE OF A SMALL WIND TURBINE

por

Gustavo Dias Fleck

Engenheiro Mecânico, Mestre em Engenharia

Tese submetida ao Programa de Pós-Graduação em Engenharia Mecânica, da Escola de Engenharia da Universidade Federal do Rio Grande do Sul, como parte dos requisitos necessários para obtenção do Título de

Doutor em Engenharia

Área de Concentração: Fenômenos de Transporte

Orientador: Prof<sup>ª</sup>. Dr<sup>ª</sup>. Adriane Prisco Petry

Aprovada por:

Prof<sup>ª</sup>. Dr<sup>ª</sup>. Sonia Magalhães dos Santos ..... EE/FURG

Prof. Dr. Francis Henrique Ramos França ..... PROMEC/UFRGS

Prof. Dr. Luiz Alberto Oliveira Rocha ..... PROMEC/UFRGS

Prof. Dr. Jakson M. Vassoler

Coordenador do PROMEC

Porto Alegre, 26 de Outubro de 2017

*To my parents, Wanderley and Roseli,  
and to my grandmother, Edi.*

## ACKNOWLEDGEMENTS

Many people contributed, in person or through institutions, to the successful completion of this thesis. First of all, I thank my parents, Wanderley Fleck and Roseli Fleck, and my grandmother, Edi Dias, from whom I received unconditional support, as well as material aid.

I extend my gratitude to Dr. Adriane Petry, my supervisor at UFRGS, and to Dr. David Wood, my supervisor during my academic exchange at University of Calgary, which lasted roughly 10 months. I am grateful to both for the friendship, the shared knowledge and the opportunity to conduct research in one of my favorite subjects. To Dr. Wood, especially, for his willingness to accept an international student and his efforts to arrange funding during my time in Calgary.

Special thanks to all the friends I made throughout these four years, both at UFRGS (laboratories GESTE and LMF) and at UCalgary (EEEL's room 269 and Petro Canada Building's room 423). They are too many to mention.

To the evaluating committee, composed of Dr. Francis França, Dr. Luiz Alberto Rocha and Dr. Sônia Santos, for the valuable feedback in the thesis review.

To all the staff at the Graduate Program in Mechanical Engineering at UFRGS, at the Department of Mechanical and Manufacturing Engineering and at the International Student Services at UCalgary.

Last but not least, to the funding agencies through which I received financial support. In Brazil, the scholarship was granted by the Ministry of Education through CAPES, and in Canada the financial aid was provided by the Government of Canada through the Emerging Leaders of the Americas Program (ELAP). The supercomputing facilities must also be acknowledged: CESUP (UFRGS's Center for Supercomputing) and Westgrid (Western Canada's supercomputing network).

## ABSTRACT

This thesis presents a methodology of two-dimensional airfoil simulation focusing on its application on the design and optimization of blades and rotors of small horizontal axis wind turbines, and its application in a set of numerical simulations involving high rotor solidity and low- $Re$  effects. This methodology includes grid generation, selection of numerical methods and validation, reflecting the most successful practices in airfoil simulation, and was applied in the simulation of the NACA 0012, S809 and SD7062 airfoils. The ANSYS Fluent commercial code was used in all simulations. Results for the isolated NACA 0012 and S809 airfoils at high Reynolds numbers show that the Transition SST ( $\gamma$ - $Re_\theta$ ) turbulence model produces results closer to experimental data than those yielded by the SST  $k$ - $\omega$  model for  $C_L$  and  $C_D$ , having also produced  $C_P$  plots that show good agreement to the same experimental data. Plots of  $C_L$ ,  $C_D$ ,  $C_F$  and  $C_P$  for the SD7062 airfoil are presented, for simulations at 20 different operating conditions. The  $C_F$  and  $C_P$  distributions evidence the negative impact of the laminar separation bubble in the range of Reynolds numbers evaluated. Results show that, for  $Re$  between 25,000 and 125,000, drag increases with decreasing  $Re$ . A blade design generated using the SWRDC optimization code, based on genetic algorithms, is presented. Three sections of the resulting blade shape were selected and were tested in a set of 45 simulations, under an array of operating conditions defined by solidity, angle of attack and TSR. Results show that the laminar separation bubble moves towards the leading edge with increasing solidity, angle of attack and TSR. Furthermore,  $C_P$  plots show an increase in pressure on both surfaces when the airfoil is subject to solidity effects, although these effects show an increase in the lift-to-drag ratio at the conditions evaluated.

Keywords: Airfoils; Low Reynolds Numbers; Computational Fluid Dynamics; Laminar Separation Bubble; Small Wind Turbines; Solidity; Transition

## RESUMO

O presente trabalho apresenta uma metodologia de simulação numérica de perfis aerodinâmicos bidimensionais com foco na utilização para o projeto e otimização de pás e rotores de pequenas turbinas eólicas de eixo horizontal, bem como o emprego desses métodos em simulações nas quais efeitos de alta solidez do rotor e baixos números de Reynolds são avaliados. Essa metodologia inclui geração de malhas, seleção de métodos numéricos e validação, tendo as escolhas sido guiadas pelas práticas mais bem sucedidas na simulação de perfis aerodinâmicos, e foi aplicada na simulação dos aerofólios NACA 0012, S809 e SD7062. O código comercial ANSYS Fluent foi utilizado em todas as simulações. Na simulação de aerofólios isolados a altos números de Reynolds dos perfis NACA 0012 e S809, o modelo Transition SST ( $\gamma$ - $Re_{\theta}$ ) apresentou resultados mais próximos a dados experimentais do que aqueles apresentados pelo modelo  $k-\omega$  SST para  $C_L$  e  $C_D$ , além de produzir resultados para  $C_P$  que mostraram boa precisão quando comparados aos mesmos dados experimentais. Resultados de  $C_L$ ,  $C_D$ ,  $C_F$  e  $C_P$  são apresentados para 20 diferentes condições de operação às quais o perfil SD7062 foi submetido, com números de Reynolds variando entre 25.000 e 125.000. As distribuições dos dois últimos coeficientes sobre os dorsos do aerofólio evidenciam com clareza a presença e magnitude da bolha de separação laminar. Os coeficientes de sustentação e arrasto mostram o impacto negativo da presença da bolha nessa faixa de números de Reynolds. Além disso, nos casos simulados, o arrasto aumenta em função da diminuição do  $Re$ . Um design de pá produzido com o auxílio do código de otimização SWRDC, baseado em algoritmos genéticos, é apresentado. Três seções ao longo da envergadura dessa pá foram simuladas em uma bateria de 45 simulações, sob diversas condições de operação em função de solidez, ângulo de ataque e razão de velocidade de ponta de pá. Esses resultados mostram que a bolha de separação laminar se move na direção do bordo de ataque com o aumento da solidez, do ângulo de ataque e da TSR. Além disso, distribuições do  $C_P$  mostram aumento de pressão em ambos os dorsos do perfil quando submetido aos efeitos da solidez, embora esses efeitos tenham sido responsáveis por um aumento na relação  $C_L/C_D$  nos casos estudados.

Palavras-chave: Aerofólios; Baixos números de Reynolds; Bolha de Separação Laminar; Dinâmica dos Fluidos Computacional; Pequenas Turbinas Eólicas; Solidez; Transição

## TABLE OF CONTENTS

<b>1</b>	<b>INTRODUCTION .....</b>	<b>1</b>
1.1	History .....	2
1.2	Small wind turbines .....	3
1.3	Aerodynamics .....	5
1.4	Airfoils and shape optimization .....	6
1.5	Purpose of this work .....	10
<b>2</b>	<b>LITERATURE REVIEW .....</b>	<b>11</b>
2.1	Design and optimization of airfoils and blades .....	11
2.2	Transition modeling in CFD .....	20
2.3	Starting performance .....	21
2.4	Solidity effects .....	23
2.5	Low Reynolds numbers and stall delay .....	25
<b>3</b>	<b>WIND TURBINE DESIGN .....</b>	<b>28</b>
3.1	The Actuator Disc concept .....	28
3.2	Power coefficient .....	30
3.3	The Betz limit .....	31
3.4	Rotor solidity .....	32
3.5	Blade Element Theory .....	33
3.6	Blade element momentum theory .....	35
3.7	Optimal blade design for variable-speed operation .....	37
3.8	Corrections to the classic methodology .....	39
3.8.1	Tip losses .....	39
3.8.2	Three-dimensional effects .....	41
3.9	The power curve .....	41
<b>4</b>	<b>MATHEMATICAL AND NUMERICAL FLOW MODELING .....</b>	<b>43</b>
4.1	Fundamental equations (Navier-Stokes and Continuity).....	43
4.2	Turbulence modeling .....	45
4.2.1	The Reynolds averaging process .....	45
4.2.2	Turbulence models.....	47
4.2.3	Original and SST $k-\omega$ models .....	49
4.2.4	Transition SST model .....	52
4.3	Numerical methods in flow simulation.....	53
4.3.1	Discretization of the governing equations .....	54
4.3.2	Spatial discretization.....	55
4.3.3	Temporal discretization .....	56
<b>5</b>	<b>TWO-DIMENSIONAL AIRFOIL SIMULATIONS .....</b>	<b>57</b>
5.1	Methods .....	57
5.1.1	Airfoil modeling .....	57
5.1.2	Values of $y^+$ at the airfoils .....	59
5.1.3	Grid construction .....	60
5.1.4	Numerical methods employed .....	60
5.1.5	Grid quality study .....	62
5.2	Results.....	63
5.2.1	NACA 0012 .....	63

5.2.2	S809 .....	65
5.2.3	SD 7062 .....	67
<b>6</b>	<b>UFRGS SMALL WIND TURBINE PROJECT .....</b>	<b>84</b>
6.1	Design constraints.....	84
6.2	Blade generated by SWRDC .....	84
6.2.1	Small Wind-Turbine Rotor Design Code .....	84
6.2.2	Conditions .....	85
6.2.3	Resulting blade .....	86
<b>7</b>	<b>HIGH ROTOR SOLIDITY AND ITS EFFECTS .....</b>	<b>90</b>
7.1	CFD simulations of selected solidity conditions .....	90
7.2	Results.....	94
7.2.1	Lift and drag coefficients.....	95
7.2.2	Pressure and skin friction coefficients .....	104
<b>8</b>	<b>CONCLUSIONS .....</b>	<b>108</b>
8.1	Advice for future work .....	110
8.2	Afterword.....	110
	<b>BIBLIOGRAPHY.....</b>	<b>111</b>
	<b>APPENDIX A – Individual <math>C_F</math> and <math>C_P</math> plots for the SD7062.....</b>	<b>118</b>
	<b>APPENDIX B – Individual <math>C_F</math> and <math>C_P</math> plots for the solidity cases .....</b>	<b>125</b>



## LIST OF FIGURES

Figure 1.1 – Examples of small wind turbines [Wood, 2011a].....	4
Figure 1.2 – Experimental flow visualization of the LSB [Lyon et al., 1997].....	8
Figure 2.1 – Examples of small turbines with curved blades.....	17
Figure 2.2 – Pareto front and airfoils obtained [Ribeiro, 2012]. .....	19
Figure 2.3 – Starting performance of the 5-kW turbine [Mayer et al., 2001] .....	23
Figure 2.4 – Vectors showing the presence of the LSB [Shah et al., 2015].....	27
Figure 3.1 – The energy extracting streamtube of a wind turbine.....	29
Figure 3.2 – Representation of an actuator disc and streamtube .....	29
Figure 3.3 – Forces, velocities and angles at a blade element.....	34
Figure 3.4 – Power coefficient versus tip speed ratio performance curve .....	37
Figure 3.5 – Power curves for two different Wind turbines operating at sea level as functions of the wind speed at hub height. Bergey 10 kW BWC XL (a) and Vestas 2 MW V80 (b). ....	42
Figure 5.1 – Airfoils simulated. Top: NACA 0012, middle: S809, bottom: DS7062.....	58
Figure 5.2 – Circular domains, external and internal (not to scale) .....	58
Figure 5.3 – Computational grid around the NACA 0012 airfoil .....	61
Figure 5.4 – Aerodynamic coefficients versus AOA calculated by SST $k-\omega$ and Transition SST compared to experimental data, NACA 0012. (a) $C_L$ , (b) $C_D$ .....	64
Figure 5.5 – $C_p$ plots vs experimental data, S809, AOA = 0 deg.....	68
Figure 5.6 – $C_p$ plots vs. experimental data, S809, AOA = 1.02 deg.....	68
Figure 5.7 – $C_p$ plots vs. experimental data, S809, AOA = 5.13 deg.....	69
Figure 5.8 – $C_p$ plots vs. experimental data, S809, AOA = 9.22 deg.....	69
Figure 5.9 – $C_L$ vs. AOA at low $Re$ , SD7062. Experimental data for $Re = 100,000$ .....	74
Figure 5.10 – $C_D$ vs. AOA at low $Re$ , SD7062. Experimental data for $Re = 100,000$ .....	74
Figure 5.11 – $L/D$ vs. AOA at low $Re$ , SD7062. Experimental data for $Re = 100,000$ .....	75
Figure 5.12 – Example of upper-surface $C_F$ plot and comparison with velocity field, with LSB shown in detail, $Re = 125,000$ , AOA = 2 deg.....	75
Figure 5.13 – Velocity vectors showing the LSB in detail, $Re = 125,000$ , AOA = 2 deg. ....	76
Figure 5.14 – $C_F$ vs. $x/c$ , SD7062, $Re = 25,000$ . Left: upper surf., right: lower surf.....	76
Figure 5.15 – $C_F$ vs. $x/c$ , SD7062, $Re = 50,000$ . Left: upper surf., right: lower surf.....	77
Figure 5.16 – $C_F$ vs. $x/c$ , SD7062, $Re = 75,000$ . Left: upper surf., right: lower surf.....	77
Figure 5.17 – $C_F$ vs. $x/c$ , SD7062, $Re = 100,000$ . Left: upper surf., right: lower surf.....	77
Figure 5.18 – $C_F$ vs. $x/c$ , SD7062, $Re = 125,000$ . Left: upper surf., right: lower surf.....	78
Figure 5.19 – $C_F$ vs. $x/c$ , SD7062, AOA = 0 deg. Left: upper surf., right: lower surf. ....	78
Figure 5.20 – $C_F$ vs. $x/c$ , SD7062, AOA = 2 deg. Left: upper surf., right: lower surf. ....	78
Figure 5.21 – $C_F$ vs. $x/c$ , SD7062, AOA = 4 deg. Left: upper surf., right: lower surf. ....	79
Figure 5.22 – $C_F$ vs. $x/c$ , SD7062, AOA = 6 deg. Left: upper surf., right: lower surf. ....	79
Figure 5.23 – $C_p$ vs. $x/c$ , SD7062, $Re = 25,000$ . Left: upper surf., right: lower surf.....	80
Figure 5.24 – $C_p$ vs. $x/c$ , SD7062, $Re = 50,000$ . Left: upper surf., right: lower surf.....	80
Figure 5.25 – $C_p$ vs. $x/c$ , SD7062, $Re = 75,000$ . Left: upper surf., right: lower surf.....	80
Figure 5.26 – $C_p$ vs. $x/c$ , SD7062, $Re = 100,000$ . Left: upper surf., right: lower surf.....	81
Figure 5.27 – $C_p$ vs. $x/c$ , SD7062, $Re = 125,000$ . Left: upper surf., right: lower surf.....	81
Figure 5.28 – $C_p$ vs. $x/c$ , SD7062, AOA = 0 deg. Left: upper surf., right: lower surf. ....	81
Figure 5.29 – $C_p$ vs. $x/c$ , SD7062, AOA = 2 deg. Left: upper surf., right: lower surf. ....	82
Figure 5.30 – $C_p$ vs. $x/c$ , SD7062, AOA = 4 deg. Left: upper surf., right: lower surf. ....	82
Figure 5.31 – $C_p$ vs. $x/c$ , SD7062, AOA = 6 deg. Left: upper surf., right: lower surf. ....	82

Figure 6.1 – Performance curves of the rotor designed with the resulting blades. (a): $C_{Pwr}$ vs. TSR curve, (b): $C_{Thr}$ vs. TSR curve .....	88
Figure 6.2 – A depiction of the resulting blade .....	89
Figure 7.1 – Local blade spacing ( $Sp$ ), defined as the distance between any point in a given blade section and the same point in the corresponding section of the adjacent blades. ....	91
Figure 7.2 – Part of the computational domain for the solidity case S3.....	92
Figure 7.3 – Example of velocity contours for an infinite airfoil cascade .....	94
Figure 7.4 – $C_L$ vs. AOA for $u = 5$ m/s, SD7062 subject to solidity effects .....	99
Figure 7.5 – $C_L$ vs. AOA for $u = 8$ m/s, SD7062 subject to solidity effects .....	99
Figure 7.6 – $C_L$ vs. AOA for $u = 11$ m/s, SD7062 subject to solidity effects .....	100
Figure 7.7 – $C_D$ vs. AOA for $u = 5$ m/s, SD7062 subject to solidity effects .....	100
Figure 7.8 – $C_D$ vs. AOA for $u = 8$ m/s, SD7062 subject to solidity effects .....	101
Figure 7.9 – $C_D$ vs. AOA for $u = 11$ m/s, SD7062 subject to solidity effects .....	101
Figure 7.10 – $L/D$ vs. AOA for $u = 5$ m/s, SD7062 subject to solidity effects .....	102
Figure 7.11 – $L/D$ vs. AOA for $u = 8$ m/s, SD7062 subject to solidity effects .....	102
Figure 7.12 – $L/D$ vs. AOA for $u = 11$ m/s, SD7062 subject to solidity effects .....	103
Figure 7.13 – Comparison between 5-30-S3 and 100k_4, left: $C_F$ , right: $C_P$ .....	105
Figure 7.14 – Comparison between 5-40-S1 and 100k_2, left: $C_F$ , right: $C_P$ .....	105
Figure 7.15 – Comparison between 8-30-S1 and 125k_4, left: $C_F$ , right: $C_P$ .....	105
Figure A.1 – SD7062 results, $Re = 25,000$ , AOA = 0 deg., left: $C_F$ , right: $C_P$ .....	118
Figure A.2 – SD7062 results, $Re = 25,000$ , AOA = 2 deg., left: $C_F$ , right: $C_P$ .....	118
Figure A.3 – SD7062 results, $Re = 25,000$ , AOA = 4 deg., left: $C_F$ , right: $C_P$ .....	119
Figure A.4 – SD7062 results, $Re = 25,000$ , AOA = 6 deg., left: $C_F$ , right: $C_P$ .....	119
Figure A.5 – SD7062 results, $Re = 50,000$ , AOA = 0 deg., left: $C_F$ , right: $C_P$ .....	119
Figure A.6 – SD7062 results, $Re = 50,000$ , AOA = 2 deg., left: $C_F$ , right: $C_P$ .....	120
Figure A.7 – SD7062 results, $Re = 50,000$ , AOA = 4 deg., left: $C_F$ , right: $C_P$ .....	120
Figure A.8 – SD7062 results, $Re = 50,000$ , AOA = 6 deg., left: $C_F$ , right: $C_P$ .....	120
Figure A.9 – SD7062 results, $Re = 75,000$ , AOA = 0 deg., left: $C_F$ , right: $C_P$ .....	121
Figure A.10 – SD SD7062 results, $Re = 75,000$ , AOA = 2 deg., left: $C_F$ , right: $C_P$ .....	121
Figure A.11 – SD7062 results, $Re = 75,000$ , AOA = 4 deg., left: $C_F$ , right: $C_P$ .....	121
Figure A.12 – SD7062 results, $Re = 75,000$ , AOA = 6 deg., left: $C_F$ , right: $C_P$ .....	122
Figure A.13 – SD7062 results, $Re = 100,000$ , AOA = 0 deg., left: $C_F$ , right: $C_P$ .....	122
Figure A.14 – SD7062 results, $Re = 100,000$ , AOA = 2 deg., left: $C_F$ , right: $C_P$ .....	122
Figure A.15 – SD7062 results, $Re = 100,000$ , AOA = 4 deg., left: $C_F$ , right: $C_P$ .....	123
Figure A.16 – SD7062 results, $Re = 100,000$ , AOA = 6 deg., left: $C_F$ , right: $C_P$ .....	123
Figure A.17 – SD7062 results, $Re = 125,000$ , AOA = 0 deg., left: $C_F$ , right: $C_P$ .....	123
Figure A.18 – SD7062 results, $Re = 125,000$ , AOA = 2 deg., left: $C_F$ , right: $C_P$ .....	124
Figure A.19 – SD7062 results, $Re = 125,000$ , AOA = 4 deg., left: $C_F$ , right: $C_P$ .....	124
Figure A.20 – SD7062 results, $Re = 125,000$ , AOA = 6 deg., left: $C_F$ , right: $C_P$ .....	124
Figure B.1 – 5-30-S1 results, solidity = 0.1, $u = 5$ m/s, TSR = 3.0, left: $C_F$ , right: $C_P$ .....	125
Figure B.2 – 5-30-S2 results, solidity = 0.2, $u = 5$ m/s, TSR = 3.0, left: $C_F$ , right: $C_P$ .....	125
Figure B.3 – 5-30-S3 results, solidity = 0.3, $u = 5$ m/s, TSR = 3.0, left: $C_F$ , right: $C_P$ .....	126
Figure B.4 – 5-32-S1 results, solidity = 0.1, $u = 5$ m/s, TSR = 3.25, left: $C_F$ , right: $C_P$ .....	126
Figure B.5 – 5-32-S2 results, solidity = 0.2, $u = 5$ m/s, TSR = 3.25, left: $C_F$ , right: $C_P$ .....	126
Figure B.6 – 5-32-S3 results, solidity = 0.3, $u = 5$ m/s, TSR = 3.25, left: $C_F$ , right: $C_P$ .....	127
Figure B.7 – 5-35-S1 results, solidity = 0.1, $u = 5$ m/s, TSR = 3.5, left: $C_F$ , right: $C_P$ .....	127
Figure B.8 – 5-35-S2 results, solidity = 0.2 $u = 5$ m/s, TSR = 3.5, left: $C_F$ , right: $C_P$ .....	127

Figure B.9 – 5-35-S3 results, solidity = 0.3, u = 5 m/s, TSR = 3.5, left: $C_F$ , right: $C_P$ .....	128
Figure B.10 – 5-37-S1 results, solidity = 0.1, u = 5 m/s, TSR = 3.75, left: $C_F$ , right: $C_P$ .....	128
Figure B.11 – 5-37-S2 results, solidity = 0.2, u = 5 m/s, TSR = 3.75, left: $C_F$ , right: $C_P$ .....	128
Figure B.12 – 5-37-S3 results, solidity = 0.3, u = 5 m/s, TSR = 3.75, left: $C_F$ , right: $C_P$ .....	129
Figure B.13 – 5-40-S1 results, solidity = 0.1, u = 5 m/s, TSR = 4.0, left: $C_F$ , right: $C_P$ .....	129
Figure B.14 – 5-40-S2 results, solidity = 0.2, u = 5 m/s, TSR = 4.0, left: $C_F$ , right: $C_P$ .....	129
Figure B.15 – 5-40-S3 results, solidity = 0.3, u = 5 m/s, TSR = 4.0, left: $C_F$ , right: $C_P$ .....	130
Figure B.16 – 8-30-S1 results, solidity = 0.1, u = 8 m/s, TSR = 3.0, left: $C_F$ , right: $C_P$ .....	130
Figure B.17 – 8-30-S2 results, solidity = 0.2, u = 8 m/s, TSR = 3.0, left: $C_F$ , right: $C_P$ .....	130
Figure B.18 – 8-30-S3 results, solidity = 0.3, u = 8 m/s, TSR = 3.0, left: $C_F$ , right: $C_P$ .....	131
Figure B.19 – 8-32-S1 results, solidity = 0.1, u = 8 m/s, TSR = 3.25, left: $C_F$ , right: $C_P$ .....	131
Figure B.20 – 8-32-S2 results, solidity = 0.2, u = 8 m/s, TSR = 3.25, left: $C_F$ , right: $C_P$ .....	131
Figure B.21 – 8-32-S3 results, solidity = 0.3, u = 8 m/s, TSR = 3.25, left: $C_F$ , right: $C_P$ .....	132
Figure B.22 – 8-35-S1 results, solidity = 0.1, u = 8 m/s, TSR = 3.5, left: $C_F$ , right: $C_P$ .....	132
Figure B.23 – 8-35-S2 results, solidity = 0.2, u = 8 m/s, TSR = 3.5, left: $C_F$ , right: $C_P$ .....	132
Figure B.24 – 8-35-S3 results, solidity = 0.3, u = 8 m/s, TSR = 3.5, left: $C_F$ , right: $C_P$ .....	133
Figure B.25 – 8-37-S1 results, solidity = 0.1, u = 8 m/s, TSR = 3.75, left: $C_F$ , right: $C_P$ .....	133
Figure B.26 – 8-37-S2 results, solidity = 0.2, u = 8 m/s, TSR = 3.75, left: $C_F$ , right: $C_P$ .....	133
Figure B.27 – 8-37-S3 results, solidity = 0.3, u = 8 m/s, TSR = 3.75, left: $C_F$ , right: $C_P$ .....	134
Figure B.28 – 8-40-S1 results, solidity = 0.1, u = 8 m/s, TSR = 4.0, left: $C_F$ , right: $C_P$ .....	134
Figure B.29 – 8-40-S2 results, solidity = 0.2, u = 8 m/s, TSR = 4.0, left: $C_F$ , right: $C_P$ .....	134
Figure B.30 – 8-40-S3 results, solidity = 0.3, u = 8 m/s, TSR = 4.0, left: $C_F$ , right: $C_P$ .....	135
Figure B.31 – 11-30-S1 results, solid. = 0.1, u = 11 m/s, TSR = 3.0, left: $C_F$ , right: $C_P$ .....	135
Figure B.32 – 11-30-S2 results, solid. = 0.2, u = 11 m/s, TSR = 3.0, left: $C_F$ , right: $C_P$ .....	135
Figure B.33 – 11-30-S3 results, solid. = 0.3, u = 11 m/s, TSR = 3.0, left: $C_F$ , right: $C_P$ .....	136
Figure B.34 – 11-32-S1 results, solid. = 0.1, u = 11 m/s, TSR = 3.25, left: $C_F$ , right: $C_P$ .....	136
Figure B.35 – 11-32-S2 results, solid. = 0.2, u = 11 m/s, TSR = 3.25, left: $C_F$ , right: $C_P$ .....	136
Figure B.36 – 11-32-S3 results, solid. = 0.3, u = 11 m/s, TSR = 3.25, left: $C_F$ , right: $C_P$ .....	137
Figure B.37 – 11-35-S1 results, solid. = 0.1, u = 11 m/s, TSR = 3.5, left: $C_F$ , right: $C_P$ .....	137
Figure B.38 – 11-35-S2 results, solid. = 0.2, u = 11 m/s, TSR = 3.5, left: $C_F$ , right: $C_P$ .....	137
Figure B.39 – 11-35-S3 results, solid. = 0.3, u = 11 m/s, TSR = 3.5, left: $C_F$ , right: $C_P$ .....	138
Figure B.40 – 11-37-S1 results, solid. = 0.1, u = 11 m/s, TSR = 3.75, left: $C_F$ , right: $C_P$ .....	138
Figure B.41 – 11-37-S2 results, solid. = 0.2, u = 11 m/s, TSR = 3.75, left: $C_F$ , right: $C_P$ .....	138
Figure B.42 – 11-37-S3 results, solid. = 0.3, u = 11 m/s, TSR = 3.75, left: $C_F$ , right: $C_P$ .....	139
Figure B.43 – 11-40-S1 results, solid. = 0.1, u = 11 m/s, TSR = 4.0, left: $C_F$ , right: $C_P$ .....	139
Figure B.44 – 11-40-S2 results, solid. = 0.2, u = 11 m/s, TSR = 4.0, left: $C_F$ , right: $C_P$ .....	139
Figure B.45 – 11-40-S3 results, solid. = 0.3, u = 11 m/s, TSR = 4.0, left: $C_F$ , right: $C_P$ .....	140

## LIST OF TABLES

Table 1.1 – Operating parameters of small wind turbines.....	3
Table 5.1 – Maximum calculated wall $y^+$ values for NACA 0012 and S809.....	60
Table 5.2 – Aerodynamic coefficients for all five grid densities, NACA 0012.....	62
Table 5.3 – $C_L$ and $C_D$ for NACA 0012, Transition SST, comp. to exp. data.....	63
Table 5.4 – $C_L$ and $C_D$ data for NACA 0012, SST $k-\omega$ , comp. to exp. data.....	64
Table 5.5 – $C_L$ vs. AOA results vs. numerical and experimental data, S809.....	66
Table 5.6 – $C_D$ vs. AOA results vs. numerical and experimental data, S809.....	66
Table 5.7 – $C_L$ values for the GCI evaluation, SD7062.....	70
Table 5.8 – $C_L$ , $C_D$ and $L/D$ results for SD7062 as functions of $Re$ and AOA.....	72
Table 6.1 – Parameters of the resulting blade.....	88
Table 7.1 – Parameters of the blade sections selected for solidity analyses.....	91
Table 7.2 – Parameters of computational domains for solidity cases.....	93
Table 7.3 – Results for the 45 solidity simulations.....	97
Table 7.4 – Lift and drag comparisons between solidity cases and their isolated-airfoil counterparts.....	106

## LIST OF ABBREVIATIONS AND ACRONYMS

ANN	Artificial neural network(s)
AOA	Angle of attack
BEM	Blade element/momentum theory
CFD	Computational fluid dynamics
DC	Direct current
DNS	Direct numerical simulation
FDM	Finite difference method
FEM	Finite element method
FVM	Finite volume method
GA	Genetic algorithm(s)
HAWT	Horizontal axis wind turbine
IEC	International Electrotechnical Commission
LES	Large-eddy simulation
LSAT	Low-Speed Airfoil Tests
LSB	Laminar separation bubble
NACA	National Advisory Committee for Aeronautics
NREL	National Renewable Energy Laboratory
N-S	Navier-Stokes
PM	Permanent magnet
RANS	Reynolds-Averaged Navier-Stokes
RPM	Revolutions per minute
S-A	Spalart-Allmaras
SIMPLE	Semi-Implicit Method for Pressure-Linked Equations
SST	Shear stress transport
SWRDC	Small Wind-turbine Rotor Design Code
TSR	Tip speed ratio

## NOMENCLATURE

Roman symbols

$A$	Area [m <sup>2</sup> ]
$a$	Axial induction factor
$a'$	Tangential induction factor
$c$	Chord length [m]
$C_D$	Drag coefficient
$C_F$	Skin friction coefficient
$C_L$	Lift coefficient
$C_p$	Pressure coefficient
$C_{Pwr}$	Power coefficient
$C_{Thr}$	Thrust coefficient
$D$	Drag [N]
$dF_D$	Drag force at blade section [N]
$dF_L$	Lift force at blade section [N]
$dF_N$	Thrust force at blade section [N]
$dF_T$	Force resulting in torque at blade section [N]
$F$	Force [N]
$f$	Arbitrary cell face; quantity under evaluation (GCI)
$F_1, F_2$	Blending functions of the SST model
$F_S$	Safety factor
$F_{sp=0}$	Value of quantity if grid spacing tends to zero (GCI)
$F_{TL}$	Prandtl tip loss factor
$Fu_d$	Rate of work by $F$ [Nm.s <sup>-1</sup> ]
$GCI_{ij}$	Value of FCI for a given solution
$h$	Linearized coefficient of $\phi$

$k$	Turbulent kinetic energy [ $\text{m}^2 \cdot \text{s}^{-2}$ ]
$k_G$	Constant used to verify the GCI
$L$	Lift [N]
$l$	Turbulent length scale [m]
$l_{mix}$	Prandtl's mixing length [m]
$N$	Number of blades
$P$	Power [W]
$p$	Pressure [Pa]
$p_G$	Order of convergence (GCI)
$R$	Total radius [m]
$r$	Local radius [m]
$r_G$	Refinement ratio (GCI)
$Re$	Reynolds number
$S$	Generic source term
$S_{ij}$	Mean strain rate tensor
$Sp$	Blade spacing [m]
$T$	Torque [N.m]
$t$	Time [s]
$t_s$	Starting time [s]
$t_{ij}$	Cauchy tensor
$U$	Mean velocity component [ $\text{m} \cdot \text{s}^{-1}$ ]
$u$	Free-stream velocity [ $\text{m} \cdot \text{s}^{-1}$ ]
$u_1$	Axial component of velocity [ $\text{m} \cdot \text{s}^{-1}$ ]
$u_2$	Tangential component of velocity [ $\text{m} \cdot \text{s}^{-1}$ ]
$u'$	Velocity fluctuation component [ $\text{m} \cdot \text{s}^{-1}$ ]
$u^*$	Wall friction velocity [ $\text{m} \cdot \text{s}^{-1}$ ]
$u_D$	Inflow velocity downstream [ $\text{m} \cdot \text{s}^{-1}$ ]
$u_M$	Mean flow velocity [ $\text{m} \cdot \text{s}^{-1}$ ]

$u_{rel}$	Relative wind velocity at blade section [ $\text{m}\cdot\text{s}^{-1}$ ]
$V$	Volume [ $\text{m}^3$ ]
$w$	Weight of objective function
$x, y, z$	Rectangular Cartesian coordinates [m]
$y^+$	Non-dimensional distance to wall

#### Subscripts

$d$	Conditions at the actuator disc
$f$	Relative to cell face
$i, j$	Relative to numbered quantities (1, 2, 3...)
$n$	Relative to time level
$nb$	Property at the neighbor cell
$w$	Conditions at the far wake
$\infty$	Free-stream value

#### Greek symbols

$\alpha$	Angle of attack [deg]
$\gamma$	Intermittency of turbulence
$\Gamma$	Vorticity magnitude; Diffusion coefficient
$\delta_2$	Momentum thickness [m]
$\delta_{ij}$	Kronecker delta
$\varepsilon$	Turbulent dissipation per unit mass [ $\text{m}^2\cdot\text{s}^{-2}$ ]
$\theta_p$	Pitch angle [deg]
$\lambda$	Tip speed ratio
$\mu$	Dynamic viscosity [Pa.s]
$\mu_t$	Turbulent (eddy) dynamic viscosity [Pa.s]



$\nu$	Kinematic viscosity [ $\text{m}^2\cdot\text{s}^{-1}$ ]
$\nu_t$	Turbulent (eddy) kinematic viscosity [ $\text{Pa}\cdot\text{s}$ ]
$\rho$	Density [ $\text{Kg}\cdot\text{m}^{-3}$ ]
$\sigma$	Local rotor solidity
$\tau$	Shear stress [ $\text{N}\cdot\text{m}^{-2}$ ]; Characteristic time step [s]
$\tau_{ij}$	Reynolds stress tensor
$\phi$	Generic scalar variable
$\varphi$	Inflow angle [deg]
$\varphi_D$	Inflow angle far downstream [deg]
$\varphi_M$	Mean inflow angle [deg]
$\psi$	Distance to closest wall [m]
$\Omega$	Rotational speed [ $\text{rad}\cdot\text{s}^{-1}$ ]
$\omega$	Specific dissipation rate [ $\text{s}^{-1}$ ]

# 1 INTRODUCTION

The strong rise in worldwide energy demand during the 20<sup>th</sup> Century, the increase in the average global temperatures and concerns related to the end of fossil resources are the main reasons behind an ongoing change in the public opinion, increasingly receptive to new, renewable energy generation alternatives.

Wind energy is among these alternatives. Being mostly a consequence of uneven heating at different points over the Earth surface, the wind resource is an indirect form of solar energy, and it is constantly being replenished by the sun. The wind provides an estimated 10 million MW of power [Joselin Herbert et al., 2007], while, at the end of 2010, all wind turbines installed around the world contributed with a share of 2.5% of the global electricity demand [WWEA, 2011]. Furthermore, studies point that wind energy has potential to represent 5% of the worldwide energy matrix before 2020, while Greenpeace defends that wind turbines will be capable of representing up to 10% of the world energy matrix at that deadline [Joselin Herbert et al., 2007].

The 20<sup>th</sup> Century has witnessed a constant increase in the worldwide interest in renewable energy sources. The last 30 years were especially positive, when large wind farms were built in many sites along the shores of the Mediterranean and North Sea, making the Europeans the pioneers in large scale wind power generation. North America and, more recently, China have seen their on-grid wind energy markets reach, in 2010, total installed capacities of 40.1 and 44.7 GW respectively [WWEA, 2011]. As of 2016, cumulative installed capacity grew by 12.6% compared to the previous year, reaching a total of 486.8 GW [GWEC, 2017].

In some regions, however, especially in developing countries such as Brazil and its neighbors in South America, off-grid small wind turbines are pointed as a promising solution to power supply shortages in remote areas. Even in developed countries, distributed power generation finds applications in road and highway lighting, mobile communication stations, yachts, water desalinization and electrification of rural properties. At the end of 2009, more than 520,000 small wind turbines have been installed worldwide, mainly in China and the USA [WWEA, 2012].

## 1.1 History

The wind turbine has had a singular history among prime movers. Its genesis is lost in antiquity, but its existence as a provider of useful mechanical power for the last thousand years has been authoritatively established. The windmill, which once flourished along with the water wheel as one of the two prime movers based on the kinetic energy of natural resources, reached its apogee of utility in the seventeenth and eighteenth centuries [Shepherd, 2009].

Since the middle ages, horizontal axis wind mills have become part of the rural economy and only fell into disuse following the advent and popularization of stationary engines powered by fossil fuels and the expansion of rural electrification. The use of wind turbines to generate electricity dates back to the end of the 19<sup>th</sup> century, with the 12 kW DC turbine built by Charles Brush in the United States and the research conducted by Poul la Cour in Denmark. Despite these efforts, there has been little interest in using wind to generate electricity during most of the 20<sup>th</sup> Century, except for battery recharging in remote locations, and these low power systems were promptly phased out when access to the grid became available.

From the 1930s on, a number of isolated attempts have been made in different countries, in which many configurations were tried in the search of standards for power generation from the wind. Despite the technological advances, there had been little real interest in employing wind energy until the rise of oil prices in 1973. The sudden rise encouraged some governments to grant substantial funding for research and development of new technologies, which have favored the production of important knowledge in science and engineering. Nevertheless, problems of operating very large turbines without support and maintenance teams based nearby and in harsh weather conditions were overall underestimated, and the reliability of the prototypes was not good. The Danish Concept of wind turbine emerged from a three-bladed, upwind, stall-regulated rotor and a synchronous generator coupled to the gearbox. This seemingly simple architecture proved to be notably successful, and was implemented in turbines up to 60-meter diameter and 1.5 MW [Gasch and Twele, 2002].

To date, the main driver for use of wind turbines to generate electrical power is the very low amount of CO<sub>2</sub> emissions (over the entire life cycle of manufacture, installation, operation and decommissioning) and the potential of wind energy to help slowing down climate

change. Nowadays, the oil prices and uncertainties involving other energy resources keep stimulating the interest in wind energy, and a number of initiatives have been established in many countries to stimulate its use [Burton et al., 2001].

## 1.2 Small wind turbines

The IEC safety standard for small wind turbines, IEC 61400-2, defines a small turbine as having a rotor swept area less than 200 m<sup>2</sup>, which corresponds roughly to a rated power of no more than 50 kW [Wood, 2011a; IEC 61400-2, 2006]. In fact, they can be further divided into different categories. As shown in table 1.1, Clausen and Wood, 1999, have divided small turbines into three categories based on typical use: micro, powering electric fences, remote telecommunications, equipment on yachts and the like; mid-range, mostly used to power a single remote house, and mini for small grids for remote communities.

Table 1.1 – Operating parameters of small wind turbines

Category	Power (kW)	R (m)	Max. RPM	Uses	Generator
Micro	1	1.5	700	Electric fences, yachts	Permanent magnet (PM)
Mid-range	5	2.5	400	Remote houses	PM or induction
Mini	20 or more	5	200	Mini grids, remote commun.	PM or induction

[Clausen and Wood, 1999]

Table 1.1 summarizes typical operating parameters for the three categories. The authors emphasize, however, that the entries in the table are typical values and there are wide variations in them all. Figure 1.1 illustrates typical examples of small wind turbines.

Small wind turbines share the basic operating principle of large turbines. However, there are some major differences in detail. Small turbines operate at lower Reynolds numbers. They usually rely on a tail fin for alignment with the wind direction and their low wind speed and starting performance are more critical [Wood, 2011b]. It is extremely significant that the starting torque is generated primarily near the hub, whereas the torque for power is concentrated near the tip. This suggests that blades may be (and in fact they are) designed for

the dual purpose of fast starting and efficient power production [Wood, 2011b]. At the same time, small turbines need to be affordable, reliable and almost maintenance free for the average person to consider installing one, which often means a sacrifice of optimal performance for simplicity in design and operation. Thus, rather than using the generator as a motor to start and accelerate the rotor when the wind is strong enough to begin producing power, small wind turbines rely solely on the torque produced by the wind acting on the blades. Furthermore, small wind turbines are often located where the generator power is required, and not necessarily where the wind resource is the best for its operation [Wright and Wood, 2004].

The higher speeds at which a small turbine typically operates, in comparison to large turbines, might become a potential source of undesirable noise, since they usually operate near the facilities that benefit from its power. Well designed wind turbines can be extremely quiet, however. One simple data correlation for the power sound level states that one-ten millionth of the turbine's power is output as noise [Wood, 2011b]. The same author points to studies in which noise data for small turbines have been measured, and concluded that these devices can be as silent as large turbines.



Figure 1.1 – Examples of small wind turbines [Wood, 2011a]

### 1.3 Aerodynamics

Aerodynamics is an applied science with many applications in engineering. Its efforts are usually aimed at a practical objective, such as the prediction of forces and moments on, and heat transfer to and from, bodies moving through a fluid (in the case, air).

The aerodynamic forces and moments on a body, no matter how complex they may be, are due to only two basic sources: pressure distribution and shear stress distribution over the body surface. The pressure ( $p$ ) acts normal to the surface, and the shear stress ( $\tau$ ) acts tangential to the surface, caused by friction between the body and the air. The net effect of the  $p$  and  $\tau$  distributions integrated over the complete body surface is a resulting aerodynamic force and moment on it. The resulting force can be split into components: lift ( $L$ ), perpendicular to  $u$ , and drag ( $D$ ), parallel to  $u$  [Anderson Jr., 2001].

The parameter  $u$  is the freestream velocity, i.e., the velocity of the undisturbed flow far away from the body. The chord ( $c$ ) is the linear distance from the leading edge to the trailing edge of the body. Sometimes, the resulting force is split into components perpendicular and parallel to the chord, which results in a normal force and an axial force. The angle of attack ( $\alpha$ ) is defined as the angle between  $c$  and  $u$ .

The lift and drag forces are often reported as functions of the lift and drag coefficients. These are dimensionless parameters defined as the force itself divided by the dynamic pressure and a reference area. If  $\rho$  and  $u$  are the density and velocity, respectively, in the freestream, far ahead of the body, then the dimensionless lift and drag coefficients are defined as follows:

$$C_L = \frac{L}{\frac{1}{2}\rho u^2 A} \quad (1.1)$$

$$C_D = \frac{D}{\frac{1}{2}\rho u^2 A} \quad (1.2)$$

In the above equations,  $\frac{1}{2}\rho u^2$  is the dynamic pressure in  $\text{N/m}^2$  and  $A$  is the reference area in  $\text{m}^2$ . For airfoils, it is defined as the chord length multiplied by the depth in the spanwise direction.

For an airfoil, at low to moderate angles of attack (usually referred to as AOA),  $C_L$  varies linearly with the AOA. In this region, the flow moves smoothly over the airfoil and is attached over most of its surface. However, as  $\alpha$  becomes larger, the flow tends to separate from the top surface of the profile [Anderson Jr., 2001]. It happens because the adverse pressure gradient slows down the flow as it approaches the trailing edge of the airfoil. In the boundary layer, viscosity also slows down the flow and the combination of the two effects, if sufficiently large, can bring the boundary layer flow to a standstill (relative to the blade surface) or even cause a reversal of flow direction. When flow reversal takes place, the flow separates from the airfoil surface and stall occurs, giving rise to loss of lift and a dramatic increase in pressure drag [Burton et al., 2001].

Two additional dimensionless quantities find their use in aerodynamics: the pressure coefficient ( $C_P$ ) and the skin friction coefficient ( $C_F$ ). Their definitions follow the same logic as that of  $C_L$  and  $C_D$ , i.e. the non-dimensionalization by the dynamic pressure, except that no reference area is involved in these cases. The following equations provide their definitions.

$$C_P = \frac{p - p_\infty}{\frac{1}{2} \rho u^2} \quad (1.3)$$

$$C_F = \frac{\tau}{\frac{1}{2} \rho u^2} \quad (1.4)$$

In the above equations,  $p$  is the local pressure,  $p_\infty$  is the free stream pressure, and  $\tau$  is the wall shear stress. The pressure and skin friction coefficients are especially useful to evaluate localized flow characteristics over solid surfaces, such as transition and separation.

#### 1.4 Airfoils and shape optimization

The choice of the airfoil to be used in wind turbine blades, both large and small, is fundamental. In the design of a commercially viable wind turbine, it is critical that the design team have an accurate assessment of the aerodynamic characteristics of the airfoils that are being considered. Errors in the aerodynamic coefficients will result in errors in the turbine's performance estimates and economic projections. The most desirable situation is to have

accurate experimental data sets for the correct airfoils throughout the design space. However, such data sets are not always available and the designer must rely on calculations [Wolfe and Ochs, 1997].

Part of the difficulty in calculating starting performance is the scarcity of information about airfoil behavior at low and very low Reynolds numbers – less than about 40,000 – and high incidence – up to 90° at the time of starting [Clausen and Wood, 1999]. As wind turbine blades are made from airfoil sections, low  $Re$  plays a major role. The lift to drag ratio usually decreases with decreasing  $Re$ , so, since the lift generates the torque on the blade but the drag reduces it, the  $C_L/C_D$  ratio is the most crucial parameter for blade design and turbine efficiency [Wood, 2011b; Ribeiro and Awruch, 2012]. Furthermore, at favorable ratios, it is desirable that lift be kept close to the maximum in order to allow for the minimum rotor diameter possible [Singh et al., 2012].

Maintaining high lift and low drag at low Reynolds numbers requires a thin airfoil to minimize the acceleration over the upper surface that produces the laminar separation bubble (LSB), one of the major responsables for the performance degradation at low  $Re$ . At very low  $Re$ , the optimum thickness approaches zero, a structurally infeasible situation [Clausen and Wood, 1999]. A small degree of surface roughness is usually associated with airfoils operating at low Reynolds conditions, where the introduction of turbulators or trip wire devices promotes early transition from laminar to turbulent flow to eliminate laminar separation bubbles and delay the possible chance of separation from the upper surfaces at higher angles of attack [Singh et al., 2012].

Figure 1.2 shows, as an example, oil flow visualization over the upper surface of the Eppler E374 airfoil tripped at 22% of the chord [Lyon et al., 1997]. The Reynolds number of the flow is 200,000 and the angle of attack is 3 degrees. The LSB produced by this situation can be seen as the region between about 45% and 60% chord, where the dotted pattern on the oil evidences a region of low flow speeds immediately followed by an area of abrupt increase on the speed. Past the 60%-chord mark, the blurred pattern indicates the reattachment of the flow, already in turbulent regime.

The NACA 0012 profile, member of the 4-digit profile family developed by the US National Advisory Committee for Aerodynamics (NACA), is one of the oldest and certainly the most tested of all airfoils; it has been studied in dozens of separate wind tunnels over a period of several decades [McCroskey, 1987]. This symmetrical, 12% thick profile has a



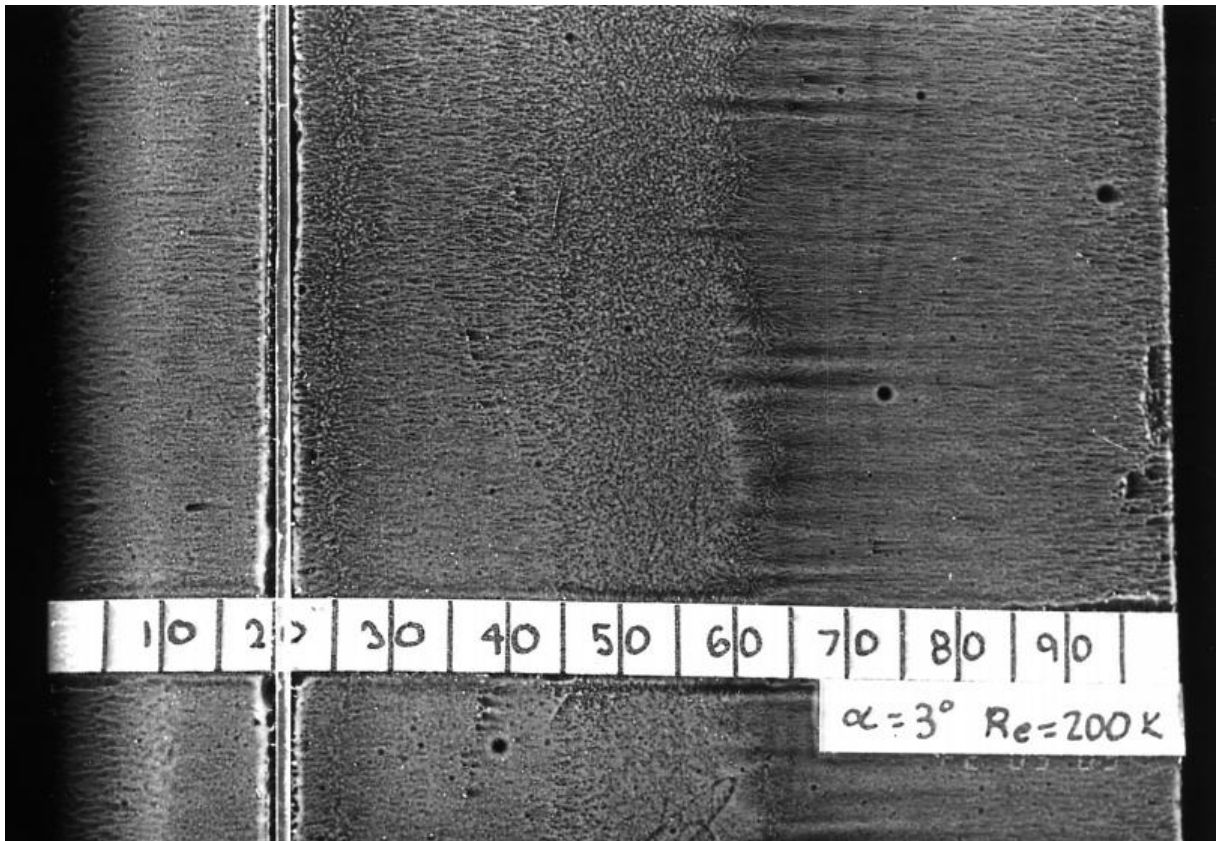


Figure 1.2 – Experimental flow visualization of the LSB [Lyon et al., 1997]

simple design and was not created with the specific purpose of being used in turbines, but the wide availability of experimental results makes it a good choice as reference for the validation of the numerical method conducted in the present work.

Airfoils created for aeronautical applications are occasionally used in wind turbines, even though the design criteria are not the same for both cases [Devinant et al., 2002; Ribeiro and Awruch, 2012]. Although it is common to divide profiles into categories such as design purpose or typical use, the application of each airfoil is by no means limited to their respective groups. The SD7062, used in several small wind turbine studies, such as in Sessarego and Wood, 2015, was initially designed for use in remote-control aircraft, but Lyon et al., 1997, included tests for this and other airfoils with leading-edge roughness to establish their potential for use on small wind turbines, especially under dirty-blade conditions.

There are, however, airfoils specifically designed for wind turbine blades. As an example, the 25 profiles created by the US National Renewable Energy Laboratory (NREL) can be cited, among which is the S809. These advanced profiles show aerodynamic and structural advantages when compared to profiles developed for aircraft [Giguère and Selig,

1998]. As other examples of airfoils suitable for use in small turbines, all those which produce high lift at low speeds can be named. Among them, there is the Selig line (S1210, S1221, S1223 and SH3055) and profiles as the Wortmann FX 63-137, Eppler E387, SG6043 and Aquila [Singh et al., 2012].

Design and optimization of wind turbine rotors are usually performed using the Momentum Theory and the Blade Element Theory. Momentum Theory analysis assumes a control volume, in which the boundaries are the surface and two cross-sections of a stream tube and the only flow is across these two cross-sections. Blade Element Theory makes an analysis of the forces on a blade section expressed as a function of lift and drag coefficients and the angle of attack. The results of these approaches can be combined in what is known as the Blade Element Momentum Theory, which is used to relate blade shape with the rotor capability of extracting energy from the wind [Manwell et al., 2002]. It is noteworthy that this methodology assumes that the blades consist of non-interacting radial elements and lift and drag can be obtained from two-dimensional airfoil data [Clausen et al., 1987], which is to say, one of the fundamental assumptions of blade element theory is that blade elements behave as airfoils. Studies to be presented in the next chapter suggest that this assumption can lead to significant error, since an airfoil is a two-dimensional body subject to an infinite flow that is uniform away from the region influenced by the body. Such a situation can not occur in a wind turbine because the blades are always separated by a finite distance in the azimuthal direction [Wood, 2011a]. The measure of the importance of this effect is the local rotor solidity,  $\sigma$ , which is the ratio between the chord length of all blade elements at a given radial position and the circumferential length described by that airfoils during rotor operation. It will be properly defined in Section 3.4.

Such methods, despite being fast and demanding little computational capacity, have many limitations, since viscous and three-dimensional effects are not taken into account [Ribeiro and Awruch, 2012]. Among the most recent trends, Computational Fluid Dynamics (CFD) is starting to profit from the latest advances in computers and is being used on the design of new airfoils and blades. Recently, optimization algorithms started to be employed in the search for the best aerodynamic shapes. They normally fall within two categories: gradient based methods and heuristic algorithms. Gradient based methods are very popular due to their speed. However, in practice, they seldom converge to global optima, which creates the need to check various initial conditions in order to have some certainty in the design. In this sense, these methods are deemed as not robust. Although considered as being slower, genetic

algorithms, which are the most popular of the heuristic algorithms, are more reliable and robust, even though their convergence is yet to be proven. Both methods have been successfully applied in the optimization of airfoils, wings and also entire airplanes [Ribeiro and Awruch, 2012].

## 1.5 Purpose of this work

Computational Fluid Dynamics (CFD) is being employed in large scale since its inception, both in industry and in academia. As of the present day, however, there is still room for improvement. Its association to every sort of engineering problem goes necessarily through validation processes. The present work intends to add to discussions on the computer-aided design of small wind turbines by applying numerical simulations to evaluate the performance of a blade subject to realistic operating conditions.

The author believes that the general purpose of this study is to contribute with the preliminary design efforts of a small HAWT by using CFD to go beyond the guidelines introduced by the classic Betz methodology. This work also takes the opportunity to discuss the simplifications upon which that methodology has been derived and how it can impact the design of a new rotor under conditions in which the blade element theory is known to underperform.

As for specific purposes, this thesis tries to present a detailed study on CFD simulation of an airfoil subject to low-Reynolds-number flows and discuss the results obtained with a state-of-the-art turbulence model, the  $\gamma$ - $Re_\theta$  (also known as Transition SST), especially regarding to the modeling of the laminar separation bubble.

Another specific purpose is to combine the low- $Re$  airfoil simulations to situations involving different degrees of local rotor solidity, as the reduced blade spacing is known to affect the flow between adjacent blade sections (or airfoils). Once again, it is desired to evaluate the turbulence model performance under such situation, as well as to produce data that contributes to the discussion on whether the presented simulation methodology allows confirming the hypothesis that solidity effects actually tend to improve rotor performance. To the author's knowledge, so far no other work presenting such analysis combining solidity and low- $Re$  effects in 2D RANS airfoil simulations has been published.

## 2 LITERATURE REVIEW

This chapter presents a collection of publications in an attempt to outline what is known about small wind turbine aerodynamics, as well as concepts and tools that will be explored throughout this thesis.

At first, a brief history of airfoil design and optimization is presented, focusing on low-Reynolds profiles, blades and entire turbine rotors. Among the many goals that designers have pursued over the years, efforts to suppress or at least minimize the effects of the laminar separation bubble stand out.

In the field of computational fluid dynamics, relevant efforts on boundary layer transition modeling in turbulence models and computational codes are presented. Provided that extensive use of approaches such as Direct Numerical Simulation and Large-Eddy Simulation remains prohibitive for most users, use of turbulence models in CFD is not yet obsolete.

Lastly, existing knowledge on issues usually associated to small wind turbines, such as starting performance and solidity effects, is presented. Fundamentals of fluid mechanics and wind turbine theory will be studied in the next chapters.

### 2.1 Design and optimization of airfoils and blades

The study and development of airfoils in large scale dates back to the 1930's, when the National Advisory Committee for Aeronautics (NACA) issued its Report No. 460 [Jacobs et al., 1933] in which the characteristics of 78 airfoil sections from wind tunnel tests were published. That was one of the first documentations of the airfoils belonging to the widely known NACA 4-digit series and the polynomial equations describing its shapes. Although many of the then known airfoils (many of which developed in Germany) had been previously assessed at relatively low Reynolds numbers, they were tested at much higher  $Re$  in the variable-density wind tunnel at the Langley Memorial Aeronautical Laboratory in the USA. It makes clear that the focus of Report No. 460 was the current 1930's aircraft and their increasing flight speeds, and it has set the pace for many others to come in the following decades.

It was not until the 1980's that the first large-scale work focusing entirely on the assessment of airfoil performance at low Reynolds numbers emerged from the Princeton

University 3×4 ft smoke tunnel. Led by Dr. Michael Selig, responsible for many well known modern airfoil designs, that effort resulted in the book *Airfoils at Low Speeds* [Selig et al., 1989]. Its primary goal was to design a new group of high-performance airfoils for radio controlled model sailplanes, but a number of existing airfoil designs, selected by the model community, was tested beforehand in order to establish baseline data. In total, 54 different airfoils have been tested; several of them were duplicated in order to examine the effects of model variability, and the DF- and SD-series of airfoils were the new designs resulting from that work.

In that book, the authors detected the main effects of low-Reynolds flows over airfoils and focused on the resulting phenomena. According to it, for airfoils operating at chord Reynolds numbers (when the profile chord length is used as characteristic dimension) between 50,000 and 500,000, the boundary layer transition from laminar to turbulent is neither abrupt nor does it usually take place while the boundary layer is attached to the airfoil. Instead, the laminar boundary layer separates, that is, it physically detaches from the airfoil surface. The flow then becomes unstable while separated, and makes the transition to turbulent flow in “mid air”. Only then does the flow reattach to the airfoil. Furthermore, if the laminar separation point is sufficiently far aft or if the Reynolds number is very low, the flow entirely fails to return to the airfoil surface. In either case large energy losses are associated with this process. This laminar separation, transition to turbulence, and turbulent reattachment encloses a region of recirculating flow aptly called the “laminar separation bubble”. This extended transition process is the main reason for the degradation in performance at low Reynolds numbers. Efforts towards drag reduction, therefore, largely concentrate on reducing the size and extent of the bubble.

The success of *Airfoils at Low Speeds* gave rise to further five reports designed the same way as the original, for which many more airfoils have been provided with decisive help of model aircraft enthusiasts. From that point on, all experiments have been performed in the Department of Aeronautical and Astronautical Engineering at the University of Illinois at Urbana-Champaign (UIUC), USA, and became known as the Low-Speed Airfoil Tests (LSAT). Volume 1 [Selig et al., 1995] presented the airfoils along with their most likely applications, and the S832 and S833 profiles were introduced as recommended for small wind turbines, although the authors stress that the profiles are by no means restricted to the proposed use. Volume 2 [Selig et al., 1996] introduced computational airfoil analysis as a way to overcome the limitation of their wind tunnel, then limited to produce flows with Reynolds

numbers no higher than 500,000. XFOIL [Drela, 1989], a code which uses a linear-vorticity stream-function panel method coupled with a viscous integral formulation that allows analyzing airfoils under a handful of different conditions (thus not being a CFD code), has been employed. Volume 3 [Lyon et al., 1997] introduced a new family of airfoils designed specifically for variable-speed wind turbines. The SG6040-6043 series was developed for 1 to 5 kW turbines and was tested at Reynolds numbers ranging from 100,000 to 500,000. The wind tunnel tests detected that the laminar separation bubble would only appear over the SG6042 profile for Reynolds numbers lower than 100,000 [Giguère and Selig, 1998]. The SD7062, first introduced in the original report as suitable for sailplanes, was tested again in Vol. 3, together with similar profiles such as the SD7032 and SD7037, this time with leading-edge roughness in order to establish its potential for use on small wind turbines. Volume 4 [Selig and McGranahan, 2004] was published as a NREL report after the LSAT program drew the attention of the US National Renewable Energy Laboratory, interested in exploiting the large expanse of low wind speed sites in the United States. It focused entirely on six airfoils for use on small wind turbines, namely E387, S822, SD2030, FX 63-137, S834 and SH3055, in an effort to improve the understanding of wind turbine aeroacoustics. Finally, Volume 5 [Williamson et al., 2012] (the last one to date) was published in 2012 and included 15 airfoils plus a flat plate tested at various leading edge configurations. The Eppler E387 profile, used as the benchmark airfoil since the inception of the LSAT program, was included in this volume and studied for comparisons between different wind tunnel facilities. As usual, all volumes brought complete data for all airfoils tested, including coordinates, lift and drag polars, performance plots, and pitching moment at the quarter-chord point.

Back in the 1980's, in an effort not related to the LSAT reports, the US National Renewable Energy Laboratory (NREL) launched its first attempt to develop airfoils specifically optimized for small wind turbines. In a joint effort with the company Airfoils, Inc., the profiles S801 to S823 were designed between 1984 and 1993, and their numbers reflect the order at which they were created [Tangler and Somers, 1995]. Most of the airfoils (including the S809) were designed to achieve a maximum  $C_L$  value largely insensitive to roughness effects, which was accomplished by ensuring that the laminar-to-turbulent transition on the suction (upper) side of the airfoil would occur very close to the leading edge. The airfoils were also designed to have the so-called soft stall characteristics, which result from progressive trailing-edge separation. In turbulent wind conditions, close to peak power,

soft stall helps mitigate power and load fluctuations resulting from local intermittent stall along the blade.

The airfoils have been divided in several families, as a function of the estimated rotor diameter range of application. The S809, selected alongside the NACA 0012 for the validation of the numerical method in this thesis, fits the needs of rotors between 10 and 15 m in diameter, producing a rated power ranging from 100 to 400 kW. It was selected due to the availability of data, both experimental and numerical [Wolfe and Ochs, 1997]. It has also been used in the blades of the 10-meter diameter NREL UAE *Phase VI* experimental turbine [Hand et al., 2001].

The abovementioned NREL report has not elaborated on the creation process of these families. The report presented the basic guidelines and stated that, because of the economic benefits provided by them, they would be expected to be the airfoils of choice for retrofit blades and most new domestic wind turbines. The design process of the S809 is well documented, though. Somers, 1997, specified two primary objectives from the design specifications. The first one was to achieve a maximum lift coefficient that was relatively low. Although the author refrained from revealing that exact  $C_L$  value, its range can be estimated from the second objective: to obtain low-profile drag coefficients over the range of lift coefficients from 0.2 to 0.8 for a Reynolds number of  $2.0 \times 10^6$ . Furthermore, two major constraints have been placed on the design process. First, the zero-lift pitching-moment coefficient must be no more negative than -0.05. Second, the airfoil thickness must be 21-percent chord.

The author comments that, given the pressure distributions over the surfaces, the design of the airfoil was reduced to the inverse problem of transforming these distributions into an airfoil shape, which was done using the Eppler Design and Analysis Program [Eppler and Somers, 1980]. When compared with similar profiles, namely the NACA 4421 and 23021 airfoils, the S809 exhibited a low maximum lift coefficient and lower drag coefficients than its counterparts, thus maintaining the favourable  $C_L/C_D$  ratio essential for a successful application in wind turbines.

Wolfe and Ochs, 1997, made numerical calculations of the S809 airfoil using the commercial code CFD-ACE and compared the results with experimental data collected at the Delft University (Netherlands)  $1.8 \text{ m} \times 2.25 \text{ m}$  low-turbulence wind tunnel. Numerical and experimental results showed discrepancies, but were useful for having pointed areas in fluid flow simulation that needed attention. At the time it was published, the code used by the

authors did not have many turbulent modeling options; none of them was capable of dealing with boundary-layer transition. The solution was to divide the computational domain in two distinct regions. The first one, comprising the front half of the airfoil, had the flow prescribed as laminar, and the second one, comprising the aft half, had the flow prescribed as turbulent. This strategy brought improvements in the numerical results but created a new problem: to estimate with some level of accuracy the transition onset point over each of the airfoil's surfaces. Moreover, each new choice of the transition point would require a new mesh to be generated.

In a further step in the development of airfoils for wind turbines, Somers, 2005, has contributed to expand the NREL S-family table by adding three new profiles. The S833, S834 and S835 have been designed for 1- to 3-meter diameter, variable-speed horizontal-axis wind turbines, promising to be quieter and more appropriate for lower Reynolds numbers than any airfoil previously developed by NREL. To achieve this, two primary objectives have been defined: the airfoils should achieve high maximum lift coefficients by preventing the lift from decreasing significantly with transition fixed near the leading edge on both surfaces, and they should show low-profile drag coefficients over specified ranges of lift coefficients. Two major constraints were placed. First, the zero-lift pitching-moment coefficient must be no more negative than -0.15. Second, the airfoil thicknesses must match the specified values of 18%, 15% and 21% for the S833, S834 and S835, respectively. The three airfoils are intended to be used at different radial positions along a blade.

The Eppler Airfoil Design and Analysis Code "PROFIL00" was used to assess the new airfoils's performance. This code, as described by Eppler, c.2000, has been under development for over half a decade and brings mathematical modeling of the two-dimensional viscous flow around airfoils to serve as an alternative for costly wind tunnel experiments. It combines a conformal-mapping method for the design of airfoils with prescribed velocity distribution characteristics, a panel method for the analysis of the potential flow about given airfoils, an integral boundary-layer method, and a compressibility correction to the velocity distributions, which is valid as long as the local flow is not supersonic. According to the author, the code has been successfully applied at Reynolds numbers from  $3 \cdot 10^4$  to  $5 \cdot 10^7$ .

Due to the limitations of the theoretical method described above, however, Somers, 2005, states that the results presented are not guaranteed to be accurate, either in an absolute or in a relative sense. The author considers that the two primary objectives have been



achieved. The airfoils exhibit docile stall characteristics and the constraints on the zero-lift pitching-moment coefficient and the airfoil thicknesses have been satisfied.

Singh et al., 2012, selected airfoils developed for various applications and tested those that presented good lift performance at low Reynolds numbers, with the purpose of developing a new airfoil optimized to small wind turbines. The optimization process was carried out by means of introducing small changes in the geometry of the selected airfoils in attempts to obtain gains in the lift coefficient and the lift-to-drag ratio. All attempts were made on the trial-and-error basis, which led to the need of new tests and analyses for each new shape. An optimized shape has ultimately emerged, and it was given the name AF300. It was tested in wind tunnel and numerically simulated using the ANSYS CFX commercial code, and the results pointed to confirm the predictions. The airfoil was able to sustain fully attached flow up to an angle of attack of 14 degrees at a Reynolds number of 75,000, at which it produced a  $C_L$  of 1.72.

Singh and Raffiudin Ahmed, 2013, used the AF300 airfoil to build the rotor of a two-bladed small wind turbine. Based on previous experience gained during the development process of the airfoil, the authors comment that profiles intended to operate under low-Reynolds conditions should be designed focusing on avoiding high suction peaks near the leading edge and strong adverse pressure gradients along the upper surface. It is also recommended that a slight degree of roughness should be used on the surfaces so as to promote a rapid transition, thus minimizing the chance of laminar separation bubble formation. The turbine has shown improvements in the starting performance when compared to the reference design.

Wind turbine design processes do not always focus only on airfoil shape. It is possible to make an appropriate choice of existing airfoils and proceed to the definition of the best blade shape as a whole. Amano and Malloy, 2009, used this logic to introduce an optimized blade shape by working on chord length and angle of attack, both as functions of the radial position of each blade section. Additionally, the authors evaluated the influence of a curved blade, as opposed to the classic concept of defining a blade by extruding its multiple sections along a straight line. Figure 2.1 illustrates a turbine with curved blades. This curvature should not be confused with the twist angle and its variation along the blade, which is a feature of all modern blades explained in the Betz theory.



Figure 2.1 – Examples of small turbines with curved blades.

The design was based on the classic Betz and Glauert methodology, which will be introduced in Ch. 3, and the NACA 4412 was the airfoil of choice. The authors justify the use of the curved blades on the expectation that it would improve the performance at high wind speeds, which turned out to be confirmed by an increase of about 20% in the maximum power extracted at wind speeds higher than 10 m/s. No significant difference was detected for lower wind speeds, though.

Recently, heuristic and gradient-based mathematical optimization methods are being successfully applied in aerodynamic shape optimization. It is possible to find studies in which both approaches have been combined in complex analyses of multi-element arrangements such as wing-flap assemblies and multi-objective problems, in which different and sometimes competing variables are analyzed at the same time. For two competing objectives, where an improvement in one of them results in a degradation of the other, the results are usually obtained as a Pareto front [Nemec and Zingg, 2004].

Nemec and Zingg, 2002, published a study covering multi-element aerodynamic shapes, such as wings equipped with flaps and slats, to present a version of the gradient-based Newton-Krylov optimization method adapted for two-dimensional Navier-Stokes simulations. The algorithm was evaluated in situations such as the improvement of lift in a take-off situation and the reduction of drag while keeping a desired lift value as a problem restriction. The work included the evaluation of a Pareto front based on the competing nature of the lift and drag coefficients, and the results were validated against data from a genetic algorithm. Though not focused strongly on the aerodynamic phenomena, their work has shown how versatile the optimization methods can be.

The demand for methods capable of identifying and avoiding local optima has led to the development of non traditional search algorithms. The evolutionary algorithms have emerged from Darwin's Theory of Evolution, among which the most well known are the genetic algorithms (GA) [Giannakoglou, 2002]. In GA terminology, a solution vector is called an individual or a chromosome. Chromosomes are made of discrete units called genes, and each gene controls one or more features of the chromosome. Genetic algorithms operate with a collection of chromosomes, called a population, which is normally randomly initiated. As the search evolves, the population includes fitter solutions, and eventually it converges, meaning that it is dominated by a single solution [Konak et al., 2006].

In aerodynamics, the individuals are airfoils, and their genetic features are the design variables. These variables can be points defined over their surfaces, called control points, and they are normally associated to Bézier curves or other parametrization methods, being free to move in a given interval. The adaptability of the airfoils to the environment (lift and drag) is the objective function, and the individuals with the best objective functions are more likely to combine their design variables with other airfoils to create the next generation [Ribeiro, 2012]. Optimization procedures that use this method are normally computationally expensive, however. Each step of the process requires a series of CFD simulations, for this is how the aerodynamic coefficients of new shapes are obtained, and a large number of steps is needed to reach an optimum [Peigin and Epstein, 2004]. To work around this problem, some authors use surrogate models as the Artificial Neural Networks (ANN). In aerodynamics, the ANN uses data from previously tested airfoils as reference (this is referred to as "training" the algorithm) so that characteristics of new airfoils are interpolated or extrapolated from these previously known data [Ribeiro, 2012].

Recently, Ribeiro, 2012, in their Master's degree thesis, used CFD combined with an optimization process based on GA and ANN in a study dedicated to wind turbines. The author has defined as study's goals the optimization of an airfoil for use in wind turbines, and presented numerical results for an unrelated airfoil at high angles of attack and for the simulation of a three-dimensional turbine. The optimization was carried out using two-dimensional, steady-state simulations using the Spalart-Allmaras (S-A) turbulence model, and the NSGA-II genetic algorithm coupled to an artificial neural network to avoid the need of a large number of CFD simulations. The airfoil GA(W)-1 was used for validation purposes. The parameters to be optimized were the lift and drag coefficients and the connection between

them, characterized by a Pareto front. Figure 2.2 illustrates the results obtained, as well as the shapes associated to each case.

Sessarego and Wood, 2015, presented a computer method to allow the design of small wind turbine blades for the multiple objectives of rapid starting, efficient power extraction, low noise, and minimal structural mass. By using the Matlab-based Small Wind Turbine Rotor Design Code (SWRDC), developed by the authors and available from them, blades of 1.1-meter length constructed using a range of blade materials were optimized focused on the first two objectives mentioned above. The code treats the multi-objective problem of optimizing power generation and starting performance in a single-objective sense by using a scalarization function of all the objective functions. Optimization is by a simple genetic algorithm, and the blade performance is assessed by the traditional Blade Element-Momentum Theory. In terms of structural resistance, all the blade designs have been found to be feasible in that the maximum strains for each material were never exceeded in any blade. With regard to the aerodynamics, generally the chord and twist increased as more importance was given to starting. This increased blade mass and hence the inertia, but this was largely compensated by the increase in starting torque. The changes were mostly at the hub region where most of the starting torque is generated, but the twist in the tip region increased from the small negative values required to maximize the power output only.

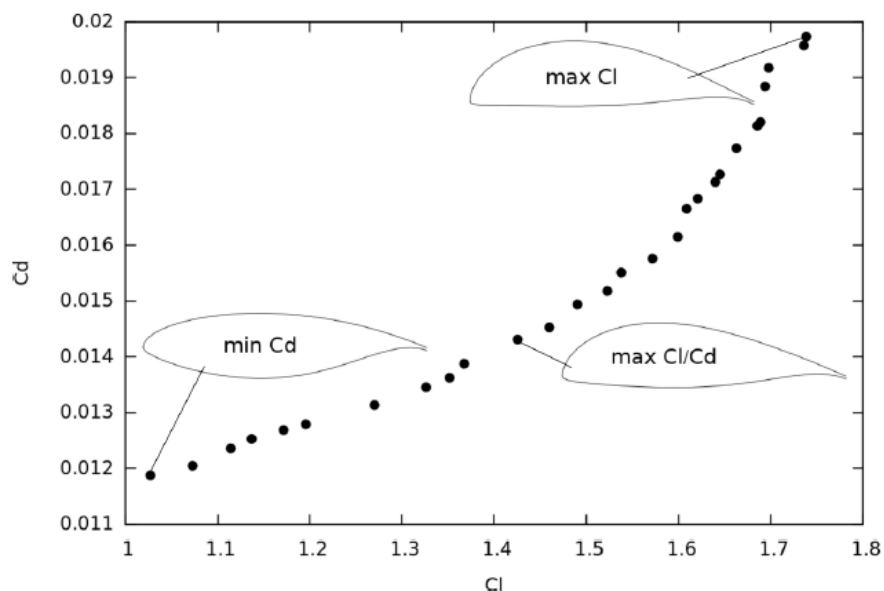


Figure 2.2 – Pareto front and airfoils obtained [Ribeiro, 2012].

## 2.2 Transition modeling in CFD

As for airfoils designed to operate at high Reynolds numbers, low-Reynolds airfoils also usually have their first performance assessments conducted in wind tunnels. At low  $Re$ , however, such wind tunnel measurements are reported to be challenging due to the requirement of higher level of accuracy in equipments due to the particular flow conditions to which these profiles are subject. For example, under the same testing conditions, a total difference of 50% in the drag coefficient measurements of the Wortmann FX63-137 airfoil was reported at three different testing facilities [Shah et al., 2015].

Since computations of flows prone to laminar separation bubble are intrinsically connected with the laminar to turbulent transition, a good modeling of it is usually the main focus of the researchers. Coupling of a transition model and a Reynolds-Averaged Navier-Stokes solver first came in 1982. Hegna, 1982, used an algebraic eddy viscosity model modified for separated adverse pressure gradient flows in the solving of the Incompressible RANS. Their study was conducted using the NACA 0012 airfoil at a chord Reynolds number of 170,000 at angles of attack of 5, 7.5, 9.5 and 11.5 degrees. Results have shown that the lift curve correctly predicted trailing-edge stall at that Reynolds number and agreed with experimental data within 5% near stall. The computed drag coefficients agreed to experimental data within 10 drag counts in the region of maximum lift-to-drag ratio (one drag count corresponds to  $1 \cdot 10^{-4}$  unit of the drag coefficient [Beck, 2010]).

More recently, some authors have successfully coupled RANS solvers equipped with a number of turbulence models to the  $e^N$  method to predict laminar to turbulent transition on low Reynolds airfoils. The  $e^N$  is a method for transition prediction based on the linear stability theory, which in turn considers a given main laminar flow upon which small disturbances are superimposed [van Ingen, 2008]. In one of them, Lian and Shyy, 2006, studied the setup of a Navier-Stokes solver, the  $e^N$  method and a RANS two-equation turbulence model to study the low Reynolds flow over a section of the SD7003 airfoil. Good agreement was obtained between the prediction and experimental measurements regarding the transition location.

Large Eddy Simulation (LES) and Direct Numerical Simulation (DNS) are suitable tools for transition prediction, as shown by Galbraith, 2009, although the current computational cost of their application is still too high for Engineering applications. The Transition SST turbulence model, commercial name of the Gamma-ReTheta ( $\gamma$ - $Re_\theta$ ) model [Council and Goni Boulama, 2012], developed by Langtry, 2006, has introduced a method to

simulate laminar to turbulent transition that could be implemented into a general RANS environment. As implemented in ANSYS Fluent and CFX, it consists of a 4-equation model, based on the SST  $k-\omega$  model, in which the additional two equations account for the turbulent intermittency and for the transition onset criterion in terms of momentum thickness. The author presented, among the cases ran for demonstration, a 2D test on an unspecified wind turbine airfoil and a 3D test, for which the subject was the turbine of the NREL UAE Phase VI experiments. For the 2D case, results from the new model reached good agreement with experimental data as well as data from XFOIL, which is a code based on the  $e^N$  approach.

### 2.3 Starting performance

It is accepted that a turbine has completed its starting phase when the aerodynamic torque acting on the blades overcomes the combined resistive torque of the drive train and electric generator. This happens at a wind speed called cut-in speed, conventionally defined as the lowest speed at which power is produced [Wood, 2001; Wright and Wood, 2004]. The starting sequence of blades designed for optimal power extraction begins with, and is dominated by, an extended “idling period” during which the blades accelerate slowly as the angles of attack slowly decrease [Mayer et al., 2001], but during a typical start  $Re$  varies with time and radial location between about  $1 \cdot 10^4$  and  $1 \cdot 10^5$ . In this range, airfoil performance at low AOA is significantly affected by the separation bubble [Wright and Wood, 2004]. Wood, 2001, states that, as the blades begin to rotate, the angle of attack can be near 90 degrees, and in this range airfoil lift and drag tends to become independent of the detailed geometry such as the thickness and camber. In other words, airfoils start to behave pretty much like flat plates at high incidence, for which the lift and drag coefficients are approximated by

$$C_L = 2 \sin \alpha \cos \alpha \quad (2.1)$$

$$C_D = 2 \sin^2 \alpha \quad (2.2)$$

where  $\alpha$  is the angle of attack. The author has shown that these equations are reasonably good fits to data from three sets of airfoils for  $\alpha > 45$  degrees, which is the range of most interest for starting. This was used to develop a simple method for estimating the aerodynamic torque on a stationary blade. A set of two blades was designed for a 5 kW turbine to be used in field

tests, and the torque estimations turned out to be underpredicted. Among the reasons cited, cascade effects resulting from the high blade solidity at the root (near 0.2) were pointed as responsible for the discrepancies.

Ebert and Wood, 1997, and Mayer et al., 2001, presented starting sequences from experiments conducted using two separate machines but with the same 5 kW-rated blades. In both studies, the free stream wind speed was in the range between 5 and 8 m/s, considerably higher than a desired cut-in speed of 3 or 4 m/s. Both references described 30 to 50 seconds of idling periods of slow rotation, with little acceleration after the initial start due to the unfavorably high angles of attack. When  $\alpha$  eventually decreased sufficiently to produce high lift-to-drag ratios, the rotor accelerated rapidly. On the basis of previous work that justified the neglect of unsteady effects and the assumption of no induced velocities at the blade, the authors used a quasi-steady blade element analysis to describe the starting process, which turned out to yield results in close agreement to field data.

Wright and Wood, 2004, developed a three-bladed, 2-meter diameter turbine designed to produce 600 W at a free stream wind speed of 10 m/s to be used in a set of experiments. Unsteady effects were again neglected and a quasi-steady analysis was used in a similar manner to that used by the previous authors. Available data for the airfoil used by them (SD7062) was combined with data for the NACA 4412 profile in order to extrapolate the former's lift and drag curves for high angles of attack. In the experiments, the blades started rotating at a wind speed of 4.6 m/s on average, but this varied between 2.5 and 7 m/s, and generally coincided with increasing wind speed. Given the uncertainty associated with lift and drag data at high  $\alpha$  and low  $Re$ , their predictions compared well with 160 measured occurrences of rotor acceleration over a large range of wind speeds. The authors remind the reader that most starting torque is generated near the hub, and most power-extracting torque comes from the tip region, so it should be possible to optimize blades with the double objective of good power performance and low starting time.

Data collected from the abovementioned 5-kW and 600-W turbines, both built and operated at the University of Newcastle, Australia, were used to develop a routine to estimate the starting torque. It was detected that starting is dominated by a period of slow acceleration, called "idling period", and this feature led to the assumption that idling is sufficiently long to justify a quasi-steady analysis of starting [Wood, 2011a]. Using the generic flat plate equations for high angle lift and drag, it was possible to derive a set of equations to determine

the aerodynamic torque for a turbine at the starting phase. Figure 2.3 shows the 5-kW turbine and its measured and calculated starting performance [Sessarego and Wood, 2015].

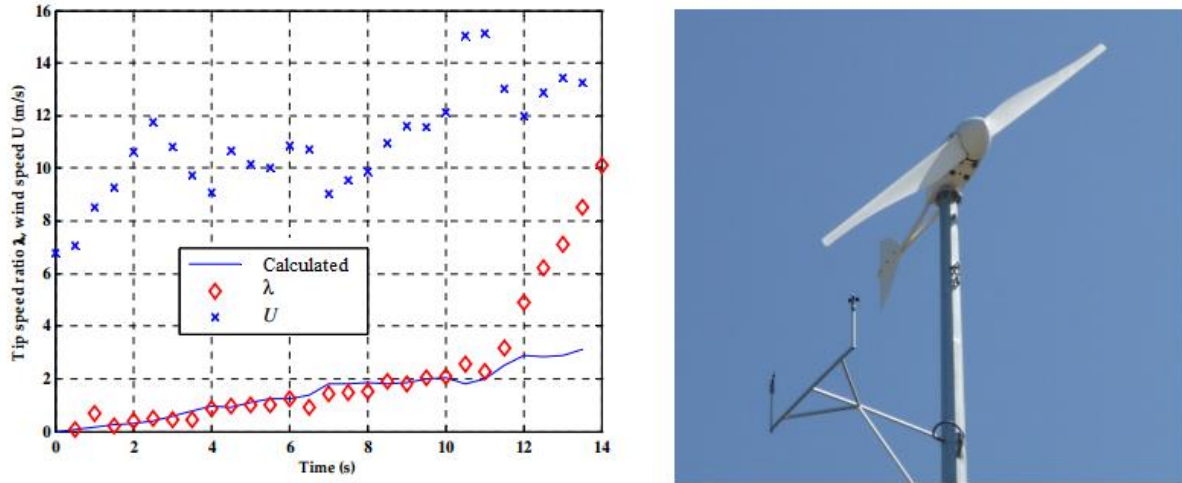


Figure 2.3 – Starting performance of the 5-kW turbine [Mayer et al., 2001]

## 2.4 Solidity effects

Windmills have been used for centuries for water pumping. They are notoriously high-solidity machines, and this configuration produces high loads of torque at low rotational speeds. The first power generating wind turbines, including prototypes built and tested in the early years of the 20<sup>th</sup> Century, resembled the water pumping machines in a large extent [Burton et al., 2001; Shepherd, 2009].

Although not usual in wind turbines, solidity effects are common in turbomachinery [Fagbenro et al., 2014], and local solidities equal to or higher than one can be found in many compressor rotors and windmills built with circular-arc blades. Suzuki et al., 2011, made a CFD analysis to predict the cascade performance of circular-arc blades for local solidity values of 0.666, 1.0 and 1.33. The authors used the well-known  $k-\epsilon$  turbulence model, which, due to its inability to predict transition, was pointed as the cause of the over-estimation in the difference between the inlet and exit flow angles of the cascade.

Fagbenro et al., 2014, developed a similar study in which the Transition SST turbulence model was employed in an attempt to better characterize transition and low- $Re$  effects. Circular-arc blade cascades were simulated at a Reynolds number of 100,000 for five local solidity configurations: 0.1, 0.5, 0.75, 1.2 and 1.5. The applied methodology was able to



model the laminar separation and the mid-air transition of the flow. It detected that, as solidity increases at constant inlet flow angle, the separation on the upper blade surface decreases whereas it increases on the pressure surface. It was shown that the calculated lift was accurately reproduced when compared to results from separate experiments, although the drag was not well predicted.

Ahmed et al., 1998, ran simulations of steady flow in a linear cascade of NACA 0012 airfoils at various angles of attack from zero to 24 degrees and two values of local solidity: 0.55 and 0.83. The main goal was to assess the effects of solidity and AOA on the flow field on lift, drag and pressure coefficients. The  $k-\epsilon$  turbulence model was employed along with the steady, control-volume based RANS methodology. The authors observed a decrease in the lift coefficient linked to the occurrence of large separation, although not as drastic as what was observed in experiments. It is mainly regarded as a consequence of the steady state analysis employed in the computations. Their study is not related to wind turbine technology, though.

Yan, 2016, in their Master's degree thesis, conducted a computational study to assess lift and drag coefficients on a cascade of NACA 4415 airfoils. The blade spacing range configured solidities ranging from 0.1 to 0.3, which, according to the author, is the common range for three-blade horizontal-axis turbines. It was detected that the maximum lift-to-drag ratio increased as solidity increased, which also caused the transition point to move upstream. Since good modeling of the boundary layer transition was needed, the choice of turbulence model fell on the Transition SST.

Garré et al., 2016, designed a small HAWT using the Betz optimum methodology and 3D-printed the blades to test the resulting 5-blade rotor in wind tunnel. Although the focus was not in solidity effects, the solidity of that rotor resulted predictably high. At 20% span, the local solidity is 1.44, and, at 4% span (the power-generating blade element closest to the hub), it is 9.5. In a comparison with a modified version of the original blades (in which the only modification was material removal for weight optimization), the original design performed 22% better in power generation and 17.8% in static torque than the modified version.

Some authors chose to carry out studies in which the global rotor solidity, instead of the local solidity, was the parameter taken into account. Duquette and Visser, 2003, listed a sample of small wind turbines and compared their performance in terms of power coefficient. The list shown that most turbines operate at tip speed ratios of five or greater and employ two or three blades with a total solidity of less than 7%. The exception was the Windflower DK

design, built with 12 blades and 17% solidity. The Windflower ranked the highest in power extraction at its rated speed, doing so with a tip speed ratio of approximately half of the next most efficient design.

The same authors conducted a study about rotor solidity and blade number on small wind turbine performance. The effects of these variables were parametrically assessed using the blade element momentum theory, being applied for a set of tip speed ratios between approximately 2 and 6, and for blade numbers of 3, 6 and 12. It was found that the range of tip speed ratio for maximum power coefficient varied with solidity and with blade number, the former having a much stronger effect than the latter. All of the studies conducted by the authors showed that an increase in blade number at a given solidity increased  $C_{Pwr}$  at the operating point. Their study indicated that, from a theoretical standpoint, the high-solidity configurations showed several possible benefits for wind turbines, bridging the gap between high-speed electric-generating HAWTs and slower, multi-bladed water-pumping machines.

## 2.5 Low Reynolds numbers and stall delay

A phenomenon first noticed on propellers in 1945 is that of lift coefficients being attained at the inboard section of a rotating blade which are significantly in excess of the maximum value possible for two-dimensional static tests [Burton et al., 2001]. In fact, the flow over blade elements can remain attached at angles of attack that would cause an isolated airfoil to stall. The power output of a rotor is measurably increased by the so-called “stall delay” phenomenon and, if included, improves the comparison of measured results with the theoretical predictions. The stall delay is an empirical fact, but its cause is not yet clear. There is also evidence that stall delay occurs on operating wind turbines [Wood, 1991], taking place predominantly towards the hub, so it's likely that solidity, which is usually larger near the hub and also delays separation, is at least partially responsible [Wood, 2011a].

One of the first studies that dealt with the stall delay phenomenon in wind turbine blades was conducted by Clausen et al., 1987, in which the authors investigated the aerodynamic behavior of a two-bladed model turbine shrouded by a constant-diameter pipe that allowed a tip clearance just small enough to minimize and localize the tip losses. The turbine was tested in wind tunnel and the results were compared to data calculated using the Blade Element Theory. The authors say that the most interesting findings were those showing the underprediction of power output at the lower values of tip speed ratio for all pitch angles.

The ratio of the predicted and measured resulting velocity approaching the blades was found to increase even when the angle of attack increased above the approximate stall angle in isolated flow. It was pointed that some mechanism could be preventing boundary layer separation from the blades at angles that would cause separation in isolated flow, and the possible mechanisms responsible for that phenomenon included low-Reynolds effects, finite chord effects, significant Coriolis or centrifugal forces and/or other forms of three-dimensionality not covered by BET.

Wood, 1991, presented an aerodynamic analysis of a horizontal-axis wind turbine, in which the main goal was to investigate the then already widely-observed phenomenon of stall delay. A fully 3D analysis was carried out to determine the parameters upon which it depends. Attention was focused on previous experiments that used the NACA 4418 profile with constant chord and untwisted blades for simplicity, and the results from that experiments were compared to calculations. This study took into consideration downstream fluid circulation and trailing vorticity modeling, pressure distributions and rotor solidity corrections, and the author's explanation for stall delay is based on the behavior of the inviscid, external flow. The main conclusion was that stall delay results from a reduction in the adverse pressure gradient on the upper surface of a blade and the consequent delay in boundary layer separation, and it appears to depend mainly on the local solidity of the blades. This phenomenon impacts the power generation, since blade elements operating in the region of stall delay produce more power than the predicted by conventional analyses which rely on two-dimensional airfoil characteristics.

Shah et al., 2015, conducted a numerical study over the laminar separation bubble and the laminar-turbulent transition over the UBD5494 airfoil, to assess its performance and suitability for use in small wind turbines. The choice of turbulence model fell on the Transition SST ( $\gamma$ - $Re_\theta$ ) in an attempt to benefit from the model's ability to predict magnitude and extent of the laminar-turbulent transition. After running simulations at several Reynolds numbers compatible to the operating conditions of small wind turbines, the authors found that, with the increase in  $Re$ , the LSB moves towards the leading edge of the airfoil and also contracts in size. This shortening, according to them, is mainly caused by the energized flow that overcomes the adverse pressure gradients and forces the turbulent flow to reattach to the airfoil surface. Furthermore, as the angle of attack increases, the separation point tends to move further upstream, and this can be followed by transition with no reattachment if the Reynolds number is low enough. In fig. 2.4 [Shah et al., 2015], the vectors evidence the

presence of the LSB as the region of flow recirculation on the UBD5494 airfoil. Arrows identify the separation and reattachment points. In the scenario depicted, the Reynolds number was 100,000, and the angle of attack was 6 degrees.

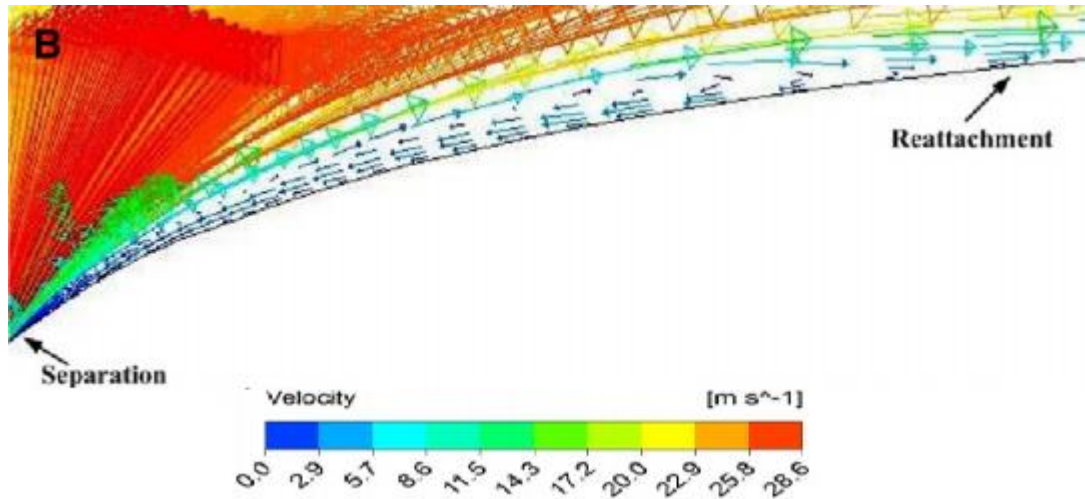


Figure 2.4 – Vectors showing the presence of the LSB [Shah et al., 2015]

### **3 WIND TURBINE DESIGN**

The study of Wind Turbine aerodynamics involves knowledge about the fundamentals of fluid mechanics, especially the Bernoulli's theorem for steady, incompressible flow, and the concept of continuity. It involves concepts of airfoil and aircraft aerodynamics as well, since blade elements and aircraft wings operate under the same physical principles, although different conditions.

The classical analysis of the wind turbine was originally developed by Betz and Glauert in the 1930's. Subsequently, the theory was expanded and adapted for solution by digital computers. In all of these methods, momentum theory and blade element theory are combined into a strip theory that enables calculation of the performance characteristics of an annular section of the rotor. The characteristics for the entire rotor are then obtained by integrating, or summing, the values obtained for each of the annular sections [Manwell et al., 2002].

This chapter presents the concepts and assumptions taken into account to develop the analytical methodology of power extraction from the wind. Those are generic and apply to turbines of all sizes [Wood, 2011a]. For this chapter there are no significant features that are specific to small turbines.

#### **3.1 The Actuator Disc concept**

A wind turbine is a device for extracting kinetic energy from the wind. By removing some of its kinetic energy the wind must slow down but only that mass of air which passes through the rotor disc is affected. It is assumed that the affected mass of air remains separate from the air which does not pass through the disc [Burton et al., 2001]. This is represented schematically in figure 3.1.

The presence of the turbine causes the approaching air, upstream, to gradually slow down, which results in a rise in its static pressure and an expansion of the streamtube. As the air passes through the rotor disc, there is a drop in static pressure, which must return to the atmospheric level for equilibrium to be achieved. This is at the expense of kinetic energy, thus causing a further slowing down of the wind. This mechanism accounts for the extraction of kinetic energy from the wind, and to understand what happens to this energy the concept of

*actuator disc* (fig. 3.2) was introduced. The actuator disc analysis does not take into account any particular turbine design; it does so just by considering the energy extraction process.

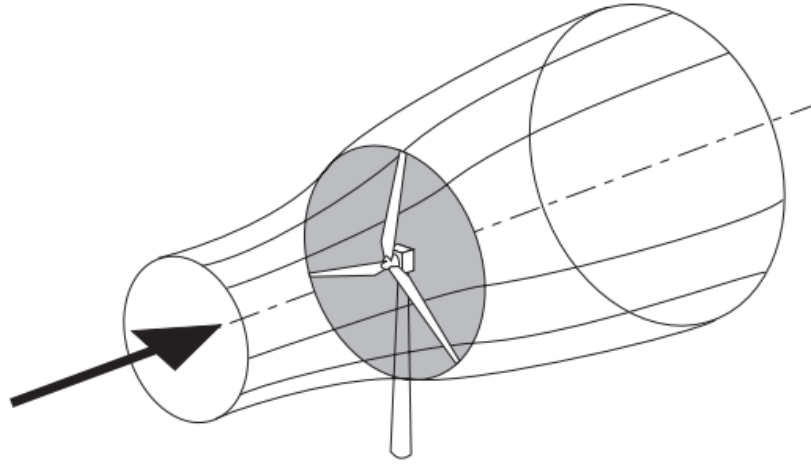


Figure 3.1 – The energy extracting streamtube of a wind turbine

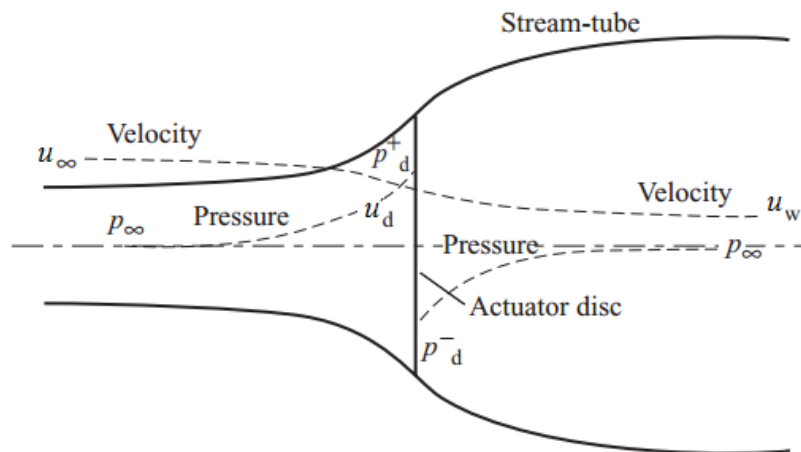


Figure 3.2 – Representation of an actuator disc and streamtube

The expansion of the streamtube is because the mass flow rate must remain constant, being the same everywhere, as defined by equation (3.1), where  $\rho$  is the air density (regarded as constant),  $A$  is the cross-sectional area of the streamtube and  $u$  is the flow velocity. The symbol  $\infty$  refers to conditions far upstream,  $d$  refers to conditions at the disc and  $w$  refers to conditions in the far wake.

$$\rho A_\infty u_\infty = \rho A_d u_d = \rho A_w u_w \quad (3.1)$$

It is usual to consider that the actuator disc induces a velocity variation which must be superimposed on the free-stream velocity. At the disc, therefore, the net streamwise velocity is

$$u_d = u_\infty (1 - a) \quad (3.2)$$

where  $u_d$  is the net streamwise velocity at the disc and  $a$  is called the axial flow induction factor, or inflow factor, defined as:

$$a = 1 - \left( \frac{u_d}{u_\infty} \right) \quad (3.3)$$

### 3.2 Power coefficient

The air that passes through the disc undergoes an overall change in velocity and a rate of momentum change equal to the overall change of velocity multiplied by the mass flow rate. The force causing this change of momentum comes entirely from the pressure difference  $(p_d^+ - p_d^-)$  across the actuator disc, which is obtained by applying Bernoulli's equation separately to the upstream and downstream sections of the streamtube. The result of this operation is that half the axial speed loss in the streamtube takes place upstream of the actuator disc and half downstream. It results in the equation for the force on the air:

$$F = (p_d^+ - p_d^-) A_d = 2\rho A_d u_\infty^2 a(1 - a) \quad (3.4)$$

As this force is concentrated at the actuator disc, the rate of work done by the force is  $Fu_d$  and hence the power extraction from the air is given by

$$Power = Fu_d = 2\rho A_d u_\infty^3 a(1 - a)^2 \quad (3.5)$$

A power coefficient  $C_{pwr}$  is then defined as

$$C_{Pwr} = \frac{\text{Power}}{\frac{1}{2} \rho u_{\infty}^3 A_d} \quad (3.6)$$

where the denominator represents the power available in the air, in the absence of the actuator disc. From this point onwards, the free-stream flow velocity ( $u_{\infty}$ ) will be denoted simply by the symbol  $u$ , without the infinity subscript. Eq. (3.6) can as well be rewritten as a function of the axial induction factor:

$$C_{Pwr} = 4a(1-a)^2 \quad (3.7)$$

Thus, the power  $P$  generated by a wind turbine, is

$$P = \frac{1}{2} C_{Pwr} \rho A u^3 \quad (3.8)$$

where  $\rho$  is the air density,  $C_{Pwr}$  is the power coefficient,  $A$  is the blade swept area and  $u$  is the wind free stream velocity.

### 3.3 The Betz limit

The maximum value of the power coefficient occurs when  $C_{Pwr}$  in eq. (3.7) is differentiated in respect to  $a$  and made equal to zero, which gives a value of  $a = 1/3$ . Replacing this in abovementioned equation results in

$$C_{Pwr, \max} = \frac{16}{27} = 0.593 \quad (3.9)$$

The maximum achievable value of the power coefficient is known as the Betz-Joukowski limit, acceptably known simply as the Betz limit [Wood, 2011a]. The limit is caused not by any deficiency in blade or rotor design, for, as yet, there is no design at all, but because the streamtube has to expand upstream of the actuator disc, which causes the cross-



section of the tube where the air is at free-stream velocity to be smaller than the area of the disc itself [Burton et al., 2001].

### 3.4 Rotor solidity

So far the turbine was modeled without considering the blades themselves. In the blade element method the forces over the rotor blades are expressed as functions of lift and drag coefficients of the airfoils, which in turn are functions of their angle of attack. The basic idea is to split the blades into  $N$  sections, and the forces are then calculated at each one of these sections, that is, at each one of these blade elements. It is assumed that the forces acting on each blade element are the same as those on an isolated airfoil of the same section, angle of attack, and effective velocity [Ivanell, 2009].

As it is usually regarded, an airfoil is a two-dimensional body in an infinite flow that is uniform away from the region influenced by the body. Such a situation can not occur in a wind turbine because the blades are always separated by a finite distance in the azimuthal direction. The measure of the importance of this effect is the local solidity, which is defined as the ratio of the chord length of a blade element,  $c$ , at a given radial position,  $r$ , times the number of blades,  $N$ , and the circumferential length described by that element:

$$\sigma = \frac{Nc}{2\pi r} \quad (3.10)$$

The local solidity should not be confused with the global rotor solidity, defined as the ratio of the frontal surface area covered by the blades and the total area swept by them. It is possible to have parts of the rotor where the local solidity is equal to or exceeds 1. It happens whenever there is blade element overlap, taking place usually at the blade root where the chords are larger. On the other hand, the global solidity can never exceed 1, as the reference area is the perpendicular projected surface according to the trajectory of the fluid, regardless of whether or not the blades overlap each other. For any case, it is to be expected that, the more blades in a rotor, the stronger will be the solidity effects.

Another difference from airfoil behavior is that the flow over blade elements can remain attached at angles of attack that would cause an isolated airfoil to stall. That phenomenon is called stall delay and, although it is usually argued that the Coriolis and

centrifugal forces in the boundary layers of the rotating blades are responsible, a correction on airfoil lift and drag for stall delay, published by Burton et al., 2001, involves only the solidity [Wood, 2011a].

### 3.5 Blade Element Theory

Having mind what was stated in the previous sections, and also considering that the flow in each streamtube is independent of that in other streamtubes, it is possible to model the forces to which each blade element is subject. When considering the different forces, three different systems are defined.

The velocity system comprises the axial velocity at the blade, which is retarded to  $u(1-a)$  due to the induction, and the angular contribution, which is a combination of angular velocity  $r\Omega$  and angular induction  $a'r\Omega$ , where  $a'$  is the tangential induction factor. The wind speed relative to the blade,  $u_{rel}$ , is the result of axial and angular contributions. This is the actual wind speed “seen” by the blade element, and is used as reference for the airfoil lift and drag coefficients. Thus, the axial and tangential velocity components are defined, respectively, as:

$$u_1 = u(1-a) \quad (3.11)$$

$$u_2 = \Omega r(1+a') \quad (3.12)$$

The forces orthogonal and parallel to the wind direction are the forces that act over the blade element.  $dF_L$  represents the lift force and  $dF_D$  represents the drag force, both at the section under consideration. The forces orthogonal and parallel to the plane of rotation are forces resulting from the transformation of the forces over the airfoil section.  $dF_T$  represents the force contribution in angular direction from the section, i.e., useful torque. The  $dF_N$  force will in this case not produce any useful energy. It will result in the thrust force over the tower.

The section pitch angle is represented by  $\theta_p$ . It is composed of the blade root pitch angle and the local twist angle.  $\varphi$  represents the relative wind angle, i.e., the section pitch angle plus the angle of attack,  $\theta_p + \alpha$ , where  $\alpha$  is the angle of attack.

From figure. 3.3, one can determine the following relationships, where  $c$  is the airfoil section chord length [Ivanell, 2009]:

$$dF_L = C_L \frac{1}{2} \rho (u_{rel})^2 c dr \quad (3.13)$$

$$dF_D = C_D \frac{1}{2} \rho (u_{rel})^2 c dr \quad (3.14)$$

$$dF_N = dF_L \cos \varphi + dF_D \sin \varphi \quad (3.15)$$

$$dF_T = dF_L \sin \varphi - dF_D \cos \varphi \quad (3.16)$$

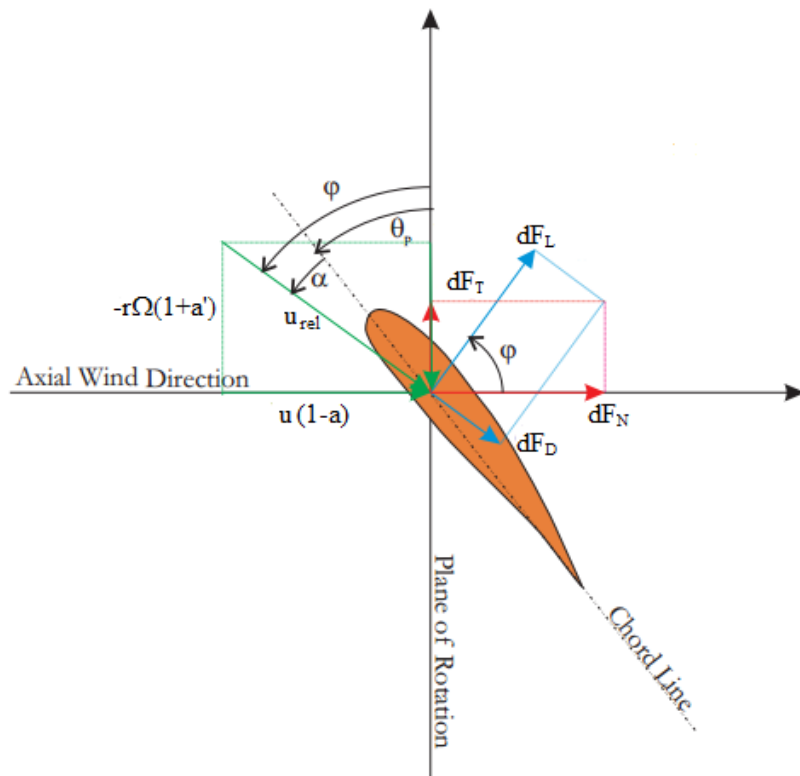


Figure 3.3 – Forces, velocities and angles at a blade element

In fig. 3.3, the arrow sizes are for illustration purposes only. They do not represent the actual magnitudes of quantities relative to each other. The total force will be the sum of the contributions from all sections multiplied by the number of blades,  $N$ . For one section of radius  $r$  the normal force, i.e., the force which will lead to a thrust force,  $F_N$ , will be:

$$dF_N = N \frac{1}{2} \rho (u_{rel})^2 (C_L \cos \varphi + C_D \sin \varphi) c dr \quad (3.17)$$

The torque,  $T$ , from a section at radius  $r$  will be:

$$dT = N r dF_T = N \frac{1}{2} \rho (u_{rel})^2 (C_L \sin \varphi - C_D \cos \varphi) c r dr \quad (3.18)$$

### 3.6 Blade element momentum theory

Equations (3.17) and (3.18) give the torque and thrust of the turbine modeled by the blade element theory. If these equations are combined with the momentum theory, the blade element momentum model can be obtained. The basic assumption of the blade element momentum (BEM) theory is that the force of a blade element is solely responsible for the change of momentum of the air which passes through the annulus swept by the element. It is therefore to be assumed that there is no radial interaction between the flows through contiguous annuli [Burton et al., 2001].

The derivation of the BEM theory equations is a lengthy process that adds little to the scope of the present work. It is relevant to know the resulting equations and the assumptions made for their derivation. For a comprehensive discussion over the mathematical background of BEM, the reader is invited to refer to the literature about wind turbine design, especially (but not restricted to) the books by Burton et al., 2001, Manwell et al., 2002 and Wood, 2011a.

The basic BEM equations are:

$$\frac{a}{1-a} = \frac{\sigma}{4 \sin^2 \varphi} \left[ (C_L \cos \varphi + C_D \sin \varphi) - \frac{\sigma}{4 \sin^2 \varphi} (C_L \sin \varphi - C_D \cos \varphi)^2 \right] \quad (3.19)$$

$$\frac{a}{1+a'} = \frac{\sigma (C_L \sin \varphi - C_D \cos \varphi)}{4 \sin \varphi \cos \varphi} \quad (3.20)$$

The calculation of torque and power developed by a rotor requires knowledge of the flow induction factors, which are obtained by solving the above equations. The solution is

usually carried out iteratively because the two-dimensional airfoil characteristics are non-linear functions of the angle of attack. The iterative procedure is to assume  $a$  and  $a'$  to be zero initially, determining  $\varphi$ ,  $C_L$  and  $C_D$  on that basis, and then to calculate new values of the flow factors.

The torque,  $T$ , developed by the blade elements of spanwise length is

$$dT = 4\pi\rho u(\Omega r)a'(1-a)r^2 dr \quad (3.21)$$

The complete rotor, therefore, develops a total torque  $T$ :

$$T = \frac{1}{2}\rho u\pi R^3\lambda \left[ \int_0^R \frac{1}{R^3} \left[ 8a'(1-a)\frac{r}{R} - \frac{u_{rel}}{u} \frac{Nc/R}{\pi} C_D(1+a') \right] r^2 dr \right] \quad (3.22)$$

Solving the BEM equations for a given, suitable blade geometrical and aerodynamic design yields a series of values for the power and torque coefficients which are functions of the tip speed ratio (TSR). The TSR, also represented by the Greek letter  $\lambda$ , is the ratio between the tangential speed of the blade tip and the free stream wind speed:

$$\text{TSR} = \lambda = \frac{\Omega R}{u} \quad (3.23)$$

where  $\Omega$  is the rotational speed (rad/s),  $R$  is the blade tip radius (m) and  $u$  is the free stream wind speed (m/s). The maximum power occurs at a TSR for which the axial flow induction factor  $a$  most closely approximates the Betz limit value of 1/3. A typical performance curve for a modern wind turbine is shown in figure 3.4.

The BEM theory is strictly only applicable if the blades have uniform circulation, that is, if  $a$  is uniform. For non-uniform circulation there is a radial interaction and exchange of momentum between flows through adjacent elemental annular rings. It cannot be stated that the only axial force acting on the flow through a given annular ring is that due to the pressure drop across the disc. However, in practice, it appears that the error involved in relaxing the above constraint is small for tip speed ratios greater than 3 [Burton et al., 2001].

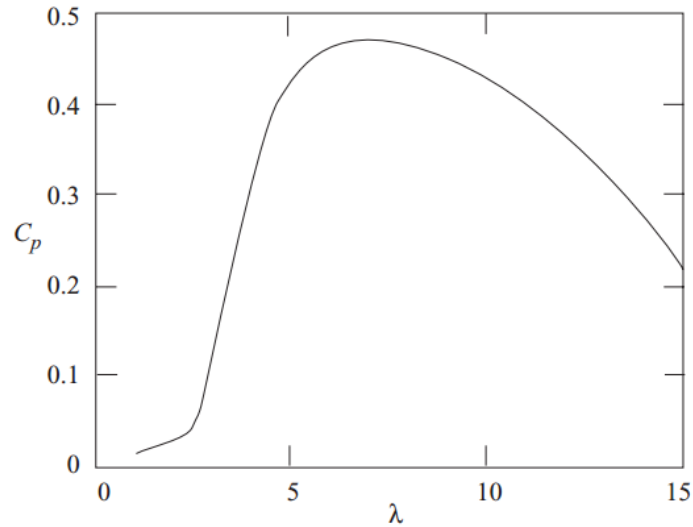


Figure 3.4 – Power coefficient versus tip speed ratio performance curve

### 3.7 Optimal blade design for variable-speed operation

A turbine operating at variable speed can maintain the constant tip speed ratio required for the maximum power coefficient to be developed regardless of the incident free-stream wind speed. Most small wind turbines fit this criterion because no pitch control is used and the operational velocity is normally regulated by the stall phenomenon at the blades. The turbine under study in the present work meets the criteria to be described by this methodology.

According to the general considerations in Section 3.3, the maximum power that can be extracted from a circular area is expressed by replacing eq. (3.9) in eq. (3.8). The result is [Gasch and Tvele, 2002].

$$P_{\text{BETZ}} = \frac{16}{27} \frac{\rho}{2} u^3 (\pi R^2) \quad (3.24)$$

where  $\pi R^2$  is the circular area swept by the rotor blades.

Having established this, the rotor should now be built in such a way that each ring element of area  $dA = 2\pi r dr$  of the swept rotor area extracts from the wind the power equivalent to

$$dP_{\text{BETZ}} = \frac{16}{27} \frac{\rho}{2} u^3 (2\pi r dr) \quad (3.25)$$

The total power developed by the rotor is the total torque,  $dT$ , multiplied by the angular velocity of the rotor,  $\Omega$ :

$$dP = \Omega dT \quad (3.26)$$

Since it is assumed that at the design point the airfoil operates close to its best lift to drag ratio, the drag coefficient is very small compared to the lift coefficient, and thus  $C_L$  is the only significant contributor to the tangential force. The mechanical power is now given by

$$dP = N\Omega r \frac{\rho}{2} C_L u_{rel}^2 c(r) dr \sin \varphi \quad (3.27)$$

Equating the mechanical power, eq. (3.27), and the Betz power, eq.(3.25), and using the flow induction factors for optimized operation,

$$a = \frac{1}{3} \quad \text{and} \quad a' = \frac{a(1-a)}{\lambda^2 \left(\frac{r}{R}\right)^2} \quad (3.28)$$

the formula for the blade chord  $c(r)$  of an optimally designed blade can be obtained:

$$c(r) = \frac{1}{N} 2\pi R \frac{8}{9C_L} \frac{1}{\lambda \sqrt{\lambda^2 \left(\frac{r}{R}\right)^2 + \frac{4}{9}}} \quad (3.29)$$

The relative velocity angle in reference to the rotor plane is given by

$$\tan \varphi = \frac{1-a}{\left(\lambda \frac{r}{R}\right)(1+a')} \quad (3.30)$$

Using the relations defined in eq. (3.28) once again, and taking into account the blade twist angle  $\theta_p(r)$  and the angle of attack  $\alpha(r)$  of the profile, the twist angle for each radial section of the blade is

$$\theta_p(r) = \arctan\left(\frac{3}{2} \frac{r}{R} \lambda\right) - \alpha(r) \quad (3.31)$$

In equations (3.29) and (3.31),  $c(r)$  is the local chord length at each blade section,  $\lambda$  is the design tip speed ratio,  $r$  is the radial position,  $R$  is the total rotor radius and  $\theta_p(r)$  is the blade twist angle as a function of the radial position. The two abovementioned equations allow the characterization of a whole blade, which can be used as a starting point for any subsequent optimization process.

Close to the blade root the inflow angle is large which could cause the blade to stall in that region. If the lift coefficient is to be held constant such that the drag is minimized everywhere, then the angle of attack also needs to be uniform at the appropriate value. For a prescribed angle of attack variation, the design pitch angle of the blade must vary accordingly. It is common practice in small wind turbines, however, to use a single angle of attack for all blade radial positions to minimize manufacturing costs.

### 3.8 Corrections to the classic methodology

Blade element momentum theory fundamentally assumes quasi two-dimensional flow, with no interaction between adjacent radial locations. However, spanwise flows are often present and cannot be accounted for with the baseline BEM technique [McCrink and Gregory, 2015].

Over time, additional relations have been introduced to deal with the limitations of the classic methodology. The main focus of these changes was to address the effects of the spanwise component on the aerodynamic performance.

#### 3.8.1 Tip losses

If the axial flow induction factor  $a$  is large at a given blade position, then the inflow angle  $\varphi$  will be small and the lift force will be almost normal to the rotor plane. The



component of the lift force in the tangential direction will be small and so will be its contribution to the torque. A reduced torque means reduced power and this reduction is known as tip loss because the effect occurs only at the outermost parts of the blade [Burton et al., 2001].

This phenomenon is a result of the finite number of blades on any real turbine and comes from the fact that the streamtube analysis – which was derived without taking any actual blade into account – assumed that the velocities and pressures are uniform in the circumferential direction, ignoring that non-uniformities must arise for a finite number of blades [Wood, 2011a].

A simple and commonly used correction for this effect is the Prandtl's Tip Loss Factor,  $F_{TL}$ , defined as the ratio of the average induction factor,  $a$ , and the value at the blades. In its simplest form, the equation for  $F$  is:

$$F_{TL} = 2 \cos^{-1}(e^{-f}) / \pi \quad (3.32)$$

where

$$f = N(R-r)/2r \sin \varphi \quad (3.33)$$

$F_{TL}$ , which is always less than unity, makes a difference of around 5% to 10% to the predicted turbine performance. According to Wood, 2011a, there is a tip loss method that rewrites the equations for the total thrust on the blade and the torque due to the circumferential force as functions of the original and modified induction factors, which are expressed by the following equations:

$$a_b = \frac{2 + Y_1 - \sqrt{4Y_1(1 - F_{TL}) + Y_1^2}}{2(1 + F_{TL}Y_1)} \quad (3.34)$$

$$a'_b = \frac{1}{(1 - aF_{TL})Y_2 / (1 - a) - 1} \quad (3.35)$$

where

$$Y_1 = 4F_{TL} \sin^2 \varphi / [\sigma (C_L \cos \varphi + C_D \sin \varphi)] \quad (3.36)$$

$$Y_2 = 4F_{TL} \sin \varphi \cos \varphi / [\sigma (C_L \sin \varphi - C_D \cos \varphi)] \quad (3.37)$$

### 3.8.2 Three-dimensional effects

A simple, empirical modification to the usually available two-dimensional, static airfoil lift coefficient data has been proposed [Burton et al., 2001]. Under these conditions, for a given airfoil, if the linear part of the  $C_L$  versus  $\alpha$  curve is extended beyond the stall angle, then  $\Delta C_L$  is the difference between this extension and the original curve for higher angles of attack. The correction to the two-dimensional curve to account for the rotational, three-dimensional effects is

$$C_{L,3D} = C_{L,2D} + 3 \left( \frac{c}{r} \right)^2 \Delta C_L \quad (3.38)$$

It is a simple relation that is easy to apply. The original study in which it was proposed found that, at a blade span position of 30%, calculations for the lift coefficient matched the measured values for the rotating blade with a difference around 2%, while the difference between measured data for static and rotating blades was around 56%.

## 3.9 The power curve

The power output of a wind turbine varies with wind speed and every wind turbine has a characteristic power performance curve. With such a curve it is possible to predict the energy production of a wind turbine without considering the technical details of its various components [Manwell et al., 2002]. The power curve gives the electrical power output as a function of the wind speed at hub height. Figure 3.5 (a) shows the power curve for the 7-meter diameter Bergey BWC XL 10 kW turbine and (b) shows one for the 80-meter diameter Vestas V80 2 MW turbine [Wood, 2011a].

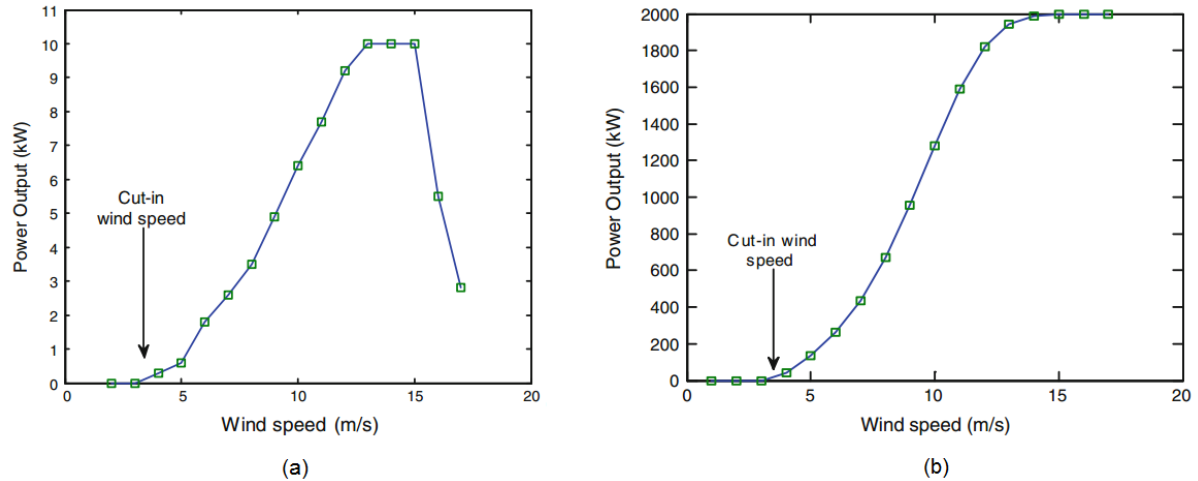


Figure 3.5 – Power curves for two different Wind turbines operating at sea level as functions of the wind speed at hub height. Bergy 10 kW BWC XL (a) and Vestas 2 MW V80 (b).

The performance of a given wind turbine can be related to three key points on the velocity scale. The cut-in speed is the minimum wind speed at which the machine will deliver useful power. Its value is a sensitive parameter that depends strongly on the blade design, cogging torque of the electrical generator and free-stream wind speed. For a good blade design, the cut-in speed should be as low as possible. The rated speed is the wind speed at which the rated power (generally the maximum power output of the electrical generator) is reached, and the cut-out speed is the maximum wind speed at which the turbine is allowed to deliver power. It is usually limited by engineering design and safety constraints [Manwell et al., 2002].

There are a number of possible control actions for large wind turbines, such as controlling the angle of attack by pitching the blades, which are not available at small scale. For nearly all large turbines but rarely for small ones, there is also a “cut-out” wind speed at which the turbine is shut down for safety reasons (for instance, 25 m/s for the V80, not shown in fig. 3.5). At this speed, the brake is activated, and not released until the wind speed has decreased. At high wind speeds, smaller turbines are often “furlled”, i.e., turned out of the wind direction by the collapse of the tail fin. Other small turbines rely on control of the generator’s field current to reduce output in high winds and shorting of the generator output for braking [Wood, 2011a]. The stall phenomenon is also used as a brake. For that, the blades are purposely designed in such a way that the flow over them would separate for wind speeds higher than a certain limit, thus highly increasing the drag and slowing down the rotor.

## 4 MATHEMATICAL AND NUMERICAL FLOW MODELING

A fluid flow is said to be laminar when it can be described as moving in well-defined layers, and there is no mixing between adjacent layers. The flow is turbulent when it fails to move in well-defined layers and those layers start to interact with each other as a result of high frequency in their mean velocity. Turbulent flow is usually defined by its characteristics: irregularity, nonlinearity, diffusivity and high Reynolds numbers. Turbulence is part of the Mechanics of Continuum, since its smallest scales are larger than the molecular scale.

The Reynolds number is the criterion that defines the flow regime. It is a nondimensional parameter that takes into account the fluid density and viscosity and the velocity with which it moves, as well as a characteristic length (e.g. pipe diameter for internal flows, chord length for airfoils subject to external flows). Transition to the turbulent regime occurs at Reynolds numbers ( $Re$ ) near 2,300 for internal flows, although it was possible to maintain laminar internal flow at diameter-based  $Re$  near 100,000 in extremely controlled environments for some experiments [Fox et al., 2004]. This is not the case, however, for external air flows involving large devices like wind turbines, which makes these flows to be categorized as essentially turbulent. For external flows over airfoils, unless otherwise stated, the Reynolds number is defined having the profile chord as reference dimension.

Compressibility is generally not an issue when working with wind turbines. Since the flow speeds at the blade tip usually never exceed 100 meters per second, equivalent to a Mach number of about 0.3, it is safe to assume that the flow affected by a wind turbine is incompressible [Schlichting, 1960; Vermeer et al., 2003].

### 4.1 Fundamental equations (Navier-Stokes and Continuity)

The Navier-Stokes (N-S) equations are a set of mathematical formulae capable of describing the fluid motion in its entirety. For the sake of simplicity, and keeping focus on the phenomena under study in this work, the following equations have been simplified to describe the incompressible flow of a Newtonian fluid not subject to any non-contact forces and without temperature variation. The system of equations is presented in Einstein's Index Notation [Schlichting, 1960]. It reads:

$$\frac{\partial u_i}{\partial x_i} = 0 \quad (4.1)$$

$$\rho \frac{\partial u_i}{\partial t} + \rho \frac{\partial}{\partial x_j} (u_i u_j) = -\frac{\partial p}{\partial x_i} + \frac{\partial}{\partial x_j} (t_{ij}) \quad (4.2)$$

where

$$t_{ij} = 2\mu s_{ij} \quad (4.3)$$

$$s_{ij} = \frac{1}{2} \left( \frac{\partial u_i}{\partial x_j} + \frac{\partial u_j}{\partial x_i} \right) \quad (4.4)$$

In the above equations,

$u_i$  and  $u_j$  are the components of the velocity vector,

$p$  is the pressure,

$t$  is the time,

$\mu$  is the dynamic viscosity, and

$\rho$  is the fluid density.

$i, j = 1, 2, 3$

Eq. (4.1) represents the principle of Mass Conservation, also called Continuity equation. Eq. (4.2) is the Momentum equation, and eqs. (4.3) and (4.4) are additional relations that have been separated from the main set for clarity. It is then a closed three-dimensional system of four unknowns. The abovementioned equations were first set up by M. Navier (1827) and S. D. Poisson (1831) on the basis of considerations on the action of intermolecular forces. Later the same equations were derived without such hypotheses by B. de Saint Venant (1843) and G. G. Stokes (1845), using, as a basis, the assumption that the normal and shear stresses are linear functions of the rate of deformation, as had already been introduced via Newton's law of friction [Schlichting, 1960].

Since the Stokes assumption for the friction forces is purely empirical, one cannot be a priori sure that the Navier-Stokes equations correctly describe the motion of a fluid [Schlichting, 1960]. For most of the practical applications, this can only be done

experimentally. Due to the nonlinear characteristics of the governing equations, their analytical solution for complex flow cases is yet to be found. Thus, the solution is being sought making use of numerical methods ranging from the Direct Numerical Simulation (DNS), in which all the spatial and temporal scales are solved, to the use of different turbulence modeling methods [Möller and Silvestrini, 2004]. Those methods will be addressed in the following section. However, known solutions, such as laminar flow through a circular pipe, as well as boundary-layer flows, agree so well with experiment that the general validity of the Navier-Stokes equations can hardly be doubted [Schlichting, 1960].

## 4.2 Turbulence modeling

Turbulent flows are characterized by vortical structures of many sizes and time scales. The larger vortices are usually comparable in size with the mean characteristic length of the flow, while the smaller scales are responsible for the dissipation of turbulent kinetic energy. It is possible, in theory, to directly solve the whole spectrum of turbulent scales using the DNS approach. This methodology does not require turbulence models, but it is not feasible for practical problems in engineering that involve flows with high Reynolds numbers. The computational cost needed to solve all the scales is connected to the Reynolds number, which makes clear that, for higher  $Re$ , the cost is prohibitive [Mo and Lee, 2011].

The Reynolds-Averaged Navier-Stokes (RANS) equations are a set of relations derived from the Flow Stability Theory, introduced originally by Osborne Reynolds in 1895. Departing from the basic fluid mechanics equations, Reynolds suggested modeling the turbulent flow as a mean flow that is affected by small disturbances that, increasing over time, facilitate the occurrence of transition to the turbulent regime. This logic led to the decomposition of the flow variables into mean and disturbance components. It introduced more terms in the basic N-S equations, creating a problem with more unknowns than equations [Snel and Schepers, 1993]. The so-called closure problem is the issue all turbulence models try to address by adding equations and assumptions to the original system.

### 4.2.1 The Reynolds averaging process

According to Wilcox, 1994, because turbulence consists of random fluctuations of the various flow properties, a statistical approach must be used to address the closure problem.

This explains the averaging concepts introduced by Reynolds in 1895, in which all quantities are expressed as the sum of mean and fluctuating parts. Since virtually all engineering problems involve inhomogeneous turbulence, time averaging is the most appropriate form of Reynolds averaging, and for such a flow the instant velocity is expressed as the sum of a mean and a fluctuating part as stated in eq. (4.5).

$$u_i(\vec{x}, t) = U_i(\vec{x}) + u_i'(\vec{x}, t) \quad (4.5)$$

In the above equation, an arrow above the variable denotes a vector. The time average of the mean velocity is again the same time-averaged value, as stated in eq. (4.6), where an overbar is shorthand for time average. The time average of the fluctuating part of the velocity is zero. That is, in eq. (4.7),

$$\overline{U_i(\vec{x})} = \lim_{\tau \rightarrow \infty} \frac{1}{\tau} \int_t^{t+\tau} U_i(\vec{x}) dt = U_i(\vec{x}) \quad (4.6)$$

$$u_i' = \lim_{\tau \rightarrow 0} \frac{1}{\tau} \int_t^{t+\tau} [u_i(\vec{x}, t) - U_i(\vec{x})] dt = U_i(\vec{x}) - \overline{U_i(\vec{x})} = 0 \quad (4.7)$$

where  $\tau$  is a characteristic time scale. While the above system is mathematically well defined, it is not feasible to realize infinite  $\tau$  in any physical flow. This is not a serious problem in practice, though. In forming out time average, it is adequate to choose a value of  $\tau$  that is very long relative to the maximum period of the velocity fluctuations. As an example, for flow at 10 m/s in a 5 cm diameter pipe, an integration time of 20 seconds would probably be adequate. In this time, the flow moves 4,000 pipe diameters [Wilcox, 1994].

Thus, by applying this strategy on the Navier-Stokes equations, the result is:

$$\frac{\partial U_i}{\partial x_i} = 0 \quad (4.8)$$

$$\rho \frac{\partial U_i}{\partial t} + \rho U_j \frac{\partial U_i}{\partial x_j} = -\frac{\partial \overline{p}}{\partial x_i} + \frac{\partial}{\partial x_j} (t_{ij} - \overline{\rho u_j' u_i'}) \quad (4.9)$$

Eqs. (4.8) and (4.9) are usually referred to as Reynolds-Averaged Navier-Stokes equations. The quantity in eq. (4.10) is known as the Reynolds Stress Tensor.

$$\tau_{ij} = -\overline{\rho u'_j u'_i} \quad (4.10)$$

The Reynolds Stress Tensor is symmetric, and thus has six independent components. Hence, six unknown quantities have been produced as a result of the Reynolds averaging, but no additional equations have been gained. So, for general three-dimensional flows, there are four unknown mean flow properties (pressure and the three velocity components) and, along with the six Reynolds-stress components, the total number of unknowns is ten. The equations are the mass conservation and the three components of the momentum equation, which means that the system is not yet closed.

#### 4.2.2 Turbulence models

The simplest of all turbulence models are known as algebraic models. These use the Boussinesq eddy-viscosity approximation to compute the Reynolds stress tensor as the product of an eddy viscosity and the mean strain-rate tensor. This eddy viscosity, or turbulent viscosity, depends upon the flow, and is often computed in terms of a mixing length, also a function of the flow. Because these two properties depend on the flow under consideration, they must be specified in advance. Thus, algebraic models are, by definition, incomplete models of turbulence.

The mixing-length hypothesis was put forth by the German engineer Ludwig Prandtl in 1925. He visualized a simplified model for turbulent fluid motion in which fluid particles gather into groups and move together as a unit. These lumps of fluid retain their  $x$ -directed momentum for a distance in the  $y$  direction,  $l_{mix}$ , that he called the mixing length. Prandtl's hypothesis leads to the following formulation:

$$\tau_{xy} = \mu_T \frac{dU}{dy} \quad (4.11)$$

where  $\tau$  is the shear stress and  $\mu_T$  is the turbulent viscosity:



$$\mu_T = \rho(l_{mix})^2 \left| \frac{dU}{dy} \right| \quad (4.12)$$

This formulation remains incomplete, however, because the mixing length is an empirical quantity. Despite this fact, it originated a series of turbulence models, among which the best known is the Baldwin-Lomax model, from 1978. These models yield good results for special cases of internal and external flow. They are regarded as computationally cheap.

The turbulence energy equation models represent the next step in the search for adequate representations for the turbulence. They are usually divided in one-equation models and two-equation models and are based on the Boussinesq approximation as well, but differ in the sense that one-equation models are incomplete as they relate the turbulence length scale to some typical flow dimension, while two-equation models provide an equation for the turbulence length scale or its equivalent and are thus complete.

The kinetic energy per unit mass of the turbulent fluctuations is denoted by the variable  $k$  and was introduced in 1945 by Prandtl. It is based on the velocity fluctuations in the three dimensions:

$$k = \frac{1}{2} \overline{u'_i u'_i} \quad (4.13)$$

Thus, in terms of the density,  $\rho$ , a turbulence length scale,  $l$ , and  $k$ , dimensional arguments dictate that the eddy viscosity is given by

$$\mu_T = \text{constant} \cdot \rho k^{1/2} l_{mix} \quad (4.14)$$

The Reynolds stress tensor is now given by eq. (4.15), where  $S_{ij}$  is the mean strain-rate tensor:

$$\tau_{ij} = 2\mu_T S_{ij} - \frac{2}{3} \rho k \delta_{ij} \quad (4.15)$$

where  $\delta_{ij}$  is the Kronecker delta. The most important and well-known models that follow these lines are the  $k$ - $\varepsilon$  and the  $k$ - $\omega$ , both two-equation models. The  $k$ - $\varepsilon$  model is the most

popular of them, relating the turbulent kinetic energy to the dissipation per unit mass, while the  $k$ - $\omega$  model relates the kinetic energy with the specific dissipation rate. Over the years, experience gathered by the application of these models in a range of flow simulation situations led to the introduction of corrections and adaptations to them. One of them is the *Shear Stress Transport* (SST) model, an adaptation of the original  $k$ - $\omega$  model that turned it into an approach capable of producing good results both for free-stream turbulent flows and flows subject to strong pressure gradients and prone to detachment.

#### 4.2.3 Original and SST $k$ - $\omega$ models

The  $k$ - $\omega$  model in its original form was the first two-equation model to be developed. It was presented in 1942 by Andrey Kolmogorov, which proceeded to complement Prandtl's turbulent kinetic energy equation with an equation for the dissipation rate per unit kinetic energy of the turbulence. This parameter was later called specific dissipation rate and denoted by the variable  $\omega$ . Kolmogorov used scale analyses to conclude that  $\omega$  has dimension  $[\text{time}]^{-1}$  and, since dissipation takes place in the smallest vortices, the dissipation rate is the rate of kinetic energy transfer from the larger to the smaller vortices, which became known as Kolmogorov's energy cascade.

The formulation rewritten by Wilcox, 1994, as shown here, is regarded as the state-of-the-art for the  $k$ - $\omega$  model. Eqs. (4.16), (4.17), (4.18) e (4.19) are the turbulent viscosity, the turbulent kinetic energy, the specific dissipation rate and the closure coefficients, respectively.

$$\mu_T = \rho k / \omega \quad (4.16)$$

$$\rho \frac{\partial k}{\partial t} + \rho U_j \frac{\partial k}{\partial x_j} = \tau_{ij} \frac{\partial U_i}{\partial x_j} = \beta^* \rho k \omega + \frac{\partial}{\partial x_j} \left[ (\mu + \sigma^* \mu_T) \frac{\partial k}{\partial x_j} \right] \quad (4.17)$$

$$\rho \frac{\partial \omega}{\partial t} + \rho U_j \frac{\partial \omega}{\partial x_j} = \alpha \frac{\omega}{k} \tau_{ij} \frac{\partial U_i}{\partial x_j} - \beta \rho \omega^2 + \frac{\partial}{\partial x_j} \left[ (\mu + \sigma \mu_T) \frac{\partial \omega}{\partial x_j} \right] \quad (4.18)$$

$$\alpha = 5/9, \quad \beta = 3/40, \quad \beta^* = 9/100, \quad \sigma = 1/2, \quad \sigma^* = 1/2 \quad (4.19)$$

In the above set of equations,  $\alpha$ ,  $\beta$ ,  $\beta^*$ ,  $\sigma$  and  $\sigma^*$  are constants. The starting point for the development of the SST model, also known as SST  $k$ - $\omega$  model, was the need for the

accurate prediction of aeronautics flows with strong adverse pressure gradients and separation. According to Menter et al., 2003, the otherwise popular  $k-\varepsilon$  model was not able to capture the proper behavior of turbulent boundary layers up to separation, and the original  $k-\omega$  model, although more accurate than the  $k-\varepsilon$  model in near wall layers, would fail for flows with pressure-induced separation.

The SST model blends the robust and accurate formulation of the  $k-\omega$  model in the near-wall region with the freestream independence of the  $k-\varepsilon$  model in the far field. It does so by multiplying both models by a blending function and adding them together. The blending function is designed to be one in the near-wall region, which activates the standard  $k-\omega$  model, and zero away from the surface, which activates the  $k-\varepsilon$  model. The SST was developed for situations typically found in the aerospace industry, but its good results have attracted users from other areas that need modeling both near and far away from walls [ANSYS, 2009].

The formulation presented here is that derived by Menter et al., 2003. It brings small updates due to the experience acquired with the use of this model since the original version was introduced by the same author in 1994. Turbulent kinetic energy is obtained from the following equation:

$$\frac{\partial k}{\partial t} + U_i \frac{\partial k}{\partial x_i} = \frac{\partial}{\partial x_i} \left[ \left( \nu + \frac{\nu_t}{\sigma_\omega} \right) \frac{\partial k}{\partial x_i} \right] + \frac{\tilde{P}_k}{\rho} - \beta^* k \omega \quad (4.20)$$

where  $k$  is the turbulent kinetic energy,  $\nu$  is the kinematic viscosity,  $\nu_t$  is the turbulent kinematic viscosity,  $\omega$  is the specific dissipation rate, as introduced by,  $\sigma_\omega$  is a model constant, and  $P_k$  is defined as

$$P_k = \rho \nu_t \frac{\partial U_i}{\partial x_j} \left( \frac{\partial U_i}{\partial x_j} + \frac{\partial U_i}{\partial x_i} \right) \rightarrow \tilde{P}_k = \min(P_k, 10\beta^* \rho k \omega) \quad (4.21)$$

The specific dissipation rate can be modeled as

$$\frac{\partial \omega}{\partial t} + U_i \frac{\partial \omega}{\partial x_i} = \frac{\partial}{\partial x_i} \left[ \left( \nu + \sigma_\omega \nu_t \right) \frac{\partial \omega}{\partial x_i} \right] + \alpha S^2 - \beta \omega^2 + 2(1 - F_1) \sigma_{\omega 2} \frac{1}{\omega} \frac{\partial k}{\partial x_i} \frac{\partial \omega}{\partial x_i} \quad (4.22)$$

In eq. (4.22),  $\alpha$  is a model variable that depends on the interpolation function.  $S$  represents a source term. The blending function,  $F_1$ , is:

$$F_1 = \tanh \left\{ \left\{ \min \left[ \max \left( \frac{\sqrt{k}}{\beta^* \omega \psi}, \frac{500\nu}{\psi^2 \omega} \right), \frac{4\rho\sigma_{\omega 2}k}{CD_{k\omega}\psi^2} \right] \right\}^4 \right\} \quad (4.23)$$

In eq. (4.23),  $\psi$  is the distance to the closest wall.  $CD_{k\omega}$  is calculated as follows:

$$CD_{k\omega} = \max \left( 2\rho\sigma_{\omega 2}k \frac{1}{\omega} \frac{\partial k}{\partial x_i} \frac{\partial \omega}{\partial x_i}, 10^{-10} \right) \quad (4.24)$$

The turbulent viscosity is defined as:

$$\nu_t = \frac{\alpha_1 k}{\max(\alpha_1 \omega, SF_2)} \quad (4.25)$$

where  $S$  is the invariant measure of the strain rate and  $F_2$  is a second blending function defined by:

$$F_2 = \tanh \left\{ \left\{ \max \left( \frac{2\sqrt{k}}{\beta^* \omega \psi}, \frac{500\nu}{\psi^2 \omega} \right)^2 \right\} \right\} \quad (4.26)$$

The remaining constants come from the original models, with some changes. Its values are:

$$\begin{aligned} \beta^* &= 9/100; \alpha_1 = 5/9; \beta_1 = 3/40; \sigma_{k1} = 0,85; \\ \sigma_{\omega 1} &= 0,5; \beta_2 = 0,0828; \sigma_{k2} = 1; \sigma_{\omega 2} = 0,856 \end{aligned} \quad (4.27)$$

$F_1$  and  $F_2$  promote the model's adaptation whether the flow experiences gradients due to the presence of walls or not.  $F_1$  is responsible for the switch between the transport equations, and  $F_2$  promotes the change between the equations for the turbulent viscosity.

#### 4.2.4 Transition SST model

The Transition SST ( $\gamma$ - $Re_\theta$ ) model was developed due to the need of predicting with some precision the point where the boundary layer ceases to be laminar and initiates the transition to the turbulent regime. So far, the available models had ignored this phenomenon, and the boundary layer was traditionally defined as fully turbulent from start to end. This model is based on the coupling of the transport equations from the SST model with two additional transport equations: one for the intermittency and other for the transition onset criterion in terms of momentum thickness,  $\delta_2$ .

According to ANSYS, 2009, intermittency,  $\gamma$ , is defined as

$$\frac{\partial}{\partial t}(\rho\gamma) + \frac{\partial}{\partial x_j}(\rho U_j \gamma) = P_{\gamma 1} - E_{\gamma 1} + P_{\gamma 2} - E_{\gamma 2} + \frac{\partial}{\partial x_j} \left[ \left( \mu + \frac{\mu_t}{\sigma_\gamma} \right) \frac{\partial \gamma}{\partial x_j} \right] \quad (4.28)$$

The sources of transition as defined as follows:

$$P_{\gamma 1} = 2F_{length} \rho S_s [\gamma F_{onset}]^{c_{\gamma 3}} \quad (4.29)$$

$$E_{\gamma 1} = P_{\gamma 1} \gamma \quad (4.30)$$

In eq. (4.29),  $S_s$  is the strain rate magnitude.  $F_{length}$  and  $F_{onset}$  are empirical correlations that control the length of the transition region and its onset point, respectively. Relations for relaminarization source and sink are defined by eqs. (4.31) e (4.32).

$$P_{\gamma 2} = (2c_{\gamma 1}) \rho \Gamma \gamma F_{turb} \quad (4.31)$$

$$E_{\gamma 2} = c_{\gamma 2} P_{\gamma 2} \gamma \quad (4.32)$$

where  $\Gamma$  is the vorticity magnitude, and  $c_{\gamma 1}$ ,  $c_{\gamma 2}$  and  $c_{\gamma 3}$  are constants. The Transition SST model was developed by German engineer Florian Menter, which had previously developed the basic SST model while working for the ANSYS, Inc. German division.

The RANS methodology coupled to two-equation turbulence models is the most used in the majority of numerical flow simulations. Its reliability is related to the quality of the

mathematical modeling, which usually depends on empirical constants. RANS methods produce widely varying results at angles of attack associated with stall. In fully turbulent flows, they are prone to overpredicting the drag, whilst also overpredicting the maximum lift and the moment magnitudes and locations [Guerra et al., 2006]. Despite that, the cost-benefit of using this approach is generally good, since most of the turbulence models were developed focusing on aeronautical applications, having had its constants defined also as a function of these applications.

### **4.3 Numerical methods in flow simulation**

The Navier-Stokes equations were introduced in section 4.1. As discussed, they are capable of describing the flow motion in its entirety. Their analytical solution can only be obtained for particular flow cases, however, for which many of their terms are suppressed due to simplifying assumptions. For most of the engineering applications, their analytical solution remains on the list of unsolved problems in mathematics.

Computational Fluid Dynamics (CFD) has been increasingly adopted as the main alternative when obtaining analytical solutions to sets of equations is either not possible or not viable. Such approach is based on the concept of discretizing the domain in a finite number of volumes or cells and, for each one of these subdivisions, solving a set of similarly discretized equations, which are derived directly from the differential equations that model the behavior of the unknowns [Patankar, 1980]. These discrete equations approximate the value of their corresponding original differential equations. Among the methods used to derive these discrete equations is the Taylor series expansion.

The traditional methods for the numerical solution of differential equations are the Finite Difference Method (FDM), Finite Volume Method (FVM) and Finite Element Method (FEM). Historically, FDM has been employed in fluid mechanics, while FEM took the direction of the structural mechanics and was applied in the solution of elasticity problems. In the 1970's, FDM had accumulated considerable experience in fluid simulations but was unsuitable to be used in complex geometries, while FEM had become capable to deal with complex geometries but lacked the tools to model the advective terms in the equations of motion. These issues, among others, motivated research to improve the FVM. In this method, the approximate equations are obtained by conservation balances in each volume, instead of dealing with the mesh nodes as its predecessors did [Maliska, 2004].

The fluid simulation market is currently dominated by four codes: PHOENICS, FLOW3D, STAR-CD and ANSYS Fluent. All are based on the Finite Volume Method [Versteeg and Malalasekera, 1995]. This thesis uses Fluent, published by American developer ANSYS, Inc. Thus, the following description covers FVM only.

ANSYS Fluent divides the flow domain in control volumes to convert a scalar transport equation in an algebraic equation that can be numerically solved. This technique consists of integrating the transport equation in each volume, which results in a discrete equation expressing the conservation laws based on the logic of a closed control volume.

#### 4.3.1 Discretization of the governing equations

The discretization of the governing equations can be more easily demonstrated if the transient conservation equation for the transport of a generic scalar variable  $\phi$  is considered. This is shown by the following equation, written in the integral form for an arbitrary control volume  $V$  as follows [Versteeg and Malalasekera, 1995; ANSYS, 2009]:

$$\int_V \frac{\partial \rho \phi}{\partial t} dV + \int \rho \phi \vec{u} \cdot d\vec{A} = \int \Gamma_\phi \nabla \phi \cdot d\vec{A} + \int_V S_\phi dV \quad (4.33)$$

The various parameters of eq. (4.33) are:

$\rho$  = density;

$\vec{u}$  = velocity vector;

$\vec{A}$  = surface area vector;

$\Gamma_\phi$  = diffusion coefficient for the variable  $\phi$  ;

$\nabla \phi$  = gradient of  $\phi$  ;

$S_\phi$  = source of  $\phi$  per unit volume.

Equation (4.33) is applied to every control volume, or cell, of the computational domain. Its discretization, in a given cell or volume, yields:

$$\frac{\partial \rho \phi}{\partial t} V + \sum_f^{N_{faces}} \rho_f \vec{u}_f \phi_f \cdot \vec{A}_f = \sum_f^{N_{faces}} \Gamma_\phi \nabla \phi_f \cdot \vec{A}_f + S_\phi V \quad (4.34)$$

where

$N_{faces}$  = number of faces bounding a cell;

$\phi_f$  = value of the variable  $\phi$  convected through face  $f$  ;

$\rho_f \vec{v}_f \cdot \vec{A}_f$  = mass flow rate through that face;

$\vec{A}_f$  = surface area of face  $f$ ;

$\nabla \phi_f$  = gradient de  $\phi$  at face  $f$  ;

$V$  = cell volume.

Eq. (4.34) is the discretized equation for the transport of the scalar  $\phi$ . It is usually nonlinear. Its linearized form can be written as:

$$h_p \phi = \sum_{nb} h_{nb} \phi_{nb} + b \quad (4.35)$$

where  $nb$  denotes the neighboring cells , and  $h_p$  e  $h_{nb}$  are the linearized coefficients for  $\phi$  e  $\phi_{nb}$ . The equations solved by the Fluent package are equivalent to those presented in this section, and can be applied to multi-dimensional and unstructured grids, composed of polyhedra of arbitrary shapes. Similar expressions can be written for every cell or volume in the mesh. This results in a set of algebraic equations with a matrix of coefficients [ANSYS, 2009].

#### 4.3.2 Spatial discretization

By default, ANSYS Fluent stores discrete values of the scalar  $\phi$  at the cell centers. However, face values  $\phi_f$  are required for the convection terms in eq. (4.34) and must be interpolated from the cell center values. This is accomplished using an upwind scheme. Upwinding means that the face value  $\phi_f$  is derived from quantities in the cell upstream relative to the direction of the normal velocity  $u_n$ . Among the available options, the second-order upwind scheme was chosen to be used in this study.

In the second-order approach, high-order accuracy is achieved at cell faces through a Taylor series expansion of the cell-centered solution about the cell centroid [ANSYS, 2009].



### 4.3.3 Temporal discretization

For transient simulations, the governing equations must be discretized in both space and time. Temporal discretization involves the integration of every term in the differential equations over a time step  $\Delta t$ . This operation is straightforward. If a generic expression for the time evolution of a variable  $\phi$  is considered, as given by:

$$\frac{\partial \phi}{\partial t} = F(\phi) \quad (4.36)$$

The second-order discretization is given by:

$$\frac{3\phi^{n+1} - 4\phi^n + \phi^{n-1}}{2\Delta t} = F(\phi) \quad (4.37)$$

In equation (4.37),

$\phi$  = a generic scalar quantity;

$n+1$  = value at the next time level,  $t + \Delta t$  ;

$n$  = value at the current time level,  $t$  ;

$n-1$  = value at the previous time level,  $t - \Delta t$  .

Once the time derivative has been discretized, it is necessary to define which time level values of  $\phi$  should be used in evaluating  $F(\phi)$ . One option is to evaluate the function at the future time level; this is referred to as “implicit” integration. Otherwise, the integration is said to be “explicit” if the function is evaluated at the current time step.

The implicit scheme has been used in this study. The advantage of the fully implicit scheme is that it is unconditionally stable with respect to time step size [ANSYS, 2009].

## 5 TWO-DIMENSIONAL AIRFOIL SIMULATIONS

This chapter is intended to describe the creation process of the computational models and discretization grids used in the present work. The airfoils, characterized by points and its coordinates, the domains, defined without any outer walls that could interfere in a situation of external flow, and the meshes, composed entirely by quadrilateral cells according to the common practices in the literature, are discussed. The particular numerical methods employed are pointed out, and grid quality studies are presented. Following, results for the aerodynamic coefficients of the three selected airfoils are presented for a range of Reynolds numbers and angles of attack. All simulations performed in this work are two-dimensional. This decision was taken to allow for easier comparisons with experimental airfoil data.

### 5.1 Methods

It is common practice to perform a validation study of the numerical methodology. It is accomplished by applying the intended methodology in the reproduction of one or more well documented cases to assess the agreement levels between results from both situations. Three airfoils were selected for this phase: NACA 0012, due to the wide availability of wind tunnel data, S809, due to it being an airfoil designed for wind turbines, and SD7062, a low-Reynolds airfoil that has been used in a number of test turbines, especially by Dr. David Wood and his colleagues at the University of Newcastle, Australia. Figure 5.1 shows the selected profiles along with the maximum thickness relative to the chord length for each one.

#### 5.1.1 Airfoil modeling

In the present work, all airfoils were modeled the same way. Each one of the two sides was described by a set of 60 points joined by a smooth line extending from the leading edge to the trailing edge. The latter was sectioned vertically at 99% chord. This is a common practice in airfoil simulation used to avoid numerical errors at that region and, thus, the delay or even the impossibility of convergence [Beck, 2010]. These errors can occur when two streams with different properties meet at a sharp edge.

For the NACA 0012 and the S809, the computational domain was divided in two circular zones. The internal zone, containing the airfoil, had a radius of 10 meters

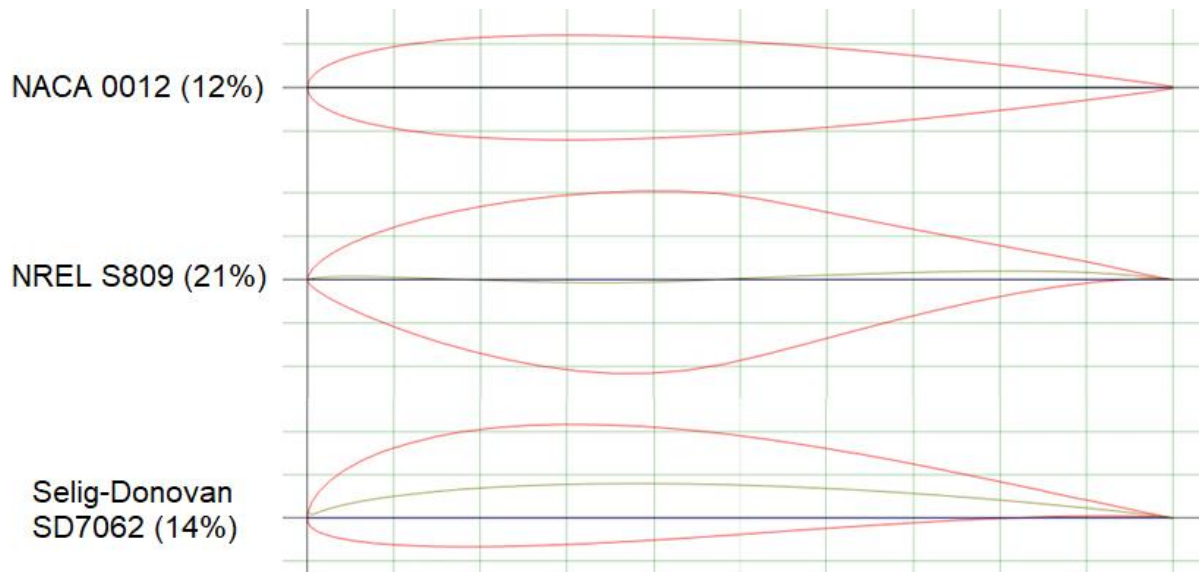


Figure 5.1 – Airfoils simulated. Top: NACA 0012, middle: S809, bottom: DS7062

(corresponding to 10 chords) and could be freely rotated around the Z-axis upon case setup to configure any angle of attack, thus eliminating the need to construct a new mesh for each AOA case. The ring-shaped external zone had internal and external diameters of 10 m and 50 m, respectively, and its position would never be changed. It contained the lines that represent the inlet and outlet boundary conditions; they were located at the western and eastern hemispheres respectively. This setup ensured that the flow entered and left the domain always parallel to the horizontal axis regardless of AOA configuration.

The two zones were connected using the interface condition, one of the boundary condition options present in the code. This condition does not impose any obstacle to the flow. It does not depend on the relative angle between the two zones, either. Figure 5.2 illustrates this approach.

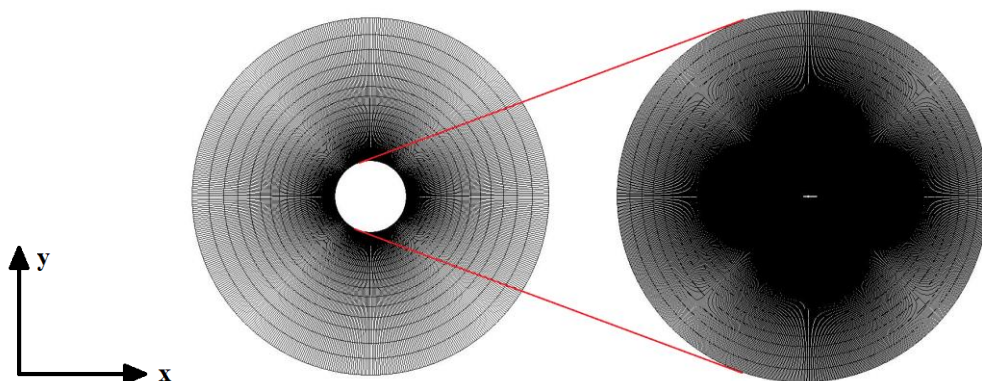


Figure 5.2 – Circular domains, external and internal (not to scale)

The two-zone setup was intended to be used for all single-airfoil simulations, but it was discarded for the SD7062 in favor of a single-zone, 50-chord radius domain. The circular shape was kept, though, and so were the inlet and outlet boundary conditions defined at the western and eastern hemispheres of the domain. This decision was taken after early simulations using a two-zone setup have shown incorrect convergence due to disagreeing fluid velocities at each side of the interface. This problem did not occur for any other airfoil.

### 5.1.2 Values of $y^+$ at the airfoils

Special attention was given to the height of the cell layers next to the airfoil's walls. All the grids were defined to yield values of  $y^+$  at the first cell layer lower than 5, since ANSYS Fluent makes different approaches to the near wall treatment according to this parameter. The  $y^+$  parameter is a form of Reynolds number based on the distance to the wall,  $\psi$ , and the friction velocity at the wall,  $u^*$ , as defined in eq. (5.1) [Schlichting, 1960]. This criterion ensures that the first cell layers in the grid are located inside the so-called "laminar sublayer", and that the flow inside this region can be characterized by the laminar stress-strain relation.

$$y^+ = \frac{\psi u^*}{\nu} \quad (5.1)$$

Considering a chord length of 1 m and a Reynolds number of  $3 \cdot 10^6$ , which is well above the maximum  $Re$  at which a small turbine is expected to operate, estimations for a maximum wall  $y^+$  at the order of 1 pointed to a maximum first cell layer height of  $2 \cdot 10^{-5}$  m. Table 5.1 presents the maximum simulated  $y^+$  values for the NACA 0012 and the S809 airfoils for all angles of attack available in the corresponding experimental studies. These simulations were run after the remaining parameters were defined in Sections 5.1.3 to 5.1.5, but their  $y^+$  results are presented in advance here. Since the maximum  $y^+$  value did not exceed 2 in any situation, all the simulations had their boundary layers properly modeled by the laminar stress-strain relation, which ruled out the need to resort to the logarithmic modeling of the region described by the Law of the Wall.

### 5.1.3 Grid construction

Construction of the grids started as soon as the conditions specified in the previous section were defined. The height of the first cell layer, adjacent to the airfoil's walls, was set at  $2 \cdot 10^{-5}$  m for all grids of all airfoils, regardless of cell count. The remainder of the domain was filled by extrapolating the cells of the first layer in the direction normal to the airfoil surfaces, respecting a maximum growth ratio of 1.2 [Beck, 2010]. Figure 5.3 illustrates, as an example, the cell layers near the NACA 0012. Darker areas represent node clustering due to their reduced dimensions.

Table 5.1 – Maximum calculated wall  $y^+$  values for NACA 0012 and S809

Airfoil	$\alpha$	$y^+$
NACA 0012	0	1.394
	1.85	1.554
	4.25	1.392
	6.05	1.643
	8.15	1.714
	10.15	1.94
S809	0	1.052
	1.02	1.192
	5.13	1.267
	9.22	1.501

### 5.1.4 Numerical methods employed

All simulations used basically the same numerical methods, having employed the pressure-based solver. Historically, the pressure-based approach was developed for low-speed incompressible flows (Mach number equal or lower than 0.3), since it does not take into account variations in the fluid density as a function of the flow velocity at any point of the domain [ANSYS, 2009]. Hence, all simulations in the present work used constant air density

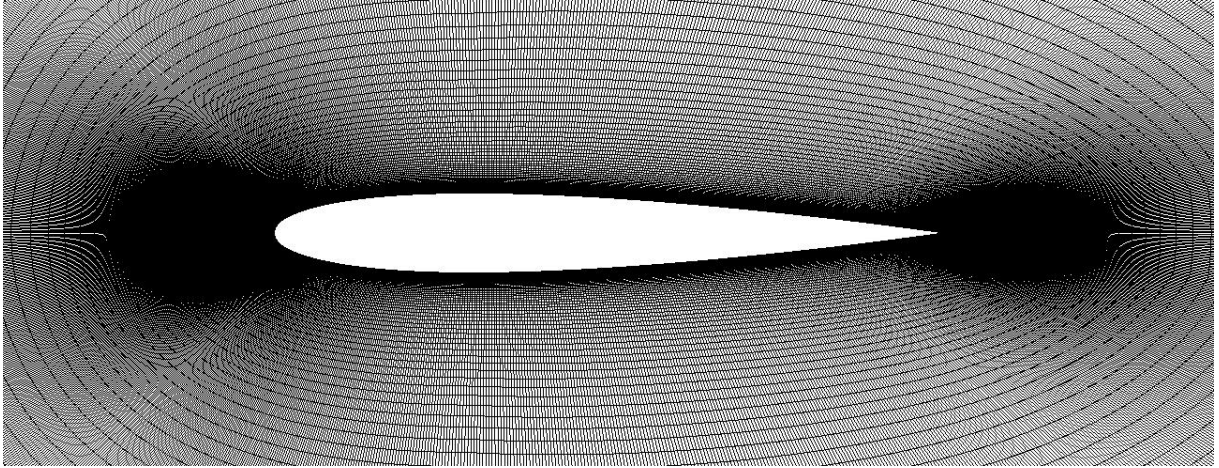


Figure 5.3 – Computational grid around the NACA 0012 airfoil

( $1.225 \text{ kg/m}^3$ ) and dynamic viscosity ( $1.7894 \cdot 10^{-5} \text{ Pa}\cdot\text{s}$ ). The segregated SIMPLE pressure-velocity coupling scheme was selected. Segregated schemes solve the governing equations individually, one at a time, hence the name. These methods are regarded as efficient in terms of memory demand.

Regarding to the spatial discretization, the choice fell on the second-order upwind scheme. When this level of accuracy is desired, quantities at cell faces are computed using an approach in which high-order accuracy is achieved through a Taylor series expansion of the cell-centered solution about the cell centroid. This formulation requires the determination of the gradients of all properties in each cell, limiting it so that no maxima or minima are introduced [ANSYS, 2009]. The second-order upwind scheme is the standard choice in the majority of simulations, since it does not add a significant increase in computational cost while still benefiting from the second-order precision.

The NACA 0012 airfoil was simulated in steady state, but complications to reach convergence led to the choice of transient simulations for the S809 and the SD7062 profiles. Whenever it was required, the time step size was set at  $5 \cdot 10^{-5}$  seconds using the second-order implicit transient scheme. Simulations would be interrupted whenever all variables would show residues no larger than  $1 \cdot 10^{-5}$  for any variable. If achieving that criterion was not possible, the simulations were allowed to run up to reaching at least 5 flow seconds.

### 5.1.5 Grid quality study

The NACA 0012 airfoil also served as parameter for a grid independence study. The methods described in the previous items were used to create a grid consisting of 34,650 cells. This initial discretization was subject to four refinement steps in which, at each stage, the cell count was doubled. This process resulted in 5 grids with total cell counts ranging from 34,650 to 554,000. For all cases, the angle of attack selected was 6 degrees, and the Reynolds number was set at  $3 \cdot 10^6$ . Table 5.2 shows the  $C_L$  and  $C_D$  results for each one of the five grid densities used in the grid independence study.

Table 5.2 – Aerodynamic coefficients for all five grid densities, NACA 0012

Name	Grid 1	Grid 2	Grid 3	Grid 4	Grid 5
Cell count	34,650	69,420	138,600	278,616	554,000
$C_D$	$1.168 \cdot 10^{-2}$	$1.18 \cdot 10^{-2}$	$1.192 \cdot 10^{-2}$	$1.191 \cdot 10^{-2}$	$1.19 \cdot 10^{-2}$
$C_L$	$6.43 \cdot 10^{-1}$	$6.475 \cdot 10^{-1}$	$6.505 \cdot 10^{-1}$	$6.506 \cdot 10^{-1}$	$6.503 \cdot 10^{-1}$

These results show that both parameters ceased to show significant variation from Grid 3 to the further refined ones. Specifically, the  $C_D$  difference between grids 3 and 5 is 0.16%, while for the same situation the  $C_L$  difference is only 0.03%. Thus, focusing on saving time and computational resources, it was decided that all meshes for the subsequent simulations would consist of about 140,000 cells. This criterion was used for the NACA 0012 and S809 simulations.

It should be noted that these grids were created at a first stage of the development of the methodology. Back then, the height of the first cell layer had been set at  $1 \cdot 10^{-4}$  m for any case, though all the other parameters were kept unchanged. This approach was abandoned in favor of the more conservative grid generation standard described in the previous sections, in which the height of the first cell layer was set at  $2 \cdot 10^{-5}$  m, five times smaller than the original value. As the direct consequence of this change is the reduction on  $y^+$  values, it was considered that keeping the old grid quality analysis would not be detrimental to the upcoming simulations. Instead, it is to be expected that lower  $y^+$  values are potentially beneficial to the results.

## 5.2 Results

The results presented below are divided into different sections for each airfoil. In all cases, data for the lift and drag coefficients are presented as functions of the angles of attack at which they were tested by the authors of the experimental studies used as references. Data for the lift-to-drag ratio are presented as well, following the pattern in which these data are normally presented in the Literature. The values of lift-to-drag ratio as functions of the angles of attack are presented as well.

### 5.2.1 NACA 0012

This section presents the results of the simulations performed on the NACA 0012 airfoil. Six angles of attack have been covered, reflecting the choices of Ladson, 1988, reference that provides the experimental data used for comparison. The Mach number is 0.15, resulting in a free stream velocity of 30 m/s. The Reynolds number is  $2 \cdot 10^6$ . The simulations were run in steady state, and two turbulence models were used: SST  $k-\omega$  and Transition SST ( $\gamma\text{-Re}_\theta$ ). Numerical methods and other relevant information are those described throughout Section 5.1. Table 5.3 presents numerical results for the lift and drag coefficients, calculated using the Transition SST model, compared to experimental data provided by Ladson, 1988, as well as the respective differences. Table 5.4, in turn, brings  $C_L$  and  $C_D$  results for the same airfoil, this time calculated using the SST  $k-\omega$  model. The source of experimental data is the same. Figure 5.4 illustrates these results.

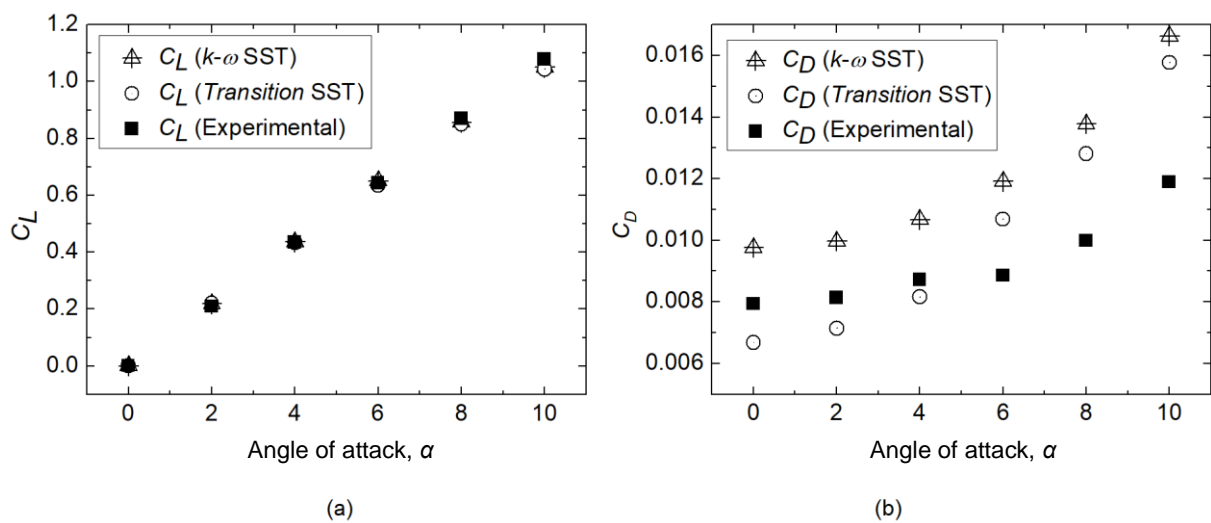
Table 5.3 –  $C_L$  and  $C_D$  for NACA 0012, Transition SST, comp. to exp. data

$\alpha$	$C_L$ (Num.)	$C_L$ (Exp.)	Diff. %	$C_D$ (Num.)	$C_D$ (Exp.)	Diff. %
0	0	0	-	0.0065	0.0062	4.839
1.85	0.201	0.194	3.608	0.0067	0.0062	8.064
4.25	0.459	0.445	3.146	0.0078	0.0067	16.418
6.06	0.646	0.625	3.36	0.0095	0.0087	9.195
8.15	0.844	0.855	-1.286	0.0132	0.0127	3.937
10.15	1.041	1.045	-0.383	0.017	0.0135	25.926



Table 5.4 –  $C_L$  and  $C_D$  data for NACA 0012, SST  $k-\omega$ , comp. to exp. data

$\alpha$	$C_L$ (Num.)	$C_L$ (Exp.)	Dif. %	$C_D$ (Num.)	$C_D$ (Exp.)	Dif. %
0	0	0	-	0.0101	0.0062	62.903
1.85	0.201	0.194	3.608	0.0103	0.0062	66.129
4.25	0.46	0.445	3.371	0.0113	0.0067	68.657
6.05	0.65	0.625	4.0	0.0125	0.0087	43.678
8.15	0.863	0.855	0.936	0.0148	0.0127	16.535
10.15	1.052	1.045	0.67	0.018	0.0135	33.333

Figure 5.4 – Aerodynamic coefficients versus AOA calculated by SST  $k-\omega$  and Transition SST compared to experimental data, NACA 0012. (a)  $C_L$ , (b)  $C_D$ 

Both turbulence models delivered lift coefficient values that show good agreement with the experimental data. The maximum difference is about 4%. Regarding to the drag coefficient, it is easy to see that the Transition SST model yielded results closer to data available for comparison than those collected from the SST  $k-\omega$  simulations. In this case, the maximum error is a little above 25% for  $\alpha = 10,15$  degrees, while four other situations show differences lower than 10%. Drag coefficient results by the SST  $k-\omega$  model fell short of expectations, however. Differences for this case are not less than 16%, reaching nearly 70% for  $\alpha = 4.25$  degrees. These differences can be attributed to the SST  $k-\omega$  model being unable to accurately predict the exact point where the boundary layer transition takes place over the airfoil. In fact, this model regards the boundary layer as fully turbulent from start to end. The

Transition SST model, in turn, takes it into account and attempts to predict not only the transition location but also its magnitude [ANSYS, 2009].

Furthermore, it is shown in the Literature that tests conducted on three airfoils (DAE51, E374 and SD6080) showed that thick trailing edges produce measurable drag penalties. In order to achieve maximum performance, at least at the higher Reynolds numbers, it is necessary to have the thinnest possible trailing edges [Selig et al., 1989]. This conclusion, drawn after a batch of experimental essays, can also be adequate to explain the difficulties in obtaining good drag agreement by numerical simulations, since it is common practice in the literature to slice the airfoil's trailing edge at 99% chord, thus leaving a blunt edge.

It is noteworthy that special attention was given to the convergence criteria of all simulations. No case was regarded as completed before its residues were lower than  $5 \cdot 10^{-5}$  for any variable. In the best scenario, residues as low as  $1 \cdot 10^{-10}$  were detected, again for any variable. As all cases run in this section used the same grids, different flow features at different angles of attack are pointed as responsible for the variations in the convergence history of the simulations.

### 5.2.2 S809

The S809 airfoil was developed by NREL especially to be used in small to mid-size wind turbine blades. It has been used in the turbine developed for the widely documented and easily accessible UAE Phase VI test series.

In the present work, the S809 was modeled and simulated according to the methodology previously applied to the NACA 0012 simulations. The two-dimensional computational domain has approximately 175,000 cells, considering both the inner and outer circular domains. Results for the lift and drag coefficients, the first ones to be presented, are compared to experimental data from Somers, 1997, who carried out their wind-tunnel experiments in Delft University (Netherlands). The Reynolds number for the simulations was set to  $2 \cdot 10^6$  to match the choice made by the authors in their test runs. Provided that the chord length is 1 m and the air properties were kept unchanged, the resulting free stream velocity is 30 m/s.

In contrast to the NACA 0012 simulations, the S809 simulations were run in transient state, for which the time step size was set to  $1 \cdot 10^{-4}$  s. Such choice is due to difficulties to achieve convergence in a first attempt, in which the simulations had been run in steady state.

Thus, the four cases covered in this section ran up to reaching 1.5 seconds, executing up to 50 iterations per time step. The other numerical methods are those exposed in Section 5.1.4. The S809 simulations used the Transition SST turbulence model exclusively.

The next two tables show the aerodynamic coefficients for the S809 airfoil compared to other numerical results as well as to experimental data, both provided by Somers, 1997. Table 5.5 presents the  $C_L$  values as a function of the angle of attack compared to data from the abovementioned reference. Similarly, table 5.6 presents the  $C_D$  results compared to data from the same study. The selected angles of attack reflect the choices made in the reference.

The results shown in tables 5.5 and 5.6 were regarded to be below the desired level. This is especially true for the  $C_L$ , since the applied methodology, from the grid generation to the numerical methods, is the same used in the NACA 0012 simulations. Regarding to the  $C_D$ , however, two angles of attack (0 and 1.02 degrees) produced results in close agreement with those from the wind tunnel, for which the difference is not higher than 6%. It should be noted that tripping wires have been used in the airfoils for the experimental tests, so as to force the transition at points very close to the leading edges.

Table 5.5 –  $C_L$  vs. AOA results vs. numerical and experimental data, S809

$\alpha$	$C_L$	$C_L$ (Num., ref.)	Diff. (%)	$C_L$ (Exp., ref.)	Diff. (%)
0	0.0988	0.1558	-36.58	0.1469	-32.74
1.02	0.2139	0.2755	-22.36	0.2716	-20.14
5.13	0.6725	0.7542	-10.83	0.7609	-11.62
9.22	1.0059	1.0575	-4.88	1.0385	-3.14

Table 5.6 –  $C_D$  vs. AOA results vs. numerical and experimental data, S809

$\alpha$	$C_D$	$C_D$ (Num., fonte)	Dif. (%)	$C_D$ (Exp., fonte)	Dif. (%)
0	0.0074	0.0062	19.35	0.007	5.71
1.02	0.0075	0.0062	20.97	0.0072	4.17
5.13	0.0096	0.0069	39.13	0.007	37.14
9.22	0.0181	0.0416	-56.49	0.0214	-15.42

Since these results were deemed unfavorable, it was decided to evaluate the pressure coefficient ( $C_p$ ) distributions over the airfoil. It can be easily seen that the  $C_p$  plots show a

much better level of agreement with the data collected from the reference, as illustrated in figures 5.5 to 5.8. These pictures show the  $C_P$  distributions for the S809 airfoil as a function of the chord length for all angles of attack previously covered, compared to experimental data from Somers, 1997.

A relatively strong drop in  $C_P$  around the airfoil mid-chord point has been detected in the four simulated AOA cases. It represents where the transition takes place. From the pictures, it can be stated that the Transition SST model makes a reasonable estimate at the upper surface in all cases, but seems to fail to adequately capture the abrupt variation around the mid-chord point detected at the lower surface. Despite this fact, one can expect better results overall than those produced by the SST  $k-\omega$  model.

### 5.2.3 SD 7062

Unlike the two airfoils previously studied, the SD7062 was simulated at a Reynolds number range from 25,000 to 125,000. These values are considered low for engineering applications in the sense that, as discussed before, airfoils subject to low- $Re$  flows are prone to a phenomenon that does not occur at higher Reynolds numbers: the laminar separation bubble.

The LSB is responsible for a considerable change in the flow behavior and a substantial increase in drag, affecting airfoils operating at Reynolds numbers below about 500,000. Yet, this is exactly the range at which most if not all small turbine blades operate, making the minimization or at least the accurate modeling of the bubble an issue of utmost importance. As will be discussed in Ch. 7, a proposed blade design was simulated and had its aerodynamic performance assessed at Reynolds numbers from about 82,000 to 318,000.

A new grid quality study was performed, this time relying on the GCI methodology. The GCI (short for Grid Convergence Index) was first proposed by Roache, 1994, as a measure of the percentage the computed value is away from the asymptotic numerical value. It indicates how much the solution would change with a further refinement of the grid. A small value of GCI indicates that the computation is within the asymptotic range.

For the GCI evaluation, three meshes with different cell counts but a constant refinement ratio were constructed around the SD7062 airfoil configured at an angle of attack of 7 degrees. Despite the varying grid densities, it was decided that the height of the first cell layer would be kept constant in order to ensure an equally constant maximum  $y^+$  value for any

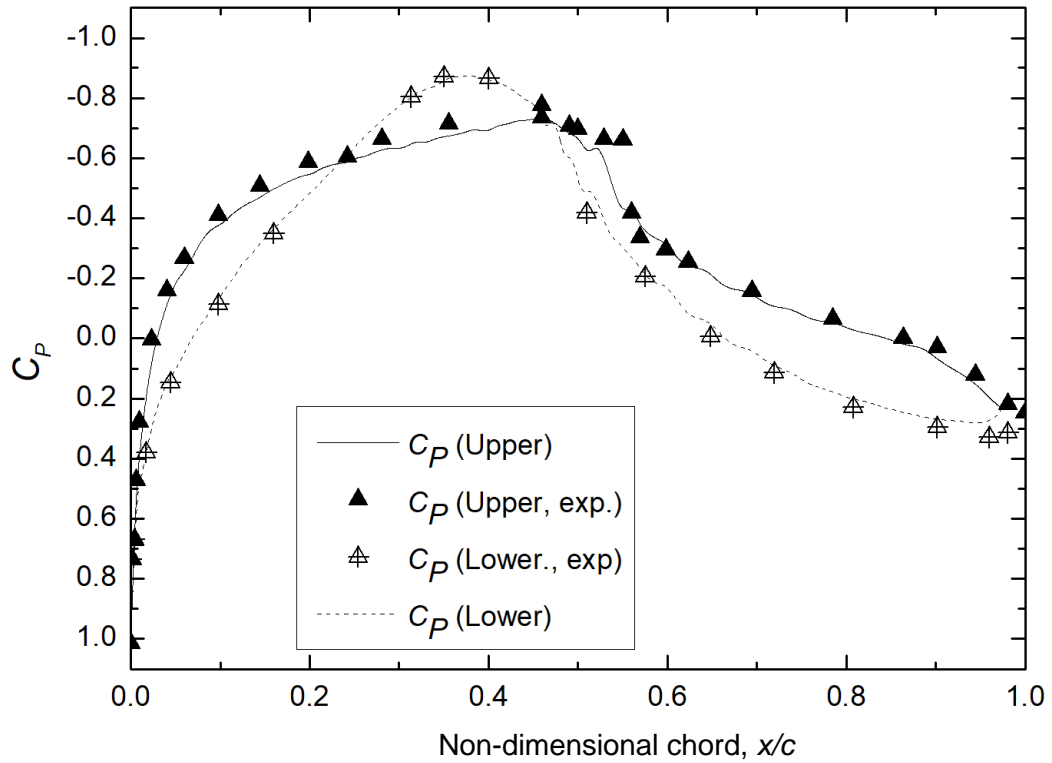


Figure 5.5 –  $C_p$  plots vs experimental data, S809, AOA = 0 deg

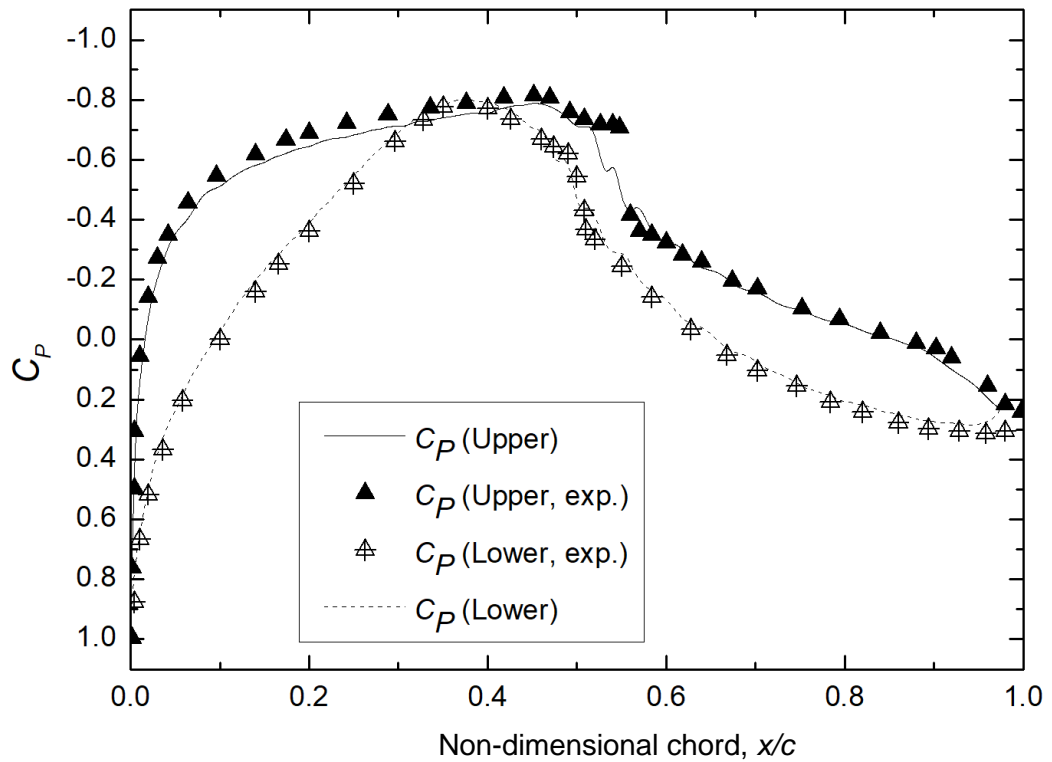


Figure 5.6 –  $C_p$  plots vs. experimental data, S809, AOA = 1.02 deg

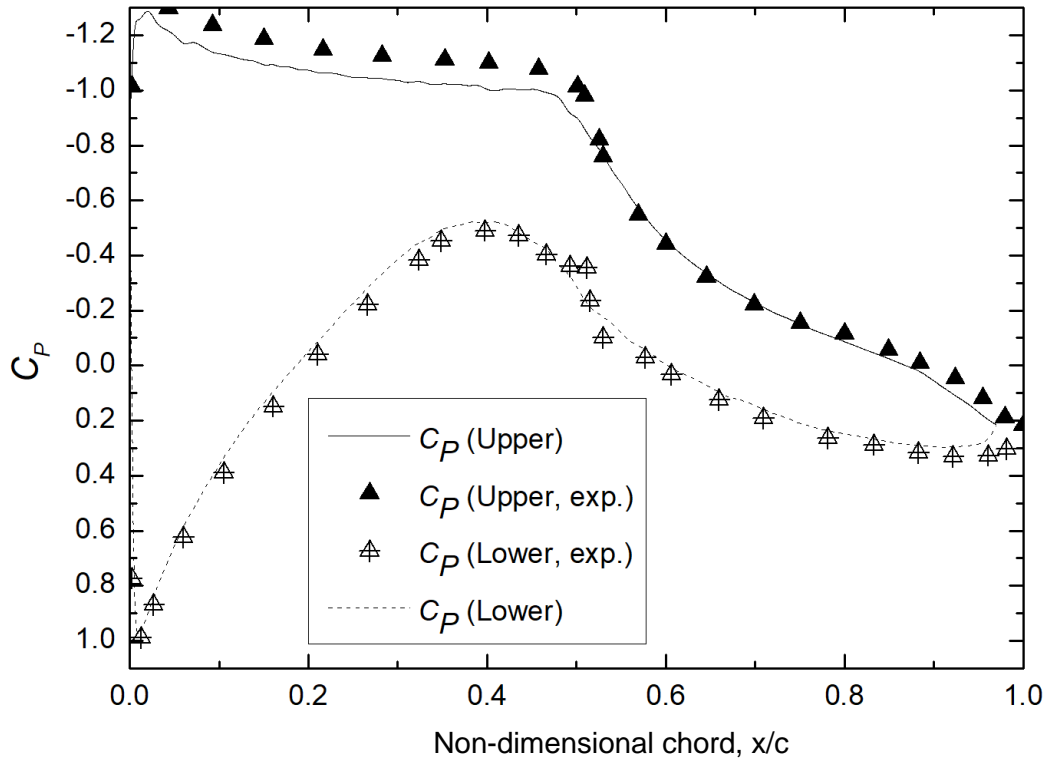


Figure 5.7 –  $C_p$  plots vs. experimental data, S809, AOA = 5.13 deg

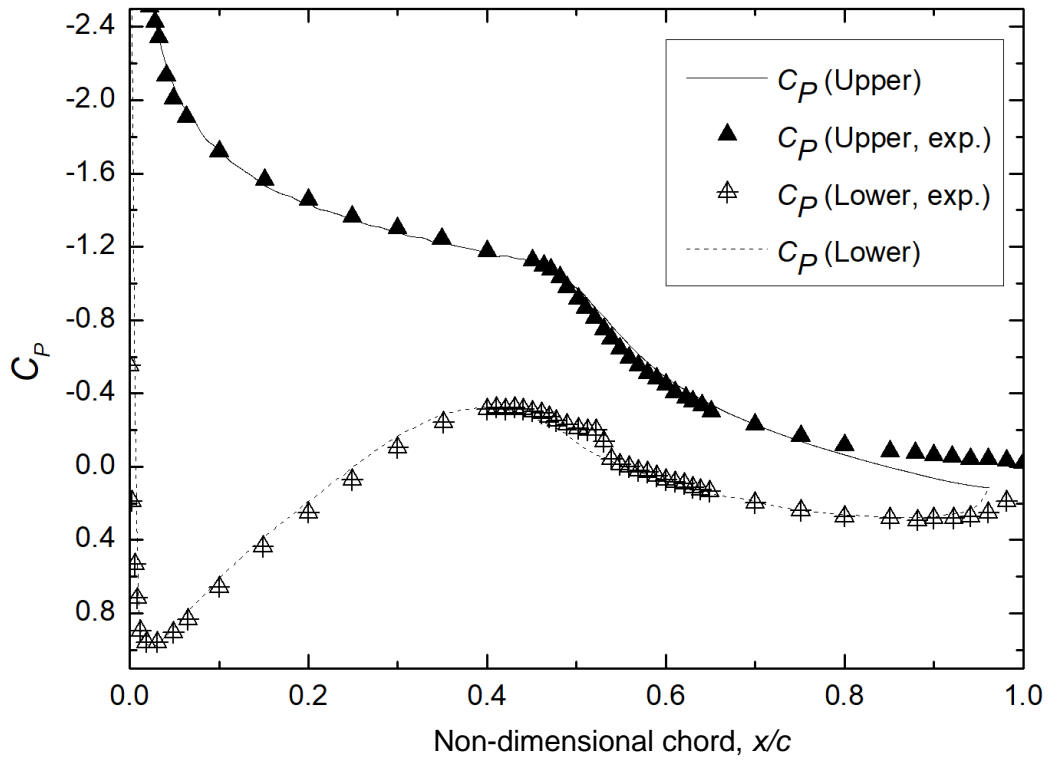


Figure 5.8 –  $C_p$  plots vs. experimental data, S809, AOA = 9.22 deg

of the grids, so the value of  $2 \cdot 10^{-5}$  meters was again adopted. The lift coefficient was the parameter selected to be evaluated. The free stream flow velocity was set to 2.693 m/s, which, with a chord length of 1 m, results in a Reynolds number of 184,000. Table 5.7 shows the  $C_L$  results collected at this stage. It is worth mentioning that the average cut-in wind speed of a turbine is around 3.5 m/s, which means that a hypothetical rotor under the conditions described above would most likely remain still.

Table 5.7 –  $C_L$  values for the GCI evaluation, SD7062

Grid	Cell count	$C_L$
1	163,800	1.075
2	328,400	1.069
3	655,200	1.03

The order of convergence  $p_G$  is calculated using eq. (5.2):

$$p_G = \ln\left(\frac{f_3 - f_2}{f_2 - f_1}\right) / \ln(r_G) \quad (5.2)$$

In eq. (5.2),  $f_1$ ,  $f_2$  and  $f_3$  are the values of the function under evaluation (in this case,  $C_L$ ) yielded by grids 1, 2 and 3 respectively. The parameter  $r_G$  stands for the refinement ratio between any grids. In the present case,  $r_G = 2$ . Solving this equation yields an order of convergence of 2.7, while the theoretical value is  $p_G = 2.0$ . The difference can be most likely attributed to factors as cells with high aspect ratios and overall grid quality, as well as characteristics of the turbulence modeling equations and other numerical modeling features.

The knowledge of  $p_G$  allows the calculation of an approximate lift coefficient value when the grid spacing tends to zero ( $f_{sp=0}$ ). This is done by applying the Richardson extrapolation using the two finest grids, as follows:

$$f_{sp=0} = f_3 + (f_3 - f_2) / (r_G^{p_G} - 1) \quad (5.3)$$

The result is  $f_{sp=0} = 1.0229$ . The grid convergence indexes for grids 1 and 2 and for grids 2 and 3 can be calculated using the following equation:

$$\text{GCI}_{ij} = 100 \left( \frac{F_S \left| (f_i - f_j) / f_i \right|}{(r_G^{p_G} - 1)} \right) \quad (5.4)$$

A safety factor ( $F_S$ ) of 1.25 was adopted as three grids were used to estimate  $p_G$ . In this analysis,  $\text{GCI}_{12}$  is 0.1268%, and  $\text{GCI}_{23}$  is 0.8292%. To check if the solutions have fallen into the asymptotic range of convergence, eq. (5.5) is used:

$$\frac{\text{GCI}_{23}}{\text{GCI}_{12} (r_G^{p_G})} = k_G \quad (5.5)$$

For this analysis,  $k_G = 1.0056$ . Since it is approximately 1, it indicates that the solutions are within the asymptotic range of convergence.

The difference observed between the lift coefficient yielded by the finer grid and the values from the other grids, however, led to the selection of the former as the standard to be used in the SD7062 analysis proper. Moreover, this choice was further fueled by difficulties to obtain convergence using the coarser grids, which has been observed in later simulations carried out for testing purposes. Thus, from this point onwards, every grid has been constructed with cell counts of about 650,000.

Five  $Re$  values were selected for this analysis: 25,000, 50,000, 75,000, 100,000 and 125,000. Each  $Re$  case was simulated for four AOA cases: 0, 2, 4 and 6 degrees, resulting in a total of 20 runs. The numerical model, constructed following the guidelines described throughout Section 5.1, was the same for all cases, having a chord length of 0.1343 m. The decision to ditch the two-zone domain led to the construction of one grid for each AOA case. Experimental data for  $Re = 100,000$  are provided by Lyon et al., 1997.

All simulations were run in transient state until they reached at least 5 flow seconds. Due to the nature of the expected phenomena, only the Transition SST turbulence model was used. The cases, along with their respective results, are summarized in table 5.8. The results include the lift and drag coefficients and the lift-to-drag ( $L/D$ ) ratio. Each case was given a label for easier referencing.



Table 5.8 –  $C_L$ ,  $C_D$  and  $L/D$  results for SD7062 as functions of  $Re$  and AOA

$Re$	Label	AOA	$C_L$	$C_D$	$L/D$
25,000	25k_0	0	0.0958	0.0434	2.21
	25k_2	2	0.3068	0.0561	5.47
	25k_4	4	0.4376	0.0711	6.15
	25k_6	6	0.5194	0.089	5.84
50,000	50k_0	0	0.2147	0.0337	6.37
	50k_2	2	0.4193	0.042	9.98
	50k_4	4	0.5614	0.0536	10.47
	50k_6	6	0.667	0.0714	9.34
75,000	75k_0	0	0.3163	0.0254	12.45
	75k_2	2	0.5185	0.0294	17.64
	75k_4	4	0.7	0.0346	20.23
	75k_6	6	0.8646	0.0421	20.53
100,000	100k_0	0	0.3636	0.0206	17.65
	100k_2	2	0.5591	0.023	24.31
	100k_4	4	0.7486	0.0267	28.04
	100k_6	6	0.927	0.032	28.99
125,000	125k_0	0	0.356	0.0168	21.19
	125k_2	2	0.5749	0.0197	29.18
	125k_4	4	0.7688	0.023	33.43
	125k_6	6	0.9565	0.0278	34.38

The results displayed in table 5.8 show that the SD7062, when subject to low- $Re$  flows, behaved as expected from the literature. According to Wood, 2011a, in a general fashion, below about  $Re = 50,000$ , transition in the separated flow may not occur before the trailing edge and, even if it occurs, there is no reattachment. Between about 70,000 and 200,000, depending on airfoil and flow conditions, it is possible to achieve laminar flow without a bubble, which can lead to impressive performance, but this phenomenon did not occur in the present work, which is evidenced by the higher drag values associated to the lower Reynolds numbers. As  $Re$  increases from 200,000 to about 500,000, the bubble gets

shorter and the drag it causes reduces, leading to higher lift-to-drag ratios. Results from table 5.8 are illustrated in figures 5.9 to 5.11.

This range of Reynolds numbers produced results in which the lower the  $Re$ , the higher the drag coefficient. It is normal under such operating conditions, and shows that the Transition SST turbulence model may be properly modeling the LSB, both in scale and in magnitude. Further evidence of the adequate modeling can be assessed in the skin friction coefficient ( $C_F$ ) plots. The  $C_F$  plots are able to translate into numbers what can be clearly seen in CFD velocity contour plots. Figure 5.12 depicts, as an example, the upper-surface  $C_F$  plot for the 125k\_2 case, superimposed on the corresponding velocity contour map. Figure 5.13 shows, also as an example, the map of velocity vectors depicting the LSB over the airfoil, also for the 125k\_2 case. The top image shows the front part of the bubble, while the bottom image shows the aft part for the same situation. The recirculation zone becomes evident in these pictures.

Figures 5.14 to 5.18 show the skin friction coefficient distributions over the SD7062 grouped by Reynolds number. Each figure contains the results for 0, 2, 4 and 6 degrees of angle of attack, where the results for the upper surface are at the left and the results for the lower surface are at the right. Similarly, figures 5.19 to 5.22 present the  $C_F$  distributions grouped by angle of attack. Each figure contains results for the following Reynolds numbers: 25,000, 50,000, 75,000, 100,000 and 125,000. Again, data for the upper surface are at the left, while data for the lower surface are at the right.

The plots shown in figures 5.14 to 5.22 clearly show the laminar separation bubble as the region bounded by two points over the upper surface at which the skin friction coefficient (and subsequently, the wall shear stress) tends to zero, comprising the area where the variation in  $C_F$  is significant. It is usually located around or just downstream from the chord midpoint. It is noteworthy that, for  $Re = 25,000$  and  $50,000$ , the flow does not reattach after separating, which is in agreement with the literature [Wood, 2011a]. In the present study, reattachment was observed from  $Re = 75,000$  upwards. Furthermore, the  $C_F$  plots make it clear that the separation point (where the bubble starts) moves upstream in the direction of the leading edge as the AOA increases. The same effect can be detected with increasing  $Re$ , though not to the same extent. The increase in  $Re$  also causes the bubble length to decrease, that is, it causes the reattachment to take place further upstream.

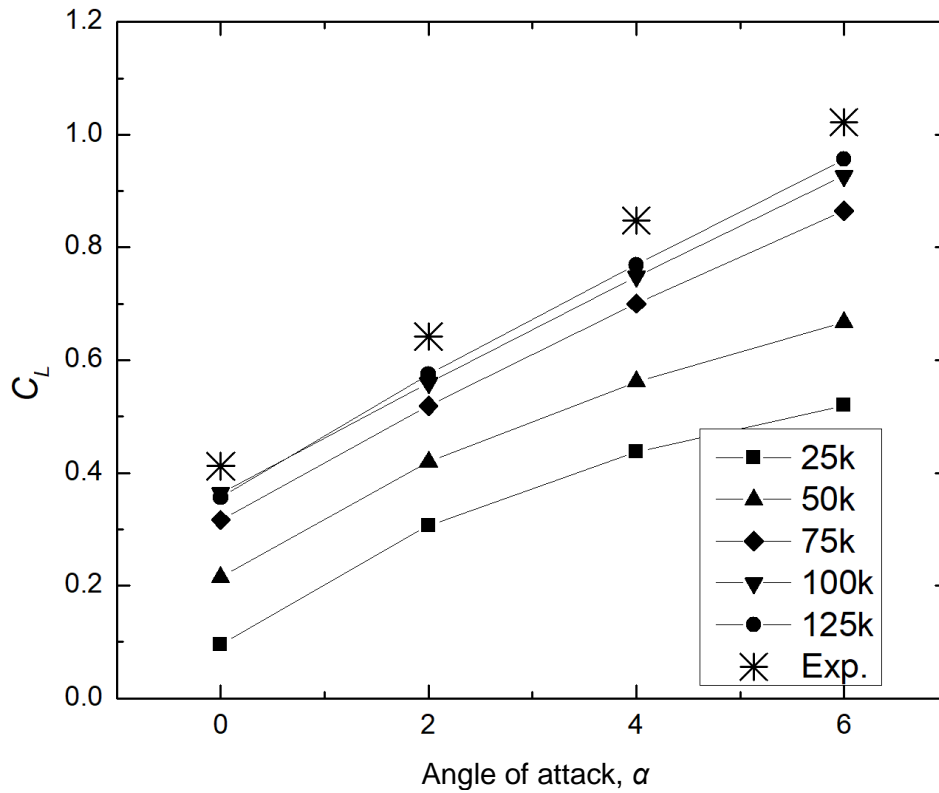


Figure 5.9 –  $C_L$  vs. AOA at low  $Re$ , SD7062. Experimental data for  $Re = 100,000$

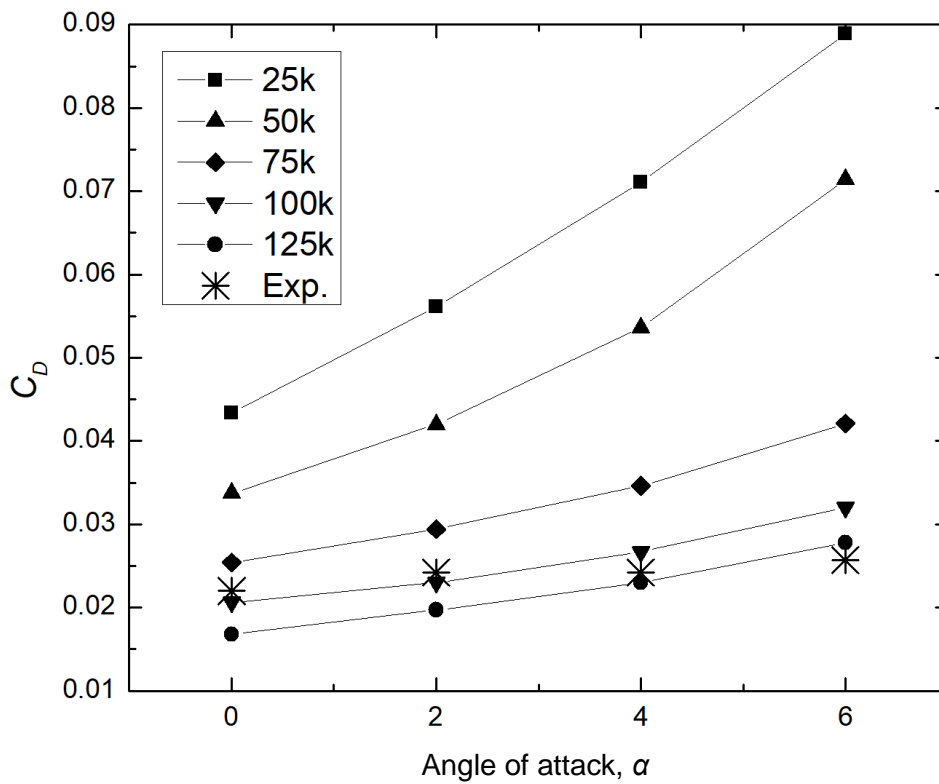


Figure 5.10 –  $C_D$  vs. AOA at low  $Re$ , SD7062. Experimental data for  $Re = 100,000$

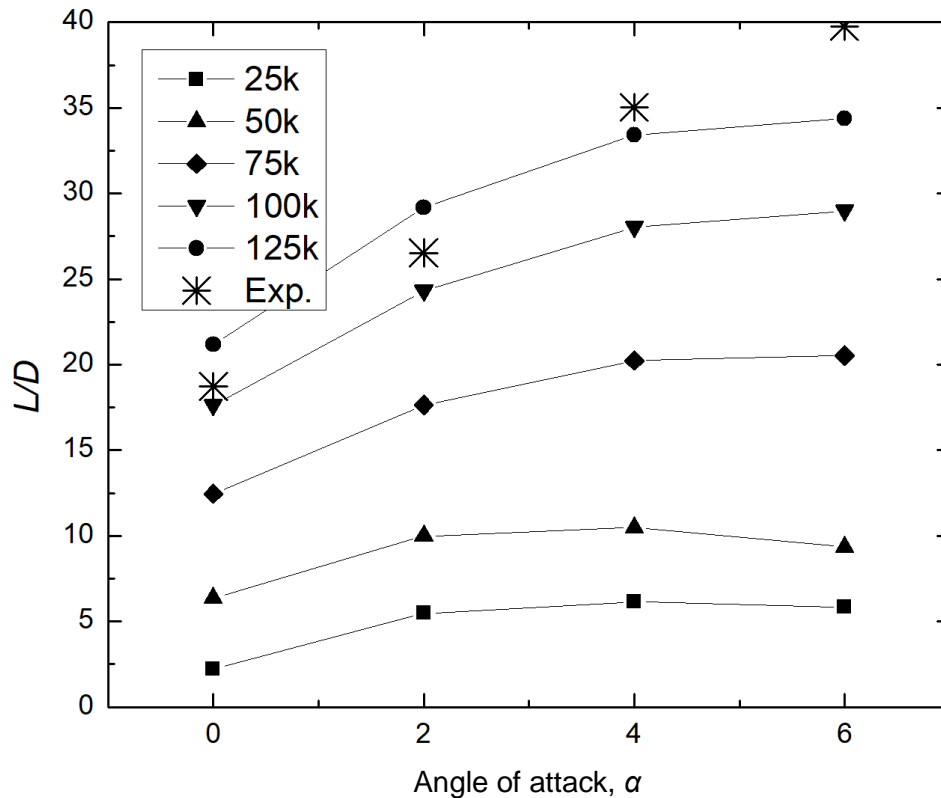


Figure 5.11 –  $L/D$  vs. AOA at low  $Re$ , SD7062. Experimental data for  $Re = 100,000$

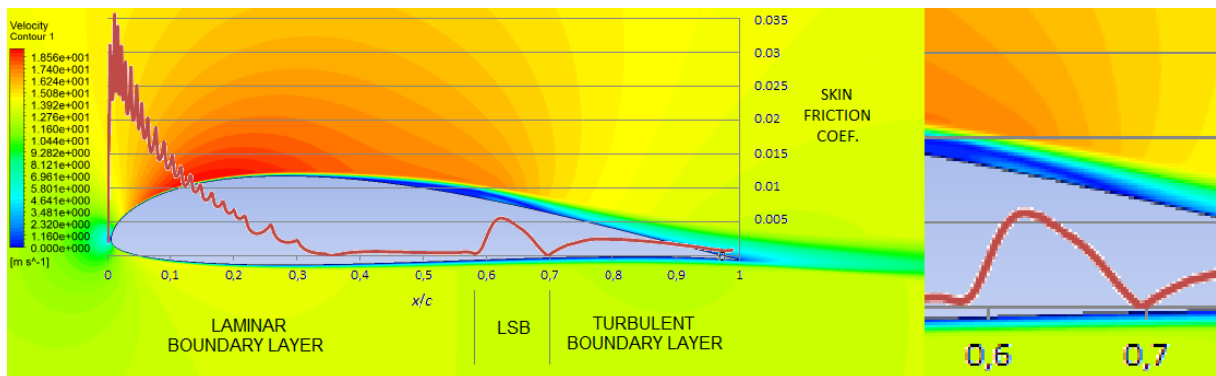


Figure 5.12 – Example of upper-surface  $C_F$  plot and comparison with velocity field, with LSB shown in detail,  $Re = 125,000$ , AOA = 2 deg.

Similarly, an increase in AOA causes the maximum  $C_F$  values to increase inside the bubble. The Reynolds number, in turn, seems to have little influence over the maximum  $C_F$  value inside the bubble, at least for the range covered in the present study. This trend was only detected in the cases where the flow effectively reattached ( $Re \geq 75,000$ ). The maximum absolute  $C_F$  value tends to decrease with increasing  $Re$ , however.

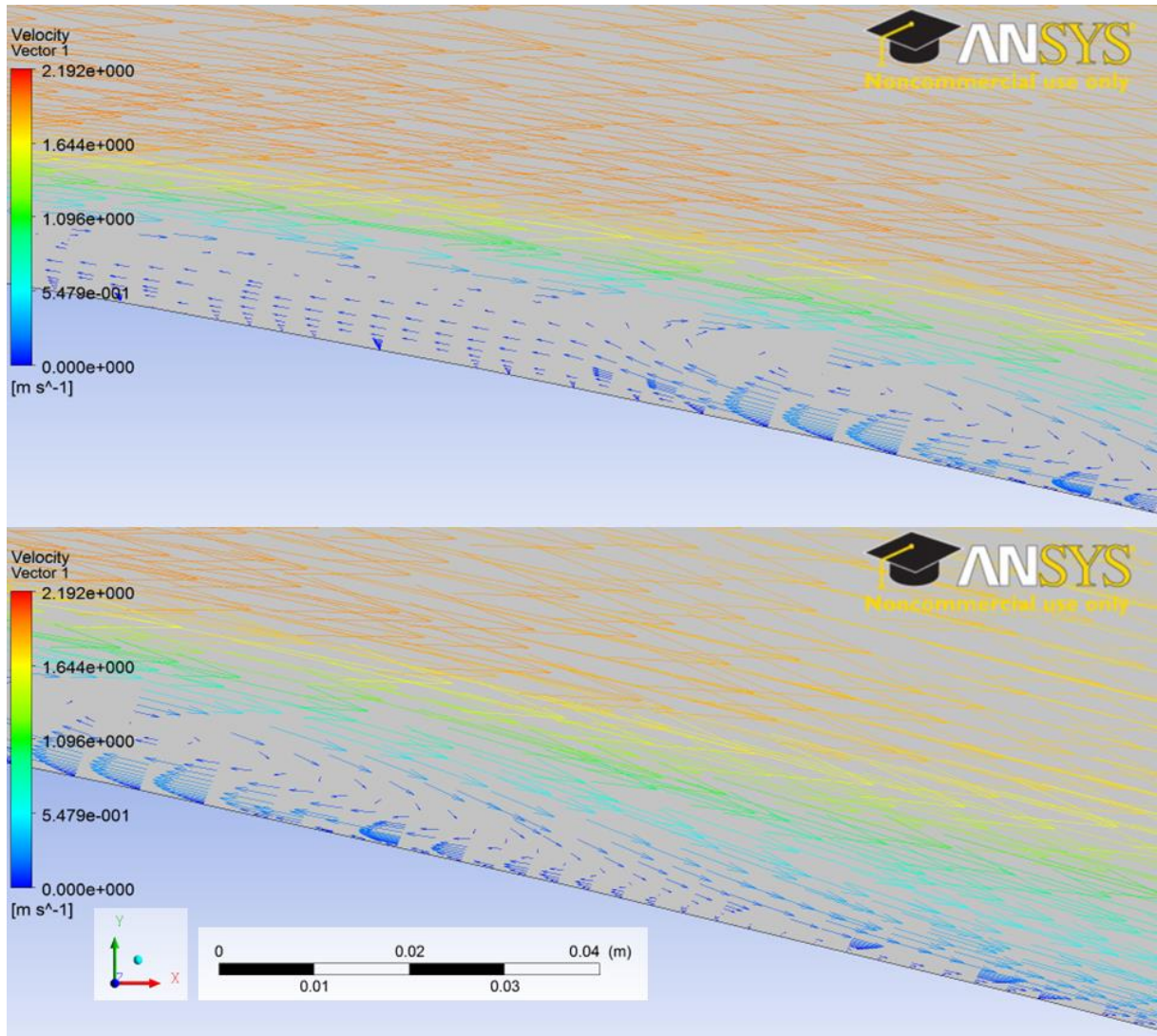


Figure 5.13 – Velocity vectors showing the LSB in detail,  $Re = 125,000$ ,  $AOA = 2$  deg.

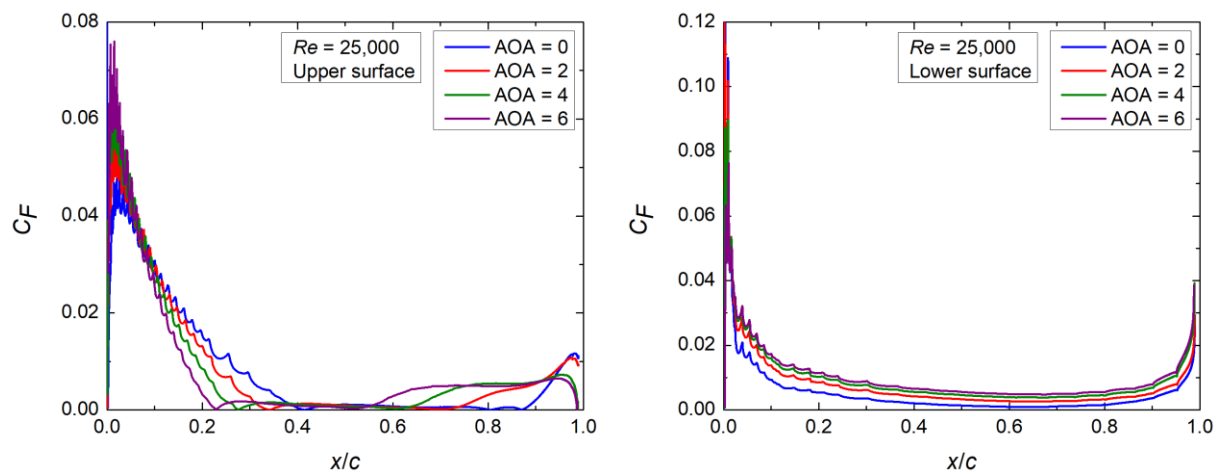


Figure 5.14 –  $C_F$  vs.  $x/c$ , SD7062,  $Re = 25,000$ . Left: upper surf., right: lower surf.

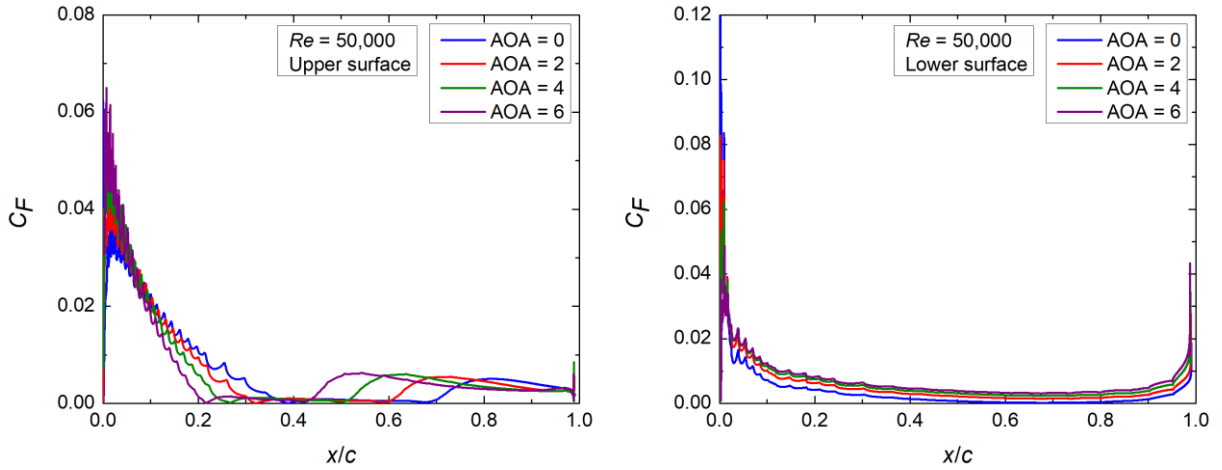


Figure 5.15 –  $C_F$  vs.  $x/c$ , SD7062,  $Re = 50,000$ . Left: upper surf., right: lower surf.

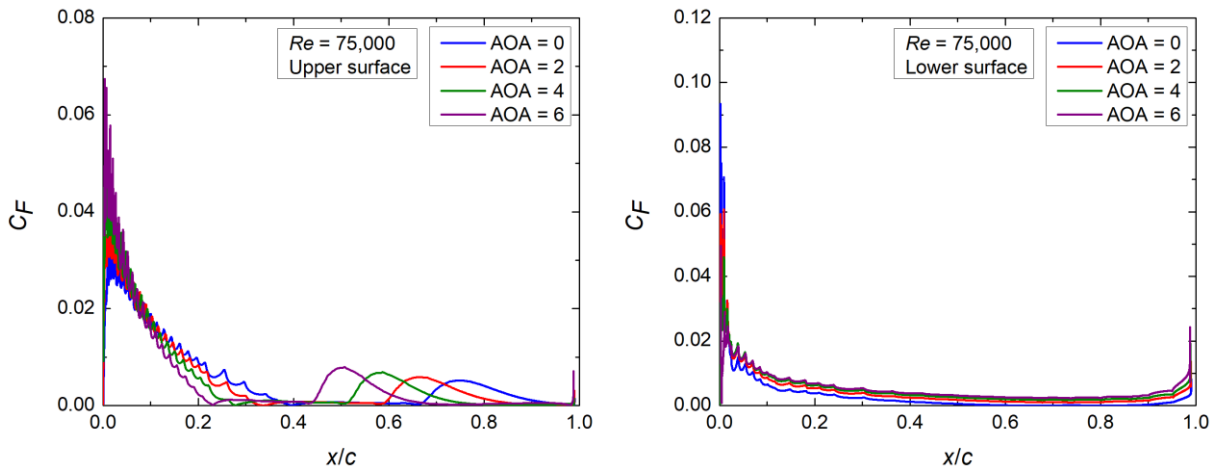


Figure 5.16 –  $C_F$  vs.  $x/c$ , SD7062,  $Re = 75,000$ . Left: upper surf., right: lower surf.

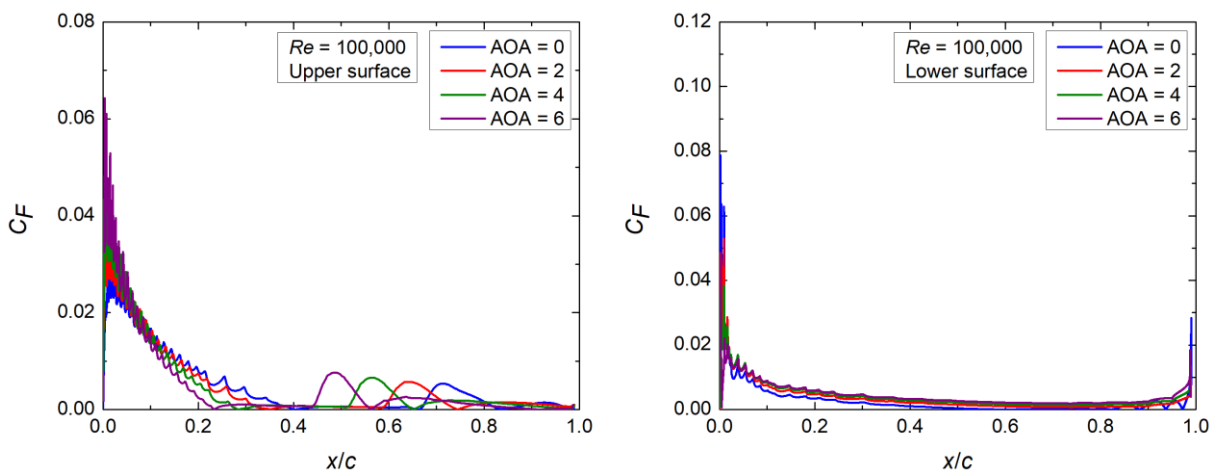


Figure 5.17 –  $C_F$  vs.  $x/c$ , SD7062,  $Re = 100,000$ . Left: upper surf., right: lower surf.

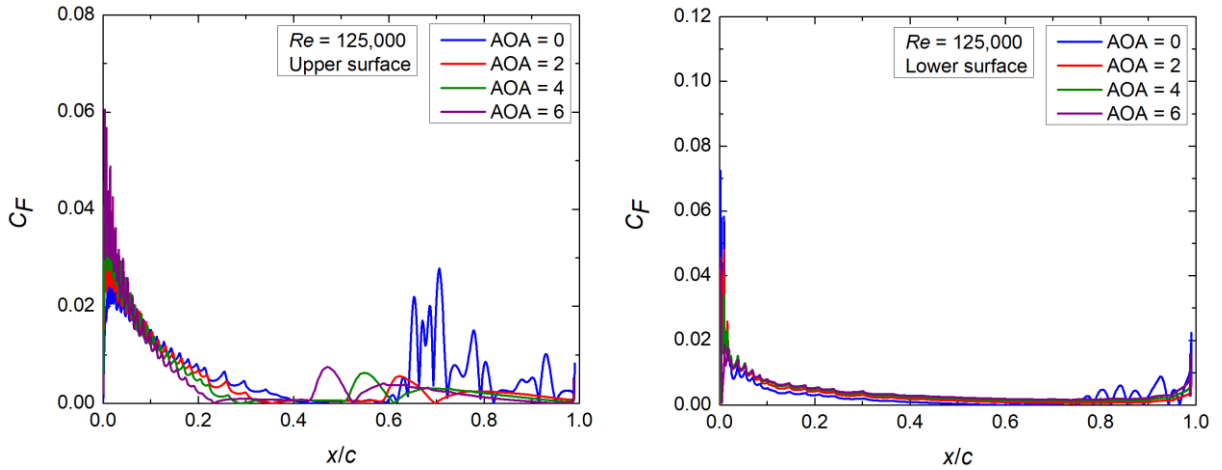


Figure 5.18 –  $C_F$  vs.  $x/c$ , SD7062,  $Re = 125,000$ . Left: upper surf., right: lower surf.

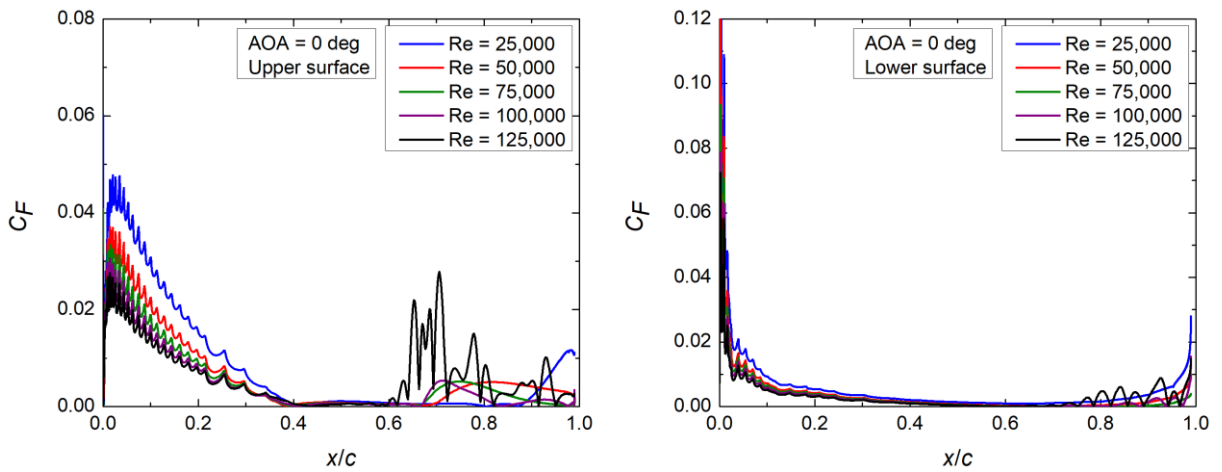


Figure 5.19 –  $C_F$  vs.  $x/c$ , SD7062, AOA = 0 deg. Left: upper surf., right: lower surf.

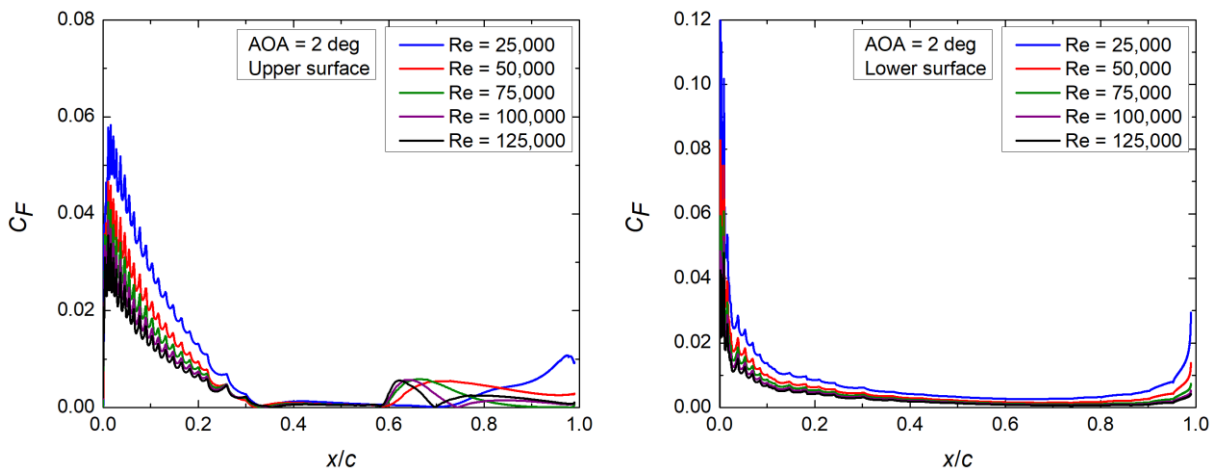


Figure 5.20 –  $C_F$  vs.  $x/c$ , SD7062, AOA = 2 deg. Left: upper surf., right: lower surf.

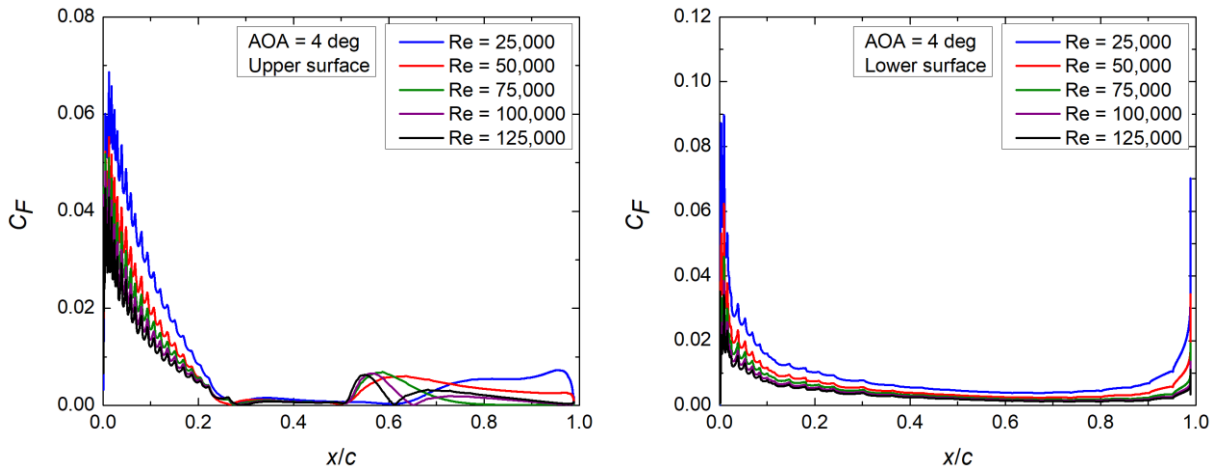


Figure 5.21 –  $C_F$  vs.  $x/c$ , SD7062, AOA = 4 deg. Left: upper surf., right: lower surf.

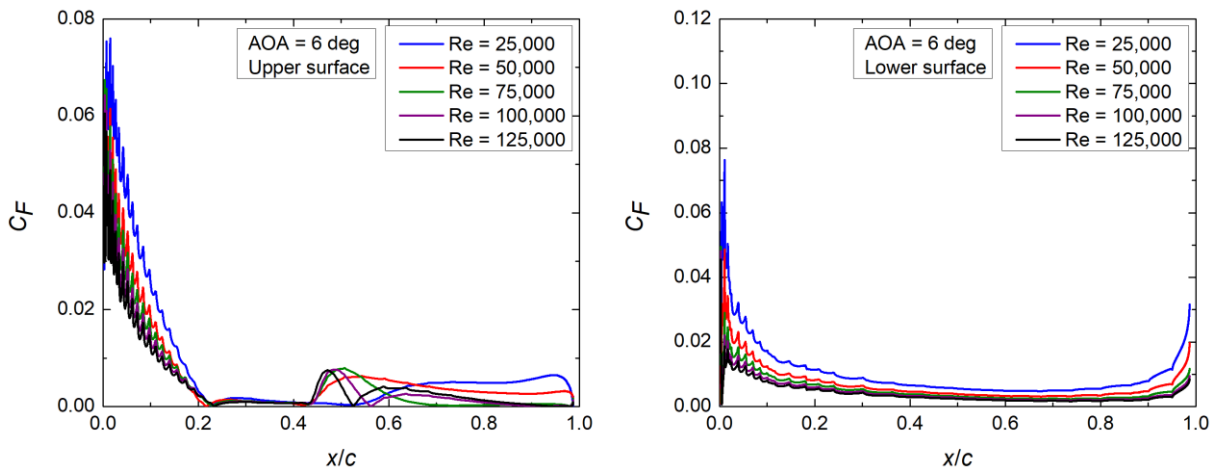


Figure 5.22 –  $C_F$  vs.  $x/c$ , SD7062, AOA = 6 deg. Left: upper surf., right: lower surf.

The trends described above can be observed, in an analogous way, in the pressure coefficient distributions, although with a lesser precision regarding to the LSB boundaries. Figures 5.23 to 5.27 show the  $C_P$  plots grouped by Reynolds number, whereas figures 5.28 to 5.31 show the  $C_P$  plots grouped by AOA. The data presentation format is the same as the one used for the  $C_F$ .



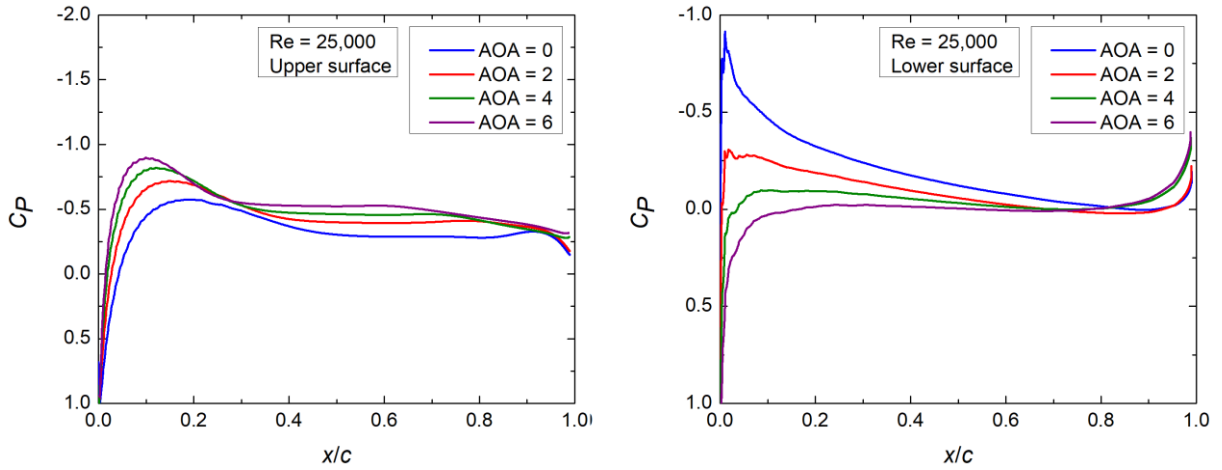


Figure 5.23 –  $C_p$  vs.  $x/c$ , SD7062,  $Re = 25,000$ . Left: upper surf., right: lower surf.

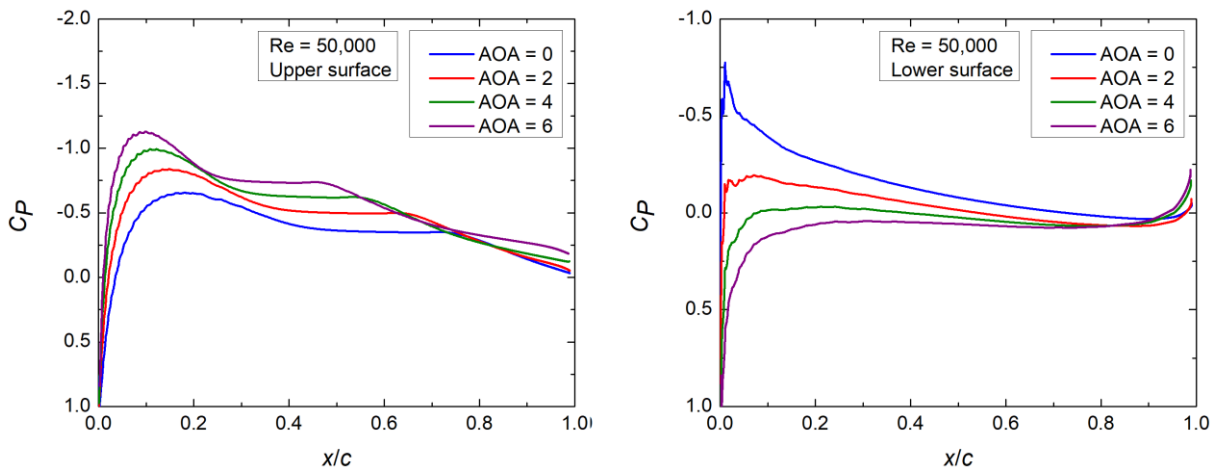


Figure 5.24 –  $C_p$  vs.  $x/c$ , SD7062,  $Re = 50,000$ . Left: upper surf., right: lower surf.

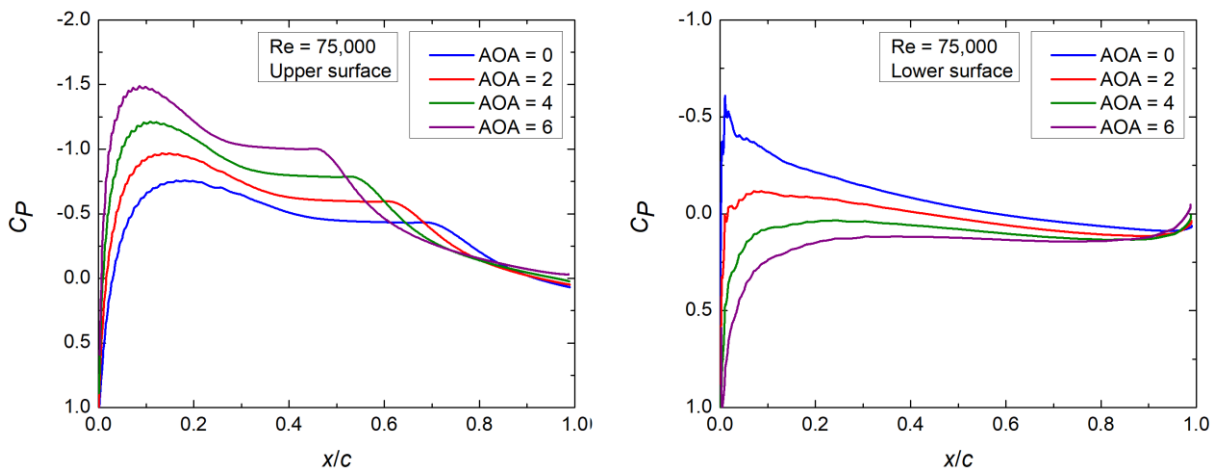


Figure 5.25 –  $C_p$  vs.  $x/c$ , SD7062,  $Re = 75,000$ . Left: upper surf., right: lower surf.

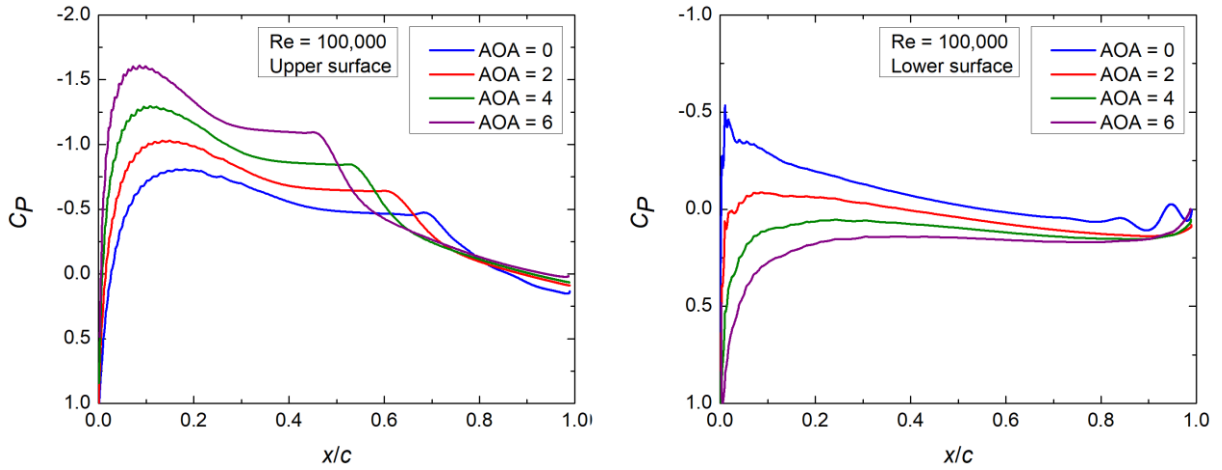


Figure 5.26 –  $C_p$  vs.  $x/c$ , SD7062,  $Re = 100,000$ . Left: upper surf., right: lower surf.

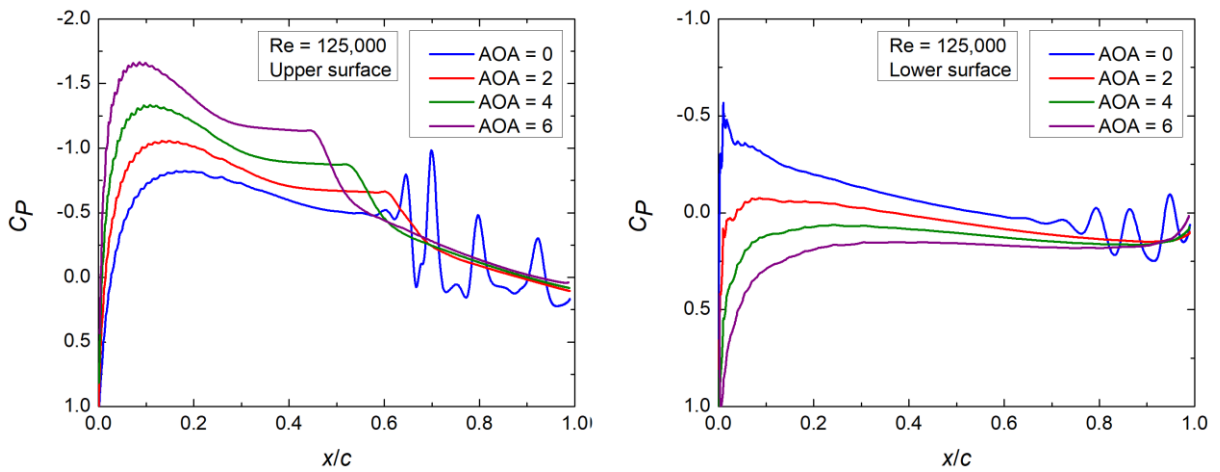


Figure 5.27 –  $C_p$  vs.  $x/c$ , SD7062,  $Re = 125,000$ . Left: upper surf., right: lower surf.

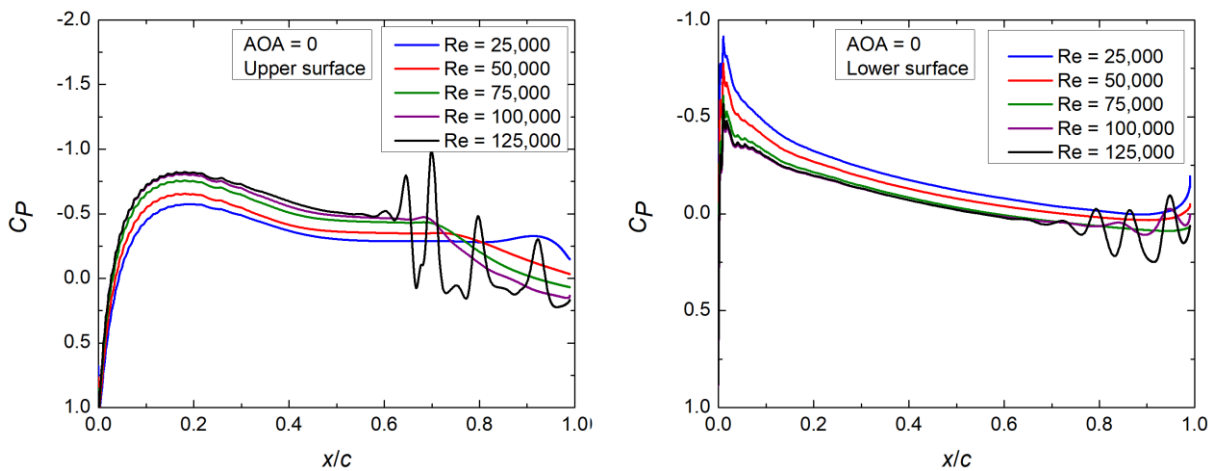


Figure 5.28 –  $C_p$  vs.  $x/c$ , SD7062, AOA = 0 deg. Left: upper surf., right: lower surf.

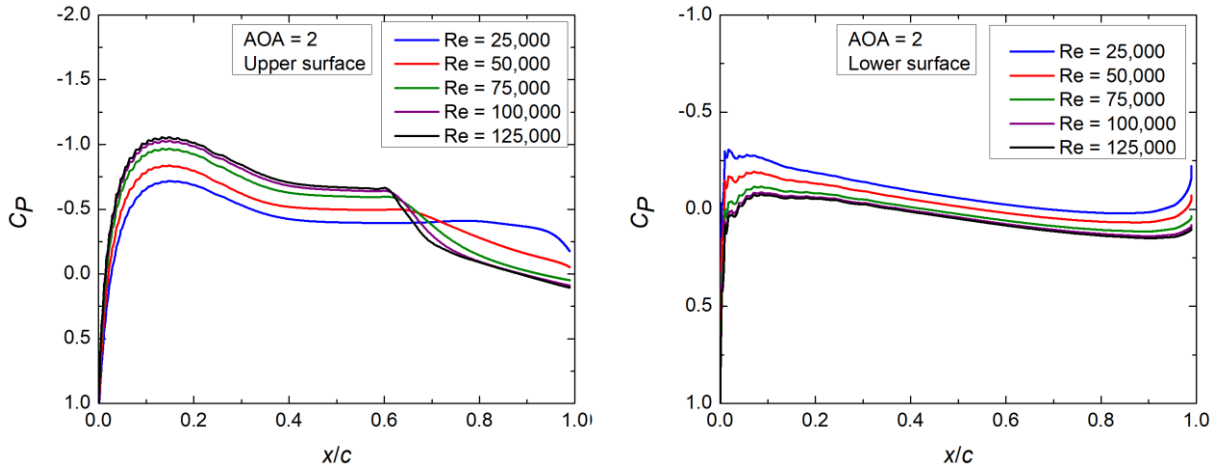


Figure 5.29 –  $C_p$  vs.  $x/c$ , SD7062, AOA = 2 deg. Left: upper surf., right: lower surf.

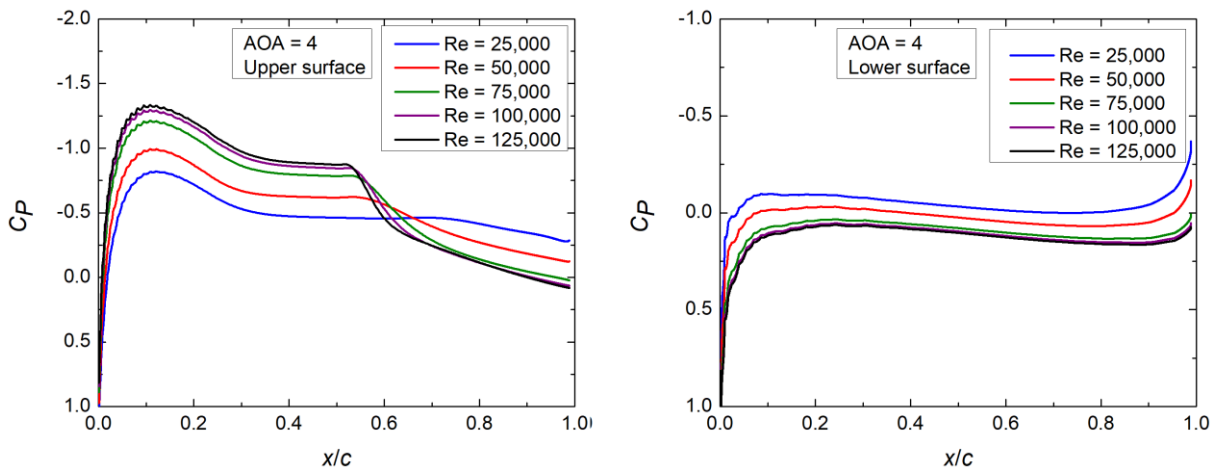


Figure 5.30 –  $C_p$  vs.  $x/c$ , SD7062, AOA = 4 deg. Left: upper surf., right: lower surf.

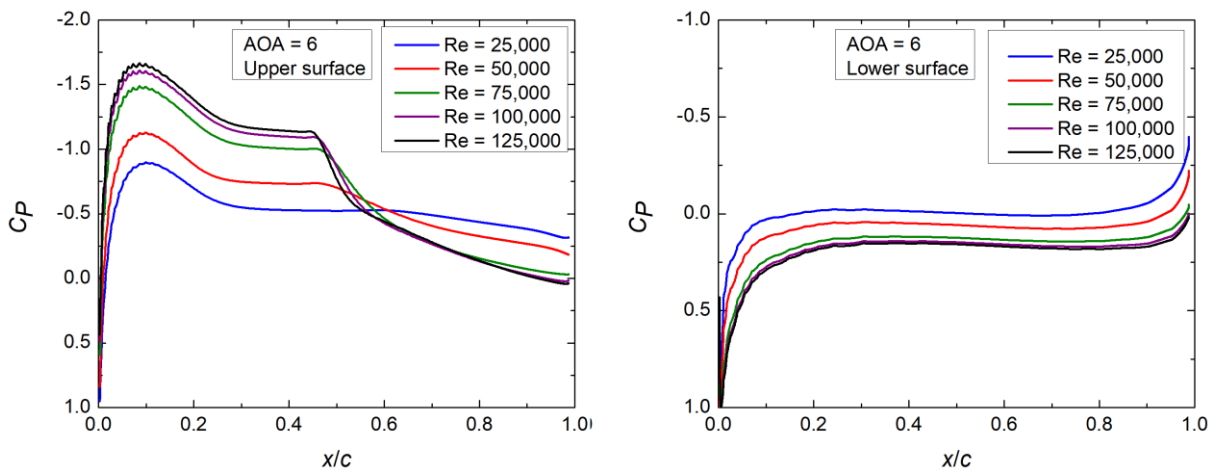


Figure 5.31 –  $C_p$  vs.  $x/c$ , SD7062, AOA = 6 deg. Left: upper surf., right: lower surf.

The behavior described is in agreement with the findings by Shah et al., 2015. In that work, the authors carried out a study on the LSB using a similar numerical methodology and the same turbulence model, although a completely different airfoil.

The case “125k\_0” yielded its  $C_F$  and  $C_P$  results in a pattern that significantly differs from that observed in the other cases. This is due to the vortex shedding failing to cease during the time this case was allowed to run. In spite of evidently compromising the results for  $C_F$  and  $C_P$ , which depend on the precise location of each point over the surfaces, the effects of such behavior did not become evident in the  $C_L$  and  $C_D$  results (see figures 5.9 to 5.11). The lift and drag forces are obtained by integrating local values over every point on the airfoil surface. Data for  $C_F$  and  $C_P$  are the instant values of the last stored time step. The  $C_L$  and  $C_D$  values presented in table 5.8, in turn, are the averages of the last 1000 time steps.

Another fact worth mentioning is the oscillatory behavior of the skin friction results at the upper surface, in the region between the leading edge and about 40% chord. This type of oscillation has been detected in other studies involving RANS simulations [Malan et al., 2009; Aftab et al., 2016], being more easily detected in simulations that used finer grids. Characteristics of numerical methods and turbulence models may be involved in this phenomenon. LES and DNS simulations [Alam and Sandham, 2000] seem not to show this feature.

Figures showing  $C_F$  and  $C_P$  results plotted separately for each one of the 20 cases run at this stage can be found in Appendix 1.

## **6 UFRGS SMALL WIND TURBINE PROJECT**

This thesis is part of a joint effort between the Departments of Mechanical and Electrical Engineering at UFRGS. The partnership was launched with the purpose of expanding the work started by Verdum, 2013, into a full project development effort, from which a new small HAWT design, optimized to operate in dense urban environments, should ultimately emerge.

It is intended that the evaluations carried out in the present work contribute to the final design of the turbine, as the main design parameters have already been defined. Characteristics of the project are summarized in the next sections.

### **6.1 Design constraints**

It was decided that the rotor would be comprised of five blades 0.75 meters long each, which would result in a rotor diameter of 1.5 m. At rated capacity, when subject to a free stream wind speed of 11 m/s, its angular velocity is expected to be 560 RPM (58.67 rad/s), resulting in a tip speed ratio (TSR) equal to 4. The airfoil selection fell on the SD7062 profile. The option for 5 blades came from the fact that a 5-blade machine would perform better than a 3-blade one at lower tip speed ratios, focusing on better starting performance and lower noise emissions when compared to more common designs.

### **6.2 Blade generated by SWRDC**

The results presented in this chapter were produced focusing on the aerodynamic performance of the blades. The included structural design is provided solely by the code, for which a fiberglass material was selected and the blade shell thickness was defined respecting a material safety factor of 2 and a load safety factor of 1.35. Fatigue behavior is not considered by the code.

#### **6.2.1 Small Wind-Turbine Rotor Design Code**

The optimizations used the Matlab code Small Wind-Turbine Rotor Design Code (SWRDC) [Sessarego and Wood, 2015], developed at the University of Calgary and available

from the authors. SWRDC uses a genetic algorithm, blade element momentum theory, simple Euler-Bernoulli beam theory, a model for starting performance evaluation from Wood, 2011a, and a noise model to design small-scale, variable-speed and fixed-pitch horizontal-axis wind turbine rotors. The optimization seeks to

$$\text{minimize} \left( \max \left[ w \frac{1/C_P(i) - 1/C_{P,\min}}{1/C_{P,\max} - 1/C_{P,\min}}, (1-w) \frac{T_S(i) - T_{S,\min}}{T_{S,\max} - T_{S,\min}} \right] \right) \quad (6.1)$$

for blade  $i$  in the current population.  $C_P$  is the conventional power coefficient at the design wind speed, taken to be 11 m/s. The weight  $w$  ( $0 \leq w \leq 1$ ) determines the relative significance of power extraction and starting. When  $w = 1$ , the optimization is purely for power.  $T_S$ , in seconds, is the starting time required to reach a tip speed ratio at a wind speed specified by the user (in this case, TSR = 1). The blade chord and twist for each section are determined using Bézier curves with a user-specified number of control points.

The code uses a genetic algorithm (GA) for optimization, whose parameters can be controlled by the user. A reasonable population size is needed to search the design space adequately. In this work, it was defined as 100 individuals. The optimization stops when the maximum number of generations is reached. The GA utilizes crossover and mutation operators. Crossover exchanges traits – chord and twist (the genes) – between two or more solutions (parents) in the hope of producing superior solutions (the offspring). Mutation ensures that each individual in the offspring is unique by altering their genes slightly.

The structural analysis offered by SWRDC is combined with the aerodynamic analysis that gives the power output and starting time. The code gives two alternate ways of assessing structural loads, both based on the Simplified Load Model (SLM) of the international safety standard for small wind turbines, IEC 61400-2 [IEC 61400-2, 2006]. Aerodynamic assessments of each individual are performed using the BEM method as described in Ch. 3.

## 6.2.2 Conditions

Once the main design constraints were defined, it was possible to move on and define the remaining parameters in order to have a final blade design. The optimization code offers a large number of options that were taken into account, from airfoil data to material properties.

A small hub radius measuring 0.075 m was defined along with the total rotor radius, to benefit from the possible absence of a physical hub due to the generator being intended to be assembled in an outer ring. This feature allowed for a better exploration of the inner blade region, responsible for the starting performance. In the BEM setup, the blade was divided in 25 evenly spaced elements, allowing a good blade discretization. The Bézier curve that controls the parameters at each blade section had 5 control points. The minimum and maximum limits for the twist angle were set to 0.1 and 88 degrees, respectively, and the minimum and maximum chord length limits were set respectively to 0.03 and 0.2 meters.

The air density was set to  $1.225 \text{ kg/m}^3$  and the dynamic viscosity to  $1.7894 \cdot 10^{-5} \text{ m}^2/\text{s}$ . For the calculation of the relative starting time, the TSR to complete starting was set to 1, which should be reached at a free stream wind speed of 4 m/s. The electric generator was modeled as having a moment of inertia of  $0.006 \text{ kg}\cdot\text{m}^2$  and a resistive torque of 0.5 N.m.

A typical fiberglass material, E-Glass, was selected. Its density is  $2540 \text{ kg/m}^3$  and its elastic modulus is 72 GPa. The blade was defined as hollow with a minimum blade shell thickness of 1 mm. For the genetic algorithm, a population size of 100 individuals was defined to be generated in each of the 250 generations. Mutation and crossover settings were set as default by the code.

The noise analysis was performed using the built-in noise data. Considering a relative surface roughness at the environment equivalent to that of a city center with tall buildings, a turbine hub height of 15 m was defined, the observer being positioned also 15 m from the tower base. The blade tip shape was set as squared, and the bluntness thickness of the blade was set to 1 mm.

The last parameters defined were the objective weight factors. Regardless of the number of objectives selected, the sum of their values must be equal to 1. The factors are 0.9 for the power coefficient, 0.089 for the starting time, 0.01 for the mass and 0.001 for the noise.

### 6.2.3 Resulting blade

After running SWRDC with all the previously discussed parameters implemented, a final blade design emerged. Table 6.1 shows the chord length and twist angle for each one of the 25 radial positions it was divided in, as well as the local blade spacing and the local

solidity, defined in eq. (3.10). A twist angle of zero means the profile chord is parallel to the rotor plane of rotation.

This design was selected after many others had been generated previously, by making small changes in parameters as chord and twist bounds and objective function factors. The main criterion used to select the final design was the shape of its power coefficient curve. Upon starting, a small wind turbine must be able to reach a power extracting TSR as soon as possible. Additionally, it is desired that the turbine operates at or close to its design power coefficient for a wide range of tip speed ratios, which results in curves with a relatively flat peak.

As can be seen in the power coefficient curve, figure 6.1 (a), the turbine is able to operate close to its maximum design  $C_{Pwr}$  for a broad range of tip speed ratios, and at a TSR of 2 a  $C_{Pwr}$  of 0.41 is reached, which is roughly 90% of the maximum  $C_{Pwr}$  of 0.456, achieved at a TSR of approximately 3.6. At the design TSR of 4, the  $C_{Pwr}$  is 0.453. Fig. 6.1 (b) shows the thrust coefficient ( $C_{Thr}$ ) curve with a relatively flat peak as well. The thrust on the blades is not as important for wind turbines as it is for propellers, which are designed to produce thrust. However, the thrust is usually transmitted to the turbine tower, and so must be included in tower foundation and design. As with the power output,  $C_{Thr}$  is strongly dependent on the TSR but not usually on  $Re$  [Wood, 2011a]. Similarly to  $C_{Pwr}$ , defined in eq. (3.6),  $C_{Thr}$  is defined as

$$C_{Thr} = \frac{\text{Thrust}}{\frac{1}{2} \rho u^2 A} \quad (6.2)$$

Figure 6.2 depicts the blade in a three-dimensional rendering. In the configuration shown, the plane of rotation would correspond to the  $XZ$ -plane. The free-stream, undisturbed wind would move upwards parallel to the  $Y$ -axis. The blade would rotate clockwise around the positive  $Y$ -axis.

A five-blade rotor operating at the design TSR of 4 under a free-stream wind speed of 11 m/s would generate a rated power of 650 Watts, resulting in a  $C_{Pwr}$  of 0.453. The torque on the turbine axis would be 11 N.m, and the thrust experienced by the tower would be 103 N. The mass of each blade would be 0.115 kg, and this rotor would be expected to produce 64.4



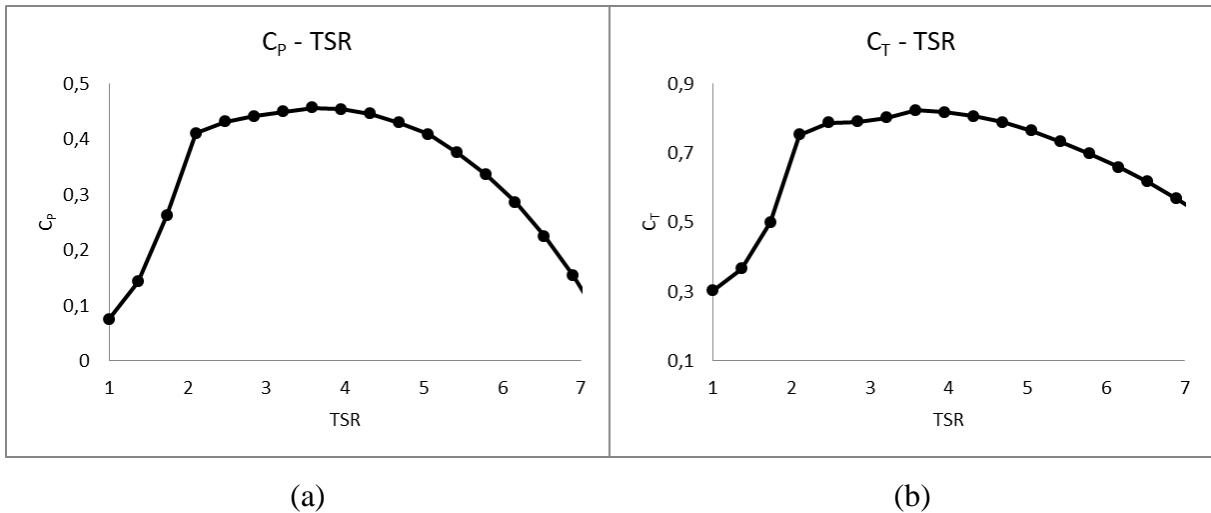


Figure 6.1 – Performance curves of the rotor designed with the resulting blades. (a):  $C_{Pwr}$  vs. TSR curve, (b):  $C_{Thr}$  vs. TSR curve

Table 6.1 – Parameters of the resulting blade

Radius (m)	Chord (m)	Twist (deg)	Bl. Spacing (m)	Solidity
0.075	0.1792	42.73	0.0942	1.9017
0.1031	0.1792	38.52	0.1296	1.3827
0.1313	0.1791	34.88	0.1649	1.0857
0.1594	0.1788	31.74	0.2003	0.8928
0.1875	0.1784	29.03	0.2356	0.7573
0.2156	0.1778	26.72	0.271	0.6562
0.2438	0.1769	24.73	0.3063	0.5776
0.2719	0.1757	23.03	0.3416	0.5144
0.3	0.1742	21.58	0.377	0.462
0.3281	0.1722	20.32	0.4123	0.4175
0.3563	0.1697	19.23	0.4477	0.379
0.3844	0.1667	18.26	0.483	0.345
0.4125	0.163	17.38	0.5184	0.3145
0.4406	0.1588	16.55	0.5537	0.2868
0.4688	0.1538	15.75	0.589	0.2612
0.4969	0.1481	14.92	0.6244	0.2372
0.525	0.1416	14.04	0.6597	0.2147
0.5531	0.1343	13.08	0.6951	0.1932
0.5813	0.126	11.98	0.7304	0.1726
0.6094	0.1169	10.7	0.7658	0.1526
0.6375	0.1068	9.21	0.8011	0.1333
0.6656	0.0956	7.45	0.8364	0.1144
0.6938	0.0835	5.37	0.8718	0.0958
0.7219	0.0703	2.9	0.9071	0.0775
0.75	0.0561	0	0.9425	0.0595

dB of noise. Since SWRDC yields a relative value for the starting time, which is only meaningful when two or more blades are compared among themselves, it was decided to exclude this value from the result report.

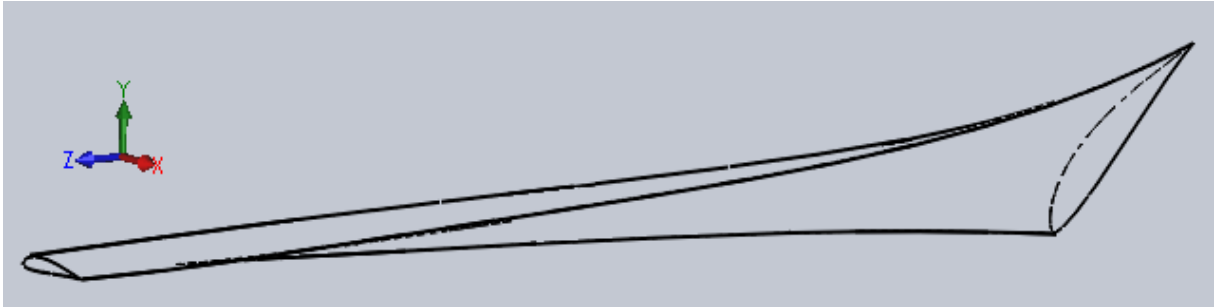


Figure 6.2 – A depiction of the resulting blade

## 7 HIGH ROTOR SOLIDITY AND ITS EFFECTS

It is agreed that the parameter that predominantly influences stall delay is the local blade solidity [Burton et al., 2001]. Although the present study does not include angles of attack high enough to proceed to a stall delay evaluation, it is said that the effects of high solidity are expected to cause an overall improvement in the performance of a wind turbine rotor even for smaller angles of attack.

This chapter is dedicated to present an evaluation that combines low-Reynolds flows over the SD7062 airfoil and solidity effects. Values of lift and drag coefficients were collected for 45 distinct configurations, and comparisons of pressure and skin friction coefficient plots are presented between selected solidity cases and isolated-airfoil situations under similar conditions.

This chapter is entirely the result of the 10-month exchange conducted by the author at the University of Calgary (Canada), under supervision of Dr. David H. Wood. Dr. Wood enjoys worldwide recognition for his contributions to small wind turbine technology. He is the author of the book *Small Wind Turbines: Analysis, Design and Application*, published in 2011.

All simulations in this chapter, as well as all the 20 SD7062 low- $Re$ , isolated-airfoil cases from Chapter 5, were run at Westgrid, western Canada's supercomputing network. The author is deeply thankful for both Dr. Wood and the Westgrid staff.

### 7.1 CFD simulations of selected solidity conditions

The proposed blade design introduced in Ch. 6 produced a 5-blade rotor, the sections of which resulted relatively wide up to about half blade span. The consequence is a rotor with elevated solidity that was considered quite suitable for the analysis of solidity effects.

In order to conduct this analysis, three radial positions along the blade span were selected, representing approximate local solidities of 0.1, 0.2 and 0.3. Such values are regarded as low, medium and high, respectively. It is expected that the study conducted here can allow a deeper insight in the flow behavior when the flows affected by adjacent blades interfere with each other.

It is usual to define the blade spacing as the inverse of eq. (3.10), the local solidity. In the present study, since it was defined that all simulations would be two-dimensional, the

blade spacing was interpreted simply as the distance from any point of a given section to the corresponding point at the adjacent blades along a circle, thus  $2\pi r/5$  for a 5-blade rotor,  $r$  being the local radius, see figure 7.1. The selected blade sections are those at radial positions equal to 0.6938 m, 0.5531 m and 0.4125 m (see table 6.1), corresponding to local solidities of approximately 0.1, 0.2 and 0.3 respectively. Table 7.1 shows other relevant parameters of the selected blade sections.

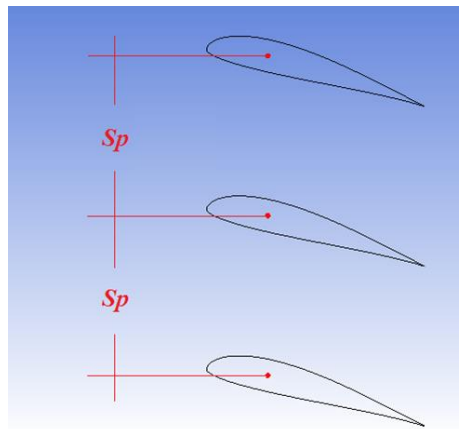


Figure 7.1 – Definition of the local blade spacing ( $S_p$ )

Table 7.1 – Parameters of the blade sections selected for solidity analyses

Label	Solidity	Radius (m)	$S_p$ (m)	$a$	$a'$
S1	0.0958	0.6938	0.8718	0.5125	0.0167
S2	0.1932	0.5531	0.6951	0.3014	0.0213
S3	0.3145	0.4125	0.5184	0.2825	0.0372

Table 7.1 summarizes local solidity, radial position, blade spacing and the axial and tangential induction factors for the solidity cases hereinafter named S1, S2 and S3.

The computational models were constructed such that they would simulate the actual operating conditions of each blade section. The plane of rotation is aligned with the vertical axis, so blades would move upwards along the  $Y$ -axis. The twist angle is defined relative to the vertical axis as well. A twist angle of zero would mean that the airfoil chord is aligned with the  $Y$ -axis.

In order to simulate rotating blades, the rotational speed was defined as the vertical component of the resulting wind speed ( $u_2$ ), defined in eq. (3.12). The horizontal component

is  $u_1$ , it is, the free stream wind speed ( $u$ ) multiplied by the factor  $(1-a)$ , where  $a$  is the axial induction factor, as defined in eq. (3.11). These two components define the resulting velocity ( $u_{rel}$ ), which is colloquially explained as the speed to which a blade section is actually subject, as illustrated in the velocity triangle (fig. 3.3). The angle between  $u_{rel}$  and the plane of rotation is  $\varphi$ , the resulting inflow angle. These components are calculated as functions of the free-stream wind velocity, which is a boundary condition of the problem. For the present study, three values of  $u$  were selected: 5, 8 and 11 m/s, the latter being the turbine's rated wind speed when operating at a TSR equal to 4. Other TSR values simulated, besides 4.0, were 3.0, 3.25, 3.5 and 3.75.

In short, three blade sections were simulated for five different tip speed ratios and three different free stream wind speeds, making a total of 45 cases. Only three different computational domains needed to be created (representing the three different blade sections and their respective spacings). The remainder of the situations could be configured by just changing velocity magnitudes and angles to represent the different resulting speeds and tip speed ratios. For each domain, the height corresponds to the local blade spacing, with the section positioned at the midpoint. The domain length corresponds to 40 chords, 20 either direction. Figure 7.2 illustrates the center part of the S3 domain as an example, with and without grid. The total length is not shown.

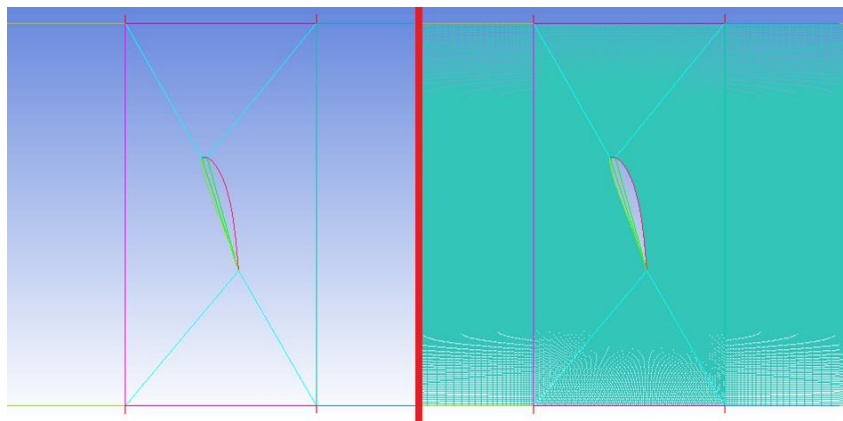


Figure 7.2 – Part of the computational domain for the solidity case S3

All domains involve the SD7062 airfoil as it was chosen as the standard for the turbine in Ch. 6. The airfoils and grid densities around them were modeled following the same

guidelines used in the simulations of the isolated airfoil presented in Section 5.2.3. Table 7.2 summarizes parameters relevant to the three domains.

Table 7.2 – Parameters of computational domains for solidity cases

Domain	Solidity	Height (m)	Length (m)	Cell count
1	0.1	0.8718	3.34	792,000
2	0.2	0.695	5.372	792,000
3	0.3	0.5184	6.52	792,000

The interaction between the adjacent blade sections was simulated by virtually replicating one domain on top of each other along the  $Y$ -axis, in what resulted in an infinite cascade of airfoils. This was accomplished by employing the translational periodic boundary condition at the upper and lower surfaces. In ANSYS Fluent, the translational periodic boundary condition allows pressure drops to occur across periodic boundaries, resulting in a situation of fully developed or “streamwise-periodic” flow [ANSYS, 2009], thus allowing flow properties to be freely transported from one domain into another. Figure 7.3 shows an example of velocity field for an airfoil cascade, where one domain is repeated in the vertical direction *ad infinitum*. Only three replicates are shown.

The remaining boundary conditions are as follows: the domain’s left surface represents the inlet, at which a prescribed flow velocity magnitude  $u_{rel}$  is applied at a given angle  $\varphi$  (see fig. 3.3). The surface to the right is the outlet, which was kept at atmospheric pressure in what is defined as pressure outlet condition. The airfoil proper was modeled as a standard, no-slip wall. In this approach, no other walls are present in the domain.

The simulations were run in transient state. All cases were allowed to run until reaching at least 5 flow seconds, at a time step equal to  $5 \cdot 10^{-5}$  seconds. Some cases were interrupted upon reaching a statistically steady regime, at which any flow variable showed a residue no larger than  $1 \cdot 10^{-5}$  and there was not any kind of vortex shedding. Not all cases reached such state, though. The results for lift, drag, pressure and skin friction coefficients are presented in the next section.

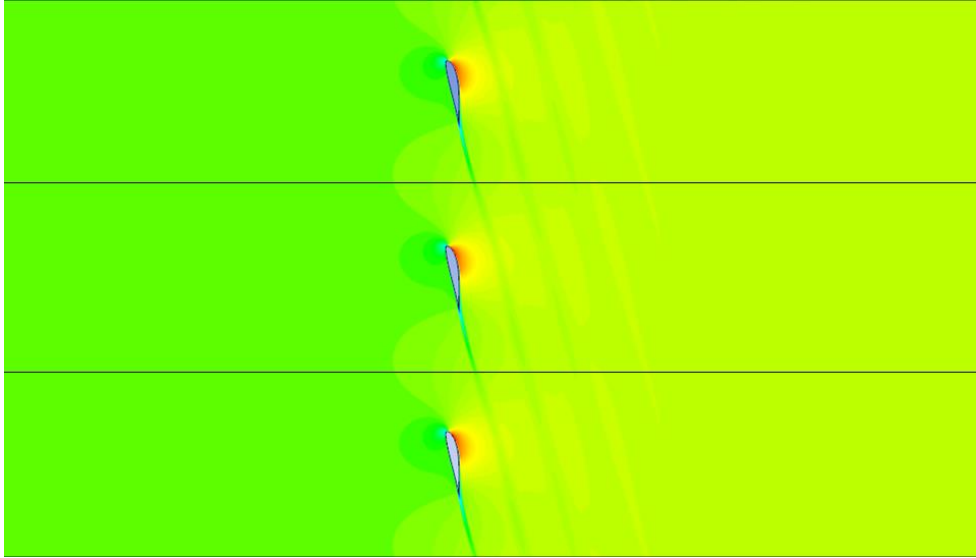


Figure 7.3 – Example of velocity contours for an infinite airfoil cascade

## 7.2 Results

Prior to evaluate the results from the computational runs, it is necessary to take into account that blade cascades affect the free stream flow angle and velocity downstream the stack. The flow approaches the stack at a given angle and leaves it at a different angle, which arises through inviscid and viscous effects [Dixon and Hall, 2010]. Assuming constant axial velocity, the mean inflow angle  $\varphi_M$  is defined as the average between the flow angle far upstream (which is the original inflow angle,  $\varphi$ ) and the flow angle far downstream ( $\varphi_D$ ):

$$\tan \varphi_M = \frac{1}{2}(\tan \varphi + \tan \varphi_D) \quad (6.3)$$

The original inflow angle is that one defined as the boundary condition for each case. The downstream inflow angle is calculated from the axial and tangential velocity magnitudes collected at a point in the domain far downstream from the blade stack, far away from the direct influence of the airfoil wakes. The effective angle of attack is then defined as a function of the mean inflow angle.

The axial and tangential velocity components used to calculate  $\varphi_D$  also provide the means to calculate the downstream flow velocity ( $u_D$ ). Then, in similar ways, a mean flow velocity ( $u_M$ ) is calculated. Thus,

$$u_M = \frac{1}{2}(u_{rel} + u_D) \quad (6.4)$$

This mean velocity must be used to calculate the resulting, effective angle of attack, and the resulting  $\alpha$  is, together with  $u_M$ , the parameter at which the lift, drag, pressure and skin friction coefficients must be collected. Table 7.3 summarizes the results for the 45 solidity cases covered in the present work. Data is presented covering the effective mean inflow angles ( $\varphi_M$ ) and velocities ( $u_M$ ) only.

The axial and tangential flow velocities are functions of the axial and tangential induction factors, respectively. Although they are constant in the classic Betz methodology, in real turbines these values vary over the blade span. Values for  $a$  and  $a'$  have been yielded by the SWRDC optimization code for each blade section. For S1,  $a = 0.5125$  and  $a' = 0.0167$ . For S2,  $a = 0.3014$  and  $a' = 0.0213$ . For S3,  $a = 0.2825$  and  $a' = 0.0372$ .

At this point, it is worth considering that, to the author's knowledge, there are no published works that assess the aerodynamic performance of wind turbine blades using two-dimensional airfoil cascades for solidity cases larger than 0.3. In fact, even this value is deemed as high since, as discusses, the BEM method excludes any solidity level, as well as any fluid motion between different streamtubes, from its analysis. Provided that the simulations ran in the present work involve a cascade of two-dimensional airfoils, it means that the boundary conditions force a flow rate between airfoils through the imposition of a prescribed velocity, while, in the realistic condition of a three-dimensional blade, the flow can move between different blade elements searching for situations that minimize head loss.

Therefore, it is considered that simulating solidity values larger than 0.3 using the two-dimensional cascade approach can lead to distorted results. For such cases, 3D simulations of entire blades or rotors tend to present results less subject to errors imposed by the 2D methodology.

### 7.2.1 Lift and drag coefficients

The SWRDC optimization code uses the classic blade element momentum theory in its design routine. The BEM analysis in the code involves an iterative technique to estimate the aerodynamic performance of a rotor design, but it does not take into account any correction to address rotational effects or the finite number of blades.



Provided that the blade has been designed relying on lift and drag data as functions of the angle of attack for each blade section, an two-dimensional analysis of the aerodynamic coefficients versus AOA was carried out for every case produced in the battery of 45 simulations. Plots of  $C_L$  vs. AOA,  $C_D$  vs. AOA and  $L/D$  vs. AOA for the SD7062 airfoil, compared to experimental data at a similar Reynolds number range, are shown in the next figures. Data for comparison comes from Lyon et al., 1997, which is the same reference used to feed the SWRDC airfoil database.

In figures 7.4 to 7.12, lines indicate the same solidity, whereas colors indicate the same TSR. Data was sorted by free stream velocity. The  $C_L$  plots include labels next to the numerical data points as an aid to locate specific cases, but these labels have been suppressed in  $C_D$  and  $L/D$  plots to avoid excessive pollution in the plot area. The symbol shape and color codes are the same for any case.

Table 7.3 – Results for the 45 solidity simulations

$u$	TSR	Solid.	Label	Orig. $\varphi$ (deg)	$u_1$ (m/s)	$u_2$ (m/s)	$u_{rel}$ (m/s)	$u_M$ (m/s)	Re( $10^5$ )	Mean $\varphi$ (deg)	Mean $\alpha$ (deg)	$C_L$	$C_D$	$L/D$
11	4	0.1	11-40-S1	7.384	5.363	41.38	41.726	42.251	2.42	7.291	1.925	0.6341	0.0128	49.614
		0.2	11-40-S2	13.055	7.685	33.141	34.021	34.595	3.18	12.834	-0.242	0.4114	0.0107	38.399
		0.3	11-40-S3	17.455	7.893	25.1	26.312	27.053	3.02	16.974	-0.405	0.4211	0.0112	37.751
	3.75	0.1	11-37-S1	7.87	5.363	38.793	39.162	39.7	2.27	7.763	2.397	0.6853	0.0137	50.095
		0.2	11-37-S2	13.892	7.685	31.07	32.006	32.671	3.0	13.606	0.53	0.497	0.0107	46.41
		0.3	11-37-S3	18.542	7.893	32.531	24.82	25.732	2.87	17.883	0.504	0.5444	0.0116	46.961
	3.5	0.1	11-35-S1	8.425	5.363	36.207	36.602	37.153	2.12	8.299	2.933	0.7425	0.0147	50.569
		0.2	11-35-S2	14.842	7.685	28.999	30.0	30.774	2.83	14.466	1.39	0.6091	0.0118	51.709
		0.3	11-35-S3	19.766	7.893	21.963	23.338	24.415	2.72	18.898	1.519	0.6863	0.0131	52.489
	3.25	0.1	11-32-S1	9.062	5.363	33.621	34.046	34.603	1.98	8.915	3.55	0.8067	0.016	50.288
		0.2	11-32-S2	15.928	7.685	26.927	28.002	28.866	2.65	15.45	2.374	0.7299	0.0131	55.517
		0.3	11-32-S3	21.157	7.893	20.394	21.868	23.101	2.58	20.038	2.659	0.8438	0.015	56.188
	3.0	0.1	11-30-S1	9.803	5.363	31.035	31.495	32.059	1.83	9.63	4.264	0.8791	0.0177	49.72
		0.2	11-30-S2	17.18	7.685	24.856	26.017	26.967	2.48	16.574	3.498	0.8658	0.0149	57.938
		0.3	11-30-S3	22.746	7.893	18.825	20.413	21.784	2.43	21.334	3.955	1.0212	0.0179	56.949
8	4.0	0.1	8-40-S1	7.384	3.9	30.094	30.346	30.701	1.75	7.299	1.933	0.6193	0.0154	40.121
		0.2	8-40-S2	13.055	5.589	24.103	24.742	25.116	2.31	12.861	-0.214	0.3781	0.0125	30.219
		0.3	8-40-S3	17.455	5.74	18.255	19.136	19.65	2.19	16.997	-0.382	0.4149	0.0135	30.64
	3.75	0.1	8-37-S1	7.87	3.9	28.213	28.482	28.847	1.65	7.771	2.406	0.6685	0.0166	40.37
		0.2	8-37-S2	13.892	5.589	22.596	23.277	23.746	2.18	13.62	0.544	0.4899	0.0129	37.97
		0.3	8-37-S3	18.542	5.74	17.114	18.051	18.696	2.09	17.903	0.524	0.5353	0.0138	38.786
	3.5	0.1	8-35-S1	8.425	3.9	26.333	26.62	26.995	1.54	8.308	2.943	0.7231	0.0179	40.317
		0.2	8-35-S2	14.842	5.589	21.09	21.818	22.36	2.06	14.485	1.409	0.5972	0.0141	42.284
		0.3	8-35-S3	19.766	5.74	15.973	16.928	17.711	1.98	18.924	1.546	0.6771	0.0156	43.333
	3.25	0.1	8-32-S1	9.062	3.9	24.452	24.761	25.14	1.44	8.926	3.561	0.784	0.0196	39.909
0.2		8-32-S2	15.928	5.589	19.583	20.365	20.971	1.93	15.472	2.396	0.7148	0.0158	45.327	

Table 7.3 – Results for the 45 solidity simulations (continued)

$u$	TSR	Solid.	Label	Orig. $\varphi$ (deg)	$u_1$ (m/s)	$u_2$ (m/s)	$u_{rel}$ (m/s)	$u_M$ (m/s)	Re( $10^5$ )	Mean $\varphi$ (deg)	Mean $\alpha$ (deg)	$C_L$	$C_D$	$L/D$
8	3.25	0.3	8-32-S3	21.157	5.74	14.832	15.904	16.772	1.87	20.073	2.694	0.8273	0.0178	46.424
	3.0	0.1	8-30-S1	9.803	3.9	22.571	22.905	23.289	1.33	9.643	4.277	0.8522	0.0218	39.154
		0.2	8-30-S2	17.18	5.589	18.077	18.921	19.589	1.8	16.6	3.524	0.8465	0.0179	47.306
		0.3	8-30-S3	22.746	5.74	13.691	14.846	15.814	1.76	21.373	3.995	0.9998	0.021	47.512
5	4.0	0.1	5-40-S1	7.384	2.438	18.809	18.966	19.15	1.09	7.317	1.951	0.5872	0.0219	26.871
		0.2	5-40-S2	13.055	3.493	15.064	15.464	15.676	1.44	12.872	-0.204	0.3796	0.0169	22.423
		0.3	5-40-S3	17.455	3.588	11.409	11.956	12.255	1.37	17.036	-0.343	0.3935	0.017	23.111
	3.75	0.1	5-37-S1	7.87	2.438	17.633	17.801	17.993	1.03	7.791	2.425	0.6301	0.0238	26.522
		0.2	5-37-S2	13.892	3.493	14.123	14.548	14.819	1.36	13.633	0.557	0.4727	0.0174	27.158
		0.3	5-37-S3	18.542	3.588	10.696	11.282	11.655	1.3	17.953	0.575	0.516	0.0187	27.55
	3.5	0.1	5-35-S1	8.425	2.438	16.458	16.637	16.832	0.962	8.332	2.966	0.6771	0.0261	25.978
		0.2	5-35-S2	14.842	3.493	13.181	13.636	13.945	1.28	14.507	1.432	0.5731	0.0192	29.918
		0.3	5-35-S3	19.766	3.588	9.983	10.608	11.052	1.23	18.982	1.604	0.6471	0.0211	30.675
	3.25	0.1	5-32-S1	9.062	2.438	15.282	15.475	15.672	0.896	8.954	3.588	0.7281	0.029	25.121
		0.2	5-32-S2	15.928	3.493	12.240	12.728	13.08	1.2	15.494	2.419	0.6837	0.0214	31.968
		0.3	5-32-S3	21.157	3.588	9.27	9.94	10.447	1.17	20.143	2.764	0.7928	0.0242	32.72
	3.0	0.1	5-30-S1	9.803	2.438	14.107	14.316	14.51	0.829	9.678	4.312	0.7798	0.0334	23.351
		0.2	5-30-S2	17.18	3.493	11.928	11.826	12.21	1.12	16.634	3.559	0.8066	0.0245	32.904
		0.3	5-30-S3	22.746	3.588	8.557	9.279	9.844	1.1	21.461	4.082	0.9544	0.0286	33.346

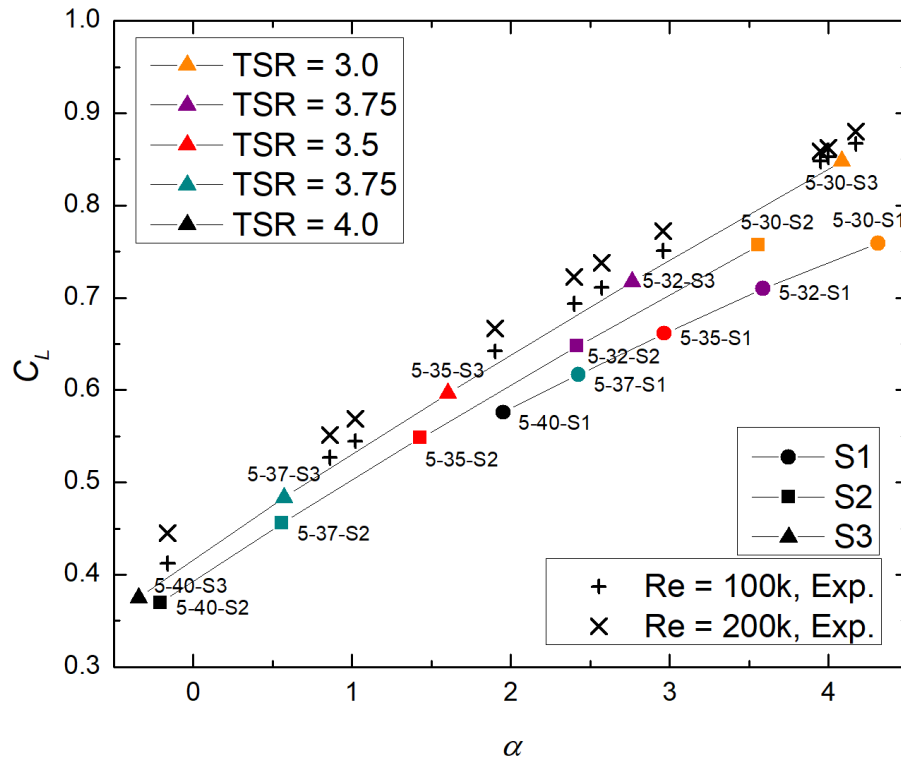


Figure 7.4 –  $C_L$  vs. AOA for  $u = 5$  m/s, SD7062 subject to solidity effects

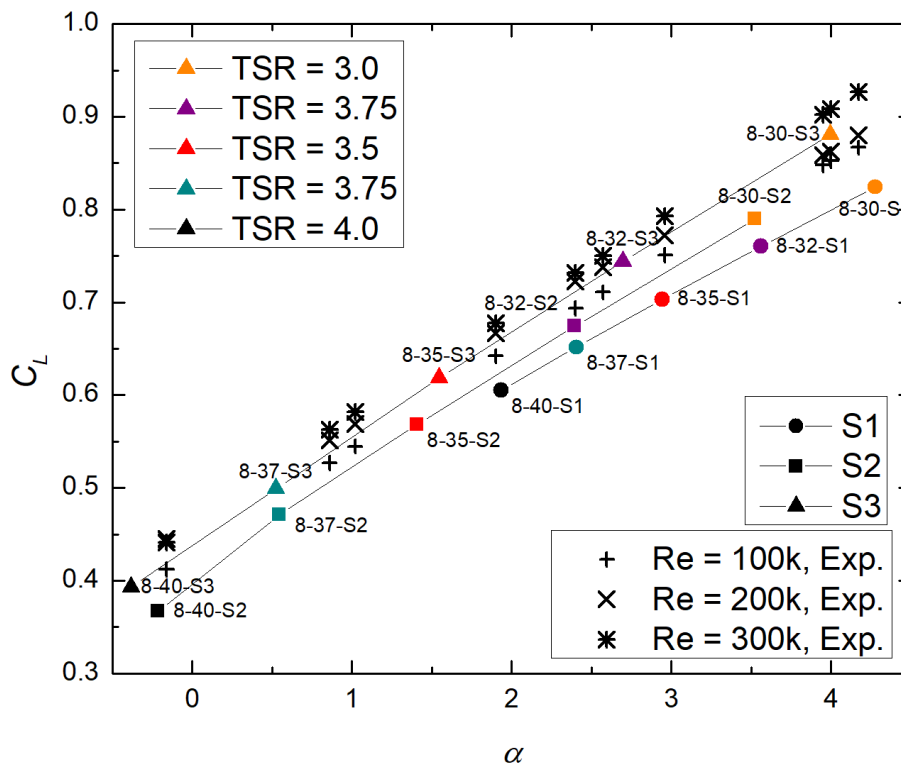


Figure 7.5 –  $C_L$  vs. AOA for  $u = 8$  m/s, SD7062 subject to solidity effects

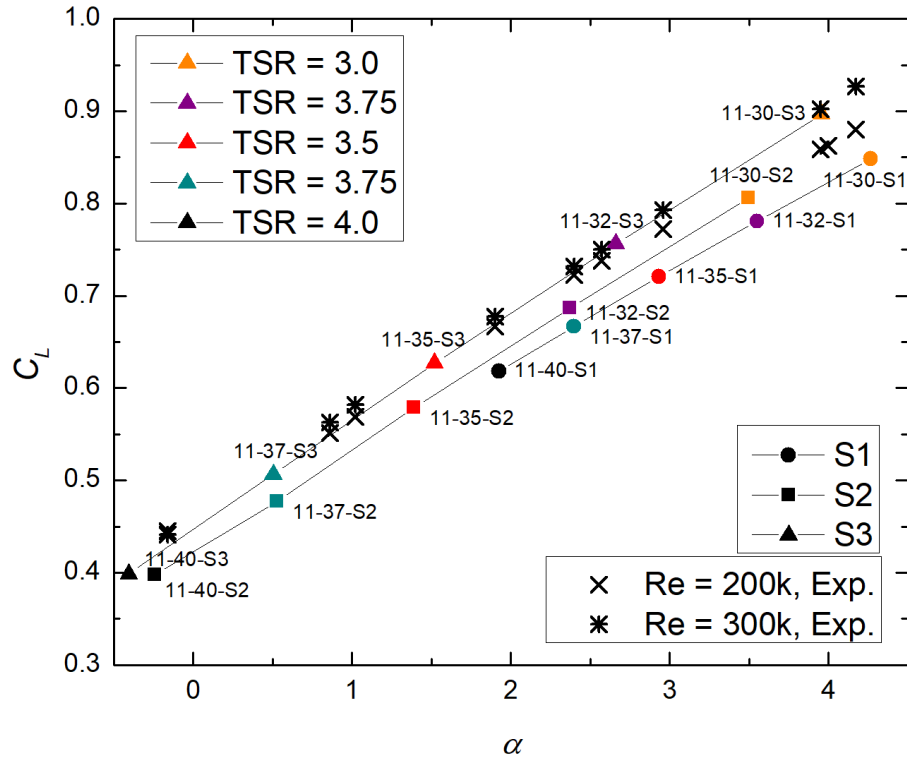


Figure 7.6 –  $C_L$  vs. AOA for  $u = 11$  m/s, SD7062 subject to solidity effects

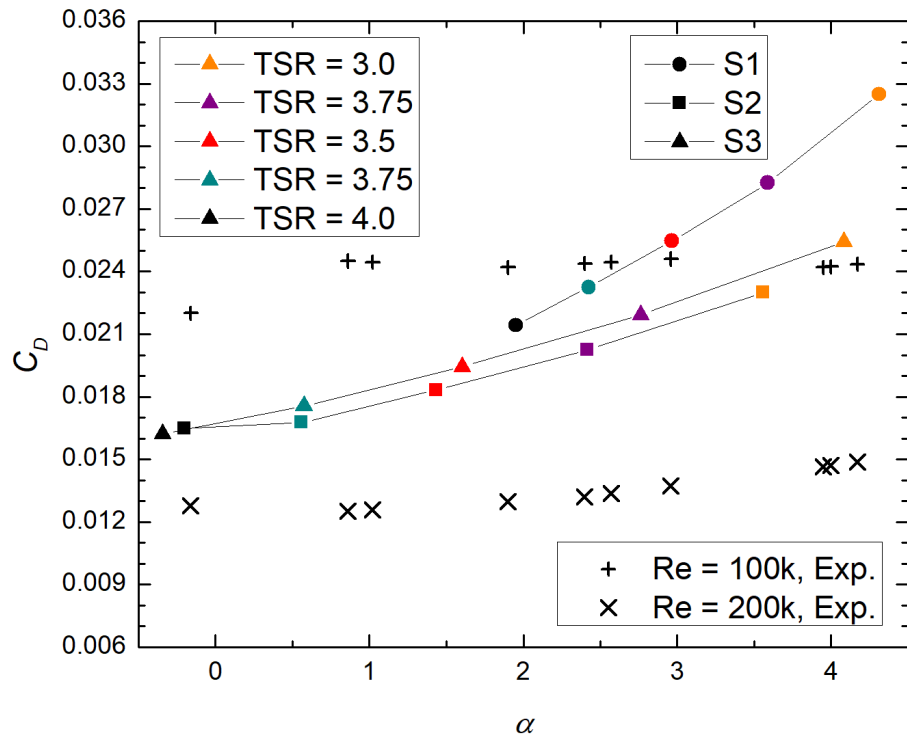


Figure 7.7 –  $C_D$  vs. AOA for  $u = 5$  m/s, SD7062 subject to solidity effects

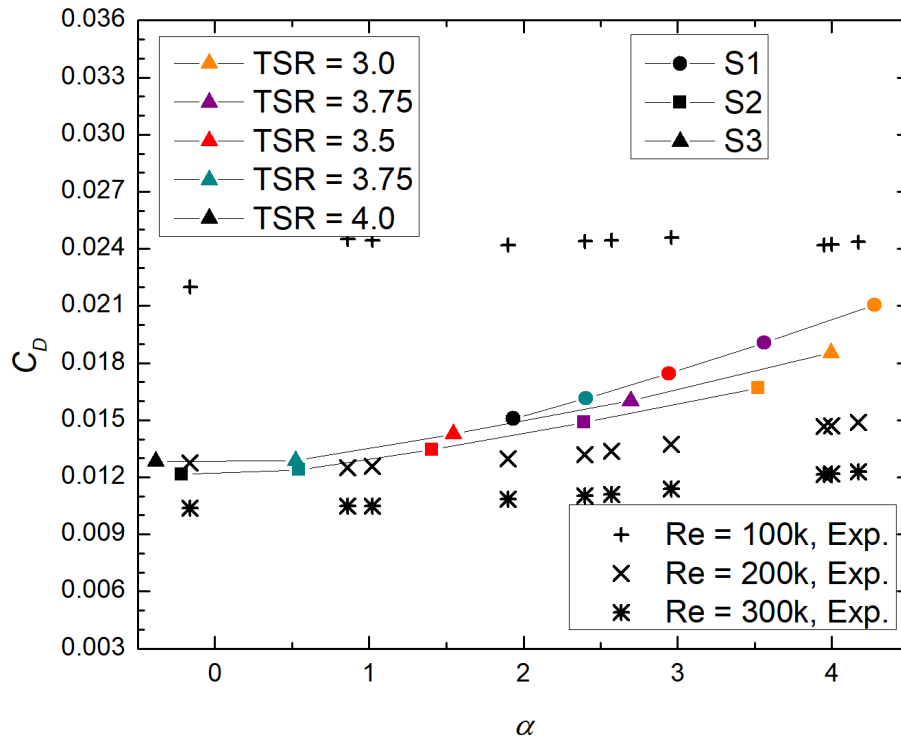


Figure 7.8 –  $C_D$  vs. AOA for  $u = 8$  m/s, SD7062 subject to solidity effects

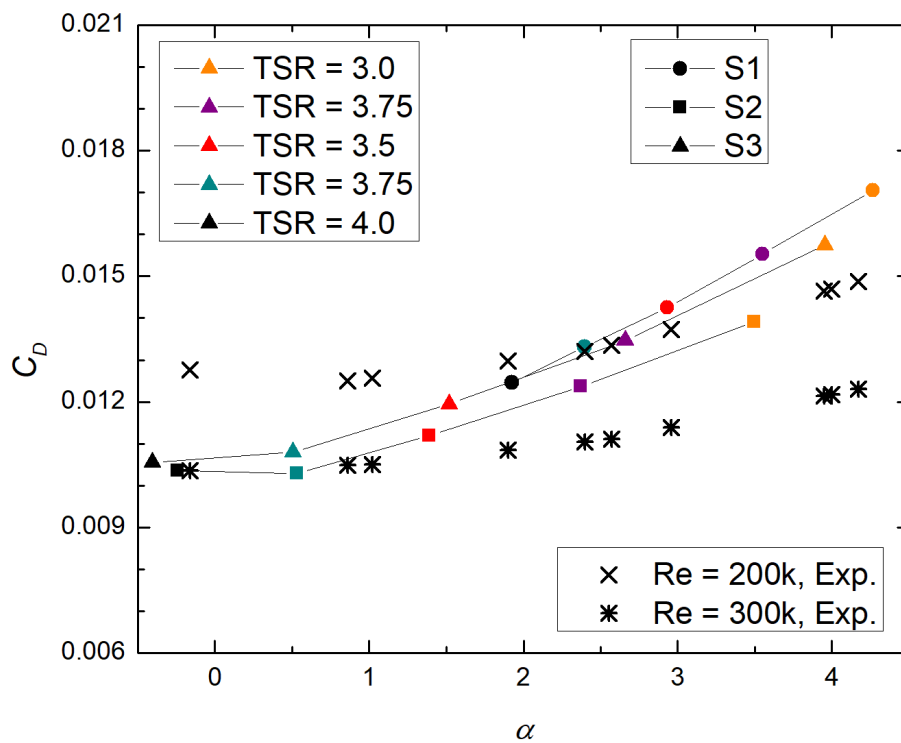


Figure 7.9 –  $C_D$  vs. AOA for  $u = 11$  m/s, SD7062 subject to solidity effects

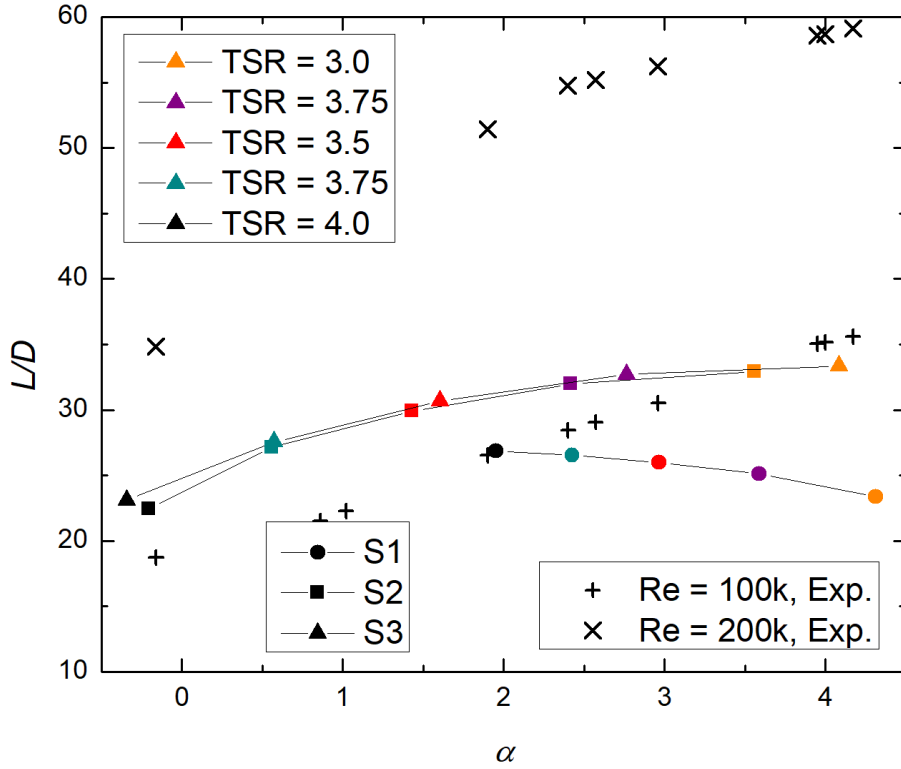


Figure 7.10 –  $L/D$  vs. AOA for  $u = 5$  m/s, SD7062 subject to solidity effects

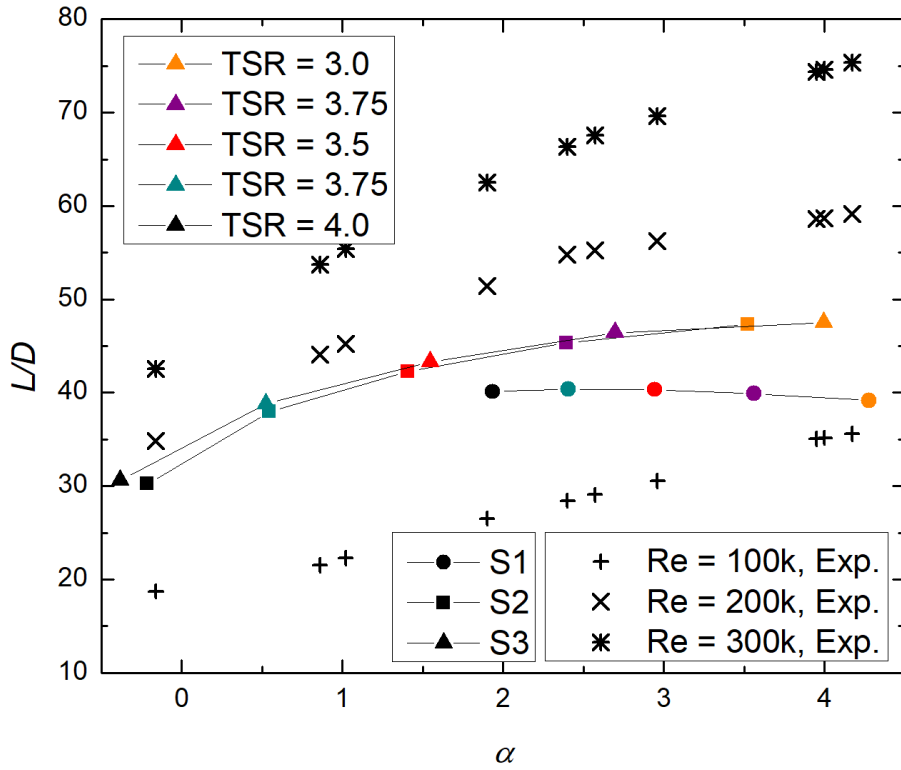


Figure 7.11 –  $L/D$  vs. AOA for  $u = 8$  m/s, SD7062 subject to solidity effects

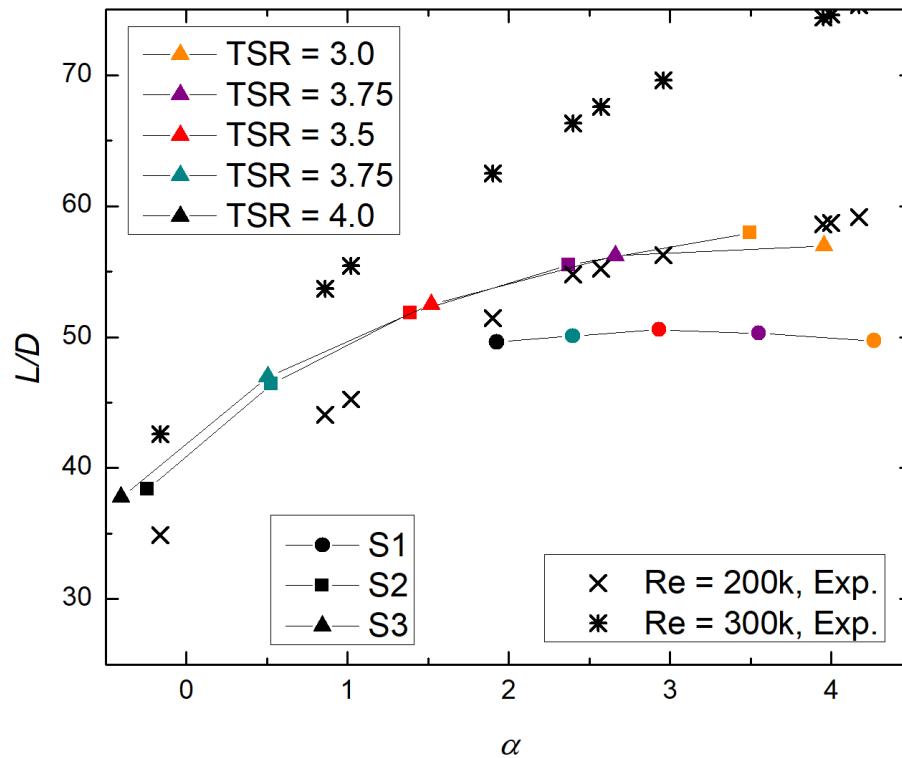


Figure 7.12 –  $L/D$  vs. AOA for  $u = 11$  m/s, SD7062 subject to solidity effects

Results depicted in figures 7.4 to 7.12 show that the lift coefficients behaved as expected, showing a trend of linear growth as a function of the angle of attack. The S1 cases, despite being subject to higher resulting wind speeds, operate at Reynolds numbers lower than those at which the S2 and S3 cases do. This is due to the small chord length of that blade section. Thus, as expected, the S1 cases produced the lowest  $C_L$  values. The S2 cases operated at the highest Reynolds numbers, but the  $C_L$  values produced by them were lower than those yielded by the S3 cases. This trend can be detected at the three free stream velocity cases that have been studied.

The drag coefficient results behaved as expected as well, regarding to the parabolic shape of the  $C_D$  vs. AOA curves. Particular values, however, are harder to be evaluated due to reasons such as inaccuracies of the numerical methods, and low- $Re$  flow nature itself. Moreover, such small magnitudes make it harder to evaluate the actual impact of large variations.

For the three situations presented above, the intermediate solidity (S2) produced the lower  $C_D$  values. The lower solidity (S1), in turn, produced the higher  $C_D$  values for the situation at which the free stream velocity ( $u$ ) was 5 m/s. This showed a downward trend with increasing  $u$ , however, since it caused the Reynolds numbers of the S1 cases to increase.



When analyzing the  $L/D$  charts, it is easy to see that the lift-to-drag curves for S2 and S3 are very close together. The fact that all cases operated at similar Reynolds numbers contributed to this. S1, in turn, has yielded the lower  $L/D$  ratios. While the S1 cases have produced drag coefficients similar to those produced by S2 and S3, they have produced lower lift coefficients.

The fact that each of the 45 cases operated at a unique Reynolds number has posed an obstacle to the comparison of their  $C_L$  and  $C_D$  values with the experimental data, which have been measured at specific  $Re$  values. Nevertheless, regarding to the lift coefficients, numerical results show a rate of increase with AOA very similar to that of the experimental data. Numerical results for the drag coefficient, in turn, show a stronger rate of increase with AOA compared to experimental data as the TSR decreases (and hence the angle of attack increases).

## 7.2.2 Pressure and skin friction coefficients

In an attempt to draw further comparisons between solidity cases and isolated-airfoil situations, three specific cases were selected out of the 45 solidity simulations for which  $Re$  and AOA most closely match simulations presented in Section 5.2.3. The solidity cases selected are the 5-30-S3 ( $Re = 1.1 \cdot 10^5$ , AOA = 4.082 deg), 5-40-S1 ( $Re = 1.09 \cdot 10^5$ , AOA = 1.95 deg) and 8-30-S1 ( $Re = 1.33 \cdot 10^5$ , AOA = 4.277 deg). Their pressure and skin friction coefficients were compared with corresponding data extracted from the 100k\_4 ( $Re = 1 \cdot 10^5$ , AOA = 4 deg), 100k\_2 ( $Re = 1 \cdot 10^5$ , AOA = 2 deg) and 125k\_4 ( $Re = 1.25 \cdot 10^5$ , AOA = 4 deg) SD7062 low- $Re$ , isolated-airfoil cases, respectively. Figures 7.13, 7.14 and 7.15 present the  $C_F$  and  $C_P$  plots versus the non-dimensional position along the chord length,  $x/c$ , for the cases in the same order specified above. In these figures,  $C_F$  is presented at the left side and  $C_P$  at the right. There is no distinction between upper and lower surfaces.

Since it was observed in Section 5.2.3 that variations in the angle of attack seem to exert a stronger influence on the  $C_F$  and  $C_P$  distributions than variations in the Reynolds number, it was decided to select the cases trying to better match the AOA between the different cases rather than the  $Re$ .

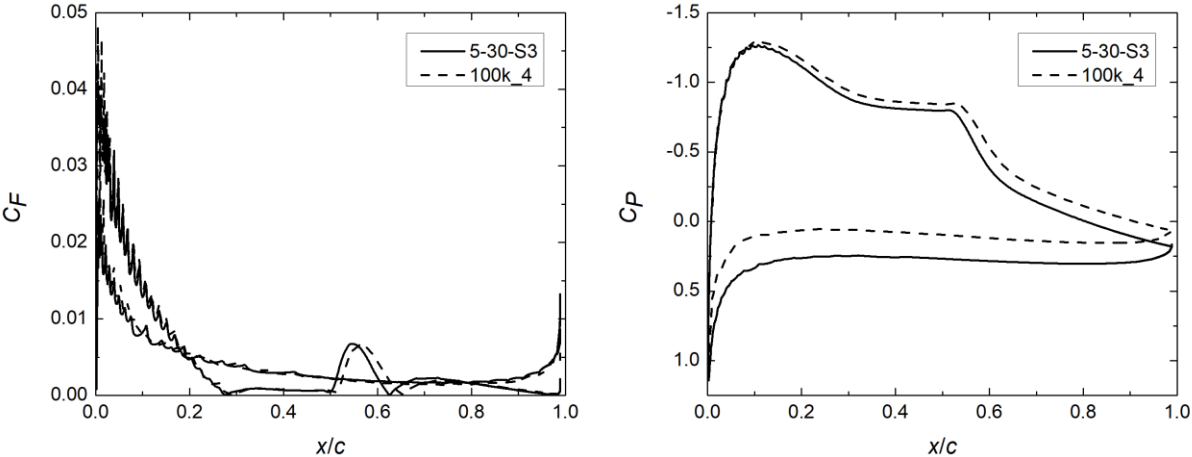


Figure 7.13 – Comparison between 5-30-S3 and 100k\_4, left:  $C_F$ , right:  $C_P$

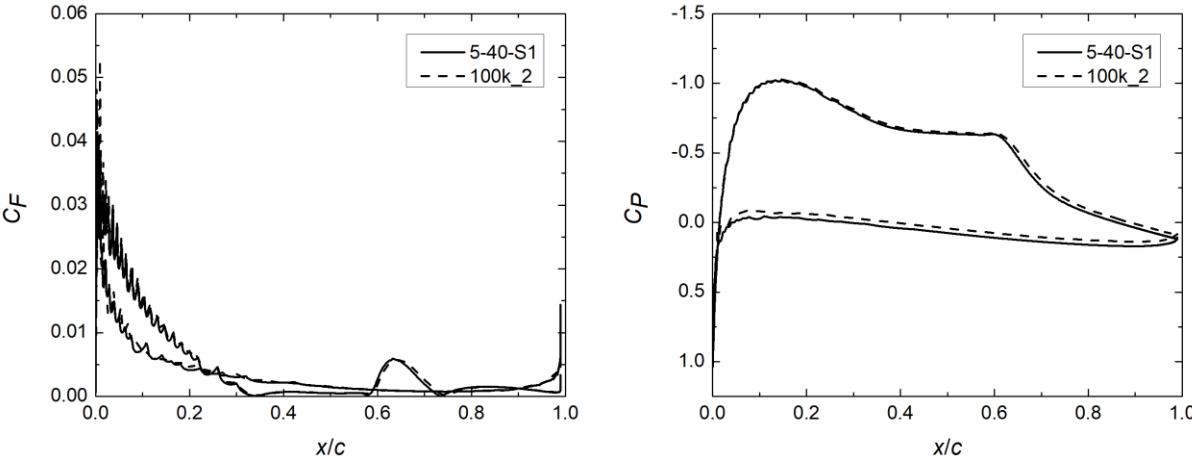


Figure 7.14 – Comparison between 5-40-S1 and 100k\_2, left:  $C_F$ , right:  $C_P$

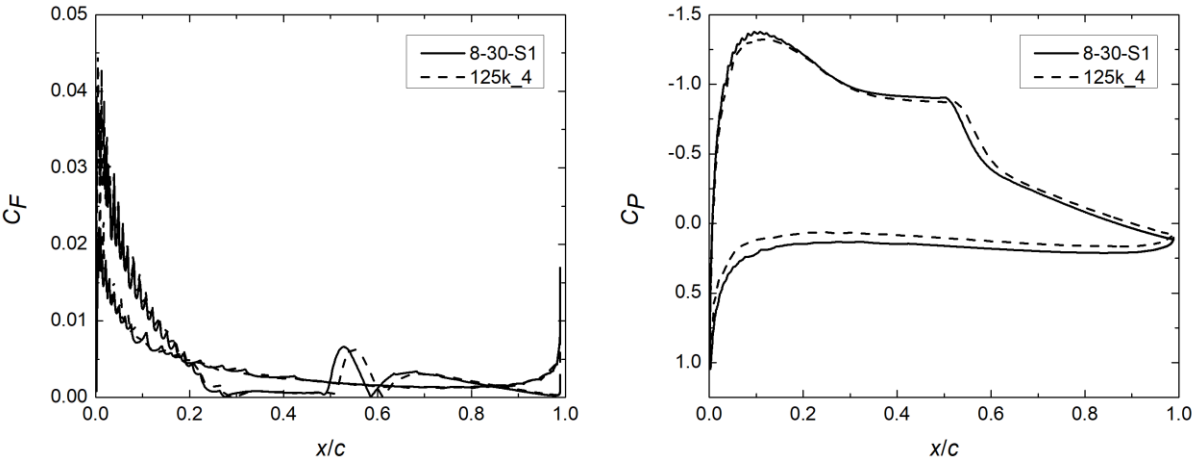


Figure 7.15 – Comparison between 8-30-S1 and 125k\_4, left:  $C_F$ , right:  $C_P$

Figures 7.13 to 7.15 show that the largest differences between cases involving solidity effects and isolated-airfoil cases appeared in the situations in which the angle of attack was 4 degrees. It is reflected especially in the position of the laminar separation bubble and in the magnitudes in the  $C_P$  distributions. For every case, this effect is more prominent on the lower surface, although some differences can be spotted on the upper surface as well, where they can be attributed mainly to the presence of the LSB. For the lower surface, this difference can be related to the effects of high solidity, which can be reinforced by the largest differences having been detected in the S3 case. Pressure on the lower surface increased in all cases, which is a desirable situation that leads to an increase in lift as well. The S3 case was the only one that saw a significant increase in  $C_P$  on the upper surface, but it was not enough to compromise the lift-to-drag ratio. In fact,  $L/D$  increased, as can be seen further ahead from table 7.4.

When  $C_F$  is analyzed, it can be seen that the cases under comparison did not show considerable differences, except for the displacement of the bubble towards the leading edge verified in the solidity cases. It should be emphasized, however, that these differences can be more strongly related to the differences in  $Re$  and AOA between the situations evaluated than solidity effects, for it is recommended that further assessments be made without significant differences in the abovementioned parameters.

In order to complement the  $C_F$  and  $C_P$  analyses, a comparison between lift and drag coefficients for the selected cases is presented. Table 7.4 summarizes the  $C_L$ ,  $C_D$  and  $L/D$  values for the six cases.

Table 7.4 – Lift and drag comparisons between solidity cases and their isolated-airfoil counterparts

Label	5-30-S3	100k_4	5-40-S1	100k_2	8-30-S1	125k_4
$C_L$	0.848	0.749	0.576	0.559	0.824	0.769
$C_D$	0.0254	0.0267	0.0214	0.023	0.021	0.023
$L/D$	33.38	28.0	26.92	24.3	39.24	33.4

All solidity cases showed higher lift coefficients and lower drag coefficients when compared with their respective isolated-airfoil cases, which, in consequence, resulted in more favorable lift-to-drag ratios. Although it is not possible to ensure that these effects are due

only to solidity, the results presented so far show considerable differences that can hardly be attributed only to the differences in angle of attack and Reynolds numbers.

Plots of  $C_F$  and  $C_P$  for all the 45 solidity cases are presented in Appendix B. As with the isolated-airfoil cases shown in Appendix A, the 45 cases are presented individually. Once again, solid lines will represent data for the upper surfaces, while dashed lines will show values for the lower surfaces.

## 8 CONCLUSIONS

A study on the aerodynamic performance of two-dimensional airfoils subject to the combined effects of low-Reynolds flows and high local rotor solidity was carried out. Since the main focus was the aerodynamic performance of airfoils under typical operating conditions of small horizontal-axis wind turbines, the basics of aerodynamics were presented, followed by a review covering history and development of airfoils designed to operate at low Reynolds numbers (typically accepted to be below 500,000). The review also covered efforts in numerical modeling of low- $Re$  boundary-layer flow as well as usual issues in small HAWT operation, such as starting performance, solidity effects and stall delay.

Wind turbine theory was summarized, starting from the classic Betz calculations from the 1920's and covering the derivation of the Blade Element Theory and Blade Element-Momentum Theory. Known simplifications and shortcomings of these two theories were highlighted, as well as later efforts to expand them to cover more realistic operating conditions. This was followed by an exposition of the numerical methods in fluid flow simulation, focusing on the expected operating range of 2D airfoil sections.

A methodology of airfoil simulation was then introduced. It covered airfoil modeling, grid construction and numerical methods that would be employed. The approach was validated using the NACA 0012 and the S809 airfoils, both subject to high-Reynolds flows as they had their numerical results compared with experimental data available in the literature. This stage also provided the chance to compare two turbulence models: the well known and tested SST  $k-\omega$  and the newer, four-equation  $\gamma-Re_0$ . Since all simulations were carried out using the ANSYS Fluent commercial code, the  $\gamma-Re_0$  is referred to as the Transition SST model. Numerical results for the NACA 0012 have shown good agreement to experimental data for the lift coefficient by both turbulence models, whereas results for the drag coefficient fell short of expectations. Transition SST yielded results closer to the data available for comparison than SST  $k-\omega$  as it was initially expected. The S809 airfoil simulations were run using the Transition SST model only, and  $C_L$  and  $C_D$  results again have shown mixed accuracy. Pressure coefficient plots were then extracted, and this data showed much closer agreement with the available wind-tunnel data.

Results for 20 computational runs using the SD7062 airfoil were then presented. Unlike the previous simulations, all cases involved five low- $Re$  situations, ranging from 25,000 to 125,000. Each one was simulated for 4 AOA configurations, from 0 to 6 degrees.

While experimental data within the intended range was available for  $Re = 100,000$  only, these runs allowed to visualize and measure the laminar separation bubble, how it behaved under different airfoil operating conditions and its effects on the airfoil's performance. Plots of pressure coefficient and (especially) skin friction coefficient provided a valuable insight on the characteristics of low- $Re$  boundary layers.

These efforts had the purpose of generating knowledge to help on the design of a new small wind turbine intended to operate in dense urban environments. The project is a joint effort by the Mechanical and Electrical Engineering departments at UFRGS and is in its initial phases. Preliminary design constraints point for a 5-blade, 0.75-meter rotor optimized to operate at a rated tip speed ratio of 4 when under a free-stream wind velocity of 11 m/s. The SD7062 was then used as the base airfoil to this design, and the Small Wind Turbine Design Code (SWRDC) was employed to yield a blade design optimized for such conditions. The code uses the blade element method to evaluate aerodynamic characteristics of new blade designs while searching for the best blade shapes making use of genetic algorithms and artificial neural networks. A final blade design then emerged and three sections of it were selected to be simulated in an analysis combining low Reynolds numbers and solidity effects. The blade sections selected were the ones that more closely represent local rotor solidities of 0.1, 0.2 and 0.3.

Finally, these three blade sections were then used in simulations configured to represent 15 different operating conditions, involving combined changes in tip speed ratio and free-stream wind velocity, yielding a total of 45 situations. All of these situations were set up to allow the modeling of adjacent blade interactions and how they affect the flow between them. Results have shown that the laminar separation bubble tends to move upstream with independently increasing solidity, angle of attack or Reynolds number, although the latter causes an effect not as strong as the former two parameters. This trend was clearly evidenced by the  $C_F$  plots. The  $C_P$  plots revealed that pressure over both sides of the airfoil tends to increase with increasing solidity. While it is positive on the lower surface, it has potential to cause an undesirable effect on the upper surface. This has shown to be overall beneficial, though, as all cases saw increase in lift and decrease in drag, thus yielding a more favorable lift-to-drag ratio.

## 8.1 Advice for future work

Since the simulations involving solidity were configured to represent actual operating conditions of a specific blade design, each case had its specific Reynolds number and angle of attack as a result. This posed an obstacle on comparisons with isolated-airfoil cases, except for three cases for which  $Re$  and AOA configurations most closely matched those of solidity cases. Thus, as an advice for further studies, it is recommended that solidity cases be configured to match the operating conditions of isolated-airfoil cases in order to allow direct comparisons between what is expected to be result of high rotor solidity and what is not.

The blade used in the present work, which has a local solidity of nearly 2.0 at the root, was designed to yield an elevated  $C_{pwr}$  value at a low TSR. Although in this case the SWRDC optimization code was left free to define the maximum root chord length, it is possible to limit this variable if achieving lower solidity values is desired or necessary. On the other hand, if the Betz blade design methodology would be used exclusively, it would result in chord lengths near the root even larger than those presented in chapter 6. As a consequence, it is advised that three-dimensional numerical studies be conducted, in which flows around different blades can be compared. Thus, local and global solidity effects can be assessed in environments that do not impose boundary conditions as restrictive as those imposed by the two-dimensional approach.

It is also suggested to expand the CFD approach to evaluate the effects of low- $Re$  flows combined with other phenomena usually experienced by wind turbine blades, such as rotational effects, stall delay, starting performance, or combinations thereof.

## 8.2 Afterword

The author hopes that this thesis will contribute in the discussion of wind turbine operation specific to low- $Re$  small rotors by making use of modern tools and concepts. It is believed that this work reached its goals and presented an academic approach to a practical engineering situation that was able to confirm the trends shown by experimental studies and by the literature as a whole. In addition, the choice and implementation of the computational tools allowed modeling with a good level of detail the many complex phenomena involved in fluid flow.

## BIBLIOGRAPHY

Aftab, S. M. A.; Mohd Rafie, A. S.; Razak, N. A.; Ahmad, K. A. Turbulence Model Selection for Low Reynolds Number Flows. **Open access**, 2016.

Ahmed, N.; Yilbas, B. S.; Budair, M. O. Computational Study into the Flow Field Developed Around a Cascade of NACA 0012 Airfoils. **Computer Methods in Applied Mechanics and Engineering**, n. 167, p. 17-32, 1998.

Alam, M.; Sandham, N. D. Direct Numerical Simulation of 'Short' Laminar Separation Bubbles with Turbulent Reattachment. **Journal of Fluid Mechanics**, Cambridge, v. 410, p. 1-28, 2000.

Amano, R. S.; Malloy, R. J. CFD Analysis on Aerodynamic Design Optimization of Wind Turbine Rotor Blades. **World Academy of Science, Engineering and Technology**, n. 60, p. 71-75, 2009.

Anderson Jr., J. D. **Fundamentals of Aerodynamics**. 3rd. ed. McGraw-Hill, New York, 2001.

ANSYS. **ANSYS FLUENT 12.0 Theory Guide**. ANSYS, Inc. Canonsburg, 2009.

Beck, P. A. Análise Metodológica de Simulações de Escoamentos Turbulentos sobre Seções de Perfis Aerodinâmicos. **Dissertação de mestrado, Universidade Federal do Rio Grande do Sul**, Porto Alegre, 2010.

Burton, T.; Sharpe, D.; Jenkins, N.; Bossanyi, E. **Wind Energy Handbook**. John Wiley & Sons, Chichester, 2001.

Clausen, P. D.; Piddington, D. M.; Wood, D. H. An Experimental Investigation of Blade Element Theory for Wind Turbines. Part 1. Mean Flow Results. **Journal of Wind Engineering and Industrial Aerodynamics**, Amsterdam, n. 25, p. 189-206, 1987.

Clausen, P. D.; Wood, D. H. Research and Development Issues for Small Wind Turbines. **Renewable Energy**, v. 16, p. 922-927, 1999.

Counsil, J. N. N.; Goni Boulama, K. Validating the URANS Shear Stress Transport  $\gamma$ - $Re\theta$  Model for Low-Reynolds-Number External Aerodynamics. **International Journal for Numerical Methods in Fluids**, v. 69, p. 1411-1432, 2012.

Devinant, P.; Laverne, T.; Hureau, J. Experimental Study of Wind-turbine Airfoil Aerodynamics in High Turbulence. **Journal of Wind Engineering and Industrial Aerodynamics**, n. 90, p. 689-707, 2002.



Dixon, S. L.; Hall, C. A. **Fluid Mechanics and Thermodynamics of Turbomachinery**. 6th. ed. Butterworth-Heinemann, Burlington, 2010.

Drela, M. **XFOIL: An Analysis and Design System for Low Reynolds Number Airfoils**. MIT Dept. of Aeronautics and Astronautics. Cambridge. 1989.

Duquette, M. M.; Visser, K. D. Numerical Implications of Solidity and Blade Number on Rotor Performance of Horizontal-Axis Wind Turbines. **Journal of Solar Energy Engineering**, v. 125, p. 425-432, 2003.

Ebert, P. R.; Wood, D. H. Observations of the Starting Behaviour of a Small Horizontal-Axis Wind Turbine. **Renewable Energy**, v. 12, No. 3, p. 245-257, 1997.

Eppler, R. **Eppler Airfoil Design and Analysis Code**. Stuttgart. c.2000.

Eppler, R.; Somers, D. M. **A Computer Program for the Design and Analysis of Low-Speed Airfoils**. **NASA TM-80210**. National Aeronautics and Space Administration. Hampton. 1980.

Fagbenro, K. A.; Mohamed, M. A.; Wood, D. H. Computational Modeling of the Aerodynamics of Windmill Blades at High Solidity. **Energy for Sustainable Development**, n. 22, p. 13-20, 2014.

Fox, R.; McDonald, A.; Pritchard, P. **Introduction to Fluid Mechanics**. 6. Ed. John Wiley & Sons. New York. 2004.

Galbraith, M. C. Implicit Large Eddy Simulation of Low-Reynolds-Number Transitional Flow Past the SD7003 Airfoil. **Thesis for obtaining the degree of Masters of Science. University of Cincinnati**, 2009.

Garré, S. O.; Paula, A. V.; Luz, J. L. R.; Vecina, T. D. J.; Petry, A. P. Experimental Evaluation of the Aerodynamic Performance of Small Wind Turbines Confectioned in 3D Prototyping. **Engenharia Térmica (Thermal Engineering)**, v. 15, n. 2, p. 15-23, 2016.

Gasch, R.; Twele, J. **Wind Power Plants: Fundamentals, Design, Construction and Operation**. Solarpraxis AG, Berlin, 2002.

Giannakoglou, K. C. Design of Optimal Aerodynamic Shapes using Stochastic Optimization Methods and Computational Intelligence. **Progress in Aerospace Sciences**, n. 38, p. 43-76, 2002.

Giguère, P.; Selig, M. S. Low Reynolds Number Airfoils for Small Horizontal Axis Wind Turbines. **Wind Engineering**, v. 21, n. 6, p. 367-380, 1997.

Giguère, P.; Selig, M. S. **New Airfoils for Small Horizontal Axis Wind Turbines**. Dept. of Aeronautical and Astronautical Engineering, University of Illinois at Urbana-Champaign. [S.l.]. 1998.

Guerri, O.; Bouhadeh, K.; Harhad, A. Turbulent Flow Simulation of the NREL S809 Airfoil. **Wind Engineering**, v. 30, p. 287-302, 2006.

GWEC. **Global Wind Statistics 2016**. Global Wind Energy Council (GWEC). Brussels. 2017.

Hand, M.; Simms, D.; Fingersh, L.; Jager, D.; Cotrell, J.; Schreck, S.; Larwood, S. **Unsteady Aerodynamics Experiment Phase VI: Wind Tunnel Test Configurations and Available Data Campaigns**. National Renewable Energy Laboratory. Golden. 2001.

Hegna, H. A. Numerical Solution of Incompressible Turbulent Flow over Airfoils near Stall. **AIAA Journal**, v. 20, No. 1, p. 29-30, January 1982.

IEC 61400-2. Norma técnica, International Electrotechnical Commission. Geneva. 2006.

Ivanell, S. **Numerical Computations of Wind Turbine Wakes**. Gotland University. Stockholm. 2009.

Jacobs, E. N.; Ward, K. E.; Pinkerton, R. M. **The Characteristics of 78 Related Airfoil Sections from Tests in the Variable-Density Wind Tunnel**. National Advisory Committee for Aeronautics. [S.l.]. 1933.

Joselin Herbert, G.; Iniyar, S.; Sreevalsan, E.; Rajapandian, S. A Review of Wind Energy Technologies. **Renewable and Sustainable Energy Reviews**, v. 11, p. 1117-1145, 2007.

Konak, A.; Coit, D. W.; Smith, A. E. Multi-Objective Optimization Using Genetic Algorithms: A Tutorial. **Reliability Engineering and System Safety**, n. 91, p. 922-1007, 2006.

Ladson, C. L. **Effects of Independent Variation of Mach and Reynolds Numbers on the Low-Speed Aerodynamic Characteristics of the NACA 0012 Airfoil Section**. NASA TM 4074. [S.l.]. 1988.

Langtry, R. B. A Correlation-Based Transition Model using Local Variables for Unstructured Parallelized CFD Codes. **Thesis for obtaining the degree of Dr.-Ing., Universität Stuttgart**, 2006.

Lian, Y.; Shyy, W. **Laminar-Turbulent Transition of a Low Reynolds Number Rigid or Flexible Airfoil**. 36th AIAA Fluid Dynamics Conference and Exhibit. San Francisco: AIAA. 2006.

Lyon, C. A.; Broeren, A. P.; Giguère, P.; Gopalarathnam, A.; Selig, M. S. **Summary of Low-Speed Airfoil Data**. SoarTech Publications, Virginia Beach, v. 3, 1997.

Malan, P.; Suluksna, K.; E., J. **Calibrating the  $\gamma$ -Re $\theta$  Transition Model for Commercial CFD**. 47th AIAA Aerospace Sciences Meeting Including the New Horizons Forum and Aerospace Exposition. Orlando: AIAA. 2009.

Maliska, C. **Transferência de Calor e Mecânica dos Fluidos Computacional**. 2. ed. LTC, Rio de Janeiro, 2004.

Manwell, F.; McGowan, J.; Rogers, A. **Wind Energy Explained: Theory, Design and Application**. John Wiley & Sons, Chichester, 2002.

Mayer, C.; Bechly, M. E.; Hampsey, M.; Wood, D. H. The Starting Behaviour of a Small Horizontal-Axis Wind Turbine. **Renewable Energy**, v. 22, p. 411-417, 2001.

McCrink, M. H.; Gregory, J. W. **Blade Element Momentum Modeling of Low-Re Small UAS Electric Propulsion Systems**. 33rd AIAA Applied Aerodynamics Conference. Dallas: AIAA. 2015.

McCroskey, W. J. **A Critical Assessment of Wind Tunnel Results for the NACA 0012 Airfoil**. NASA Technical Memorandum 100019. Moffett Field. 1987.

Menter, F. R.; Kuntz, M.; Langtry, R. Ten Years of Industrial Experience with the SST Turbulence Model. **Turbulence, Heat and Mass Transfer**, n. 4, 2003.

Mo, J.; Lee, Y. Numerical Simulation for Prediction of Aerodynamic Noise Characteristics on a HAWT of NREL Phase VI. **Journal of Mechanical Science and Technology**, v. 25, p. 1341-1349, 2011.

Möller, S.; Silvestrini, J. **Turbulência vol. 4**. Editora da ABCM, Porto alegre, 2004.

Nemec, M.; Zingg, D. W. Newton-Krylov Algorithm for Aerodynamic Design Using the Navier-Stokes Equations. **AIAA Journal**, v. 40, n. 6, p. 1146-1154, 2002.

Nemec, M.; Zingg, D. W. Multipoint and Multi-Objective Aerodynamic Shape Optimization. **AIAA Journal**, v. 42, n. 6, p. 1057-1065, 2004.

Patankar, S. **Numerical Heat Transfer and Fluid Flow**. McGraw-Hill, New York, 1980.

Peigin, S.; Epstein, B. Robust Optimization of 2D Airfoils Driven by Full Navier-Stokes Computations. **Computers & Fluids**, n. 33, p. 1175-1200, 2004.

Ribeiro, A. F. P. Otimização e Dinâmica dos Fluidos Computacional Aplicadas a Turbinas Eólicas, Thesis for obtaining the Master's degree, Federal University of Rio Grande do Sul, 2012.

Ribeiro, A. F. P.; Awruch, A. M. An Airfoil Optimization Technique for Wind Turbines. **Applied Mathematical Modelling**, n. 36, p. 4898-4907, 2012.

Roache, P. J. Perspective: A Method for Uniform Reporting of Grid Refinement Studies. **Journal of Fluids Engineering**, v. 116, p. 405-413, 1994.

Schlichting, H. **Boundary Layer Theory**. 4. ed. McGraw Hill, New York, 1960.

Selig, M. S.; Donovan; Fraser. **Airfoils at Low Speeds**. H. A. Stokely, publisher, Virginia Beach, 1989.

Selig, M. S.; Guglielmo, J. J.; Broeren, A. P.; Giguère, P. **Summary of Low-Speed Airfoil Data**. SoarTech Publications, Virginia Beach, v. 1, 1995.

Selig, M. S.; Lyon, C. A.; Giguère, P.; Ninham, C. P.; Guglielmo, J. J. **Summary of Low-Speed Airfoil Data**. SoarTech Publications, Virginia Beach, v. 2, 1996.

Selig, M. S.; McGranahan, B. D. **Wind Tunnel Aerodynamic Tests of Six Airfoils for Use on Small Wind Turbines**. National Renewable Energy Laboratory. Golden. 2004.

Sessarego, M.; Wood, D. H. Multi-Dimensional Optimization of Small Wind Turbine Blades. **Renewables: Wind, Water and Solar**, n. (2:9), p. 1-11, 2015.

Shah, H.; Mathew, A.; Lim, C. M. Numerical Simulation of Flow Over an Airfoil for Small Wind Turbines using the  $\gamma$ -Re $\theta$  Model. **International Journal of Energy and Environment Engineering**, v. 6, p. 419-429, 2015.

Shepherd, D. G. Historical Development of the Windmill. In: SPERA, D. **Wind Turbine Technology: Fundamental Concepts of Wind Turbine Engineering**. 2. ed. New York: ASME, 2009.

Singh, R. K.; Raffiudin Ahmed, M. Blade Design and Performance Testing of a Small Wind Turbine Rotor for Low Wind Speed Applications. **Renewable Energy**, n. 50, p. 812-819, 2013.

Singh, R. K.; Raffiudin Ahmed, M.; Zullah, M. A.; Lee, Y. H. Design of a Low Reynolds Number Airfoil for Small Horizontal Wind Turbines. **Renewable Energy**, n. 42, p. 66-76, 2012.

Snel, H.; Schepers, J. Investigation and Modelling of Dynamic Inflow Effects. **EWEC '93 Conference**, Travemünde, 1993.

Somers, D. M. **Design and Experimental Results for the S809 Airfoil**. NREL/SR-440-6918. Golden. 1997.

Somers, D. M. **The S833, S834, and S835 Airfoils**. NREL/SR-500-36340. National Renewable Energy Laboratory. Port Matilda. 2005.

Suzuki, M.; Setoguchi, T.; Kaneko, K. Prediction of Cascade Performance of Circular-Arc Blades with CFD. **International Journal of Fluid Machinery and Systems**, v. 4, n. 4, p. 360-366, 2011.

Tangler, J. L.; Somers, D. M. **NREL Airfoil Families for HAWTs**. NREL/TP-442-7109. Golden. 1995.

van Ingen, J. L. **The eN Method for Transition Prediction. Historical Review of Work at TU Delft**. 38th Fluid Dynamics Conference and Exhibit. Seattle: AIAA. 2008.

Verdum, V. Projeto de Aerogerador com Segurança Inerente para Aplicação Urbana. **Thesis for obtaining the Master's degree, Federal University of Rio Grande do Sul**, 2013.

Vermeer, L.; Sorensen, J.; Crespo, A. Wind Turbine Wake Aerodynamics. **Progress in Aerospace Sciences**, v. 39, p. 467-510, 2003.

Versteeg, H.; Malalasekera, W. **An Introduction to computational fluid dynamics: The Finite Volume Method**. Longman Group Ltd, Harlow, 1995.

Wilcox, D. C. **Turbulence Modeling for CFD**. DCW Industries, Inc., La Cañada, 1994.

Williamson, G. A.; McGranahan, B. D.; Broughton, B. A.; Deters, R. W.; Brandt, J. B.; Selig, M. S. **Summary of Low-Speed Airfoil Data**. SoarTech Publications, Virginia Beach, v. 5, 2012.

Wolfe, W.; Ochs, S. CFD Calculations of S809 Aerodynamic Characteristics. **AIAA Journal**, n. 973, 1997.

Wood, D. H. A Three-Dimensional Analysis of Stall-Delay on a Horizontal-Axis Wind Turbine. **Journal of Wind Engineering and Industrial Aerodynamics**, n. 37, p. 1-14, 1991.

Wood, D. H. A Blade Element Estimation of the Cut-in Wind Speed of a Small Turbine. **Wind Engineering**, v. 25, No. 4, p. 249-255, 2001.

Wood, D. H. **Small Wind Turbines: Analysis, Design and Application**. Springer, London, 2011a.

Wood, D. H. Small Wind Turbines. In: SATHYAJITH, M.; GEETA, S. P. **Advances in Wind Energy Conversion Technology**. Berlin: Springer, 2011b. Ch. 8.

Wright, A. K.; Wood, D. H. The Starting and Low Wind Speed Behaviour of Small Horizontal Wind Turbines. **Journal of Wind Engineering and Industrial Aerodynamics**, n. 92, p. 1265-1279, 2004.

WWEA. **10th World Wind Energy Conference & Renewable Energy Exhibition Report**. World Wind Energy Association. Cairo. 2011.

WWEA. **Small Wind World Report 2012 Summary**. World Wind Energy Association. Husum. 2012.

Yan, H. Computational Modeling of Cascade Effect on Blade Elements with an Airfoil Profile. **Thesis for obtaining the degree of Master of Science. University of Calgary**, 2016.

## APPENDIX A – Individual $C_F$ and $C_P$ plots for the SD7062

In this appendix, plots for the pressure and skin friction coefficients from the simulations of the SD7062 airfoil in its isolated, low- $Re$  configuration are presented, as described in Section 5.2.3.

Each figure shows the plots for each  $Re$  and AOA configuration studied in the abovementioned Section, where  $C_F$  is at the left and  $C_P$  is at the right. Both  $C_F$  and  $C_P$  graphs bring results for the upper and lower surfaces in the same plot.

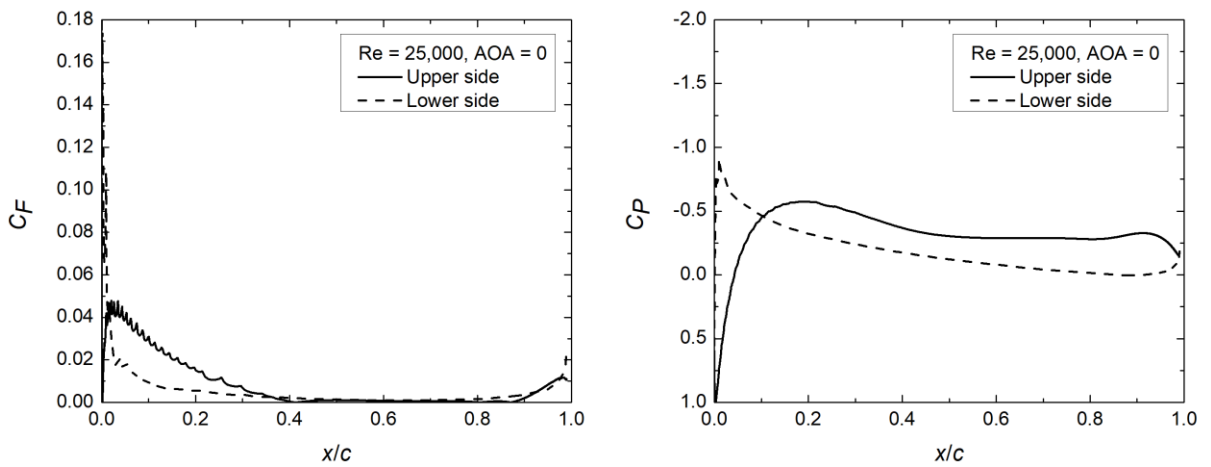


Figure A.1 – SD7062 results,  $Re = 25,000$ ,  $AOA = 0$  deg., left:  $C_F$ , right:  $C_P$

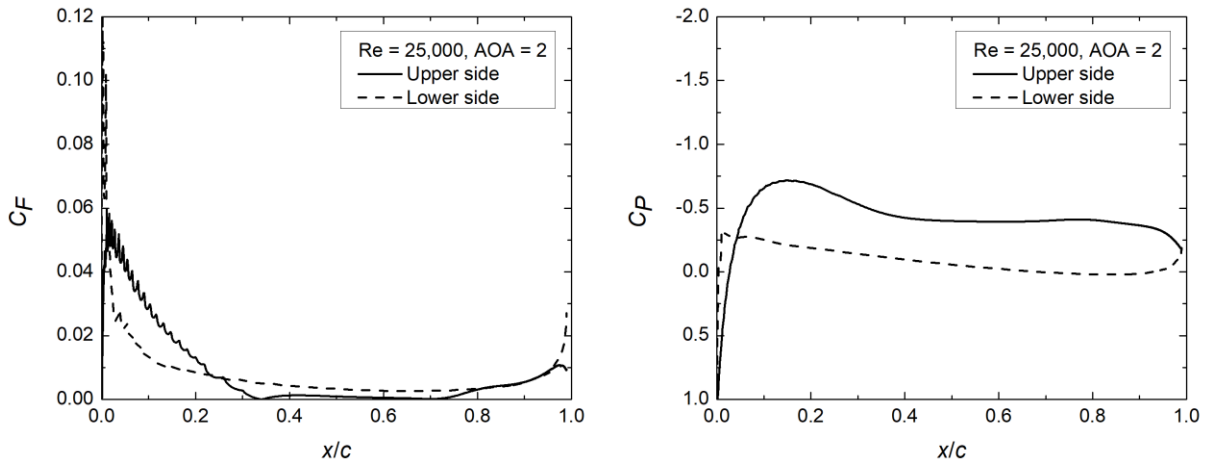


Figure A.2 – SD7062 results,  $Re = 25,000$ ,  $AOA = 2$  deg., left:  $C_F$ , right:  $C_P$

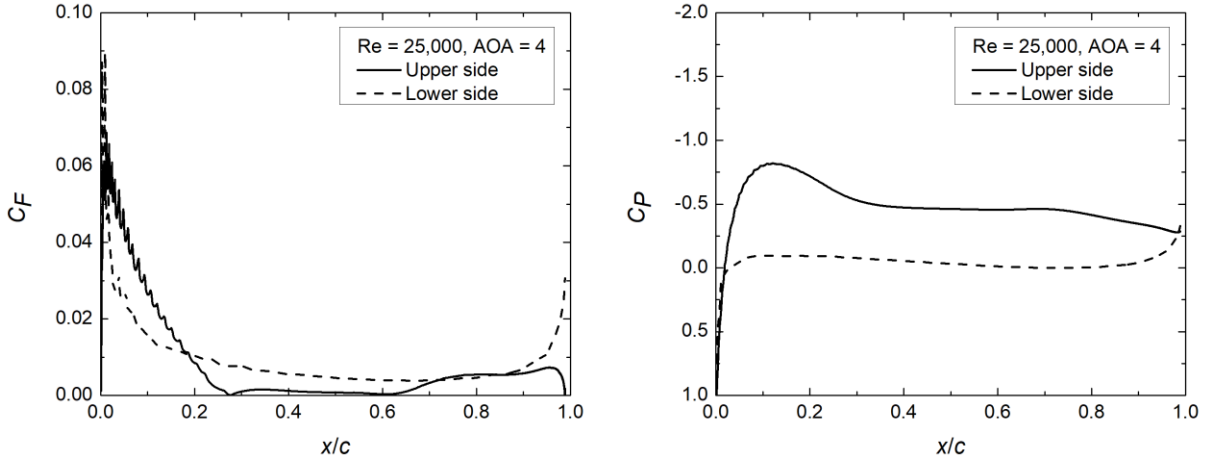


Figure A.3 – SD7062 results,  $Re = 25,000$ , AOA = 4 deg., left:  $C_F$ , right:  $C_P$

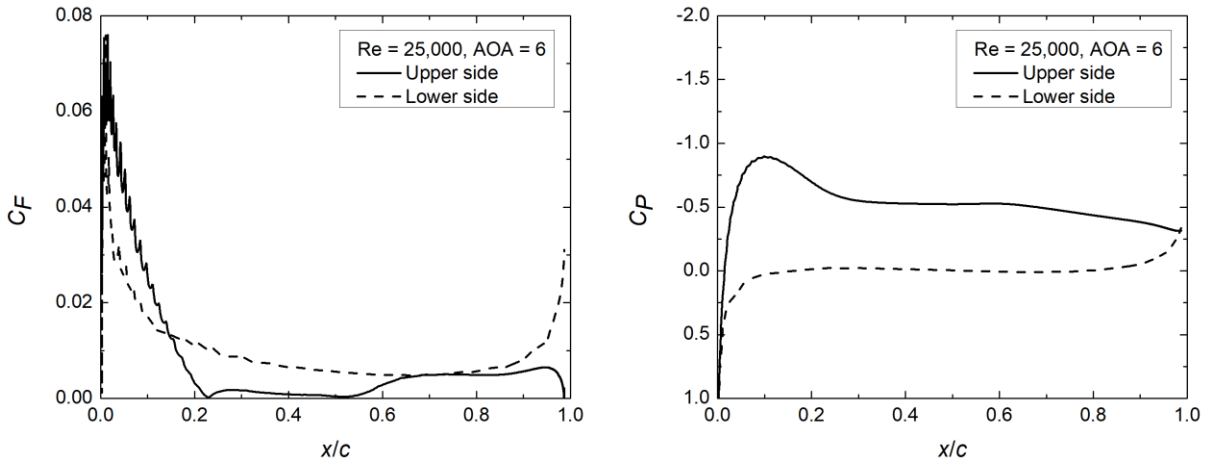


Figure A.4 – SD7062 results,  $Re = 25,000$ , AOA = 6 deg., left:  $C_F$ , right:  $C_P$

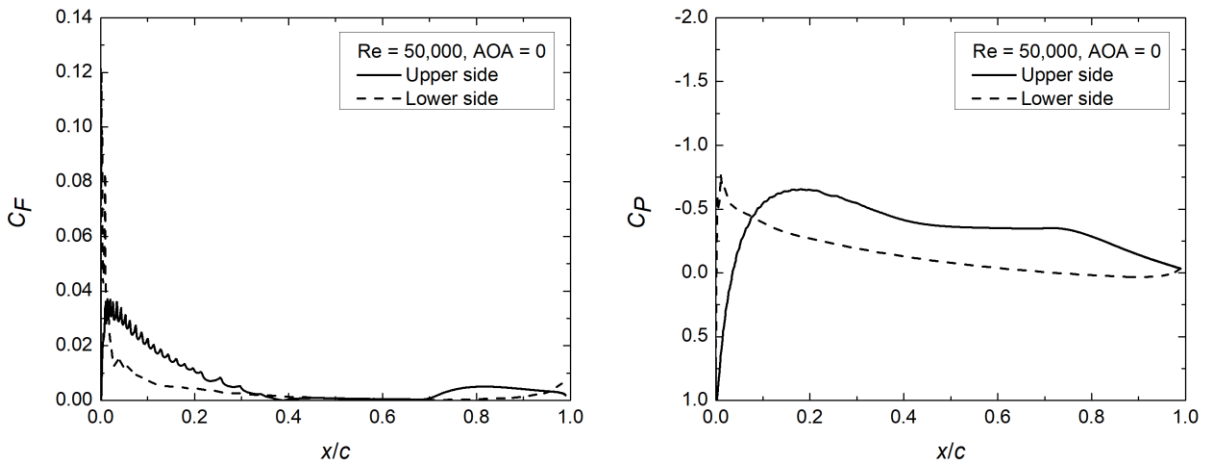


Figure A.5 – SD7062 results,  $Re = 50,000$ , AOA = 0 deg., left:  $C_F$ , right:  $C_P$



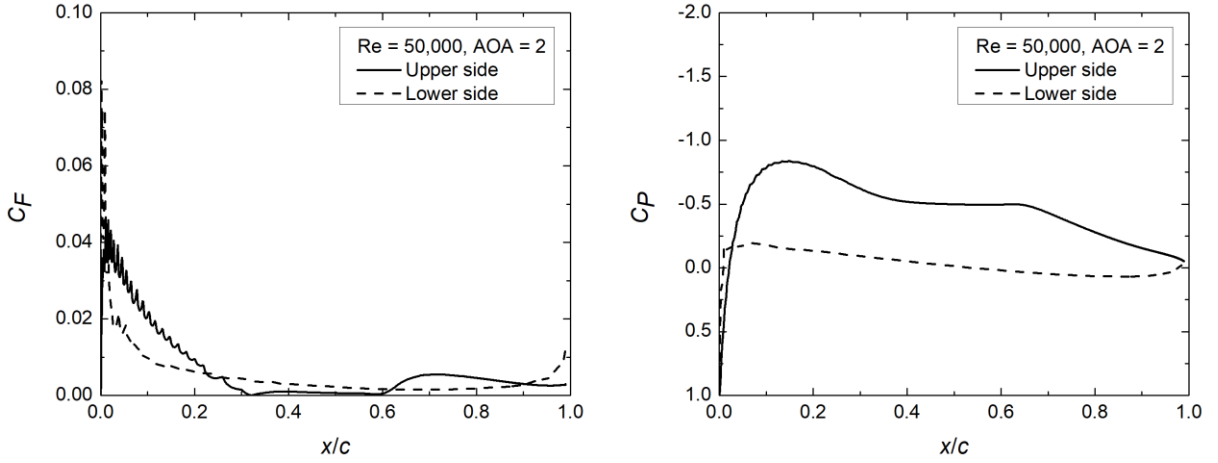


Figure A.6 – SD7062 results,  $Re = 50,000$ , AOA = 2 deg., left:  $C_F$ , right:  $C_P$

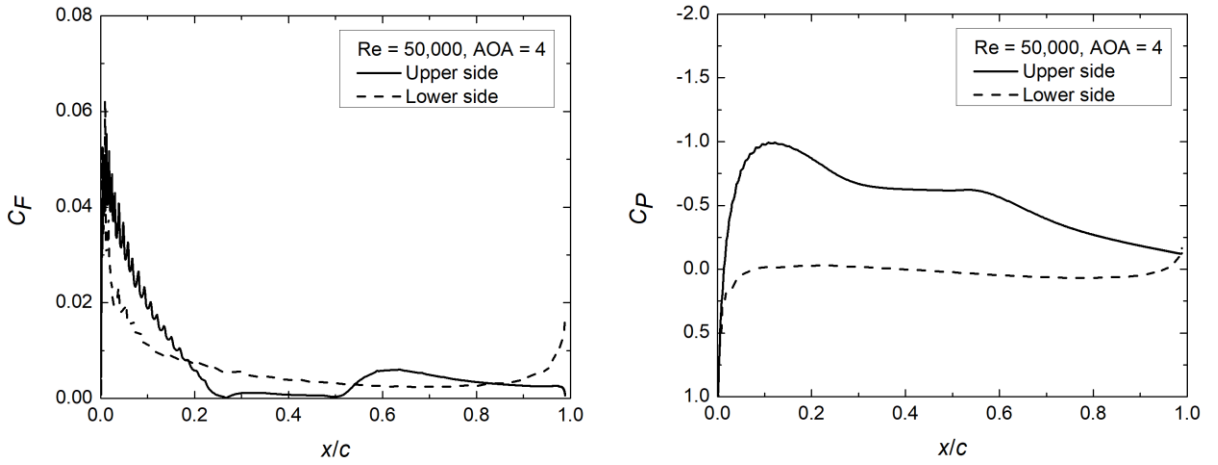


Figure A.7 – SD7062 results,  $Re = 50,000$ , AOA = 4 deg., left:  $C_F$ , right:  $C_P$

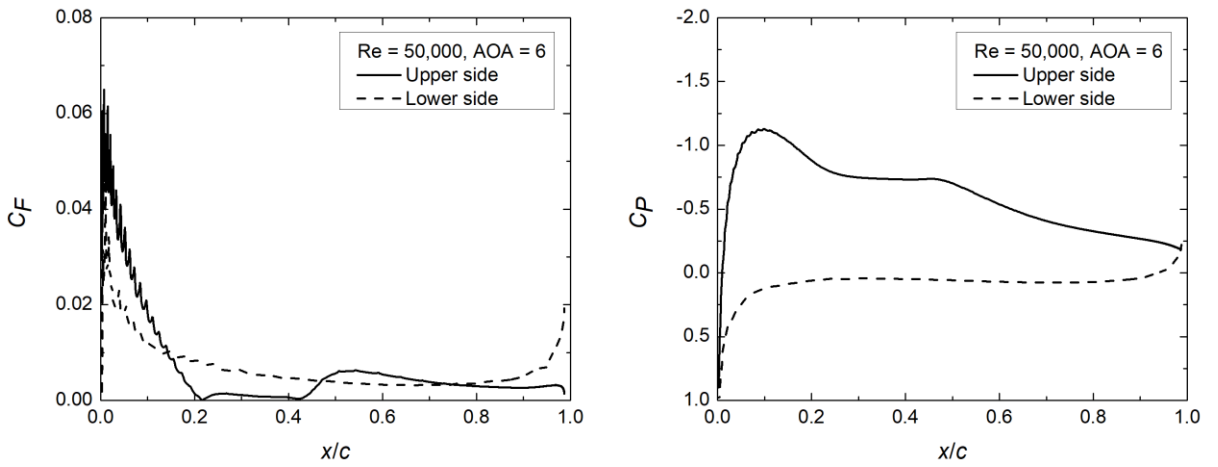


Figure A.8 – SD7062 results,  $Re = 50,000$ , AOA = 6 deg., left:  $C_F$ , right:  $C_P$

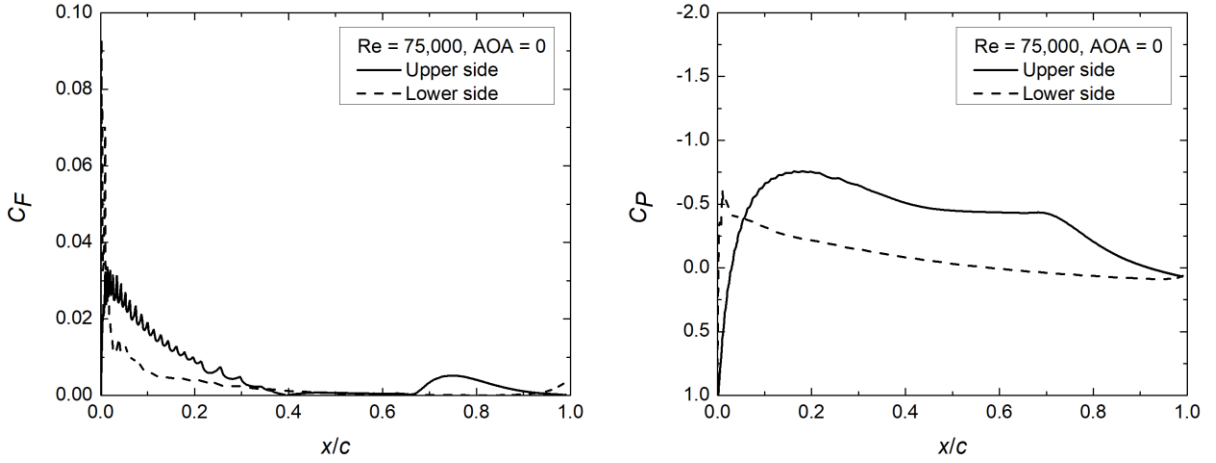


Figure A.9 – SD7062 results,  $Re = 75,000$ , AOA = 0 deg., left:  $C_F$ , right:  $C_P$

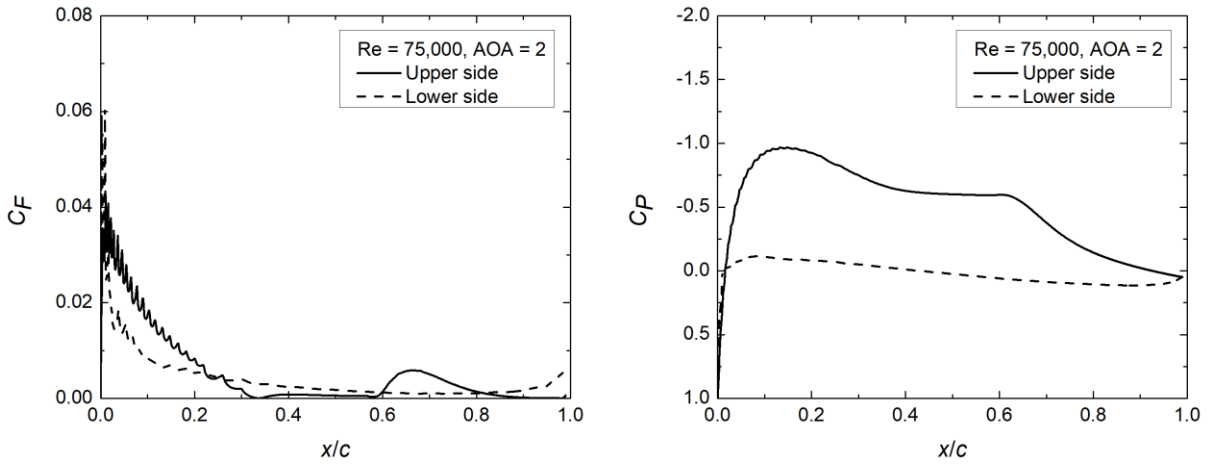


Figure A.10 – SD SD7062 results,  $Re = 75,000$ , AOA = 2 deg., left:  $C_F$ , right:  $C_P$

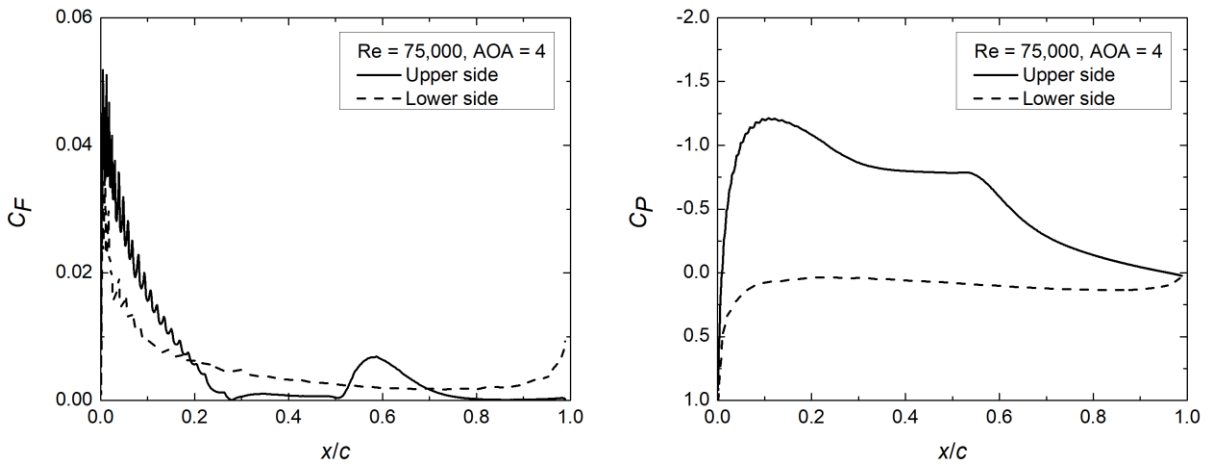


Figure A.11 – SD7062 results,  $Re = 75,000$ , AOA = 4 deg., left:  $C_F$ , right:  $C_P$

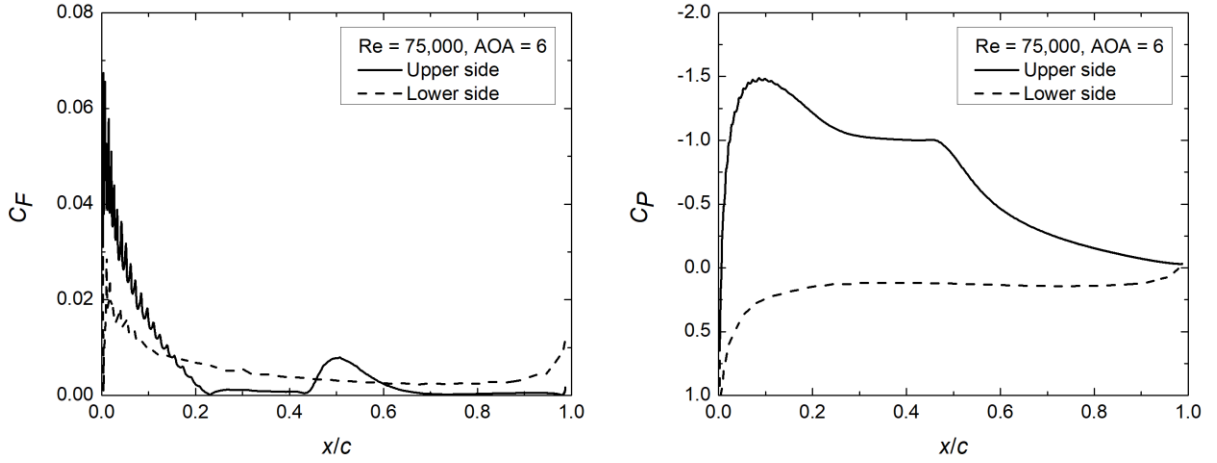


Figure A.12 – SD7062 results,  $Re = 75,000$ ,  $AOA = 6$  deg., left:  $C_F$ , right:  $C_P$

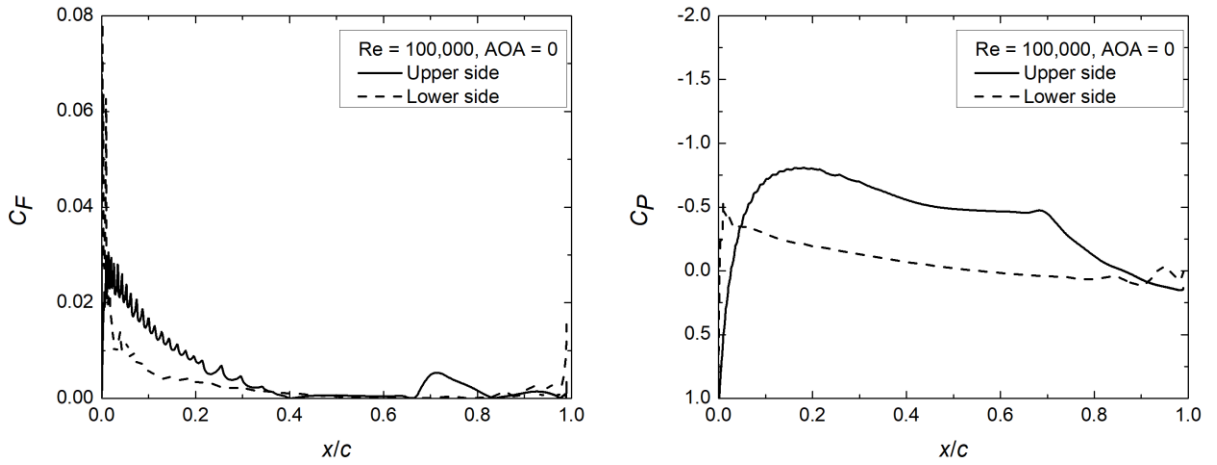


Figure A.13 – SD7062 results,  $Re = 100,000$ ,  $AOA = 0$  deg., left:  $C_F$ , right:  $C_P$

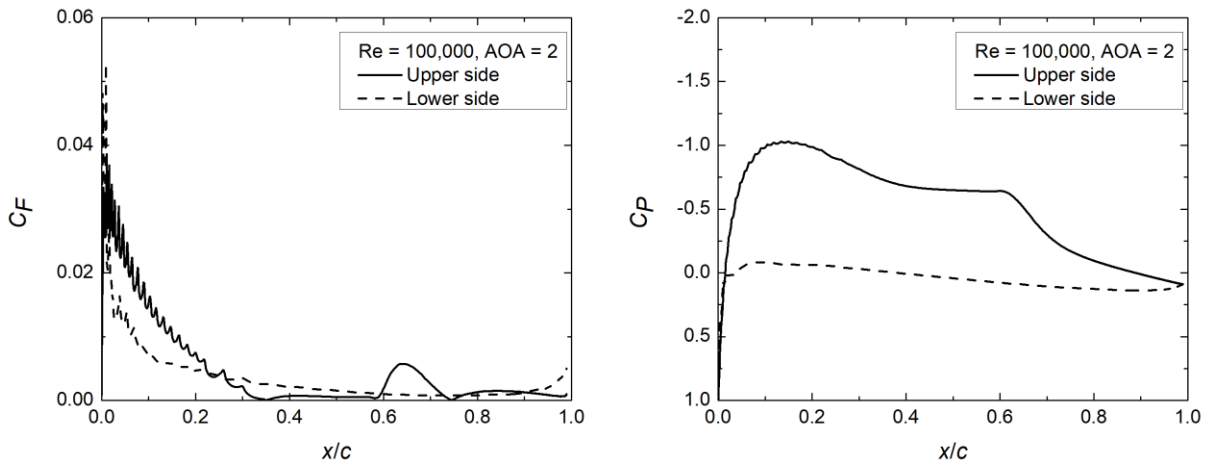


Figure A.14 – SD7062 results,  $Re = 100,000$ ,  $AOA = 2$  deg., left:  $C_F$ , right:  $C_P$

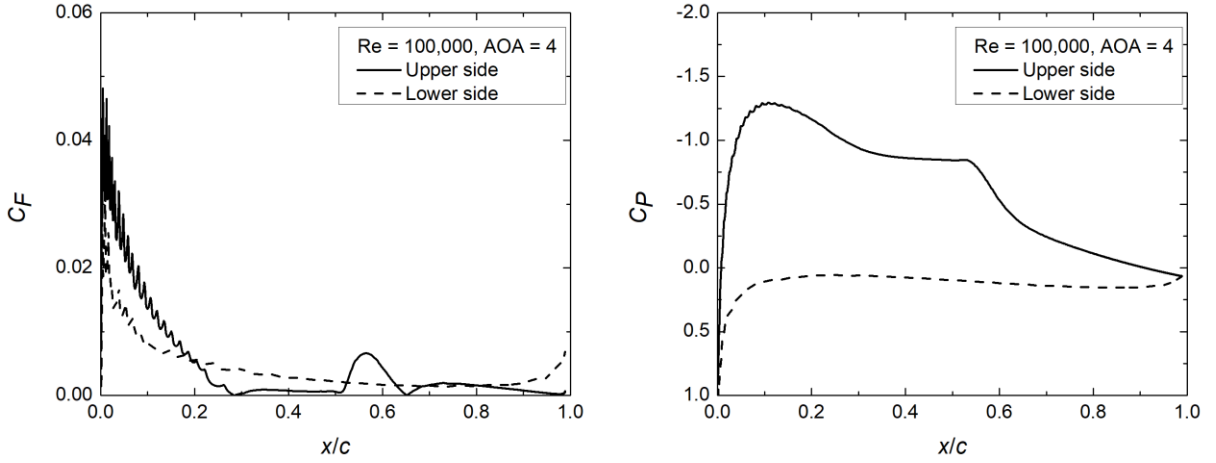


Figure A.15 – SD7062 results,  $Re = 100,000$ ,  $AOA = 4$  deg., left:  $C_F$ , right:  $C_P$

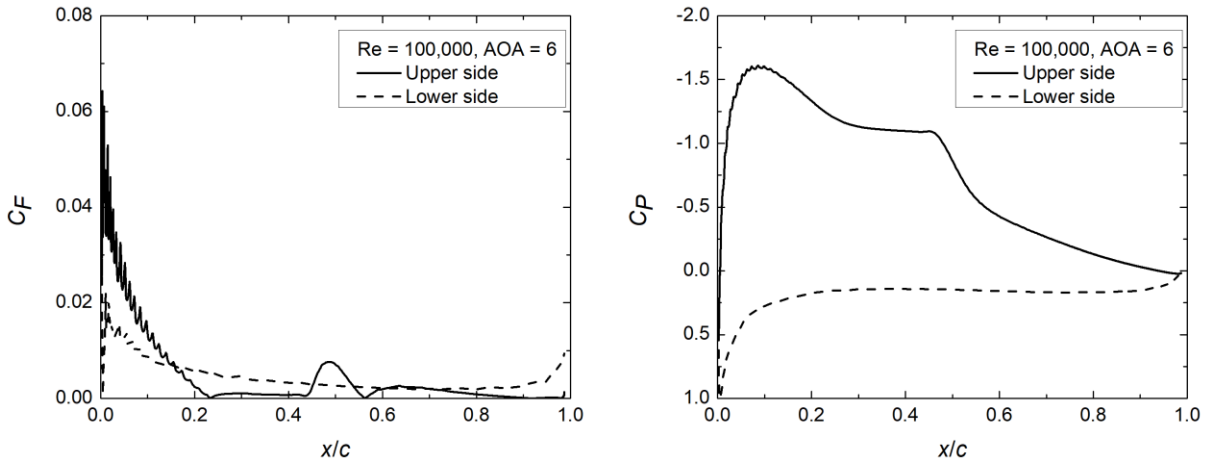


Figure A.16 – SD7062 results,  $Re = 100,000$ ,  $AOA = 6$  deg., left:  $C_F$ , right:  $C_P$

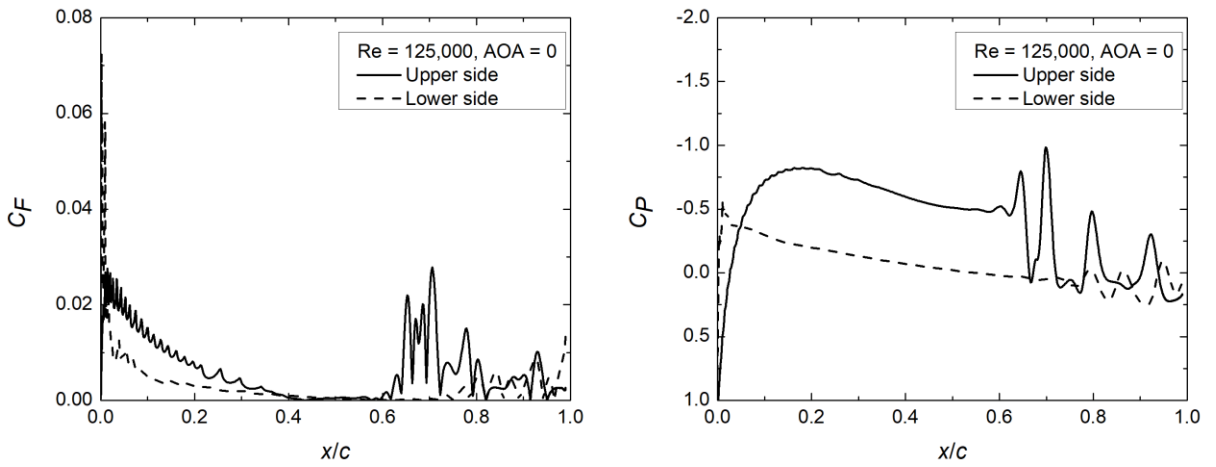


Figure A.17 – SD7062 results,  $Re = 125,000$ ,  $AOA = 0$  deg., left:  $C_F$ , right:  $C_P$

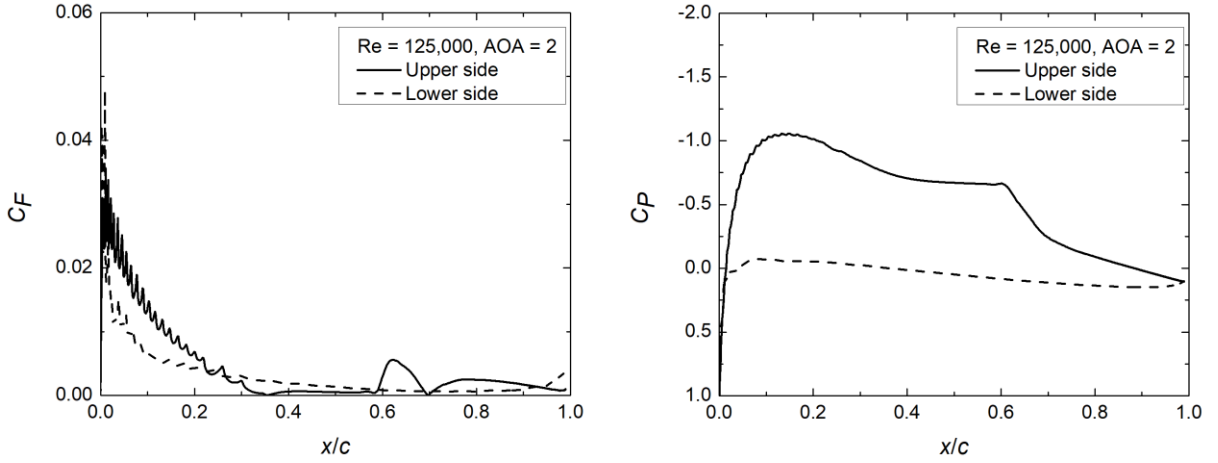


Figure A.18 – SD7062 results,  $Re = 125,000$ ,  $AOA = 2$  deg., left:  $C_F$ , right:  $C_P$

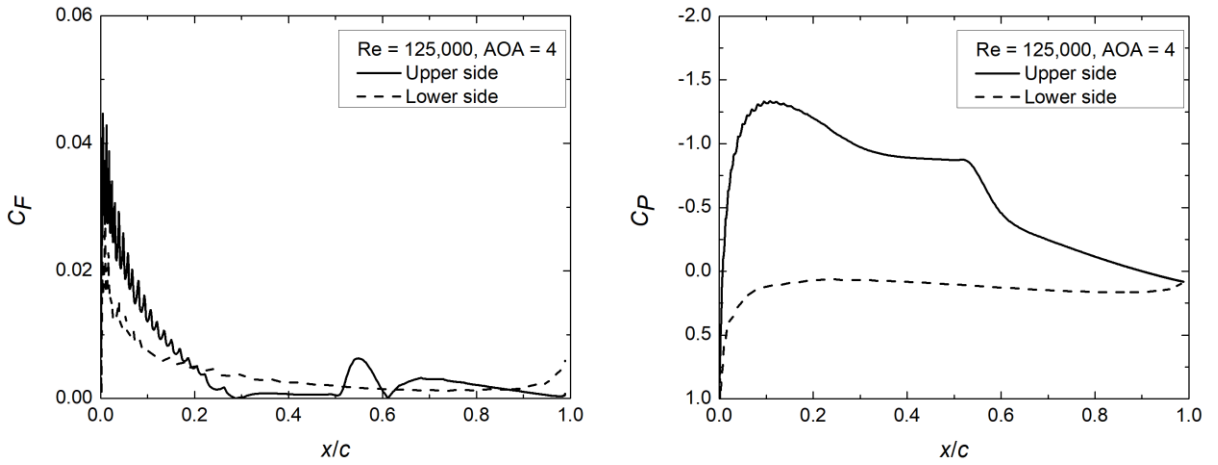


Figure A.19 – SD7062 results,  $Re = 125,000$ ,  $AOA = 4$  deg., left:  $C_F$ , right:  $C_P$

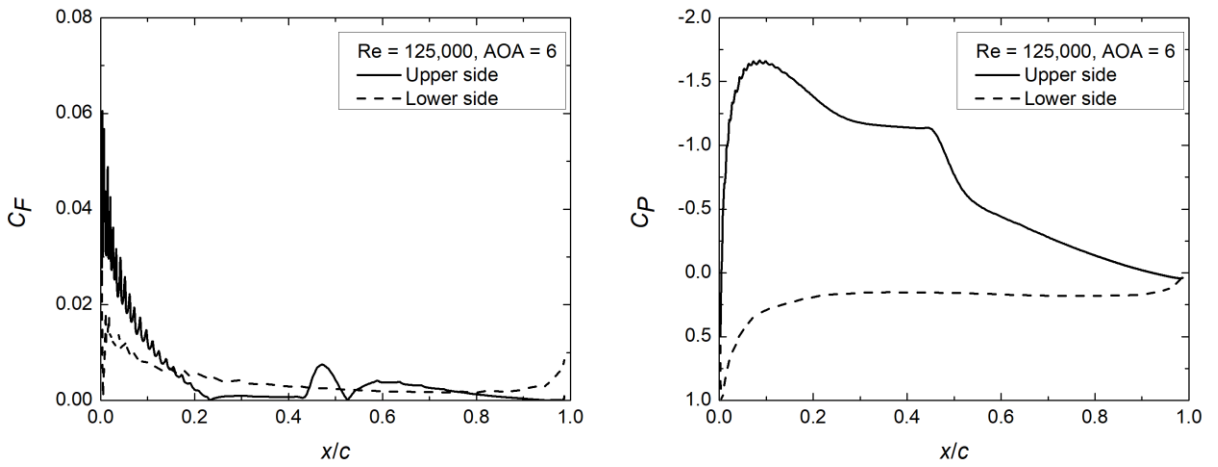


Figure A.20 – SD7062 results,  $Re = 125,000$ ,  $AOA = 6$  deg., left:  $C_F$ , right:  $C_P$

## APPENDIX B – Individual $C_F$ and $C_P$ plots for the solidity cases

In this appendix, individual plots for the pressure and skin friction coefficients from the simulations of the 45 solidity cases are presented, as described in Chapter 7.

Each figure shows the plots for each  $Re$  and AOA configuration studied in the abovementioned Chapter, where  $C_F$  is at the left and  $C_P$  is at the right. Both  $C_F$  and  $C_P$  graphs bring results for the upper and lower surfaces in the same plot.

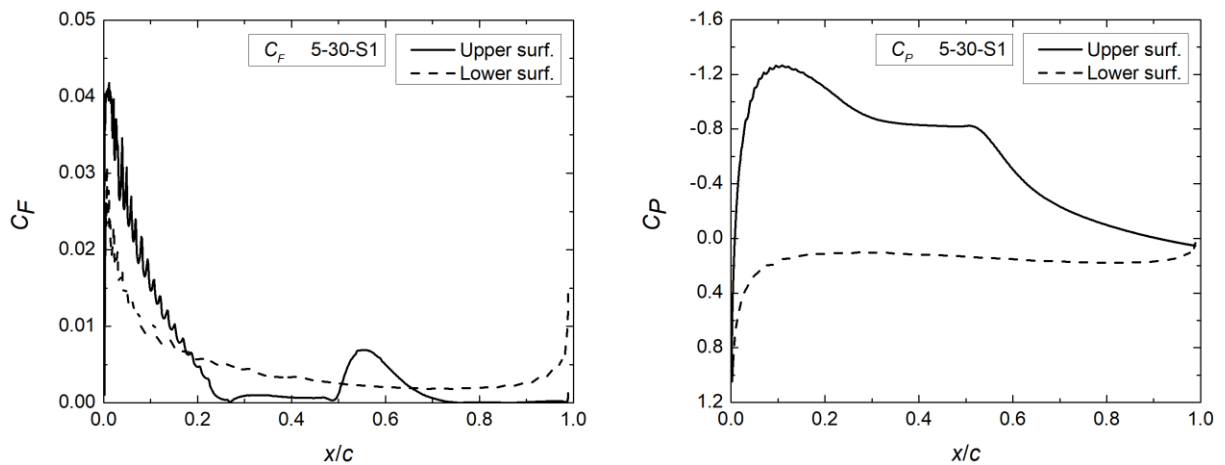


Figure B.1 – 5-30-S1 results, solidity = 0.1,  $u = 5$  m/s, TSR = 3.0, left:  $C_F$ , right:  $C_P$

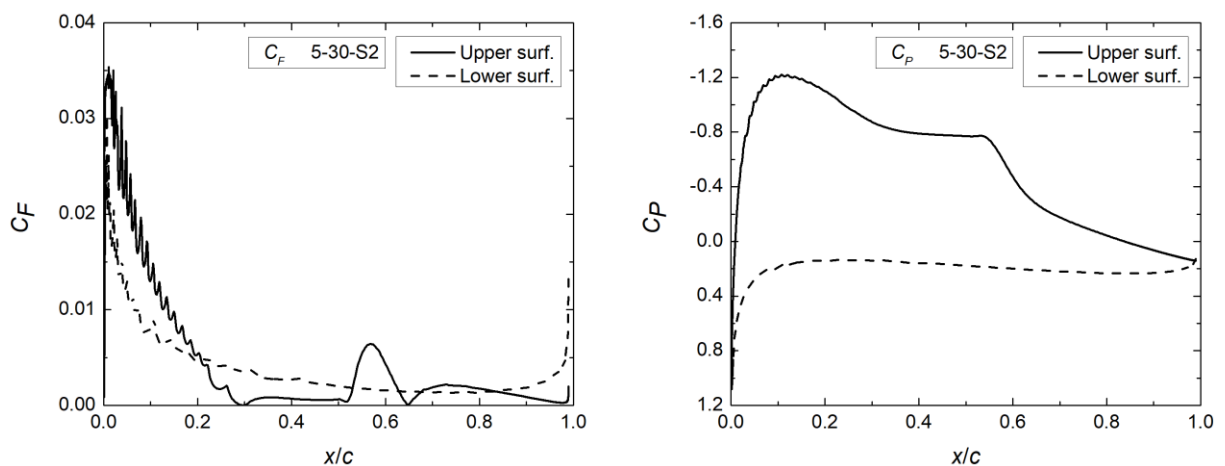


Figure B.2 – 5-30-S2 results, solidity = 0.2,  $u = 5$  m/s, TSR = 3.0, left:  $C_F$ , right:  $C_P$

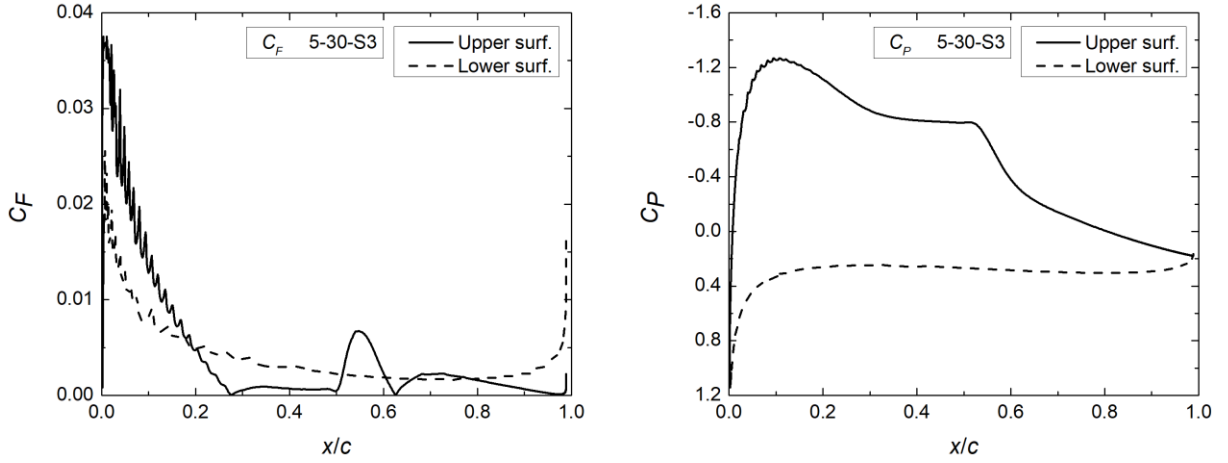


Figure B.3 – 5-30-S3 results, solidity = 0.3,  $u = 5$  m/s, TSR = 3.0, left:  $C_F$ , right:  $C_P$

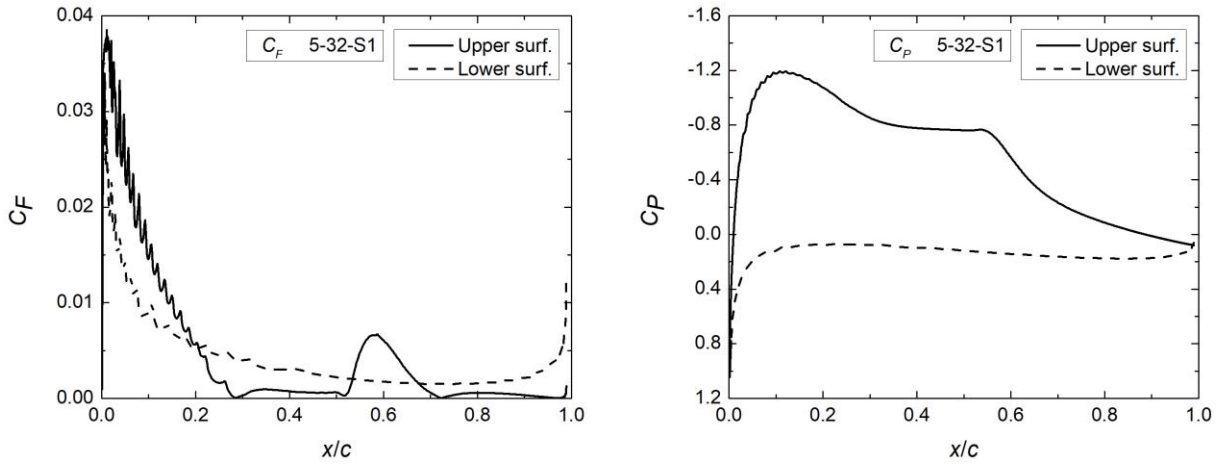


Figure B.4 – 5-32-S1 results, solidity = 0.1,  $u = 5$  m/s, TSR = 3.25, left:  $C_F$ , right:  $C_P$

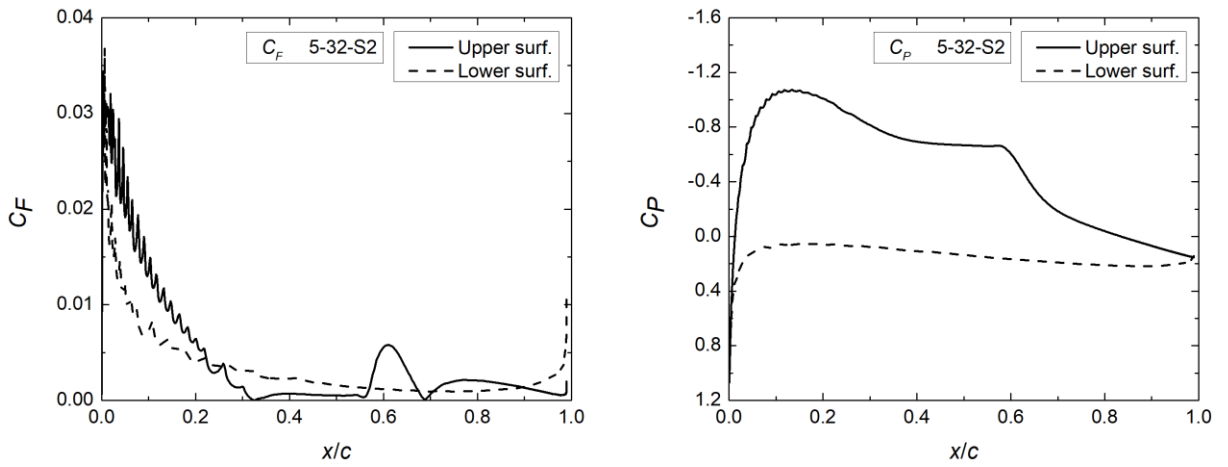


Figure B.5 – 5-32-S2 results, solidity = 0.2,  $u = 5$  m/s, TSR = 3.25, left:  $C_F$ , right:  $C_P$

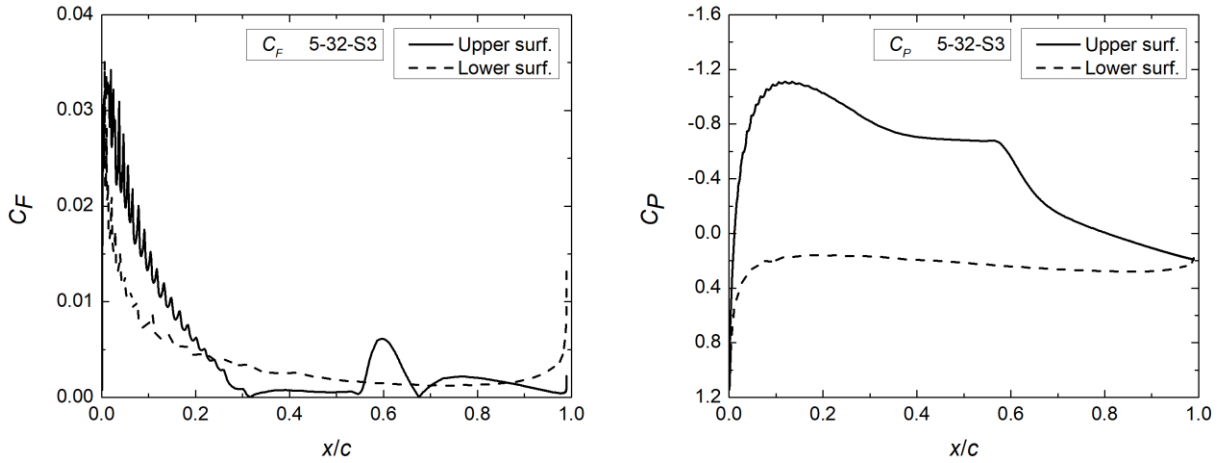


Figure B.6 – 5-32-S3 results, solidity = 0.3,  $u = 5$  m/s, TSR = 3.25, left:  $C_F$ , right:  $C_P$

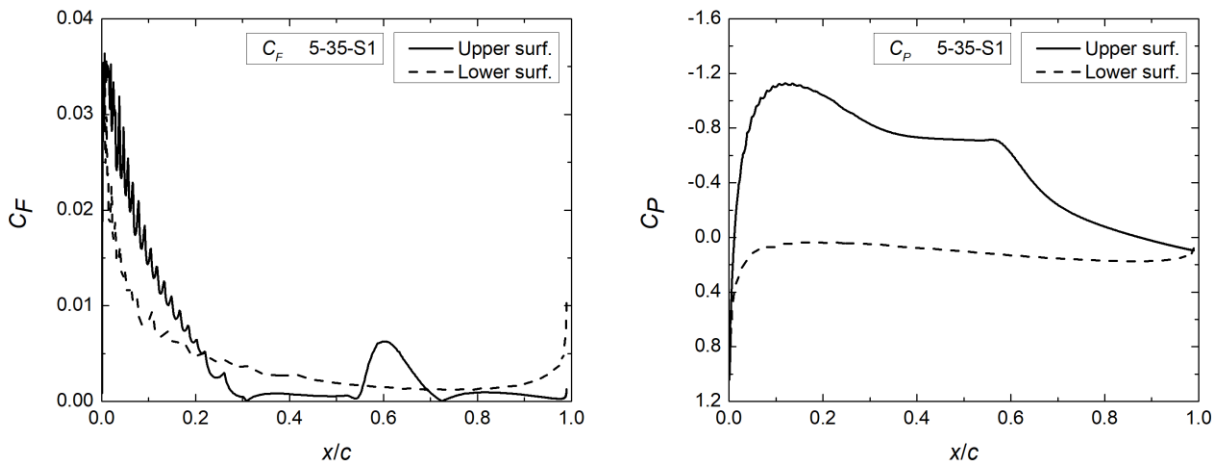


Figure B.7 – 5-35-S1 results, solidity = 0.1,  $u = 5$  m/s, TSR = 3.5, left:  $C_F$ , right:  $C_P$

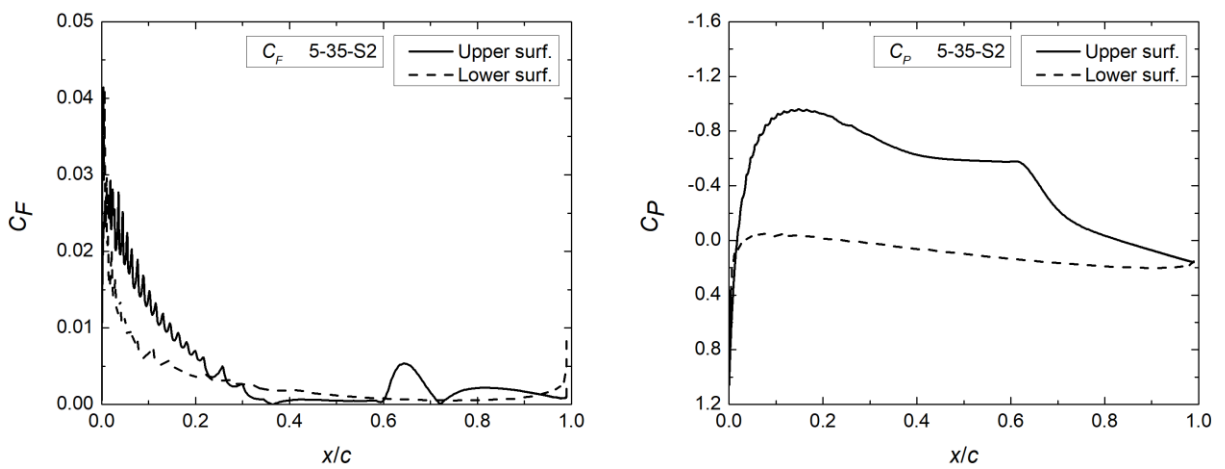


Figure B.8 – 5-35-S2 results, solidity = 0.2  $u = 5$  m/s, TSR = 3.5, left:  $C_F$ , right:  $C_P$



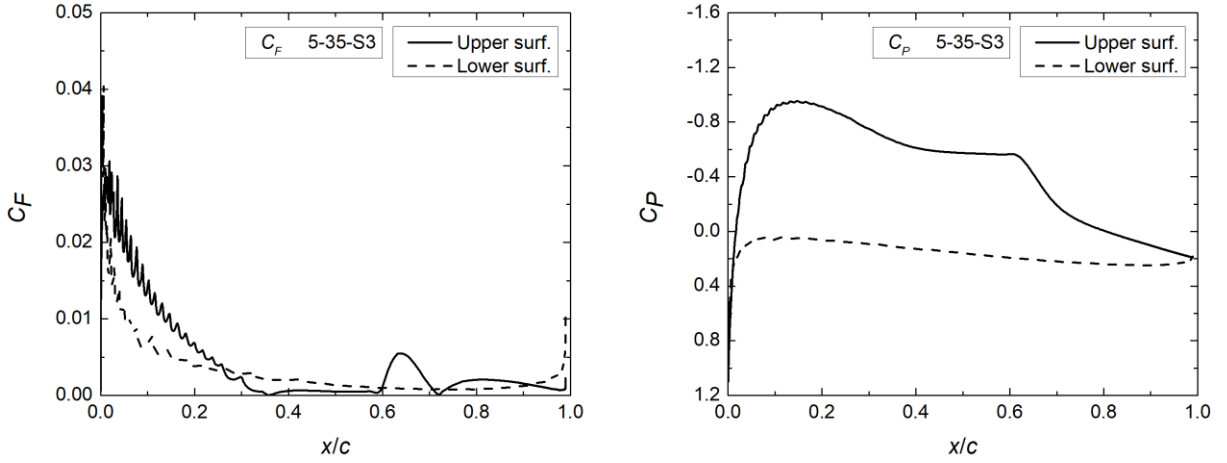


Figure B.9 – 5-35-S3 results, solidity = 0.3,  $u = 5$  m/s, TSR = 3.5, left:  $C_F$ , right:  $C_P$

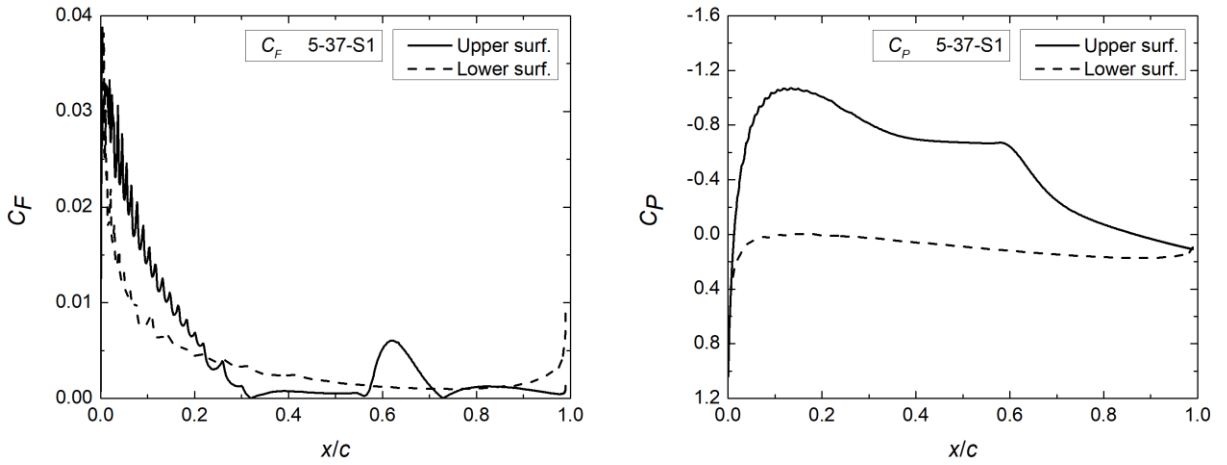


Figure B.10 – 5-37-S1 results, solidity = 0.1,  $u = 5$  m/s, TSR = 3.75, left:  $C_F$ , right:  $C_P$

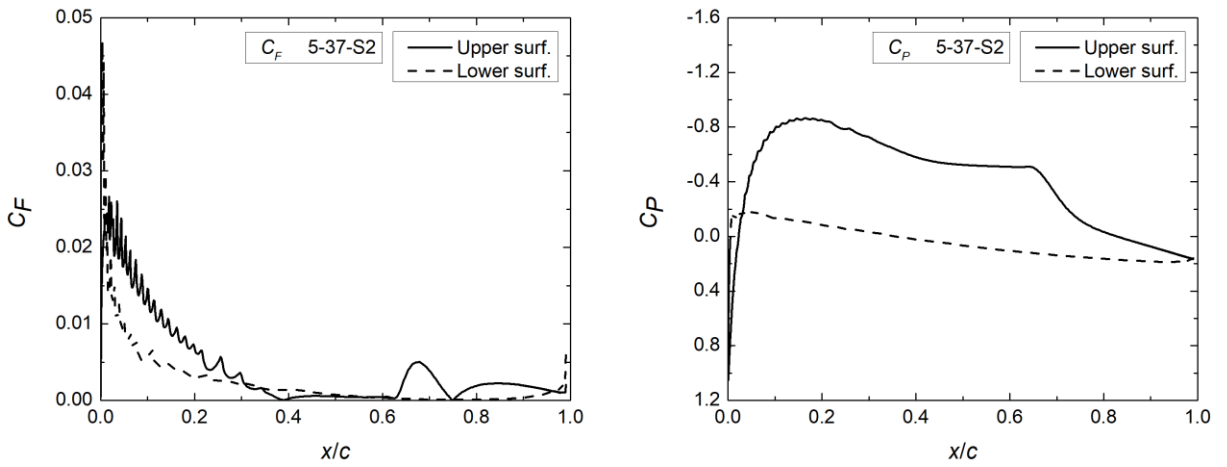


Figure B.11 – 5-37-S2 results, solidity = 0.2,  $u = 5$  m/s, TSR = 3.75, left:  $C_F$ , right:  $C_P$

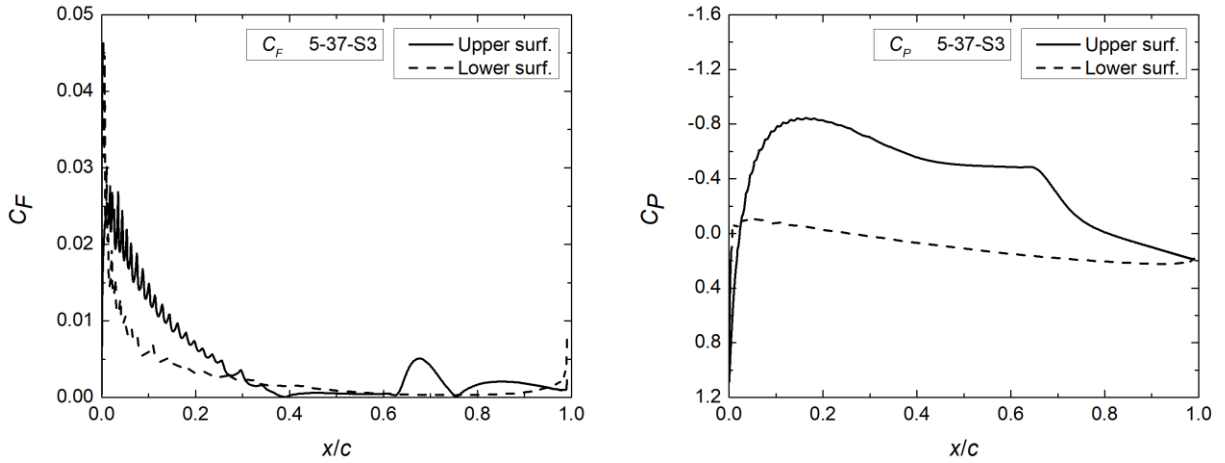


Figure B.12 – 5-37-S3 results, solidity = 0.3,  $u = 5$  m/s, TSR = 3.75, left:  $C_F$ , right:  $C_P$

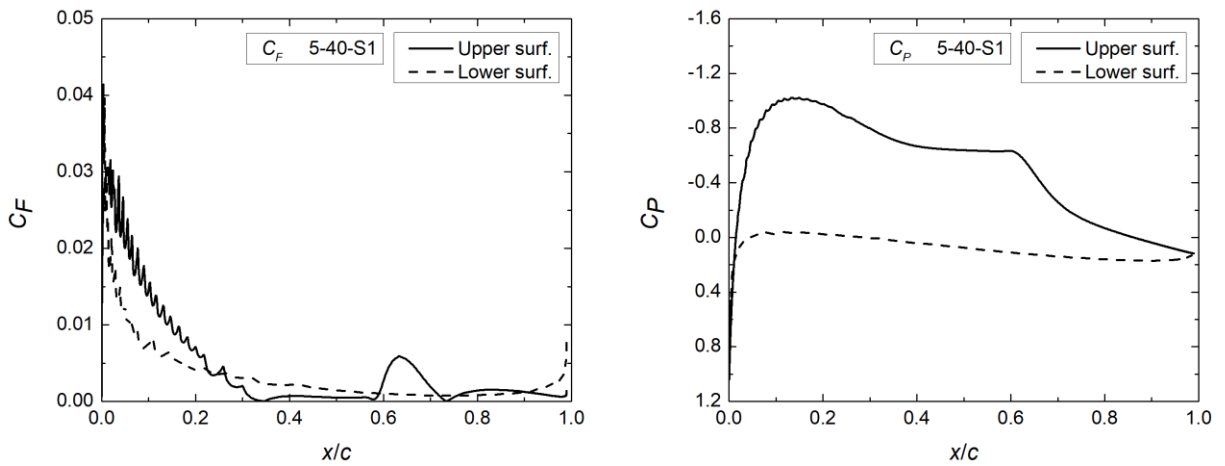


Figure B.13 – 5-40-S1 results, solidity = 0.1,  $u = 5$  m/s, TSR = 4.0, left:  $C_F$ , right:  $C_P$

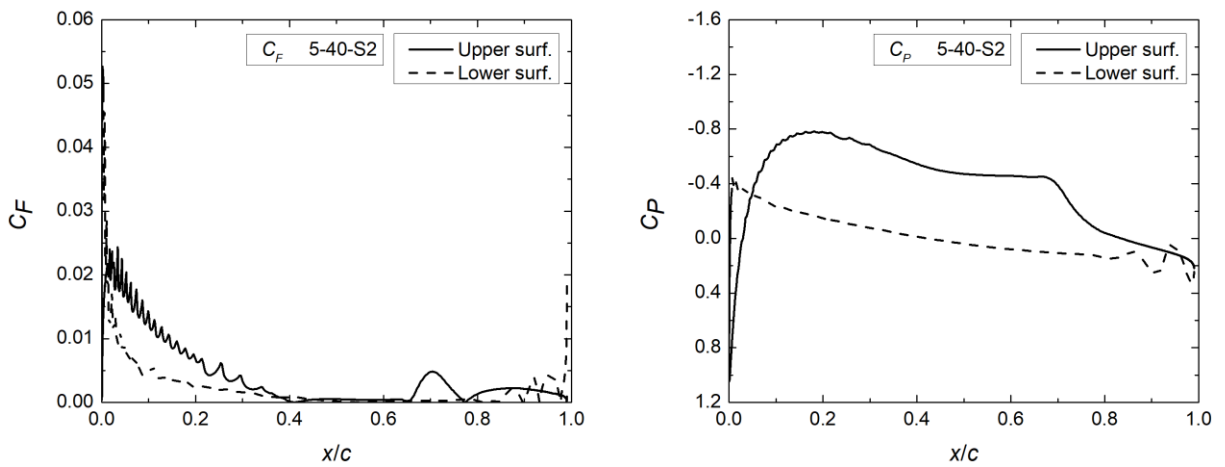


Figure B.14 – 5-40-S2 results, solidity = 0.2,  $u = 5$  m/s, TSR = 4.0, left:  $C_F$ , right:  $C_P$

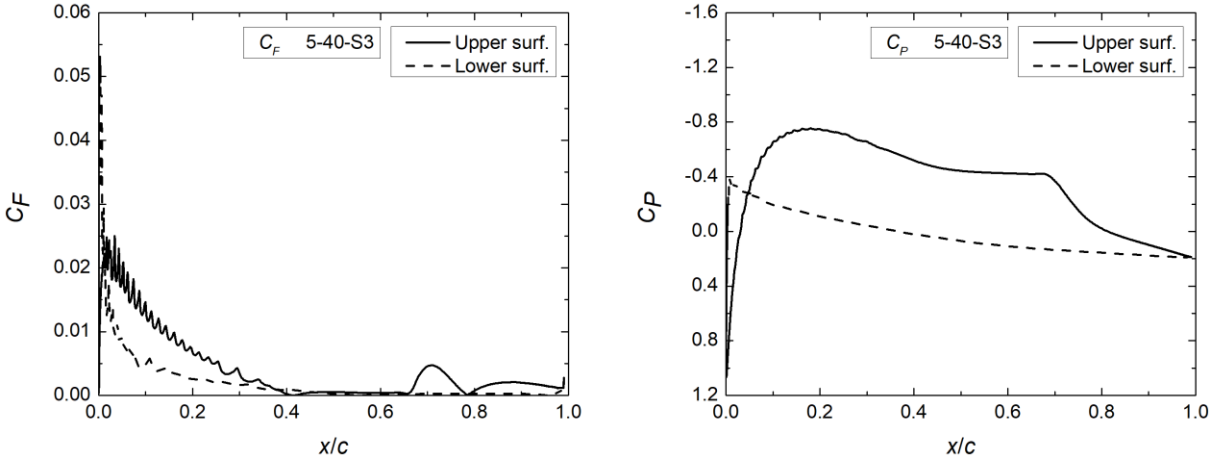


Figure B.15 – 5-40-S3 results, solidity = 0.3,  $u = 5$  m/s, TSR = 4.0, left:  $C_F$ , right:  $C_P$

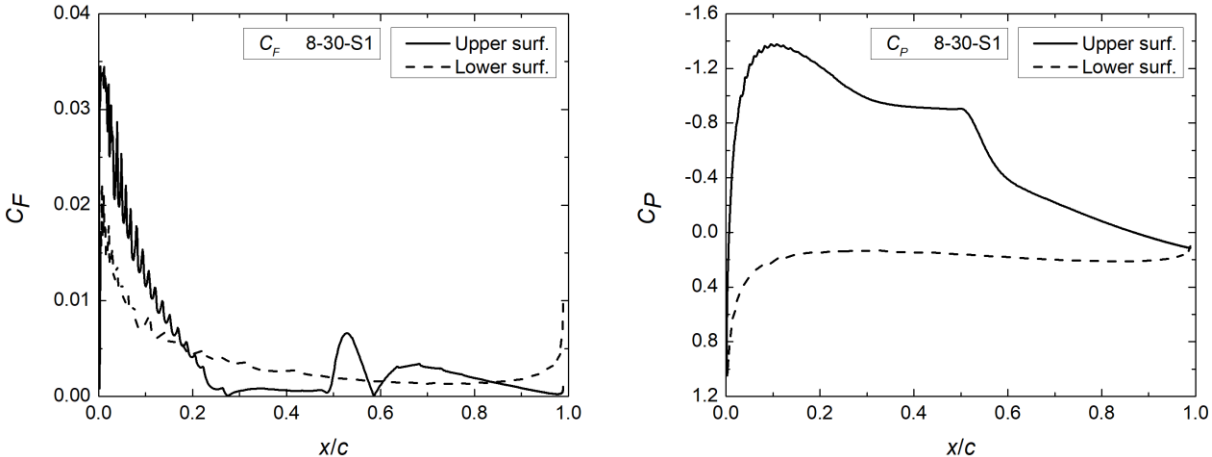


Figure B.16 – 8-30-S1 results, solidity = 0.1,  $u = 8$  m/s, TSR = 3.0, left:  $C_F$ , right:  $C_P$

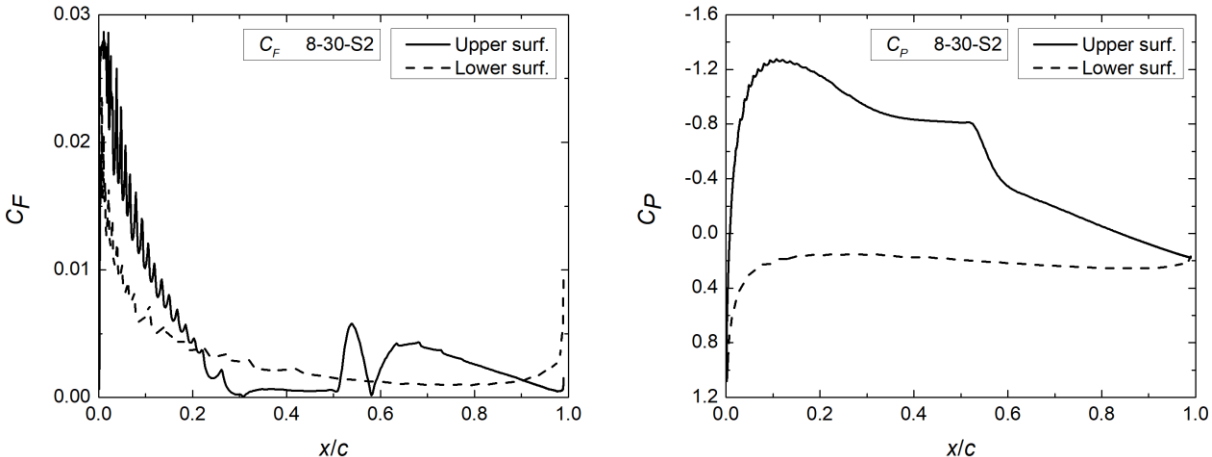


Figure B.17 – 8-30-S2 results, solidity = 0.2,  $u = 8$  m/s, TSR = 3.0, left:  $C_F$ , right:  $C_P$

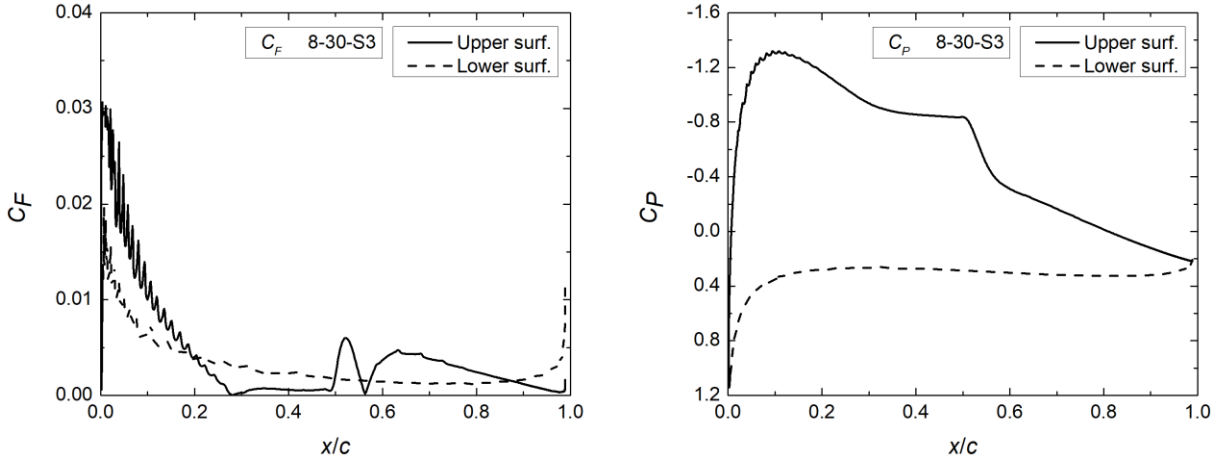


Figure B.18 – 8-30-S3 results, solidity = 0.3,  $u = 8$  m/s, TSR = 3.0, left:  $C_F$ , right:  $C_P$

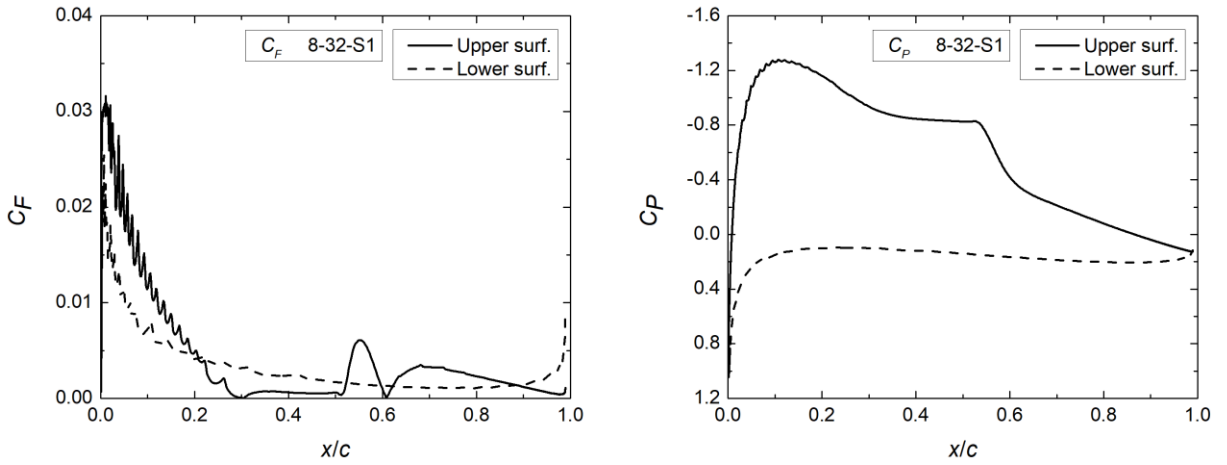


Figure B.19 – 8-32-S1 results, solidity = 0.1,  $u = 8$  m/s, TSR = 3.25, left:  $C_F$ , right:  $C_P$

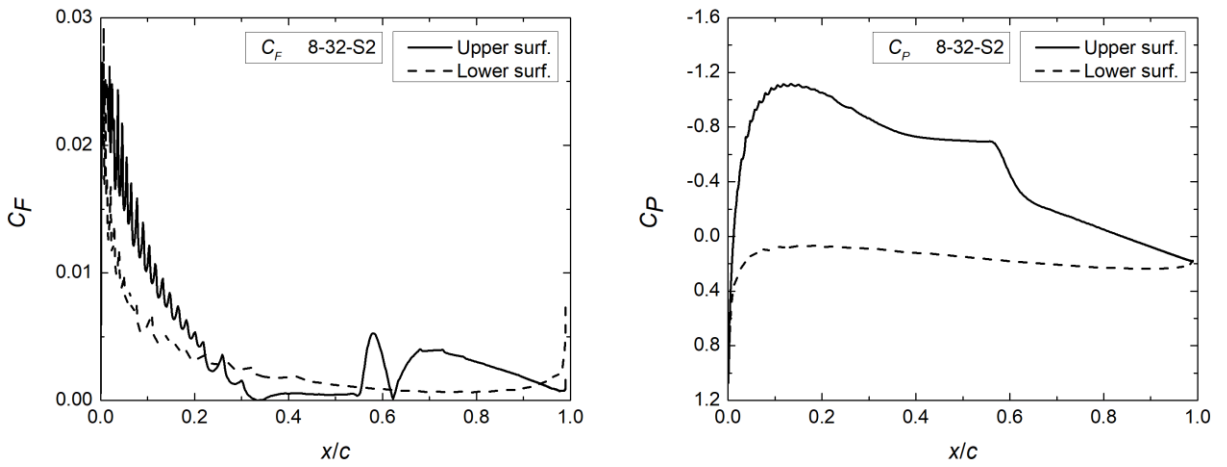


Figure B.20 – 8-32-S2 results, solidity = 0.2,  $u = 8$  m/s, TSR = 3.25, left:  $C_F$ , right:  $C_P$

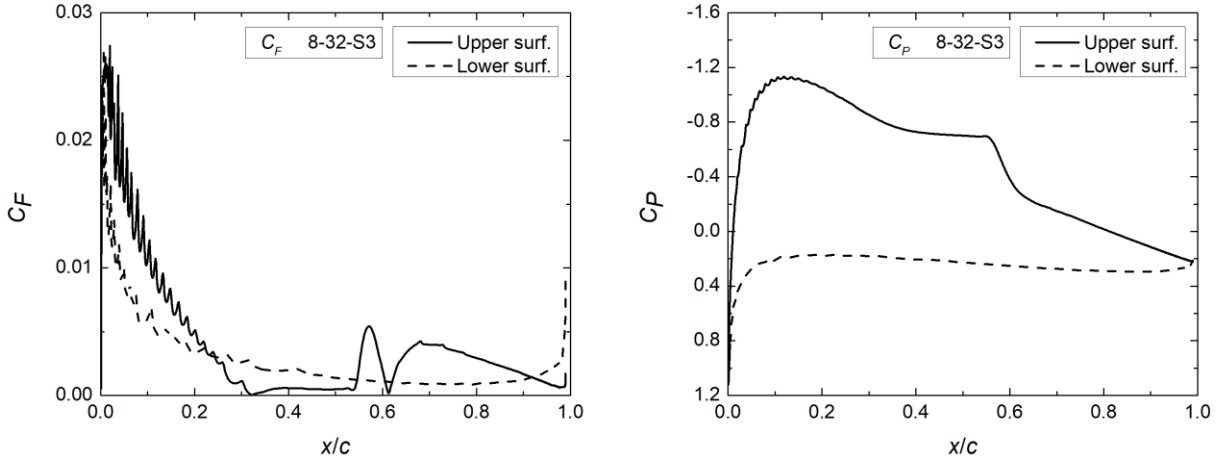


Figure B.21 – 8-32-S3 results, solidity = 0.3,  $u = 8$  m/s, TSR = 3.25, left:  $C_F$ , right:  $C_P$

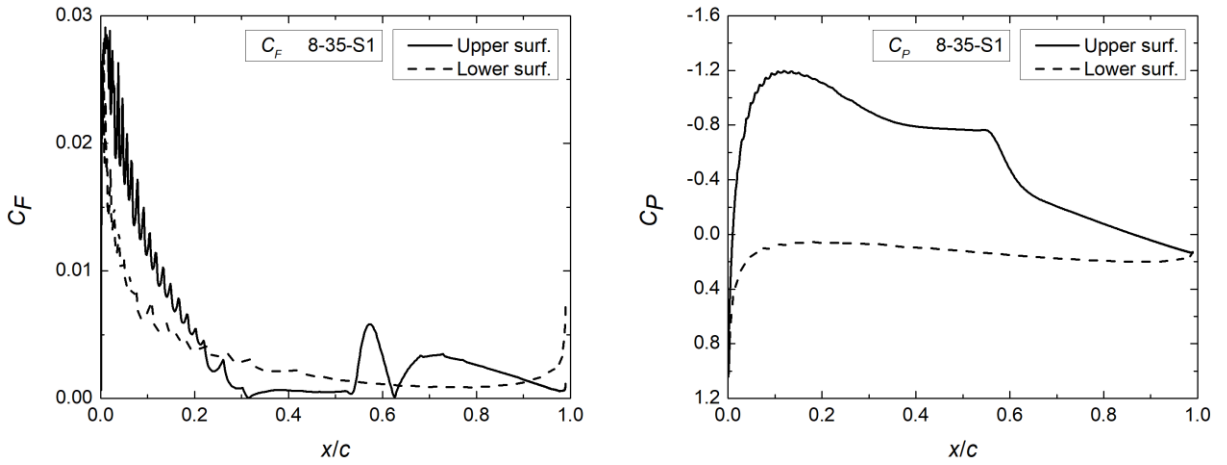


Figure B.22 – 8-35-S1 results, solidity = 0.1,  $u = 8$  m/s, TSR = 3.5, left:  $C_F$ , right:  $C_P$

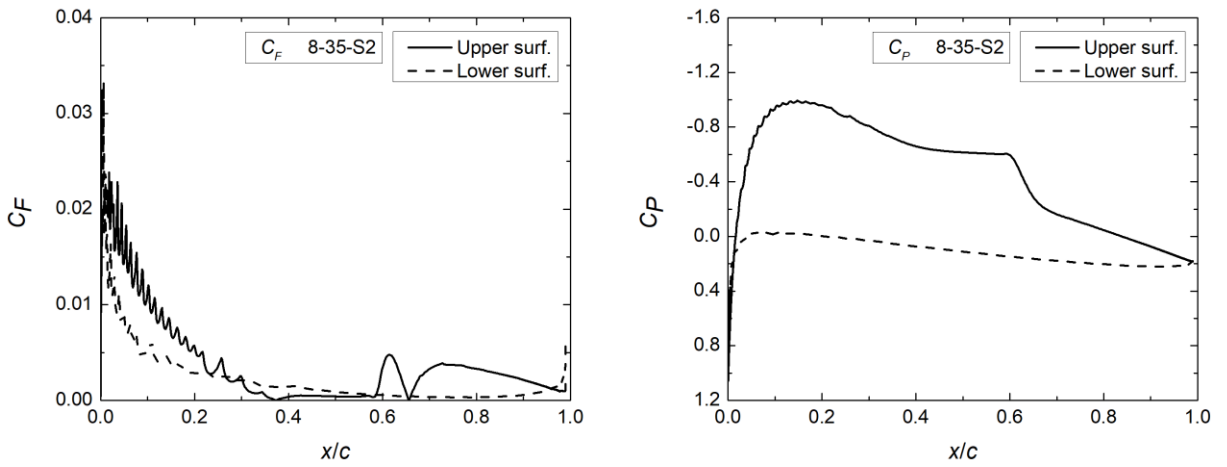


Figure B.23 – 8-35-S2 results, solidity = 0.2,  $u = 8$  m/s, TSR = 3.5, left:  $C_F$ , right:  $C_P$

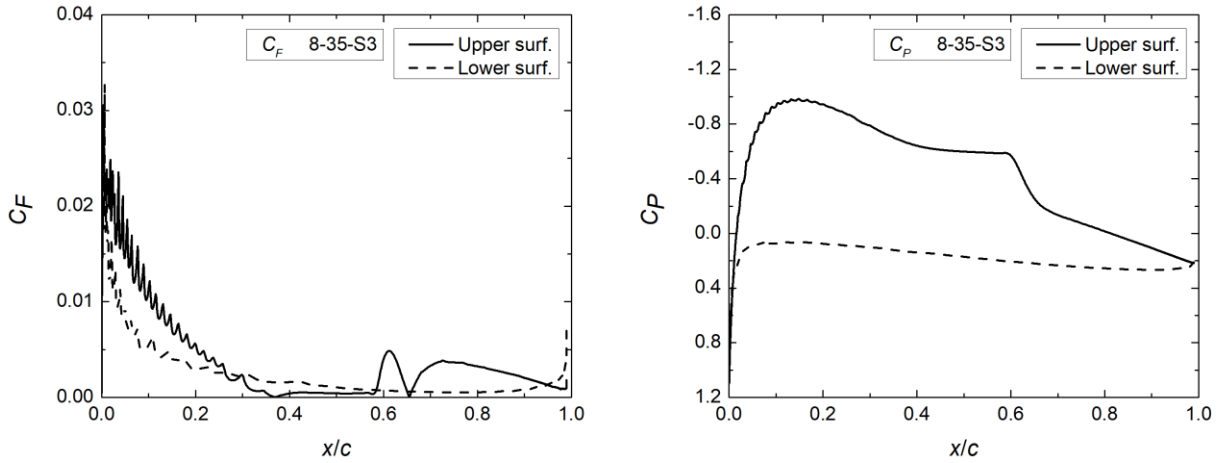


Figure B.24 – 8-35-S3 results, solidity = 0.3,  $u = 8$  m/s, TSR = 3.5, left:  $C_F$ , right:  $C_P$

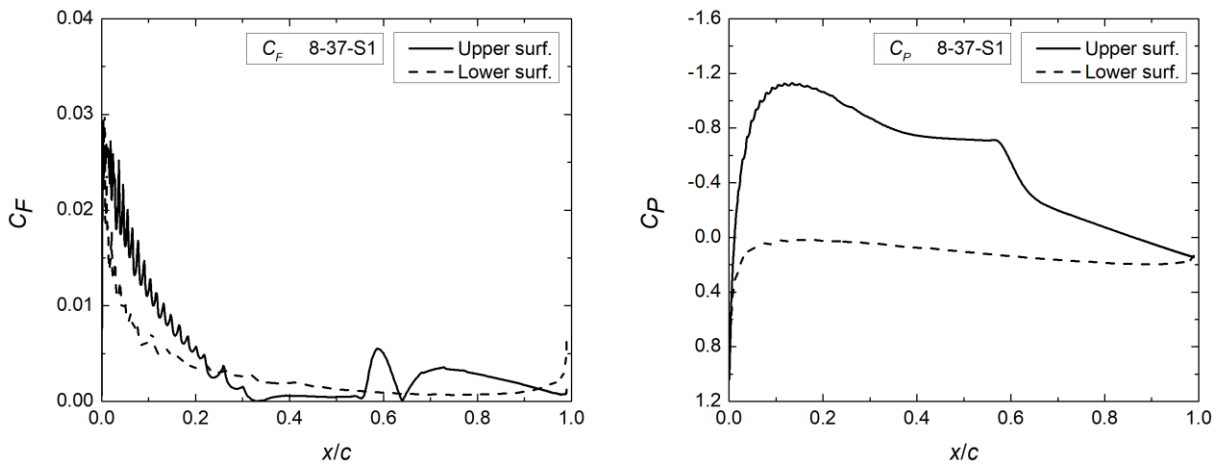


Figure B.25 – 8-37-S1 results, solidity = 0.1,  $u = 8$  m/s, TSR = 3.75, left:  $C_F$ , right:  $C_P$

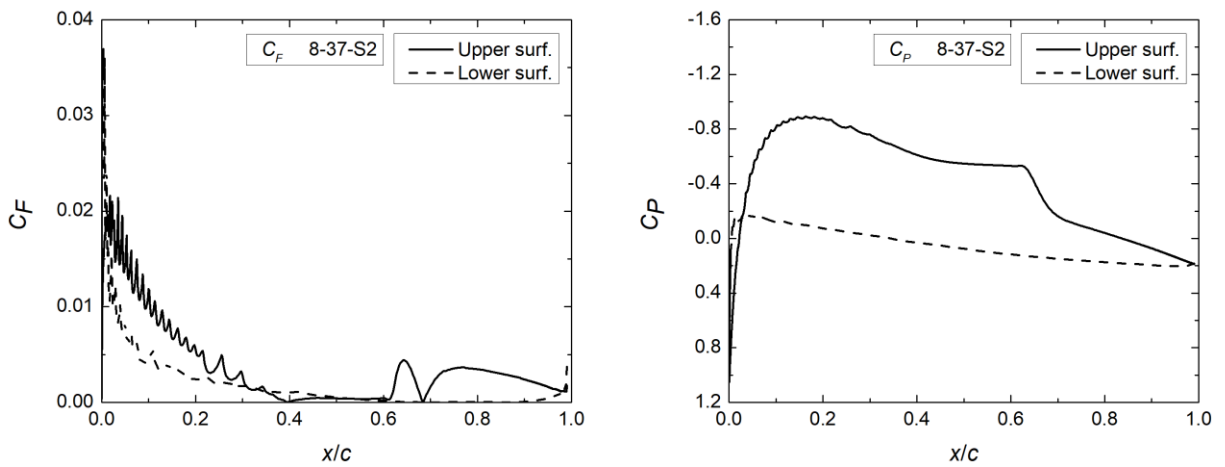


Figure B.26 – 8-37-S2 results, solidity = 0.2,  $u = 8$  m/s, TSR = 3.75, left:  $C_F$ , right:  $C_P$

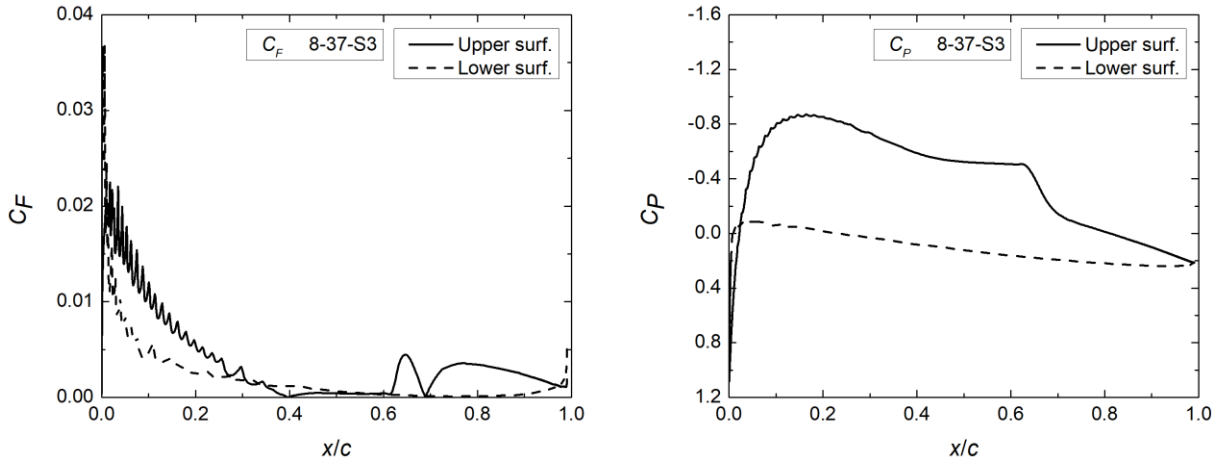


Figure B.27 – 8-37-S3 results, solidity = 0.3,  $u = 8$  m/s, TSR = 3.75, left:  $C_F$ , right:  $C_P$

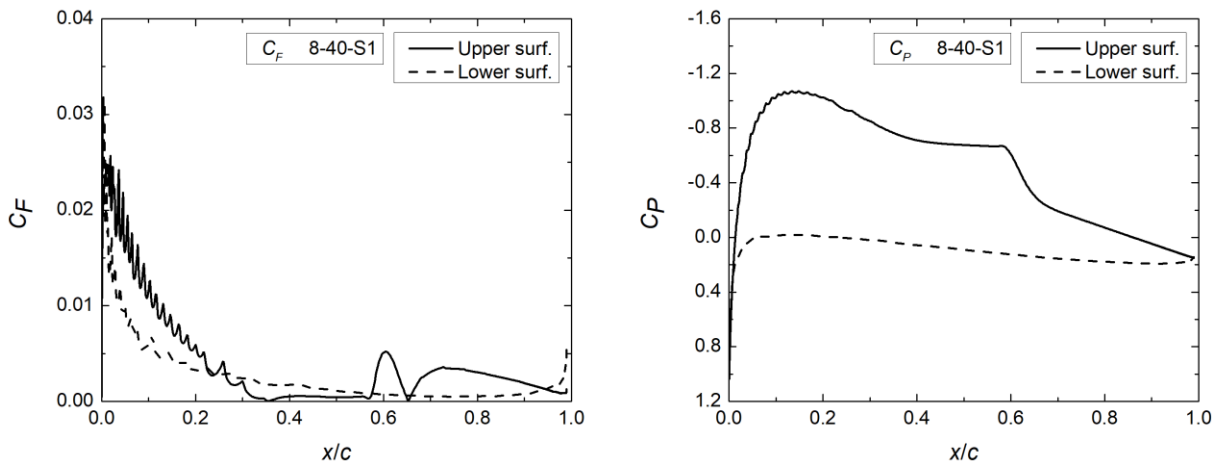


Figure B.28 – 8-40-S1 results, solidity = 0.1,  $u = 8$  m/s, TSR = 4.0, left:  $C_F$ , right:  $C_P$

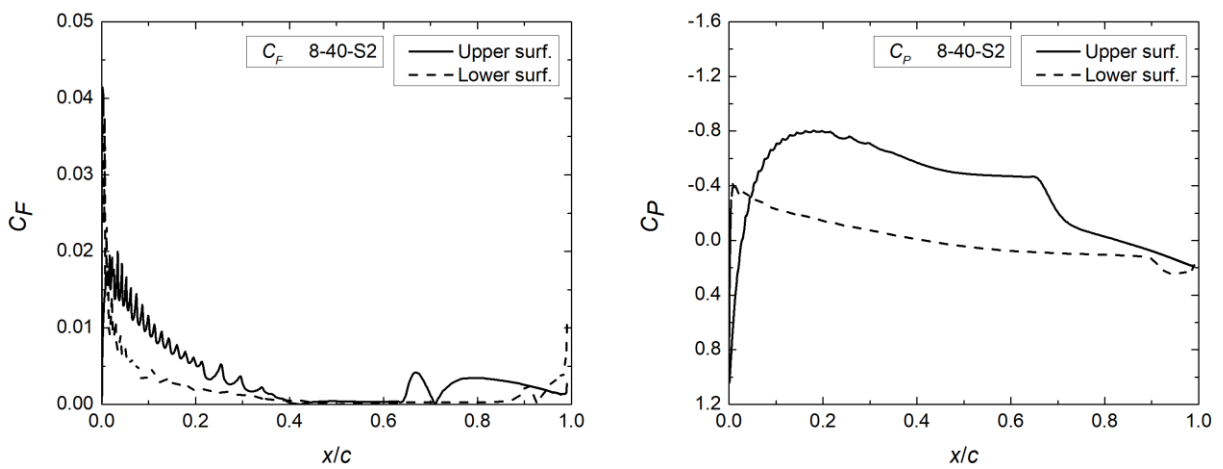


Figure B.29 – 8-40-S2 results, solidity = 0.2,  $u = 8$  m/s, TSR = 4.0, left:  $C_F$ , right:  $C_P$

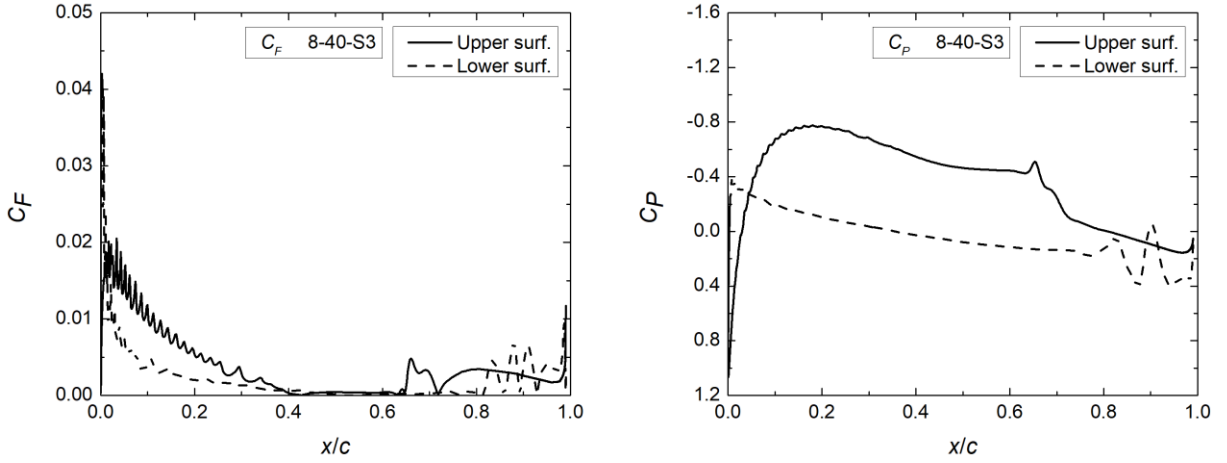


Figure B.30 – 8-40-S3 results, solidity = 0.3,  $u = 8$  m/s, TSR = 4.0, left:  $C_F$ , right:  $C_P$

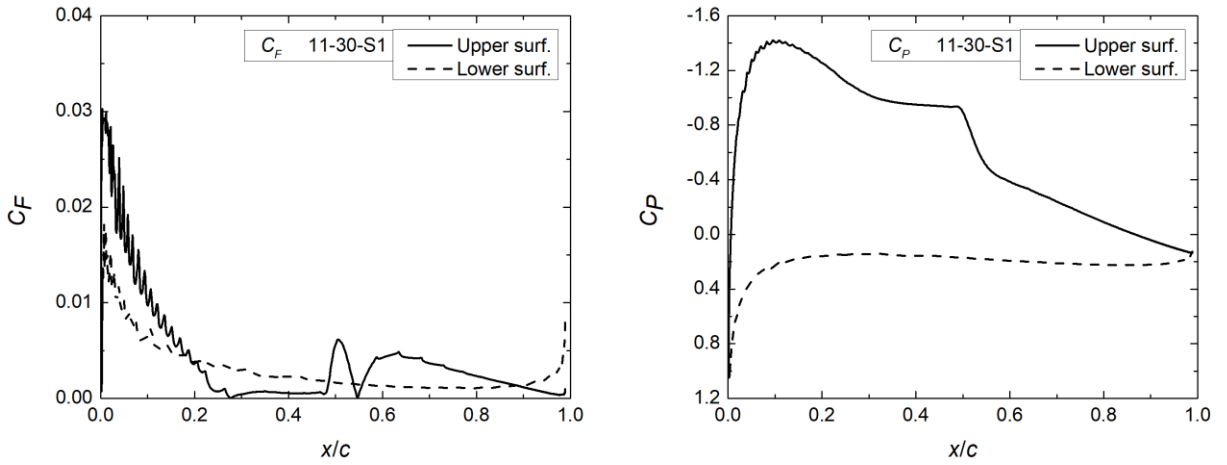


Figure B.31 – 11-30-S1 results, solid. = 0.1,  $u = 11$  m/s, TSR = 3.0, left:  $C_F$ , right:  $C_P$

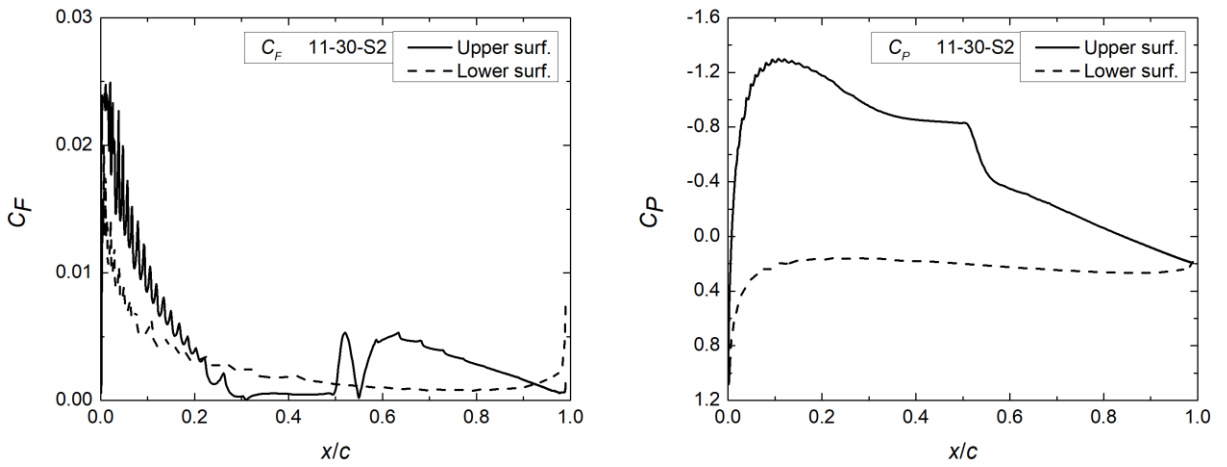


Figure B.32 – 11-30-S2 results, solid. = 0.2,  $u = 11$  m/s, TSR = 3.0, left:  $C_F$ , right:  $C_P$



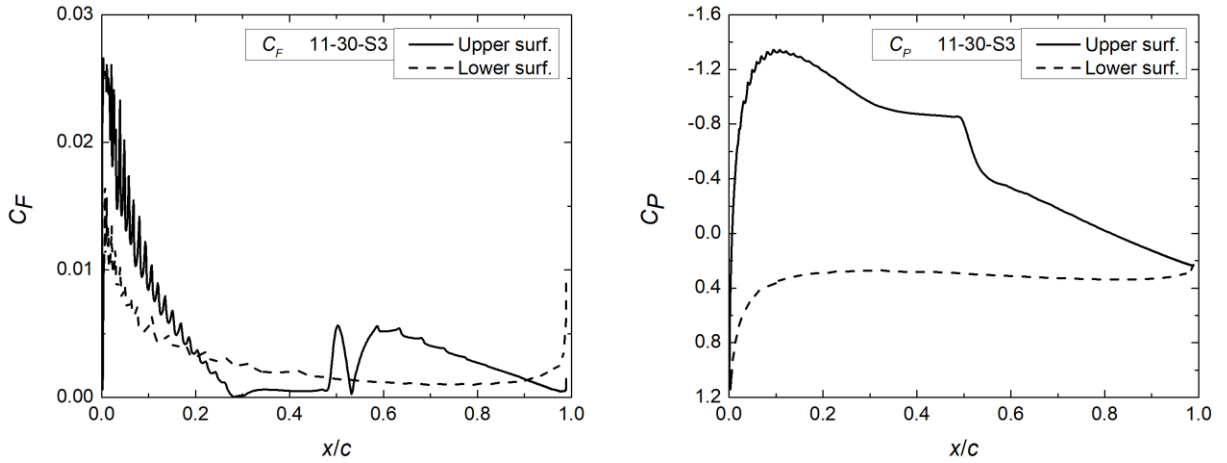


Figure B.33 – 11-30-S3 results, solid. = 0.3,  $u = 11$  m/s, TSR = 3.0, left:  $C_F$ , right:  $C_P$

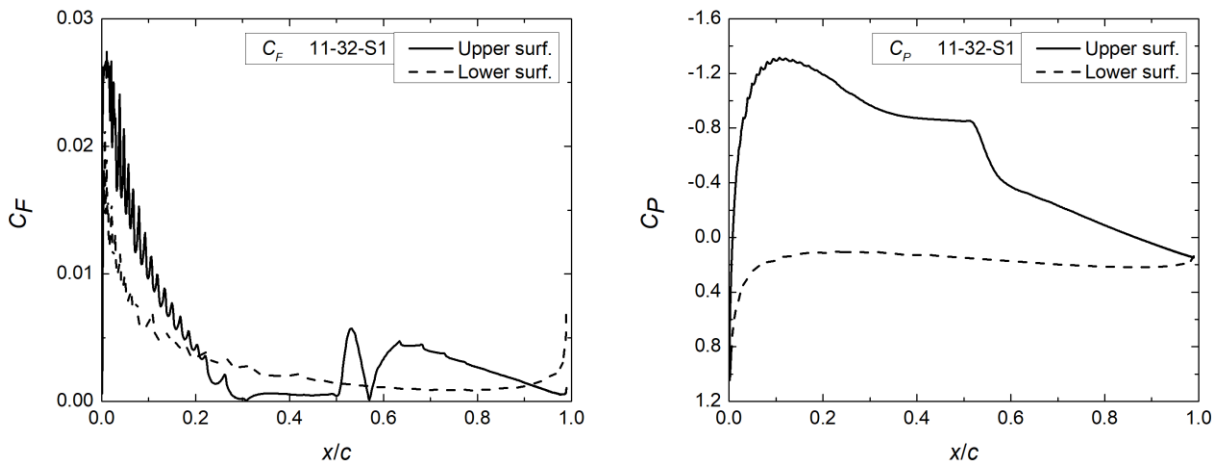


Figure B.34 – 11-32-S1 results, solid. = 0.1,  $u = 11$  m/s, TSR = 3.25, left:  $C_F$ , right:  $C_P$

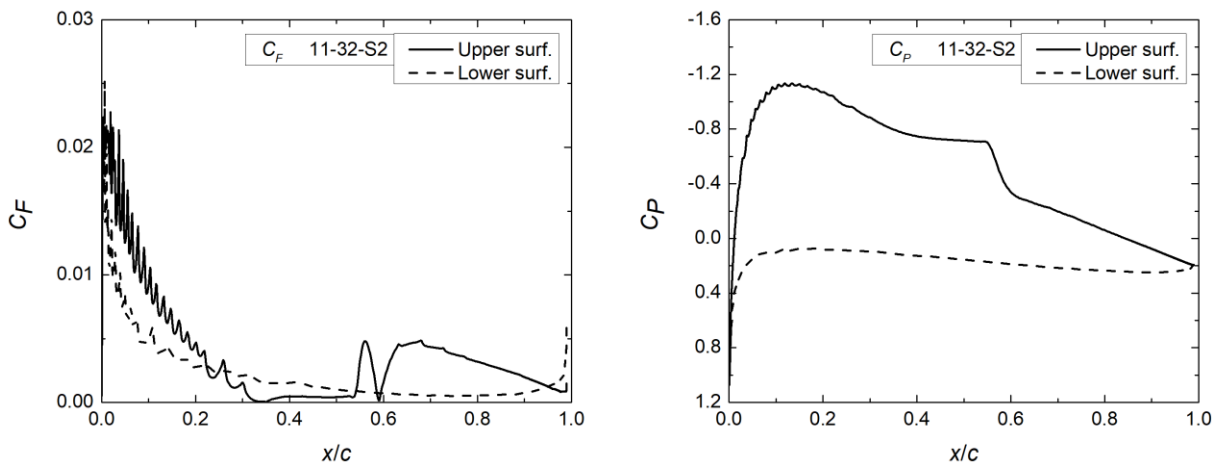


Figure B.35 – 11-32-S2 results, solid. = 0.2,  $u = 11$  m/s, TSR = 3.25, left:  $C_F$ , right:  $C_P$

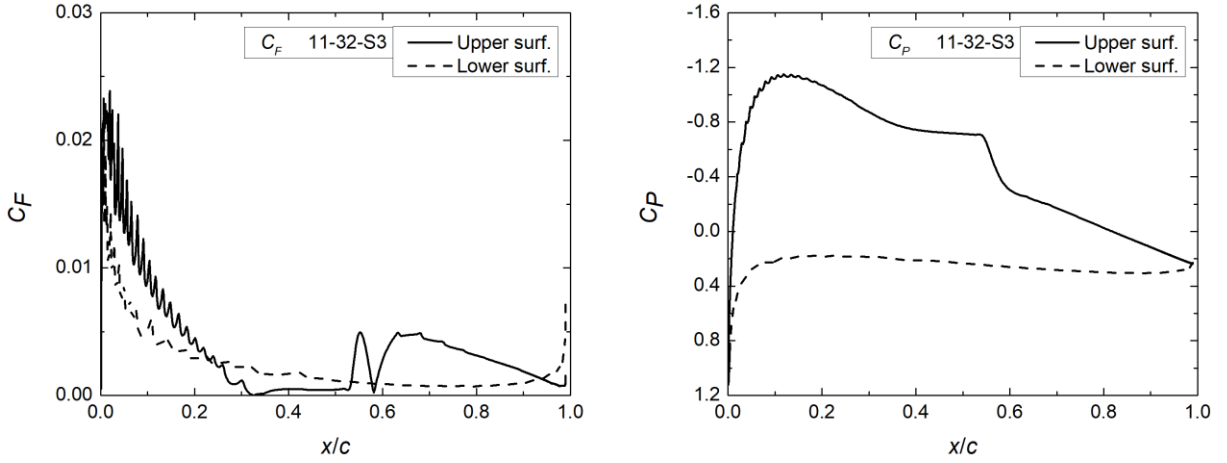


Figure B.36 – 11-32-S3 results, solid. = 0.3,  $u = 11$  m/s, TSR = 3.25, left:  $C_F$ , right:  $C_P$

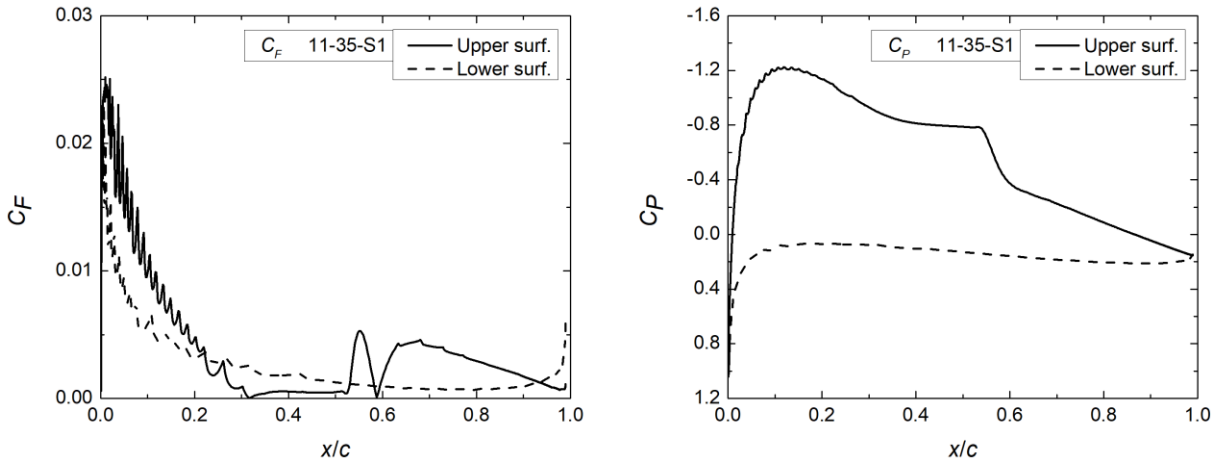


Figure B.37 – 11-35-S1 results, solid. = 0.1,  $u = 11$  m/s, TSR = 3.5, left:  $C_F$ , right:  $C_P$

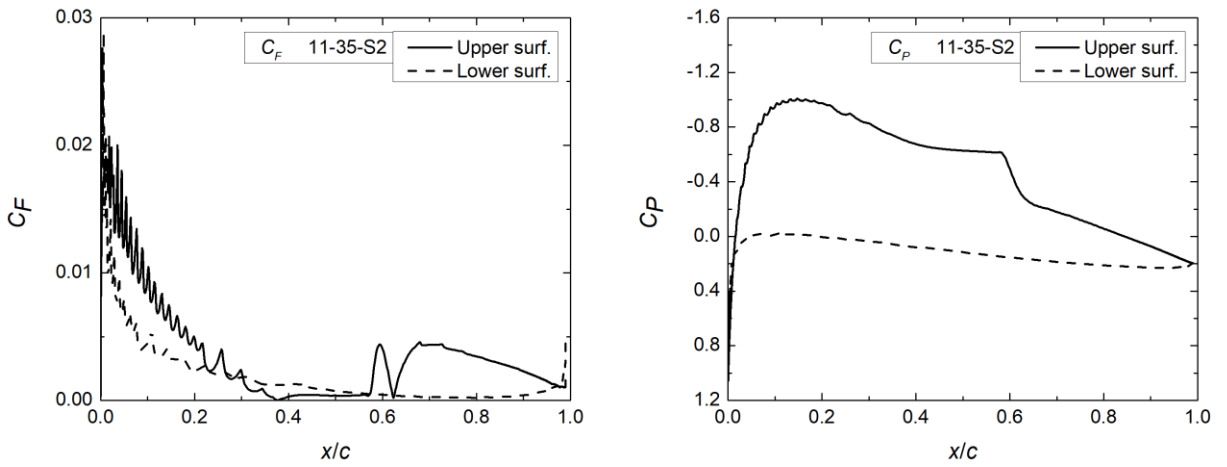


Figure B.38 – 11-35-S2 results, solid. = 0.2,  $u = 11$  m/s, TSR = 3.5, left:  $C_F$ , right:  $C_P$

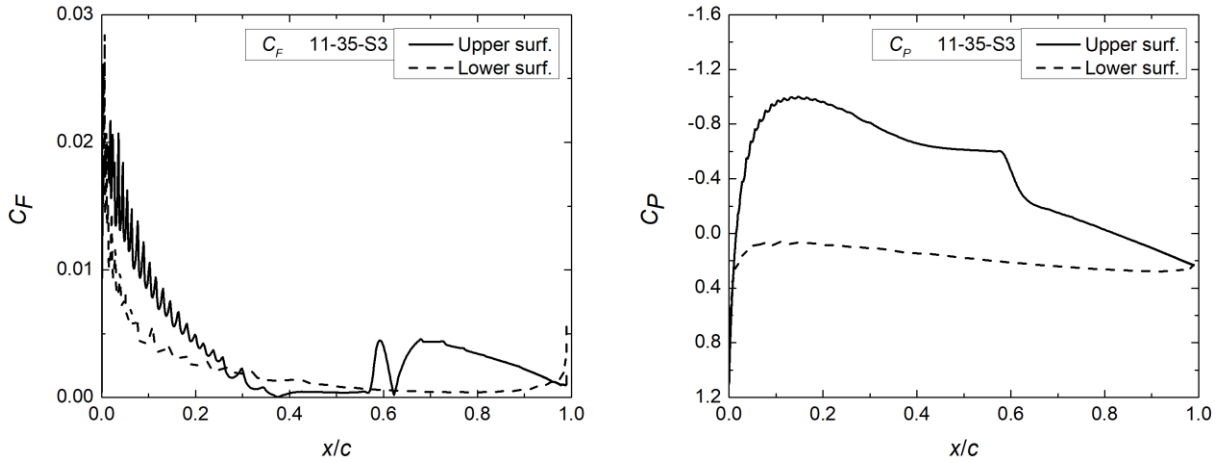


Figure B.39 – 11-35-S3 results, solid. = 0.3,  $u = 11$  m/s, TSR = 3.5, left:  $C_F$ , right:  $C_P$

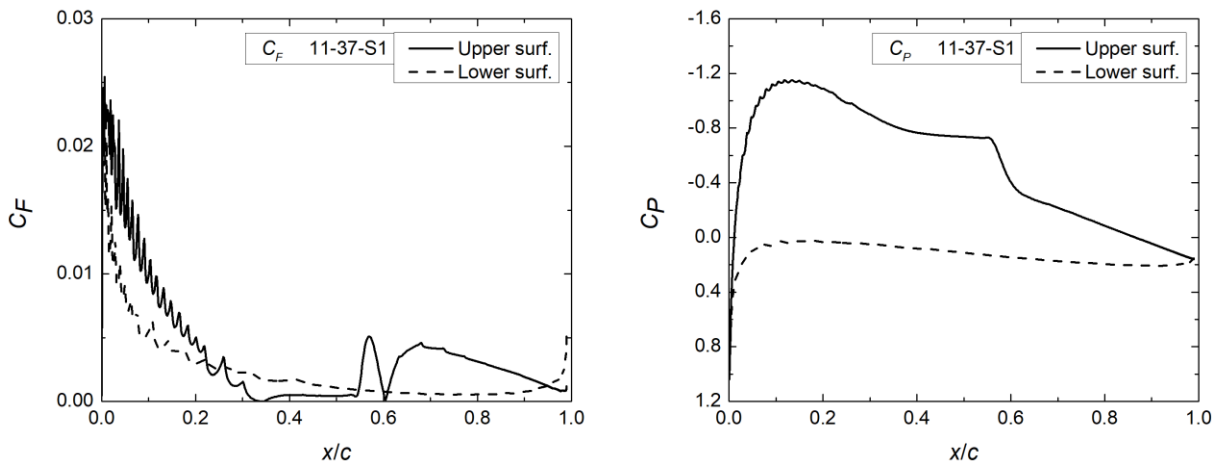


Figure B.40 – 11-37-S1 results, solid. = 0.1,  $u = 11$  m/s, TSR = 3.75, left:  $C_F$ , right:  $C_P$

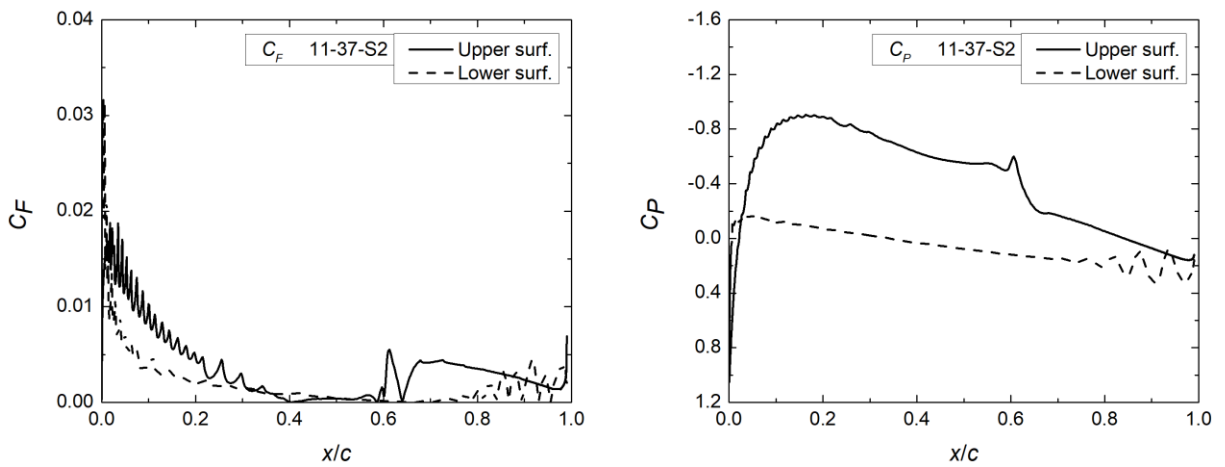


Figure B.41 – 11-37-S2 results, solid. = 0.2,  $u = 11$  m/s, TSR = 3.75, left:  $C_F$ , right:  $C_P$

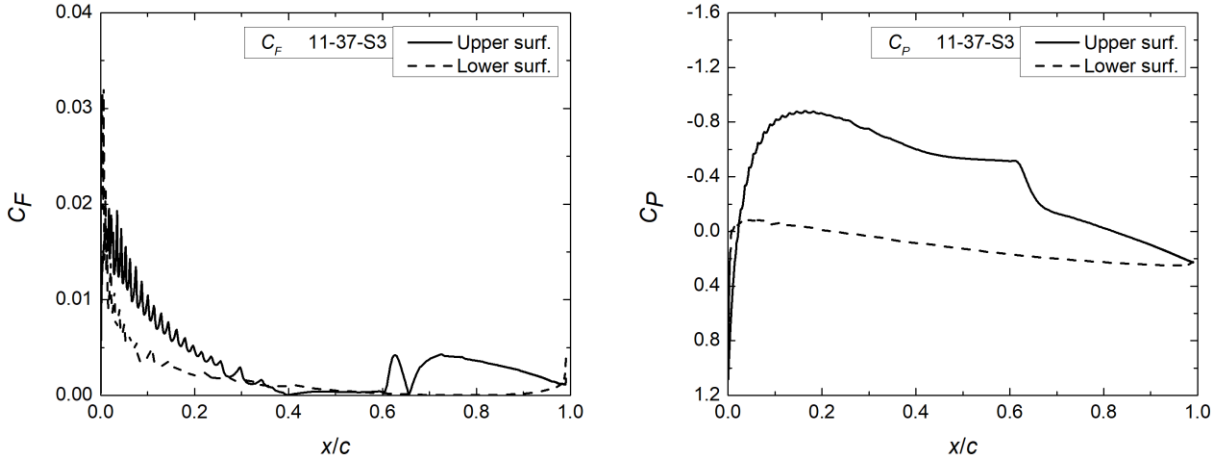


Figure B.42 – 11-37-S3 results, solid. = 0.3,  $u = 11$  m/s, TSR = 3.75, left:  $C_F$ , right:  $C_P$

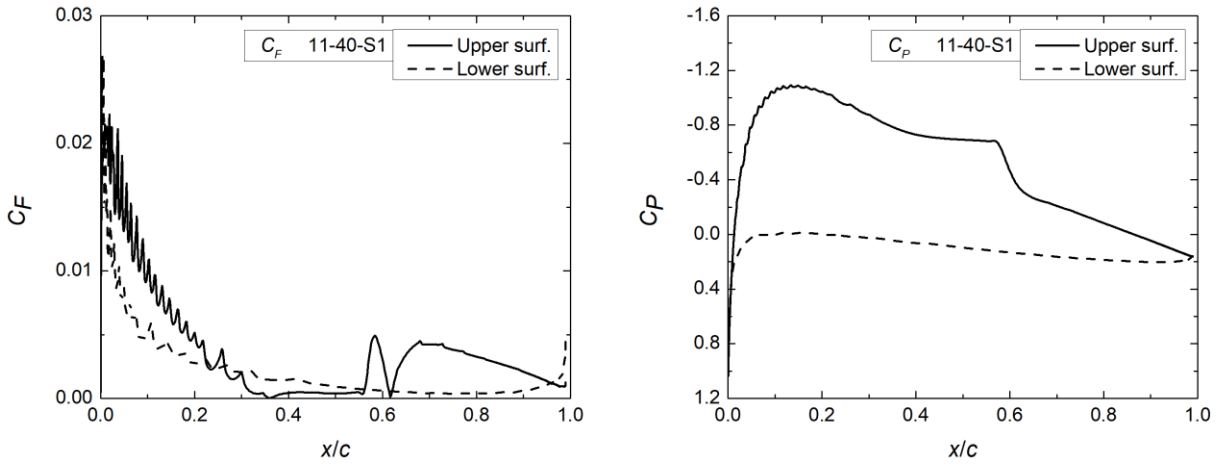


Figure B.43 – 11-40-S1 results, solid. = 0.1,  $u = 11$  m/s, TSR = 4.0, left:  $C_F$ , right:  $C_P$

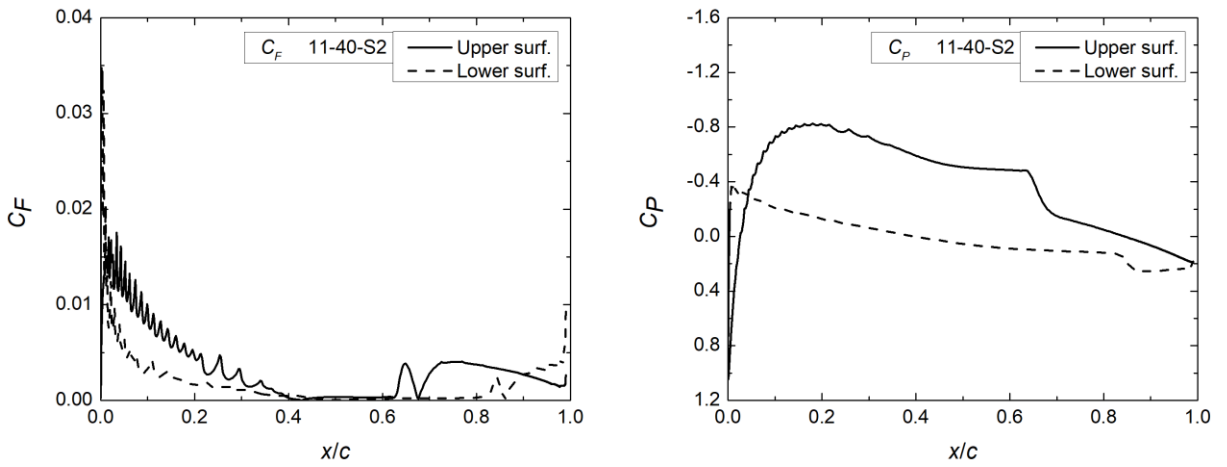


Figure B.44 – 11-40-S2 results, solid. = 0.2,  $u = 11$  m/s, TSR = 4.0, left:  $C_F$ , right:  $C_P$

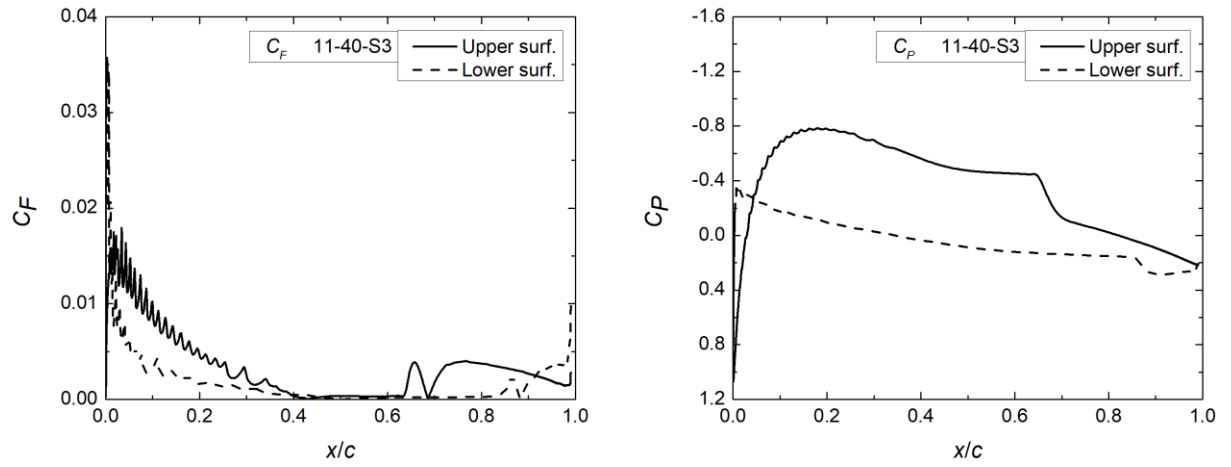


Figure B.45 – 11-40-S3 results,  $\sigma = 0.3$ ,  $u = 11$  m/s,  $\text{TSR} = 4.0$ , left:  $C_f$ , right:  $C_p$